

**Dijet Photoproduction
and the
Structure of the Proton
with the
ZEUS Detector**

September 27, 2006

Christopher Targett-Adams

University College London
2006

Thesis submitted to the University College London
in accordance with the requirements of the degree of
Doctor of Philosophy in the Faculty of Science.

Abstract

The photoproduction cross section for high- E_T dijets has been measured using the ZEUS detector at HERA using an integrated luminosity of 81.8 pb^{-1} . The events were required to have a virtuality of the incoming photon, Q^2 , of less than 1 GeV^2 and a photon-proton centre-of-mass energy in the range $142 < W_{\gamma p} < 293 \text{ GeV}$. Each event contains at least two jets satisfying transverse-energy requirements of $E_{T,1} > 20 \text{ GeV}$ and $E_{T,2} > 15 \text{ GeV}$ and pseudorapidity requirements of $-1 < \eta_{1,2} < 3$ with at least one of the jets satisfying $-1 < \eta < 2.5$. These data have been used to further constrain the parton densities in the proton. The measurements are compared to next-to-leading order QCD predictions and show sensitivity to the choice of the parton densities in the photon and to the effects of higher orders.

Acknowledgements

The successful completion of this thesis would not have been possible without the help and support of a large number of people. Foremost, I would like to thank my supervisor, Jonathan Butterworth, for his help and guidance over the course of my PhD. A large amount of credit must also be given to Matthew Wing who performed the second analysis which supported the work presented in this thesis and gave me invaluable help throughout my PhD. I would also like to thank Claire Gwenlan for all her input regarding the fitting aspect of my thesis work. I would also like to give a general thank you to all the other people from UCL and the ZEUS collaboration who have provided me with help and support over the last few years.

Introduction

This thesis describes the analysis of dijet production in photoproduction, using the ZEUS detector at HERA, and the application of such measurements in determining structural information about the proton and photon.

At ZEUS, electrons and positrons were collided with protons at a centre of mass energy of $\sqrt{s} = 318$ GeV. The analysis presented in this thesis is concerned with the 1998-00 data set which amounts to an integrated luminosity of 81.8 pb^{-1} .

The topics presented in this thesis fall into three categories. Firstly, the incorporation of existing ZEUS photoproduction dijet data into fits (performed by the ZEUS collaboration) to determine the parton densities of the proton is presented (these are the so-called ZEUS QCD fits). One of the results of incorporating the jet data into the fit was a significant improvement in the precision of the extracted gluon parton density function (PDF). Next, a study was conducted to ascertain which dijet photoproduction cross-sections display the most sensitivity to the uncertainties of the underlying gluon PDF. Thirdly, the measurement of such optimised cross-sections along with a series of generic dijet cross-sections is presented. The cross-sections measured in this thesis have been compared to the most up-to-date photon parameterisations and updated ZEUS QCD fits have been performed which include the new optimised cross-sections.

Dijet cross-sections were measured in the laboratory frame for jets with transverse energy $E_{T,jet} > 20$ and 15 GeV and pseudorapidity range $-1 < \eta_{jet} < 3$, with at least one of the jets satisfying $-1 < \eta_{jet} < 2.5$. This is the first time that a photoproduction measurement has been conducted in the pseudorapidity range $2.5 < \eta < 3$. The variable x_γ^{obs} , a measure of the fractional photon momentum entering the hard process, was used to enhance the sensitivity of the measurements to the photon structure.

Next-to-leading order (NLO) QCD predictions were found to agree reasonably well for most dijet distributions at high- x_γ^{obs} but poorly described the measured data at low- x_γ^{obs} . The level of agreement in the low- x_γ^{obs} case is dependent on the transverse energy involved and the photon parameterisation used in the prediction. At low transverse energies, the data is well described by the AFG, GRV and SAL photon parameterisations but poorly described at higher transverse energies. On the other hand, the CJK photon parameterisation overestimates the data at low transverse energies but describes the data reasonably well at higher transverse energies.

The differential cross-section as a function of $|\Delta\phi|$ is of particular interest as it is directly sensitive to higher-order topologies and provides an excellent test of NLO QCD. It was found that the data was very poorly described by the NLO calculation which suggests that the theoretical predictions need to be conducted to higher-orders to provide a reasonable description of all the ZEUS dijet photoproduction distributions.

The inclusion of the optimised cross-section measurements in a new QCD fit

to ZEUS data did not result in a significant improvement in the precision of the extracted gluon PDF. The optimised cross-section data did not significantly constrain the gluon PDF beyond the jet data which was already included in the fit.

Outline

Chapter 1 briefly describes the HERA machine and ZEUS detector with most emphasis being placed on the components which are used directly in this analysis. Chapter 2 gives an introduction to the theoretical concepts which underpin the work presented in this thesis. In chapter 3 a discussion is given of the general principles that are used during the course of making an experimental cross-section measurement with particular emphasis on the machinery and methods which are employed by the ZEUS collaboration. In chapter 4 the discussion moves on to discuss the fits which are carried out by the ZEUS collaboration to determine the parton densities of the proton. In particular this chapter will discuss the method by which photoproduction dijet cross-sections can be included in the fits, which the author was personally responsible for. During chapter 5 details are given of the optimisation study that was performed in order to attempt to ascertain photoproduction dijet cross-sections which show particular sensitivity to the gluon parton density. During the course of chapters 6 and 7 details will be given of the reconstruction of kinematic variables and the selection of dijet photoproduction events. In chapter 8 a step-by-step guide is given to illustrate the method used to measure a particular cross-section and compare the result to theoretical predictions. Chapter 9 then extends this work and presents the cross-section results for all cross-sections that have been considered during the course of the present analysis. Finally, chapter 10 discusses the impact that the new cross-section measurements have when included in a new set of fits to determine the parton densities of the proton. Due to the large number of cross-sections which have been considered in this thesis a lot of information has been segregated from the main body of text and deferred to appendices in order to make the main body of the document less cumbersome and to place the main focus on the final results.

Contents

Abstract	1
Acknowledgements	2
Introduction	3
Outline	5
Contents	6
List of Figures	11
List of Tables	15
1 HERA and the ZEUS Detector	19
1.1 HERA	19
1.1.1 A brief history of HERA	19
1.1.2 Description of HERA	20
1.2 The ZEUS coordinate system	22
1.3 The ZEUS detector	23
1.4 The Tracking Detectors	23
1.4.1 The Central Tracking Detector (CTD)	23
1.4.2 The Forward Detector (FDET)	26
1.4.3 The Rear Tracking Detector (RTD)	26
1.4.4 The Small Angle Rear Tracking Detector (SRTD)	27
1.5 The Uranium Calorimeter (CAL)	27
1.6 The Luminosity Monitor	29
1.7 The ZEUS Trigger and Data Acquisition System.	30
1.7.1 The First Level Trigger	31

1.7.2	The Second Level Trigger	32
1.7.3	The Third Level Trigger	32
1.8	The HERA Upgrade	32
2	QCD and $e^\pm p$ Physics	34
2.1	e^\pm Scattering	34
2.2	The e^\pm Cross-Section	36
2.3	Scaling Violations and Parton Distribution Functions	37
2.3.1	The Factorisation Theorem of QCD	39
2.4	Photoproduction	40
2.5	Direct Photoproduction	41
2.6	Resolved Photoproduction	43
2.7	Definition of Jets	45
2.7.1	The k_T Algorithm	45
3	Monte Carlo Simulation and Data Correction	48
3.1	Using Simulated Data in Particle Physics Analyses	48
3.2	Monte Carlo Event Generators	50
3.2.1	HERWIG Monte Carlo	52
3.2.2	PYTHIA Monte Carlo	53
3.3	AMADEUS (aka ZDIS)	54
3.4	FUNNEL and the ZEUS MC Chain	55
3.5	Hadronisation Corrections	57
3.6	Acceptance Corrections	58
3.7	Bin-By-Bin Correction	59
4	Determination of Parton Densities	62
4.1	Introduction	62
4.2	Brief History of the ZEUS QCD Fits	64
4.2.1	The ZEUS-S,ZEUS- α_s and ZEUS-O Fits	64
4.2.2	The ZEUS-Type5 Fit	65
4.2.3	The ZEUS-Jets Fit	65
4.3	Fitting Method	65
4.3.1	Parameterisation of the PDFs	66
4.3.2	Definition of the χ^2 and the Determination of PDF Errors	67
4.4	Adding γp Dijet Data into the Fit: Part 1	68

4.4.1	An Outline of the Problem	69
4.4.2	Derivation of the Cross-Section Grid	70
4.4.3	Reconstructing the Cross-Section	73
4.4.4	Calculation of the Cross-Section Grid	73
4.4.5	Deconvolution of α_s	76
4.4.6	Calculation of the α_s Independent Cross-Section Grid	77
4.4.7	Cross-Section Grids: Summary	78
4.5	Adding γp Dijet Data into the Fit: Part 2	79
4.6	Results of Adding Jet Data into the Fit	82
4.6.1	The Fitting of Resolved Cross-Sections	85
5	Optimisation of γp Dijet Cross-Sections	88
5.1	Making Precise Measurements of the Gluon PDF	88
5.2	Why γp Dijets?	92
5.3	Optimisation Study	92
5.3.1	Method of Optimisation	92
5.3.2	Phase Space Regions Considered	93
5.3.3	Considerations of the Study	93
5.3.4	Optimisation	95
5.3.5	Optimisation Study Results	96
5.3.6	Discussion	100
5.4	Final Cross-Section Definitions	103
5.5	Remaining issues	111
6	Event Reconstruction	113
6.1	Tracking and Vertex Reconstruction	113
6.2	Calorimeter Cell Energy Reconstruction	113
6.3	Definition of Jets	114
6.4	Electron Identification	115
6.5	The Reconstruction of y and Q^2	115
6.5.1	The Electron Method	115
6.5.2	The Jacquet-Blondel Method	116
6.6	Reconstruction of Other Dijet Variables	116
6.7	Jet Energy Corrections	117
6.7.1	Jet Resolutions	117
6.7.2	Correction of the Jet Transverse Energies	118
6.8	Energy Scale Uncertainty for Jets	122

7	Event Selection	125
7.1	Trigger Selection	125
7.1.1	First Level Trigger Selection	126
7.1.2	Second Level Trigger Selection	127
7.1.3	Third Level Trigger Selection	128
7.2	Offline Event Selection	129
7.3	Subsample selection	131
7.4	Trigger Efficiencies	131
7.5	Monte Carlo Description of Data	135
7.5.1	Weighting the MC	135
7.5.2	Control Plots	138
7.5.3	Underlying event	139
7.6	Dijet Resolutions	143
8	Cross-Section Measurement	147
8.1	Data Cross-Section Measurement	147
8.1.1	Unfolding the Cross-Section	147
8.1.2	Jet Energy Scale Uncertainty	148
8.1.3	Systematic Uncertainties	150
8.2	Theoretical Predictions	153
9	Results and Discussion - Part I	158
9.1	Differential Cross-Section with respect to x_γ^{obs}	158
9.2	Differential Cross-Section with respect to x_p^{obs}	160
9.3	Differential Cross-Sections with respect to $E_{T,1}$ and \bar{E}_T	163
9.4	Differential Cross-Section with respect to $\bar{\eta}$	163
9.5	Differential Cross-Section with respect to $ \Delta\phi $	169
9.6	Optimised Cross-Sections	170
9.6.1	Low- x_γ^{obs} Optimised Cross-Sections	170
9.6.2	High- x_γ^{obs} Optimised Cross-Sections	177
9.7	Photon Structure	177
10	Results and Discussion - Part II	189
10.1	Grid Reconstruction of the Optimised Cross-Sections	189
10.2	QCD Fits Using Optimised Cross-Sections	190
10.3	Future Prospects	206
10.4	Summary	208

A	Running Couplings and the Renormalisation Scale	210
B	Error Analysis	212
	B.1 Purity	213
	B.2 Efficiency	213
	B.3 Correction Factor	213
C	CTEQ and MRST Gluon PDF Errors	215
D	Calculation of the PDF Uncertainties	217
	D.1 Total PDF Uncertainties	217
	D.2 Gluon PDF Uncertainties	218
E	Jet Energy Scale Study	219
	E.1 γp Sample Definition	219
	E.1.1 Trigger and Cleaning Cuts	219
	E.1.2 Jet Cuts	220
	E.2 Correction Procedure	220
	E.3 Results of the Correction Procedure	222
	E.4 DIS Check	222
	E.5 DIS Sample Definition	226
	E.5.1 Trigger and Cleaning Cuts	226
	E.5.2 Jet Cuts	227
	E.6 Discussion	227
F	Efficiencies and Purities	231
G	Hadronisation Corrections	237
H	Theoretical Uncertainties I	243
I	Theoretical Uncertainties II	249
J	Cross-Section Tables	255
K	Systematic Uncertainty Tables	265
	Bibliography	285

List of Figures

1.1	The HERA ep collider and its experiments	21
1.2	HERA delivered luminosity during the period 1994-2000	22
1.3	The ZEUS coordinate system	23
1.4	The ZEUS detector in yz and xy views	24
1.5	Detailed schematics of the CTD	25
1.6	Structure of the FCAL and RCAL towers	28
1.7	Shower profiles in the calorimeter	29
1.8	The ZEUS Luminosity Monitor	30
1.9	Physics luminosity taken between 1996-2000	30
1.10	ZEUS Trigger and data acquisition system.	31
2.1	The kinematic variables of $e^\pm p$ scattering at HERA	35
2.2	F_2 as a function of Q^2 in different bins of x	38
2.3	Altarelli-Parisi splitting functions	39
2.4	Boson-Gluon fusion and QCD Compton scattering	42
2.5	Gluon-gluon fusion and flavor excitation from the photon	44
3.1	The ZEUS MC chain and its various software components	57
4.1	The six high- x_γ^{obs} cross-sections included in the ZEUS-Jets fit	68
4.2	A check of the ZEUS-Jets grid reconstructed cross-sections	80
4.3	A check of the ZEUS-Jets- α_s grid reconstructed cross-sections	81
4.4	Ratios for the ZEUS-Jets grid reconstructed cross-sections	83
4.5	Ratios for the ZEUS-Jets- α_s grid reconstructed cross-sections	84
4.6	Gluon uncertainty for the ZEUS-Jets fit	86
4.7	The χ^2 profile of the ZEUS-Jets- α_s fit	87
5.1	Higgs production at hadron colliders	89

5.2	Cross-section predictions for Higgs production at the LHC and the Tevatron	90
5.3	PDF uncertainty bands for Higgs boson production at the LHC and Tevatron	91
5.4	PDF errors of the low- x_γ^{obs} optimised cross-sections	104
5.5	PDF errors of the low- x_γ^{obs}	105
5.6	PDF errors of the high- x_γ^{obs} optimised cross-sections	106
5.7	PDF errors of the high- x_γ^{obs} optimised cross-sections	107
5.8	Enhanced plot of optimised cross-section G	108
5.9	Parton contribution to the low- x_γ^{obs} cross-sections	109
5.10	Parton contribution to the high- x_γ^{obs} cross-sections	110
6.1	Jet resolutions I	119
6.2	Jet resolutions II	120
6.3	Jet energy correction functions	121
6.4	Corrected jet resolutions	123
7.1	Data and Monte Carlo comparisons	130
7.2	Trigger efficiencies in the η_1 - η_2 plane	133
7.3	Trigger efficiencies for distributions of $E_{T,1}$ and η_2	134
7.4	Comparison between data and MC trigger efficiencies	136
7.5	x_γ^{obs} direct-resolved fit	137
7.6	x_γ^{obs} low- E_T direct-resolved fit	139
7.7	Control plots I	140
7.8	Control plots II	141
7.9	ZEUS 1994 x_γ^{obs} measurement	142
7.10	Dijet resolutions I	144
7.11	Dijet resolutions II	145
8.1	Various stages of the differential cross-section measurement	149
8.2	Experimental uncertainties	150
8.3	Calculating the hadron level theoretical prediction	154
8.4	$\alpha_s(M_Z)$ and scale uncertainty	157
9.1	Measured differential cross-section with respect to x_γ^{obs} I	159
9.2	Measured differential cross-section with respect to x_γ^{obs} II	160
9.3	Measured differential cross-section with respect to x_p^{obs}	161

9.4	x_p^{obs} versus x_γ^{obs} for data events	162
9.5	Measured differential cross-section with respect to $E_{T,1}$	164
9.6	Measured differential cross-section with respect to \bar{E}_T	165
9.7	Measured differential cross-section with respect to $\bar{\eta}$	166
9.8	Measured differential cross-section with respect to $ \Delta\phi $ I	167
9.9	Measured differential cross-section with respect to $ \Delta\phi $ II	168
9.10	Low- x_γ^{obs} optimised cross-sections I	171
9.11	Low- x_γ^{obs} optimised cross-sections II	172
9.12	High- x_γ^{obs} optimised cross-sections I	173
9.13	High- x_γ^{obs} optimised cross-sections II	174
9.14	Photon PDF comparisons I	179
9.15	Photon PDF comparisons II	180
9.16	Photon PDF comparisons III	181
9.17	Photon PDF comparisons IV	182
9.18	ZEUS 1996-97 cross-sections with respect to x_γ^{obs}	183
9.19	Comparison of the NLO parton densities	184
9.20	Comparison of the gluon densities	185
9.21	Sensitivity of cross-sections to the gluon density	187
10.1	ZEUS-Jets optimised grid reconstructed cross-sections	190
10.2	Gluon PDF for the ZEUS-Jets optimised fit I	192
10.3	Gluon PDF for the ZEUS-Jets optimised fit II	193
10.4	Gluon PDF for the ZEUS-Jets optimised fit III	194
10.5	Gluon PDF for the ZEUS-Jets optimised fit IV	195
10.6	Fractional improvement in the gluon PDF I	196
10.7	Fractional improvement in the gluon PDF II	197
10.8	Gluon PDF uncertainties for the various ZEUS fits I	198
10.9	Gluon PDF uncertainties for the various ZEUS fits II	199
10.10	Gluon PDF uncertainties for the various ZEUS fits III	200
10.11	Gluon PDF uncertainties for the various ZEUS fits IV	201
10.12	Gluon PDF uncertainties for the various ZEUS fits V	202
10.13	Gluon PDF uncertainties for the various ZEUS fits VI	203
10.14	Gluon PDF uncertainties for the various ZEUS fits VII	204
10.15	Gluon PDF uncertainties for the various ZEUS fits VIII	205
C.1	Comparison of gluon densities from CTEQ and MRST I	215

C.2	Comparison of gluon densities from CTEQ and MRST II	216
E.1	Monte Carlo and data comparison	221
E.2	$\langle r_{tracks} \rangle$ and $\langle r_{dijets} \rangle$ comparison	223
E.3	r_{tracks} and r_{dijets} control plots and ratio	224
E.4	r_{tracks} and r_{dijets} control plots and ratio (corrected)	225
E.5	Distribution of $E_T^{jet}/P_{T,DA}$ I	228
E.6	Distribution of $E_T^{jet}/P_{T,DA}$ II	229
E.7	Distribution of $E_T^{jet}/P_{T,DA}$ III	230
F.1	x_γ^{obs} and x_p^{obs} efficiencies and purities.	232
F.2	E_T and \bar{E}_T efficiencies and purities.	233
F.3	$\bar{\eta}$ and $ \Delta\phi $ efficiencies and purities.	234
F.4	Low- x_γ^{obs} optimised efficiencies and purities.	235
F.5	High- x_γ^{obs} optimised efficiencies and purities.	236
G.1	x_γ^{obs} and x_p^{obs} hadronisation corrections.	238
G.2	E_T and \bar{E}_T hadronisation corrections.	239
G.3	$\bar{\eta}$ and $ \Delta\phi $ hadronisation corrections.	240
G.4	Low- x_γ^{obs} optimised hadronisation corrections.	241
G.5	High- x_γ^{obs} optimised hadronisation corrections.	242
H.1	x_γ^{obs} and x_p^{obs} $\alpha_s(M_Z)$ theoretical uncertainties.	244
H.2	E_T and \bar{E}_T $\alpha_s(M_Z)$ theoretical uncertainties.	245
H.3	$\bar{\eta}$ and $ \Delta\phi $ $\alpha_s(M_Z)$ theoretical uncertainties.	246
H.4	Low- x_γ^{obs} optimised $\alpha_s(M_Z)$ theoretical uncertainties.	247
H.5	High- x_γ^{obs} optimised $\alpha_s(M_Z)$ theoretical uncertainties.	248
I.1	x_γ^{obs} and x_p^{obs} scale theoretical uncertainties.	250
I.2	E_T and \bar{E}_T scale theoretical uncertainties.	251
I.3	$\bar{\eta}$ and $ \Delta\phi $ scale theoretical uncertainties.	252
I.4	Low- x_γ^{obs} optimised scale theoretical uncertainties.	253
I.5	High- x_γ^{obs} optimised scale theoretical uncertainties.	254

List of Tables

1.1	θ - ϕ coverage of the calorimeter	27
3.1	Generated HERWIG MC specification	55
3.2	Generated PYTHIA MC specification	56
4.1	Parameters characterising the cross-section grids	70
4.2	Parton flavour codes	79
4.3	Grid parameters used in the ZEUS-Jets fit	82
5.1	Classification of the $E_{T,1}$ and $E_{T,2}$ cuts	94
5.2	Classification of the η_1 and η_2 cuts	94
5.3	Classification of the x_γ^{obs} cuts	95
5.4	Classification of the y cuts	95
5.5	Main quantities of interest in the optimisation study	96
5.6	Example selection criteria	96
5.7	Top 25 optimised cross-sections I	97
5.8	Top 25 optimised cross-sections II	98
5.9	Top 25 optimised cross-sections III	99
5.10	The 12 cross sections of [51]	101
5.11	The 8 optimised cross-sections chosen for measurement	102
5.12	Optimised cross-sections nomenclature	102
6.1	Calorimeter cell energy corrections	114
6.2	Fitted parameters for the jet energy correction functions	122
7.1	PYTHIA and HERWIG direct and resolved MC weights	138
7.2	Dijet resolutions	143
8.1	Sources of systematic error	152

9.1	Experimental uncertainties of the low- x_γ^{obs} cross-sections	175
9.2	Experimental uncertainties of the high- x_γ^{obs} cross-sections	176
E.1	Jet energy scale correction factors	222
J.1	Results of the measurement for the differential cross-section with respect to x_γ^{obs}	255
J.2	Results of the measurement for the differential cross-section with respect to x_p^{obs} ($x_\gamma^{obs} > 0.75$).	256
J.3	Results of the measurement for the differential cross-section with respect to x_p^{obs} ($x_\gamma^{obs} \leq 0.75$).	256
J.4	Results of the measurement for the differential cross-section with respect to $E_{T,1}$ ($x_\gamma^{obs} > 0.75$).	257
J.5	Results of the measurement for the differential cross-section with respect to $E_{T,1}$ ($x_\gamma^{obs} \leq 0.75$).	257
J.6	Results of the measurement for the differential cross-section with respect to \bar{E}_T ($x_\gamma^{obs} > 0.75$).	258
J.7	Results of the measurement for the differential cross-section with respect to \bar{E}_T ($x_\gamma^{obs} \leq 0.75$).	258
J.8	Results of the measurement for the differential cross-section with respect to $\bar{\eta}$ ($x_\gamma^{obs} > 0.75$).	259
J.9	Results of the measurement for the differential cross-section with respect to $\bar{\eta}$ ($x_\gamma^{obs} \leq 0.75$).	259
J.10	Results of the measurement for the differential cross-section with respect to $ \Delta\phi $ ($x_\gamma^{obs} > 0.75$).	260
J.11	Results of the measurement for the differential cross-section with respect to $ \Delta\phi $ ($x_\gamma^{obs} \leq 0.75$).	260
J.12	Results of the measurement for the differential cross-section with respect to x_p^{obs} ($x_\gamma^{obs} \leq 0.75$, OptA).	261
J.13	Results of the measurement for the differential cross-section with respect to x_p^{obs} ($x_\gamma^{obs} \leq 0.75$, OptB).	261
J.14	Results of the measurement for the differential cross-section with respect to x_p^{obs} ($x_\gamma^{obs} \leq 0.75$, OptC).	262
J.15	Results of the measurement for the differential cross-section with respect to x_p^{obs} ($x_\gamma^{obs} \leq 0.75$, OptG).	262

J.16	Results of the measurement for the differential cross-section with respect to x_p^{obs} ($x_\gamma^{obs} > 0.75$, OptD).	263
J.17	Results of the measurement for the differential cross-section with respect to x_p^{obs} ($x_\gamma^{obs} > 0.75$, OptE).	263
J.18	Results of the measurement for the differential cross-section with respect to x_p^{obs} ($x_\gamma^{obs} > 0.75$, OptF).	264
J.19	Results of the measurement for the differential cross-section with respect to x_p^{obs} ($x_\gamma^{obs} > 0.75$, OptH).	264
K.1	Systematic uncertainties for the measurement of the differential cross-section with respect to x_γ^{obs}	266
K.2	Systematic uncertainties for the measurement of the differential cross-section with respect to x_p^{obs} ($x_\gamma^{obs} > 0.75$).	267
K.3	Systematic uncertainties for the measurement of the differential cross-section with respect to x_p^{obs} ($x_\gamma^{obs} \leq 0.75$).	268
K.4	Systematic uncertainties for the measurement of the differential cross-section with respect to $E_{T,1}$ ($x_\gamma^{obs} > 0.75$).	269
K.5	Systematic uncertainties for the measurement of the differential cross-section with respect to $E_{T,1}$ ($x_\gamma^{obs} \leq 0.75$).	270
K.6	Systematic uncertainties for the measurement of the differential cross-section with respect to \bar{E}_T ($x_\gamma^{obs} > 0.75$).	271
K.7	Systematic uncertainties for the measurement of the differential cross-section with respect to \bar{E}_T ($x_\gamma^{obs} \leq 0.75$).	272
K.8	Systematic uncertainties for the measurement of the differential cross-section with respect to $\bar{\eta}$ ($x_\gamma^{obs} > 0.75$).	273
K.9	Systematic uncertainties for the measurement of the differential cross-section with respect to $\bar{\eta}$ ($x_\gamma^{obs} \leq 0.75$).	274
K.10	Systematic uncertainties for the measurement of the differential cross-section with respect to $ \Delta\phi $ ($x_\gamma^{obs} > 0.75$).	275
K.11	Systematic uncertainties for the measurement of the differential cross-section with respect to $ \Delta\phi $ ($x_\gamma^{obs} \leq 0.75$).	276
K.12	Systematic uncertainties for the measurement of the differential cross-section with respect to x_p^{obs} ($x_\gamma^{obs} \leq 0.75$, OptA).	277
K.13	Systematic uncertainties for the measurement of the differential cross-section with respect to x_p^{obs} ($x_\gamma^{obs} \leq 0.75$, OptB).	278

K.14 Systematic uncertainties for the measurement of the differential
cross-section with respect to x_p^{obs} ($x_\gamma^{obs} \leq 0.75$, OptC). 279

K.15 Systematic uncertainties for the measurement of the differential
cross-section with respect to x_p^{obs} ($x_\gamma^{obs} \leq 0.75$, OptG). 280

K.16 Systematic uncertainties for the measurement of the differential
cross-section with respect to x_p^{obs} ($x_\gamma^{obs} > 0.75$, OptD). 281

K.17 Systematic uncertainties for the measurement of the differential
cross-section with respect to x_p^{obs} ($x_\gamma^{obs} > 0.75$, OptE). 282

K.18 Systematic uncertainties for the measurement of the differential
cross-section with respect to x_p^{obs} ($x_\gamma^{obs} > 0.75$, OptF). 283

K.19 Systematic uncertainties for the measurement of the differential
cross-section with respect to x_p^{obs} ($x_\gamma^{obs} > 0.75$, OptH). 284

Chapter 1

HERA and the ZEUS Detector

This chapter will give an introduction to the HERA accelerator and ZEUS detector. After giving a brief history of and introduction to HERA we shall go on to discuss the ZEUS detector, which will be covered in some detail.

1.1 HERA

1.1.1 A brief history of HERA

The Hadron Electron Ring Accelerator¹ (HERA) is the largest of the accelerator rings located at the Deutsches Elektronen Synchrotron (DESY) in Hamburg, Germany. HERA represents a fundamentally different accelerator strategy in respect that it is the world's first and only collider which collides beams which consist of two distinct species of particle, namely positrons² and protons. This is in contrast to the rest of the world's particle accelerators which have made use of particles and antiparticles: electrons and positrons, protons and antiprotons. HERA can be viewed as a "super electron microscope" vital in unearthing fundamental structural information about the proton which is undoubtedly one of the most important hadrons in the universe.

The concept of HERA as an *ep* collider requires two distinct accelerators in which each species of particle is accelerated separately. The beams are subsequently directed head-on into each other to provide the actual collisions. Before the advent of HERA no one had ever tried to build such a facility and the

¹The German name is Hadron Elektron Ring Anlage which is what HERA actually stands for.

²HERA has a history of colliding both electrons and positrons. Unless explicitly stated, positrons will be the term used to describe both particles.

technological challenges posed were formidable. The construction of HERA was formally approved on April 6th 1984 and the accelerator celebrated its startup right on schedule (and having kept to budget) on November 8th 1990.

The civil engineering work for HERA involved the excavation of four underground (experimental) halls, each of them seven stories deep and intersected by a 6.3-kilometre long tunnel, built 10-25 m below the ground, which houses the two HERA accelerators. In total the construction of HERA involved the removal of 180,000 cubic meters of earth.

As soon as the first tunnel quarter (between the south and west halls) had been drilled installation began: cables, water pipes, light and ventilation; before the first magnets of the electron storage ring were put in place. By the time the tunnel had finished been drilled (in August 1987) half of the electron storage ring had been put in place and merely a year later the first electron beam was accelerated. Then came the most critical part, the construction of the proton accelerator with its state-of-the-art superconducting magnets and liquid helium cooling system. A total of 650 superconducting magnets were delivered to DESY from companies in Germany and Italy. After been tested in the magnet test hall at DESY they were installed above the electron ring inside the tunnel. Completion of the proton magnet system was achieved on September 19, 1990. Protons were stored in the machine for the first time during the night of April 14-15 1991 and on October 19, 1991; HERA delivered its first electron-proton collisions.

1.1.2 Description of HERA

To summarise the last section, HERA is a 6.3 km (in circumference) tunnel built 10-25 m under the ground which houses two accelerators, one for protons and one for electrons. A schematic of the HERA accelerator along with the smaller accelerators which feed it is shown in figure 1.1. The HERA accelerator is designed to accelerate electrons to 30 GeV and protons to 820 GeV (yielding a centre of mass energy of 314 GeV). The design energy of the electron beam is limited by the radio frequency power required to compensate the energy losses incurred via synchrotron radiation. The proton beam energy is limited by the 4.65 T maximum magnetic field of the bending dipoles. During 1998 the proton accelerator magnets were upgraded and the proton energy was increased to 920 GeV. The electron beam is operated slightly below its design energy of 30 GeV at 27.5 GeV. This gives a centre-of-mass energy, of the colliding system, of 300 GeV (in the case of

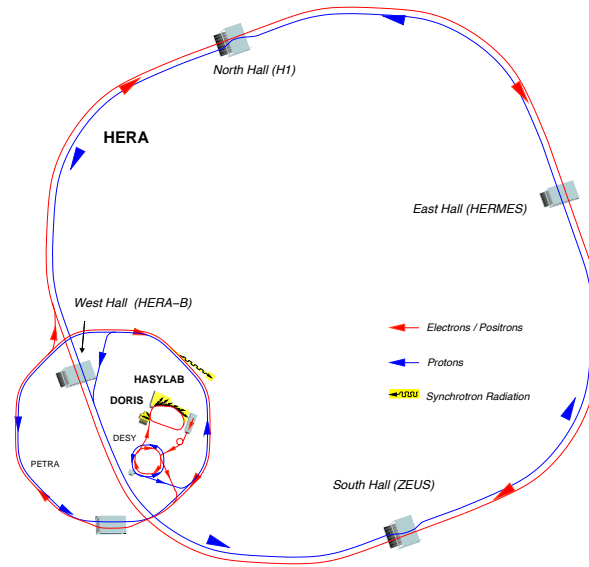


Figure 1.1: The HERA ep collider and its experiments. Also shown is the smaller preacceleration ring, PETRA

820 GeV protons) and 318 GeV (in the case of 920 GeV protons). The two beams travel through evacuated storage rings and collide inside the ZEUS and H1 [1] detectors which are located in the south and north halls respectively (see figure 1.1).

The proton injection occurs in four stages. Firstly, H^- ions are accelerated to 50 MeV in a linear accelerator. These ions are subsequently stripped of their positrons before being injected into the DESY III storage ring and accelerated up to 7.5 GeV. The DESY III ring accommodates 11 bunches with a 96 ns bunch spacing, identical to the HERA bunch spacing. From here they are passed into the PETRA II storage ring and accelerated to 40 GeV. The PETRA II ring accommodates 70 bunches with a 96 ns bunch spacing which are finally injected into the HERA ring. When HERA contains 180 bunches (the full capacity of the ring) the proton beam is accelerated to 820(920) GeV.

The lepton injection process also occurs in four stages. First, the leptons are accelerated to 220 and 450 MeV by the linear accelerators LINAC's I and II respectively. The beam is then transferred to DESY II where it is accelerated up to 7 GeV and then injected into PETRA II until 70 bunches have been accumulated (with the same bunch spacing of 96 ns as the protons). The leptons are then accelerated to 14 GeV within PETRA II. Finally, the lepton beam is

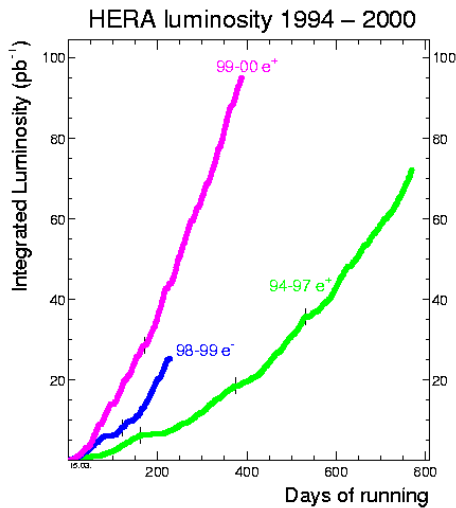


Figure 1.2: HERA delivered luminosity during the period 1994-2000

injected into HERA, at a slightly reduced beam energy of 12 GeV, before they are ramped up to 27.52 GeV within the main accelerator.

The west and east halls contain HERA's two fixed target experiments. HERA-B [2], in the west hall, makes use of the proton beam to study the CP violation of the $B^0\bar{B}^0$ system. HERMES [3], located in the east hall, uses the electron beam to investigate the spin structure of the nucleon.

In 1995 the electron accelerator was used to accelerate positrons because of lifetime problems with the electron beam. A switch back to electrons was made during 1998-99 before they were replaced once again by positrons. Positrons remained the lepton of choice up until 2005 when electrons were once again introduced back into the machine. At the time of writing, HERA is accelerating electrons.

Figure 1.2 shows the luminosity that has been delivered by HERA to the ZEUS experiment during the period from 1994-2000 during the various lepton running periods. The analysis presented in this thesis actually uses data from 1998-2000.

1.2 The ZEUS coordinate system

The ZEUS coordinate system (figure 1.3) is a right-handed coordinate system in which x points towards the centre of HERA, y points up and z points along the proton beam direction.

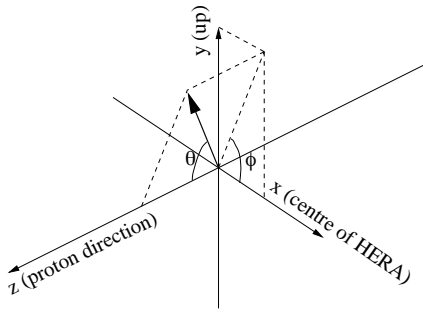


Figure 1.3: The ZEUS coordinate system

1.3 The ZEUS detector

The ZEUS detector is a multi-purpose detector, located in the south hall of HERA, with almost full solid angle coverage. Its primary components consist of the inner tracking detector, namely the Central Tracking Detector, which is situated in the 1.43 T magnetic field of a superconducting solenoid, the uranium-scintillator calorimeter, muon detector chambers and the luminosity monitor. There is also an array of other dedicated detectors designed to increase the reach of the ZEUS detector towards the forward and backward directions. Cross-sectional views of the ZEUS detector are shown in figure 1.4.

A thorough description of the ZEUS detector can be found in [4]. However, a short description of the components relevant to this thesis will be given here.

1.4 The Tracking Detectors

1.4.1 The Central Tracking Detector (CTD)

The CTD [5] is a large volume cylindrical multi-wire drift chamber with a length of 205 cm, an inner radius of 18.2 cm and an outer radius of 79.4 cm. The CTD is designed to measure, with high precision, the trajectories and momenta of charged particles which pass through it and is consequently essential in the reconstruction of the hadronic final state. The CTD is filled with a gas mixture of Argon (Ar), Ethane (C_2H_6) and Carbon Dioxide (CO_2). The gas mixture, which acts as an ionisation medium, is maintained in the approximate ratio $Ar:CO_2:C_2H_6 = 0.85:0.05:0.10$ at near atmospheric pressure. Particle identification is achieved through a measurement of the ionisation energy loss dE/dx .

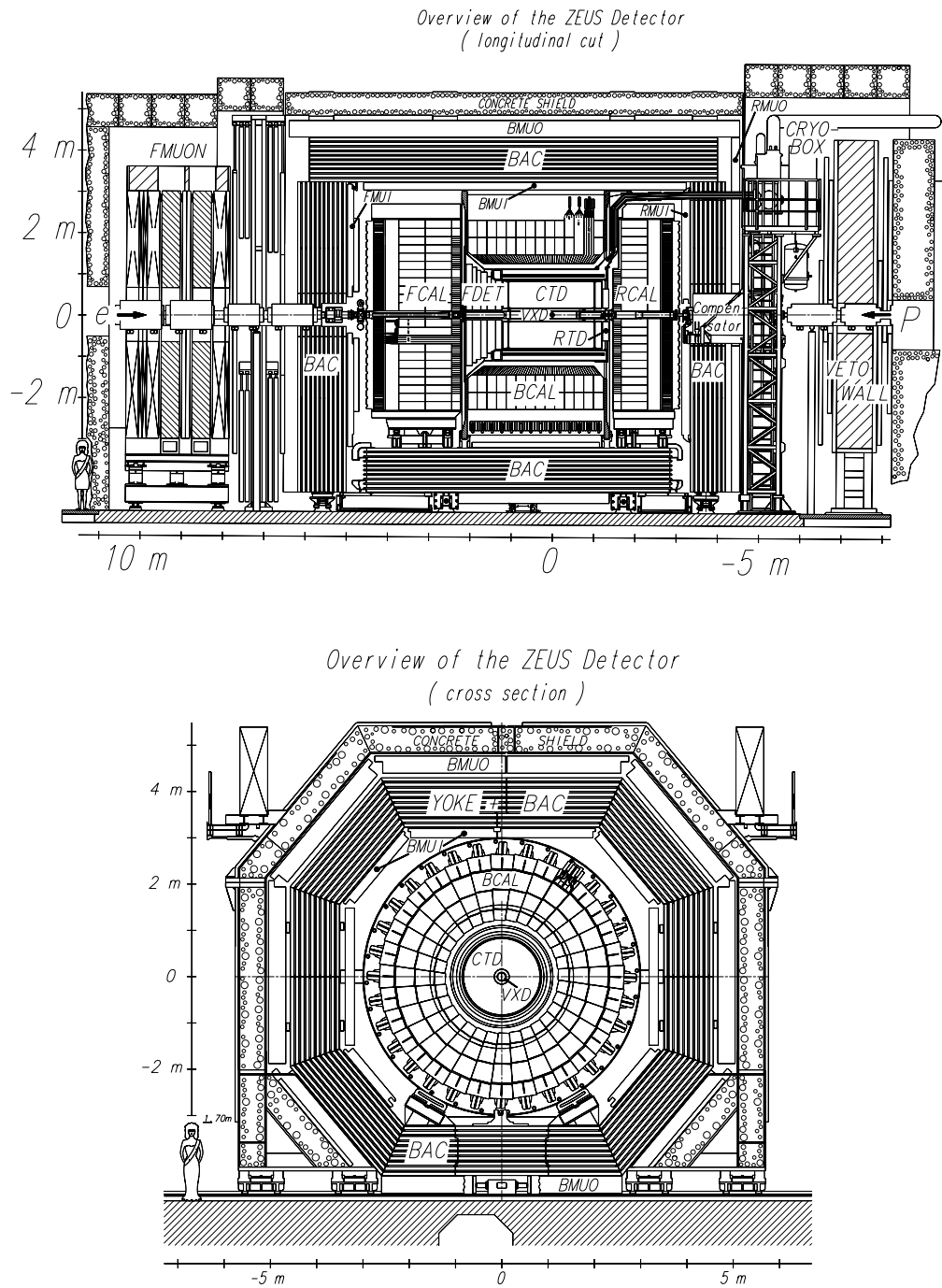


Figure 1.4: The ZEUS detector in yz (top) and xy (bottom) views

The CTD provides the majority of the total angular acceptance of the tracking detectors with a polar angle coverage of $15^\circ < \theta < 164^\circ$ ($-1.96 < \eta < 2.03$).

The CTD consists of 4,608 sense wires grouped into 8-wire cells. The cells are organised into 9 superlayers (see figure 1.5). This forms a total of 72 radial layers of sense wires. In total, there are 24,192 wires in the CTD. The 19,584 wires which are not sense wires consist of field wires, shaper wires and ground wires. These particular arrays of wires are responsible for shaping the electric field within the CTD and to ensure a uniform field within each cell (figure 1.5). This field ensures a Lorentz angle of 45° controlling the drift electrons to follow radially transverse paths. A charged particle, traversing a particular cell, will cause ionisation in the surrounding gas. The ionised electrons shower close to the sense wires with the positive ions being repelled and drifting towards the negative field wires, thereby giving a pulse which is measured with an electronic read-out.

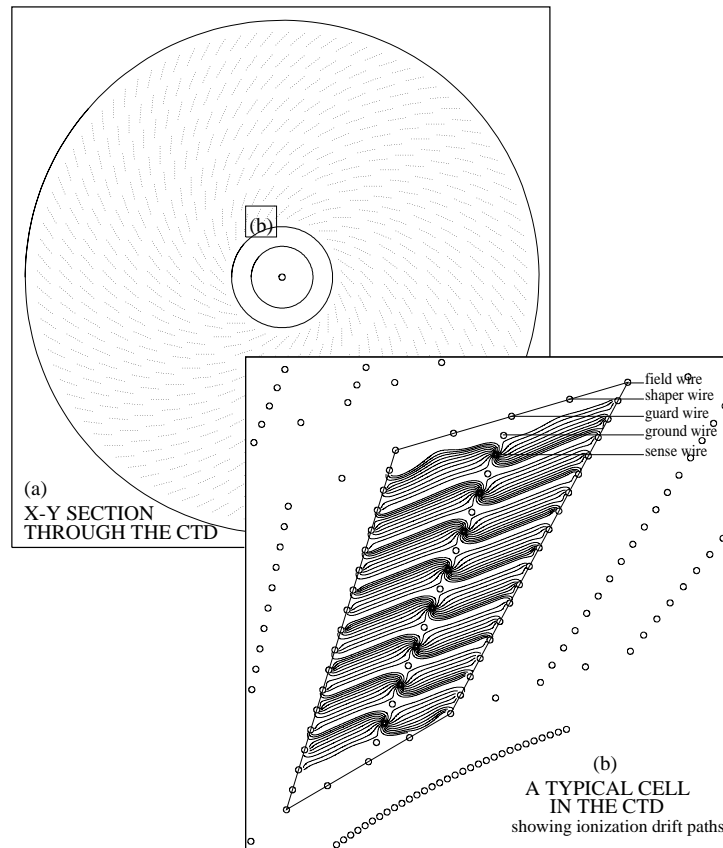


Figure 1.5: (a) $r - \phi$ cross-section through the CTD, showing the nine superlayers. (b) A representation of a single cell

Each of the odd superlayers are axial layers that contain wires which are parallel to the beam axis. The remaining layers contain wires which are elevated at a small stereo angle ($\pm 5^\circ$) to the beam axis. The respective layers are known as axial and stereo superlayers. The stereo layers aid the z position reconstruction of the tracks. Using the stereo hit information allows z resolutions of ~ 2 mm to be obtained. The first three axial layers are also equipped with a z -by-timing system with a resolution of ± 4 cm, the poorer resolution being compensated by a much shorter delay than the stereo reconstruction (several nanoseconds versus several hundred milliseconds) allowing the use of z -by-timing information for first level trigger purposes (see section 1.7.1). The z -by-timing system works by reconstructing the z position of a sense wire hit by the difference in arrival time of the pulses on the sense wires at each endplate of the CTD.

The transverse momentum resolution for a track that has traversed all superlayers is $\sigma(p_T)/p_T \approx \sqrt{(0.0058p_T)^2 + (0.0065)^2 + (0.0014/p_T)^2}$, where p_T is in GeV [6].

1.4.2 The Forward Detector (FDET)

The FDET is the collective term for a group of seven tracking detectors positioned just beyond the front end of the CTD. The FDET consists of three planar drift chambers (collectively known as the Forward Tracking Detector (FTD)) interleaved with a total of four Transition Radiation Detectors (TRDs). The FTDs are used for general purpose tracking in the forward region whereas the TRDs take on the special responsibility of positron identification. The FDET extends the forward reach of the tracking detectors to a polar angle of 7.5° (2.73 in pseudorapidity).

1.4.3 The Rear Tracking Detector (RTD)

The RTD is positioned just beyond the rear end of the CTD and consists of three layers of drift cells with their wires orientated at 0° , $+60^\circ$ and -60° with respect to the xz plane. It covers the polar angle range $160^\circ < \theta < 170^\circ$ ($-2.44 < \eta < -1.73$) and is designed to improve the precision of the tracking in the rear direction.

1.4.4 The Small Angle Rear Tracking Detector (SRTD)

The SRTD, positioned immediately behind the RTD, has two very important uses. Firstly, its primary task is to improve the angular resolution for the scattered positron by making an accurate measurement of the scattered positron in the xy plane at a z position of -1.46 m (where the detector is situated). The SRTD can achieve a position resolution of 5 mm in x and y . Secondly, the SRTD can be used as a presampler for the calorimeter by allowing the energy loss in the inactive material (cables and flanges) in front of the rear calorimeter to be quantified. This allows an energy correction to be applied for the energy lost in the inactive material and hence improve the calorimeter energy resolution. Together, the two main functions of the SRTD lead to an improved position and energy measurement of the scattered positrons in the rear direction.

1.5 The Uranium Calorimeter (CAL)

The ZEUS calorimeter [7] is a high resolution sampling calorimeter essential for the reconstruction of jets and the hadronic final state. In this thesis, the reconstruction of jets is based exclusively on calorimeter information.

The CAL covers almost 99.9% of the total solid angle and is subdivided into the forward (FCAL), barrel (BCAL) and rear (RCAL) calorimeters. The angular coverage of each CAL section is shown in table 1.1.

CAL Section	Polar Angle	Pseudorapidity
FCAL	$1.6^\circ \geq \theta < 36.7^\circ$	$1.1 < \eta \leq 4.3$
BCAL	$36.7^\circ \geq \theta < 129.1^\circ$	$-0.75 < \eta \leq 1.1$
RCAL	$129.1^\circ \geq \theta < 177.4^\circ$	$-3.8 < \eta \leq -0.75$

Table 1.1: Polar angle and pseudorapidity coverage of the various calorimeter sections

The fundamental unit of the CAL is the cell. Energy deposits in the calorimeter as a whole are taken as the sum of the individual energy deposits in each CAL cell. Each calorimeter cell consists of alternating layers of 3.3 mm depleted Uranium and 2.6 mm scintillator material. This gives an effective radiation length in the ECAL of 0.74 cm and an effective interaction length in the HCAL of 20.7 cm. Wavelength shifter bars, located on the left and right of each cell collect the light produced within each cell. A photo-multiplier tube connected to each shifter bar subsequently reads out the light collected within the cell.

Cells are arranged together to form 20 cm x 20 cm towers. Each tower is subdivided longitudinally into an electromagnetic calorimeter (EMC) and hadronic calorimeter (HAC). In the FCAL and BCAL each tower is implemented as two (20 cm x 20 cm) HAC cells and four (5 cm x 20 cm) EMC cells. The RCAL tower structure differs only in that there are two (10 cm x 10 cm) EMC cells instead of four. The structure is illustrated in figure 1.6.

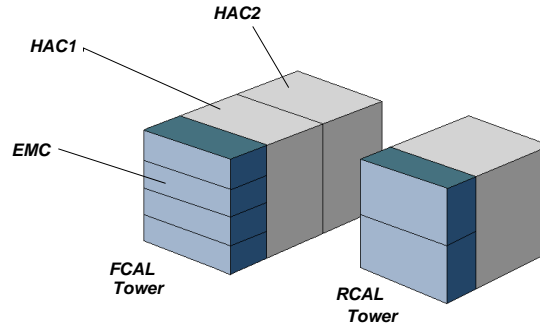


Figure 1.6: Structure of the FCAL and RCAL towers

Calorimeter towers are arranged together, longitudinally in the case of the FCAL and RCAL and radially in the case of the BCAL, to form calorimeter modules. The calorimeters themselves consist of assemblies of modules.

The ZEUS calorimeter is a compensating calorimeter which implies that the response of the calorimeter to electromagnetic and hadronic showers of equal energy should be the same. Figure 1.7 shows the typical electromagnetic and hadronic shower profiles.

The energy resolution of the ZEUS calorimeter measured under test beam conditions has been found to be

$$\frac{\sigma(E)}{E} = \frac{35\%}{\sqrt{E}} \oplus 2\% \quad (1.1)$$

for hadrons and

$$\frac{\sigma(E)}{E} = \frac{18\%}{\sqrt{E}} \oplus 1\% \quad (1.2)$$

for positrons where the energy is measured in GeV [7].

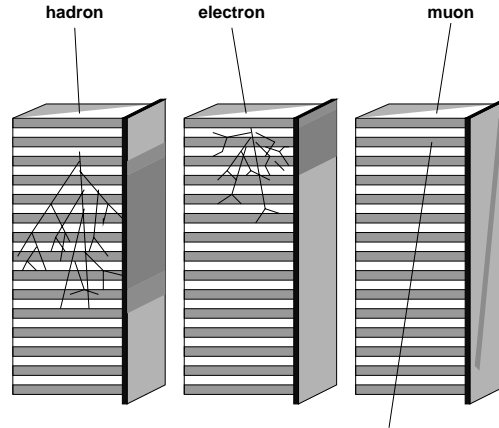


Figure 1.7: Typical shower profile in the ZEUS calorimeter for various types of particle

1.6 The Luminosity Monitor

A cross-section measurement is simply the ratio of the number of observed events (corrected for detector effects) to the integrated luminosity. Therefore, a precise measurement of the integrated luminosity is essential in order to obtain the correct absolute normalisation of the final measured cross-section.

The luminosity measurement in ZEUS is determined by the measurement of the rate of Bremsstrahlung processes from the Bethe-Heitler [8] process,

$$ep \rightarrow e'p\gamma \quad (1.3)$$

The cross-section for this process at fixed photon scattering angle, θ_γ , and energy, E_γ , is well known to about 0.5%. The cross-section, σ_{BH} , and a measurement of the photon rate, N_γ , for photons in the appropriate range of θ_γ and E_γ can be used to obtain the luminosity via the formula $\mathcal{L} = N_\gamma/\sigma_{BH}$.

The luminosity monitoring system used in ZEUS is shown in figure 1.8. The monitor consists of a positron calorimeter placed at $z = -35$ m and a photon calorimeter at $z = -107$ m which are both lead-scintillator sampling calorimeters. The accuracy of the luminosity measurement varies from 1.1% for the 1996 positron runs to 2.25% for the 2000 positron runs. The total amount of physics luminosity (luminosity remaining after the rejection of bad runs etc) taken between 1996-2000 is illustrated in figure 1.9.

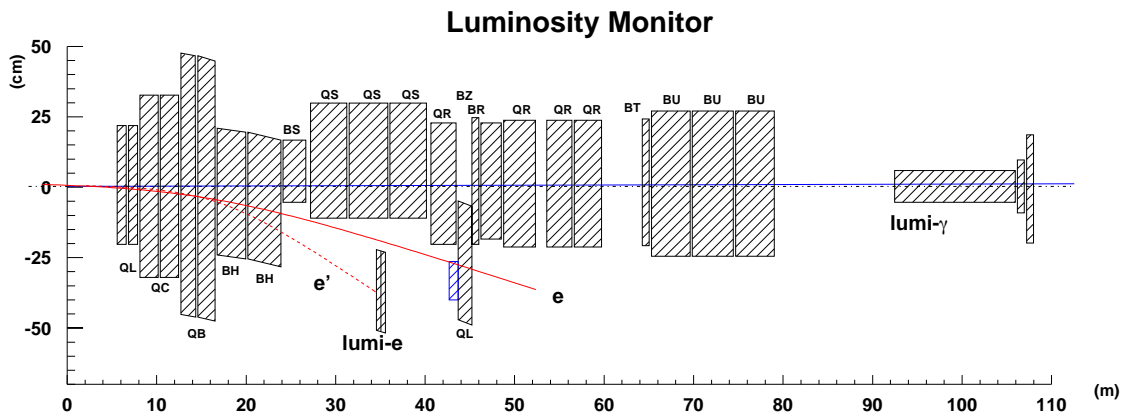


Figure 1.8: The ZEUS Luminosity Monitor

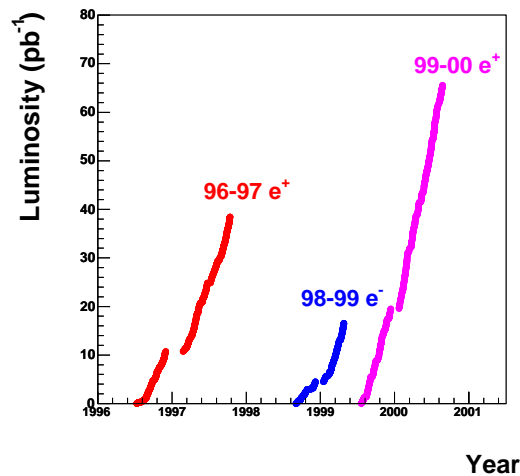


Figure 1.9: Physics luminosity taken between 1996-2000

1.7 The ZEUS Trigger and Data Acquisition System.

The nominal bunch crossing rate of the HERA accelerator is ~ 10 MHz (this corresponds to one bunch crossing every 96 ns). The rate of recorded $e^\pm p$ interactions is only of the order of 10 Hz. The ZEUS trigger and data acquisition system is designed to efficiently select the true physics interactions from the substantial background whilst keeping the background acceptance rate down to a level which is manageable by the data acquisition (DAQ) system. Much of this background is dominated by interactions between the proton beam and residual gas in the beam pipe, so called beam gas interactions, which contribute ~ 100 kHz.

In order to achieve the required reduction in rate ZEUS utilises a three level trigger system. A schematic representation of the trigger and DAQ system is shown in figure 1.10

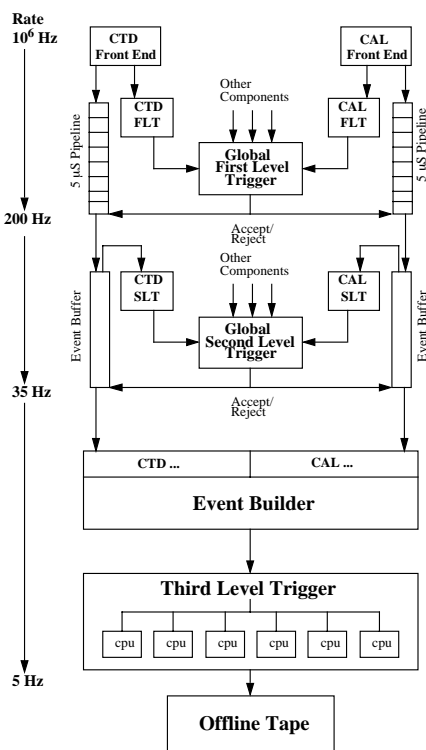


Figure 1.10: Schematic diagram of the ZEUS Trigger and data acquisition system

1.7.1 The First Level Trigger

Most components have their own First Level Trigger (FLT), built from custom designed electronics. Most components are incapable of making a useful trigger decision within the 96 ns time interval between bunch crossings and as such the data is stored in a $\sim 5 \mu\text{s}$ pipeline which is clocked synchronously with the beam crossing. During this time a coarse set of information is computed by the respective FLT's. Each component is required to make a decision within $2 \mu\text{s}$ of the bunch crossing. This decision is then passed on to the Global First Level Trigger (GFLT) which decides whether or not to accept or reject the event and passes its decision back to each component within $5 \mu\text{s}$. The FLT is designed to reduce the interaction rate from ~ 10 MHz to ~ 1 kHz.

1.7.2 The Second Level Trigger

Following a GFLT accept, the complete component data is sent to the relevant component's Second Level Trigger (SLT) memory buffers. The component SLTs are software based triggers which run on a dedicated network of Transputers which are a part of that component's electronics. Due to the longer time ($\sim 6000 \mu\text{s}$) and larger amount of information available and the flexibility of the GFLT architecture, algorithms much more complicated than those at the GFLT can be employed to make a more informed decision on whether or not to accept the event. The SLT is designed to reduce the interaction rate to $\sim 100 \text{ Hz}$.

1.7.3 The Third Level Trigger

Following a GFLT accept the complete event information is passed to the Event Builder (EVB) which fills the data structure used by the Third Level Trigger (TLT). The TLT is a software based trigger which runs on a dedicated farm of Silicon Graphics CPUs. Due to the longer processing times available ($\sim 300 \text{ ms}$) a stripped down version of the full offline reconstruction code can be performed. This allows a sophisticated reconstruction of the event to be made which includes the calculation of kinematic variables and positron identification as well as running jet finders. The TLT is designed to reduce the interaction rate to $\sim 10 \text{ Hz}$. Accepted events are written to mass storage (tape) via a dedicated $\sim 1 \text{ MBytes}^{-1}$ optical link (FLINK). The total elapsed time between bunch crossing and TLT accept is only 0.3 s.

1.8 The HERA Upgrade

The luminosity provided by HERA between 1992-2000 has led to the accumulation of large amounts of data with the ZEUS detector. Such data has provided information on many areas of particle physics. However, to make statistically rich measurements of relatively rare processes, such as heavy-flavour production, it was decided to upgrade HERA in order to maximise luminosity with a goal of achieving 1 fb^{-1} by 2005. The luminosity rate was designed to be increased by a factor of 5 which followed from a decrease in the cross-sectional area of the beams by about a factor of 4. Many systems in HERA had to be upgraded for this to be achieved including the interaction regions of both H1 and ZEUS.

ZEUS used the allocated upgrade time (about two years) to carry out maintenance work on the detector and install several new detectors. The first major component added to the detector array was the Straw Tube Tracker (STT) which was designed to improve the track finding efficiency in the forward region of the detector. The second major component installed was the Micro-Vertex Detector (MVD), a silicon strip detector designed to improve tracking capabilities close to the interaction point allowing for secondary vertex tagging of long lived particles and a better vertex resolution.

Various technical problems hampered the start up of the machine in 2002. These resulted mainly from large levels of synchrotron radiation from the positron beam and poor vacuum conditions in the proton beam pipe. The vacuum conditions improved over time but further redesign was necessary to improve the synchrotron radiation. In the first part of 2004, 43.74 pb^{-1} of gated positron luminosity was taken using ZEUS. During the remainder of 2004 and 2005, 152.26 pb^{-1} of gated electron luminosity was taken. Work on the analysis of the new data is underway. The analysis presented in this thesis does not use any post-upgrade data and is restricted to the 1998-2000 data set.

Chapter 2

QCD and $e^\pm p$ Physics

This chapter reviews some of the theoretical concepts which underpin the analysis presented in this thesis. It is assumed that the reader has a basic level of knowledge of Quantum Chromo Dynamics (QCD). A general description of $e^\pm p$ physics shall be given before the presentation of the more specific theoretical areas which are relevant to this thesis.

2.1 e^\pm Scattering

The basic process of a lepton proton interaction is shown schematically in figure 2.1. This process is mediated by a W^\pm , in the case of Charged Current (CC) interactions, and a Z^0 or γ in the case of Neutral Current (NC) interactions. The analysis in this thesis is concerned only with NC $e^\pm p$ interactions via the exchange of a γ , with the processes of W^\pm and Z^0 exchange being regarded as negligible. The result of this scattering process, in which a virtual photon interacts with the proton (labelled P), can be a high multiplicity hadronic final state (labelled X). The process of NC γ exchange can therefore be summarised as

$$e^\pm + P \rightarrow e^\pm + X . \quad (2.1)$$

We shall label the incoming and outgoing lepton four-momenta by k^μ and k'^μ respectively. The momentum of the target proton shall be labelled by p^μ and the momentum transfer by $q^\mu = k^\mu - k'^\mu$. The following standard $e^\pm p$ scattering variables can then be defined:

$$Q^2 = -q^2 , \quad (2.2)$$

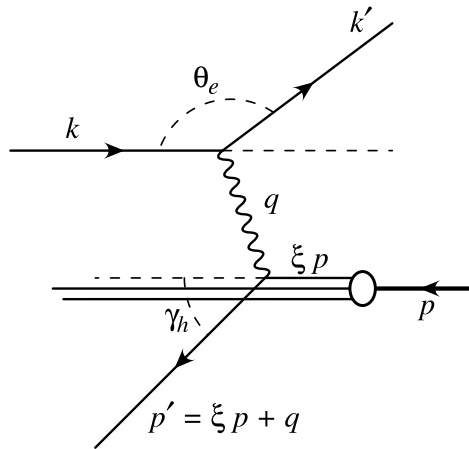


Figure 2.1: The kinematic variables of $e^\pm p$ scattering at HERA

$$x = \frac{Q^2}{2p \cdot q} \text{ and} \quad (2.3)$$

$$y = \frac{p \cdot q}{p \cdot k'}. \quad (2.4)$$

For a given centre of mass energy, $\sqrt{s} = \sqrt{(k+p)^2}$, only two of the above kinematic variables are required for a complete description of the $e^\pm p$ scattering kinematics via

$$Q^2 = s \cdot x \cdot y, \quad (2.5)$$

where Q^2 , the negative square of the four momentum transfer, is always positive and specifies the virtuality of the exchanged photon. In the rest frame of the proton, y defines the fraction of the e^\pm energy transferred to the proton; $y = \frac{E_\gamma}{E}$. On the other hand, x defines the fraction of the protons momentum carried by the struck quark in the interaction. The terms Bjorken x and Bjorken y are often used interchangeably with x and y . In particular, x is often referred to as the Bjorken scaling variable.

Q^2 is a very important variable which warrants further discussion. In the exchange of a photon the e^\pm cross-section falls rapidly with Q^2 due to the inclusion of the $\frac{ig_{\mu\nu}}{Q^2}$ propagator term in the expression for the cross-section. We will see later

that in actual fact the double differential cross-section with respect to x and y falls with the inverse square of Q^2 .

For large Q^2 this variable provides the hard-scale (see appendix A) of the $e^\pm p$ interaction and allows perturbative calculations to be performed. This is applicable down to a scale known as Λ_{QCD} which has an experimentally determined value of 0.2 ± 0.1 GeV [12]. Events where Q^2 can be safely used as the hard-scale (i.e. $Q^2 \gg \Lambda_{QCD}$) are referred to as Deep Inelastic Scattering (DIS). For low Q^2 the interaction proceeds as the exchange of a quasi-real photon and such events are referred to as photoproduction (γp). In this low Q^2 regime we have to choose a different scale, most commonly the transverse momentum of the outgoing partons from the interaction. In practice, events for which $Q^2 < 1$ GeV² are classified as photoproduction and those for which $Q^2 > 1$ GeV² are classified as DIS. As a final note in this section, it must be pointed out that due to the aforementioned dependence of the $e^\pm p$ cross-section on Q^2 , γp processes significantly dominate the $e^\pm p$ cross-section.

2.2 The e^\pm Cross-Section

The double differential cross-section with respect to x and Q^2 for NC $e^\pm p$ scattering is given by [11]

$$\frac{d^2\sigma(e^\pm p)}{dx dQ^2} = \frac{2\pi\alpha^2}{xQ^4} [Y_+ F_2(x, Q^2) \mp Y_- x F_3(x, Q^2) - y^2 F_L(x, Q^2)] , \quad (2.6)$$

where

$$Y_\pm = 1 \pm (1 - y)^2 . \quad (2.7)$$

The structure functions F_L , F_3 and F_2 are dimensionless functions of x and Q^2 which quantify the structure of the proton. The longitudinal structure function F_L quantifies the contribution to the cross-section from the exchange of longitudinally polarised virtual photons, and is only important at high Q^2 and high y due to the suppressive y^2 term which precedes F_L in equation 2.6. The structure function, F_3 describes parity violating Z^0 exchange which is negligible for $Q^2 \ll M_Z^2$. Assuming we are not dealing with the high- Q^2 regime (which we shall not be in this thesis), equation 2.6 can be rewritten as

$$\frac{d^2\sigma(e^\pm p)}{dx dQ^2} = \frac{2\pi\alpha^2}{xQ^4} [Y_+ F_2(x, Q^2) - y^2 F_L(x, Q^2)] . \quad (2.8)$$

The F_2 structure function provides the contribution to the cross-section from the exchange of transversely polarised virtual photons and, in the kinematic regime that we are interested in, dominates the cross-section. At leading order (LO) F_2 can be written as the linear combination of the momentum distributions of the quarks and anti-quarks of the proton,

$$F_2(x, Q^2) = \sum_i e_i^2 [xq_i(x, Q^2) + x\bar{q}_i(x, Q^2)] , \quad (2.9)$$

where the sum runs over the quark flavors, e_i is the electronic charge of quark flavor i and $q_i(x, Q^2)$ is the probability density of finding quark i with a momentum fraction (of the proton) x at a scale of Q^2 (these are the so-called parton distribution functions (PDFs) and will be referred to frequently throughout the remainder of this thesis).

If F_2 has no dependence on Q^2 which is the case in the naive parton model of the proton, then it is said to scale. In the QCD model of the proton, the presence of gluon emission from the constituent partons (a term which will be used to collectively refer to quarks, anti-quarks and gluons) leads to a dependence of F_2 (or more specifically the PDFs) on Q^2 . This is referred to as the scaling violation of F_2 (see figure 2.2).

It may appear from equation 2.9 that there is no dependence of F_2 on the gluon PDF (the sum does not include the gluon). This is misleading because as we shall see in the next section the dependence of the PDFs (and therefore F_2) on Q^2 does indeed depend on the gluon. The structure function, F_2 , is therefore indirectly dependent on the gluon via scaling violations.

2.3 Scaling Violations and Parton Distribution Functions

The dependence of the the proton PDFs on Q^2 is modelled by the DGLAP evolution equations [13]:

$$\frac{dq_i(x, Q^2)}{d\log Q^2} = \frac{\alpha_s}{2\pi} \int_x^1 \frac{dy}{y} \left[q_i(y, Q^2)P_{qq} \left(\frac{x}{y} \right) + g(y, Q^2)P_{qg} \left(\frac{x}{y} \right) \right] \text{ and} \quad (2.10)$$

$$\frac{dg(x, Q^2)}{d\log Q^2} = \frac{\alpha_s}{2\pi} \int_x^1 \frac{dy}{y} \left[\sum_i q_i(y, Q^2)P_{gq} \left(\frac{x}{y} \right) + g(y, Q^2)P_{gg} \left(\frac{x}{y} \right) \right] , \quad (2.11)$$

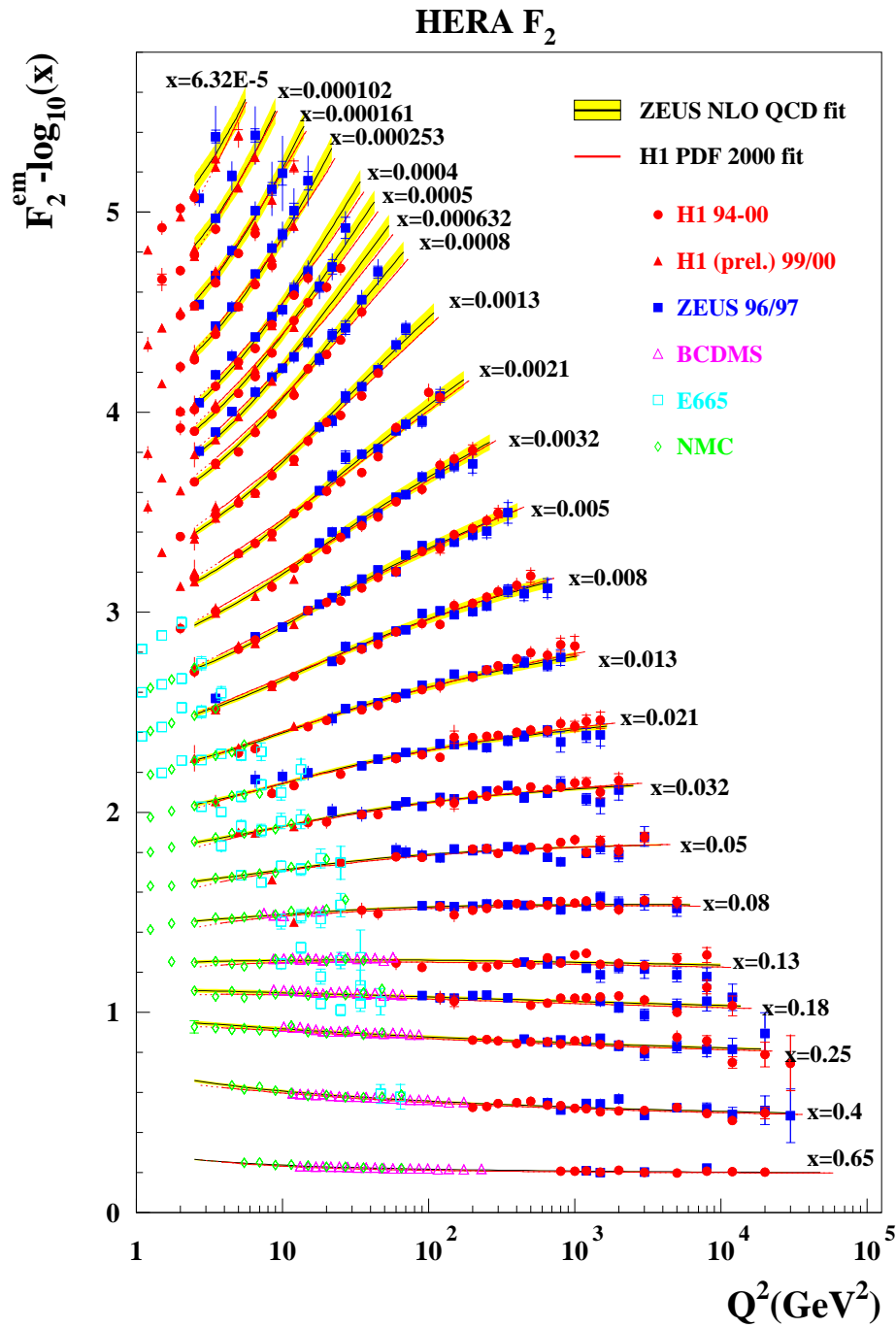


Figure 2.2: F_2 as a function of Q^2 in different bins of x

where $q_i(y, Q^2)$ and $g(y, Q^2)$ denote the quark and gluon PDFs respectively. The functions P_{qq} , P_{qg} , P_{gq} and P_{gg} are the Altarelli-Parisi splitting functions. The function $P_{jk}(z)$ represents the probability of parton j , produced from the splitting of parton k , carries a fraction z of particle k 's momentum. The processes represented by each of the four splitting functions are depicted in figure 2.3.

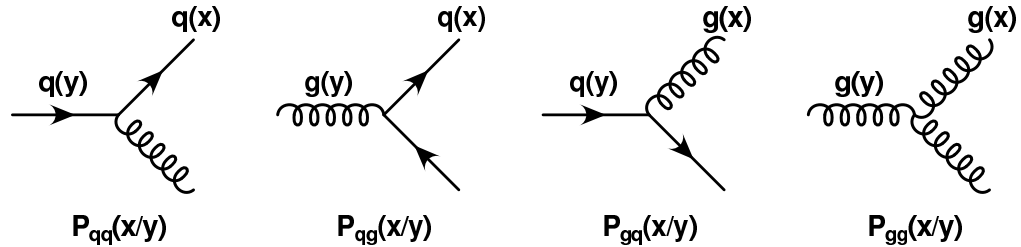


Figure 2.3: The Altarelli-Parisi splitting functions to first order, used in the DGLAP evolution equations.

The DGLAP equations effectively tell us that given $q_i(x, Q^2)$ or $g(x, Q^2)$ at some initial scale Q_0^2 then the value of $q_i(x, Q^2)$ or $g(x, Q^2)$ can be predicted for an arbitrary value of Q^2 . So although the quark and gluon distributions can not, themselves, be calculated (within the bounds of perturbative QCD) their dependence on Q^2 can be predicted.

2.3.1 The Factorisation Theorem of QCD

So far, much of our discussion has been centred about the parton PDFs. Yet, little has been said as to what exactly the PDFs are. In section 2.2 we interpreted $q_i(x, Q^2)$ ($g(x, Q^2)$) as a probability density function which allows the likelihood of finding a quark (gluon), with a momentum fraction x when the proton is probed at a given scale Q^2 , to be determined. There is, however, much more to the PDFs than this rather simple interpretation. For a proper understanding of what the PDFs are one needs a grasp of the concepts behind the factorisation theorem of QCD. Factorisation states that a QCD cross-section can be written as the convolution of two terms: a perturbatively calculable hard scattering cross section and a non-perturbative (incalculable) parton density. Factorisation allows the cross-section for $e^\pm p$ scattering to be written as

$$\sigma_{e^\pm p}(k, p) = \sum_i \int f_i(x, \mu_F^2) \hat{\sigma}_{e^\pm i}(x, k, \alpha_s(\mu_R^2), \mu_F^2) dx, \quad (2.12)$$

where k and p are the incident positron and proton momenta. The fraction of the proton momentum carried by the struck quark is denoted as usual by x . The scale which α_s runs with is denoted by μ_R and is called the renormalisation scale (i.e. this scale determines what value of α_s you use in the calculation of the hard scattering matrix elements). The scale at which the perturbatively calculable hard scattering cross-section is divided from the non-perturbative parton density is denoted by μ_F and called the factorisation scale. This scale is very important and it defines the boundary at which the cross-section is to be factored. A parton emitted from the incoming quark or gluon at a small scale ($< \mu_F$) is considered part of the proton structure and absorbed into the parton distribution function, $f_i(x, \mu_F^2)$. A parton emitted at a large scale ($> \mu_F$) is considered part of the hard interaction. The scales, μ_R and μ_F , should be chosen to be of the order of the hard scale which characterises the hard interaction. It is usual, in the case of DIS, to choose $\mu_R = \mu_F = Q$ (which justifies the earlier notation which denoted the PDFs to be functions of x and Q^2) but it should be noted that these scales need not be set equal to one another and are indeed arbitrary parameters. In low, finite order perturbative calculations, the resulting cross sections will display a dependence on the choice of μ_R and μ_F (these are often the dominant uncertainties on the theoretical cross-section), however, at higher orders the perturbative coefficients change in such a way that the resulting cross-sections are independent of μ_R and μ_F .

Therefore, the PDFs contain information about all the non-perturbative soft physics which describe the structure of the proton. They have to be determined empirically. Chapter 4 will discuss in detail how the proton PDFs are determined from cross-section data.

2.4 Photoproduction

The analysis presented in this thesis is concerned with photoproduction and so this topic will be now covered in further detail. As stated previously, photoproduction occurs when the exchanged virtual photon has $Q^2 \sim 0$, whereby it behaves as if it is almost (quasi) real. Such exchanges provide the dominant contribution to the $e^\pm p$ cross section. We begin by discussing how γp scattering is related to $e^\pm p$ scattering.

In the kinematic limit as $Q^2 \rightarrow 0$ the exchanged photons are massless and transversely polarised bosons which are emitted collinearly with the beam line.

In this low region of Q^2 we effectively deal with the interaction between a beam of real photons and a beam of protons.

Via the equivalent photon approximation (EPA), the γp and $e^\pm p$ cross-sections can be related as

$$\frac{d^2\sigma^{e^\pm p}}{dydQ^2} = f_\gamma^{e^\pm}(y, Q^2)\sigma^{\gamma p}(y, Q^2), \quad (2.13)$$

where $f_\gamma^{e^\pm}(y, Q^2)$ can be thought of as the probability of finding a photon emitted from the e^\pm with an energy of $E_\gamma = yE_e$. Using the Weizsacker-Williams Approximation [14] this can be written as

$$f_\gamma^{e^\pm}(y, Q^2) = \frac{\alpha}{2\pi Q^2} \left(\frac{1 - (1 - y)^2}{y} - 2 \frac{(1 - y) Q_{min}^2}{y Q^2} \right), \quad (2.14)$$

where $Q_{min}^2 = m_e^2 y^2 / (1 - y)$ is the kinematic lower bound.

In the photoproduction regime the four momentum transfer is too soft and does not provide a suitable scale for perturbative calculations to be made. However the three momentum transfer associated with low virtuality photon interactions can still be large and give rise to a final state of high transverse momentum outgoing partons. Thus, the transverse momenta of the outgoing partons from the photoproduction reaction, or some function of the momenta, can be used to provide a suitable scale for perturbative calculations to be made.

Photoproduction is a rich area of study which, through the advent of HERA, can be probed to high energies. We will now go on to discuss two classifications of photoproduction reactions which will complete this introduction to the theoretical grounding of $e^\pm p$ physics, the so-called Direct and Resolved photoproduction processes.

2.5 Direct Photoproduction

Interactions in which the photon couples directly to a parton in the proton are termed direct photoproduction interactions. In such interactions the photon is said to behave in a point-like manner. The two LO direct photoproduction processes are shown in figure 2.4. The Boson-Gluon Fusion (BGF) process is directly sensitive to the gluon content of the proton. Because of this, photoproduction processes are in general more sensitive to the gluon content of the proton than DIS processes, because in DIS the dominant contribution

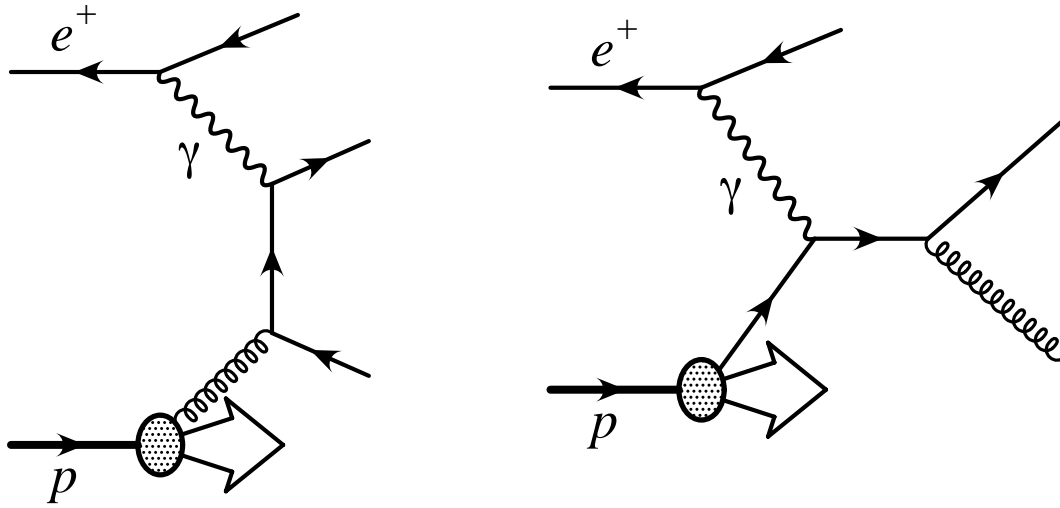


Figure 2.4: The two dominant LO direct photoproduction processes: (a) Boson-Gluon fusion (b) QCD Compton scattering

comes from the exchanged photon coupling directly to a quark, and not a gluon, in the proton. The second class of LO direct processes is the QCD Compton (QCDC) process whereby the incoming photon couples directly to a quark within the proton, with an emission of a gluon by the excited quark in the final state. At low scales the relative contribution of the two direct processes is dominated by the BGF process. At higher scales, however, QCDC is the dominant process. This is explained by looking at the relative probabilities of interactions between gluons and quarks at low and high scales. In order to proceed we must consider the quantity x_p which is defined as the fraction of the protons momentum carried by the struck parton in the hard interaction and can be defined in terms of the outgoing partonic transverse energies and pseudorapidities as

$$x_p = \sum_i \frac{E_{T,i} e^{\eta_i}}{E_p}, \quad (2.15)$$

where the sum runs over all the outgoing partons from the hard interaction. The transverse energy (equivalent to momentum for massless partons) of the i^{th} outgoing parton is denoted by $E_{T,i}$ and similarly its pseudorapidity is labelled η_i . Experimentally, the observable quantity x_p^{obs} is defined, which is obtained by running the sum of equation 2.15 over the two highest transverse energy jets (see section 2.7 for the definition of a jet),

$$x_p^{obs} = \sum_{i=1}^2 \frac{E_{T,i} e^{\eta_i}}{E_p}, \quad (2.16)$$

where the sum is run over jet quantities instead of parton quantities. The quantity $E_{T,1}$ corresponds to the transverse energy of the highest transverse energy jet (the so-called leading jet) and $E_{T,2}$ corresponds to the transverse energy of the second highest transverse energy jet (the so-called trailing jet). Similar notation is used to label the pseudorapidity of the two jets.

The scale of the interaction is typically chosen to be some function of the outgoing parton's transverse energy (for example the mean outgoing transverse energy). From equation 2.15 one can see that a low scale event is therefore characterised by a relatively low value of x_p and higher scale events tend to lead to higher values of x_p (for a given configuration of pseudorapidities). At high scales therefore we are dealing with high- x_p interactions and, at high- x_p , such interactions are more probable with a valence quark rather than a gluon as these tend to carry most of the protons momentum. Thus, the QCDC process dominates at high scales.

2.6 Resolved Photoproduction

In contrast to direct photoproduction, where the photon participates directly in the hard interaction, resolved photoproduction describes the situation where the photon acts as a source of partons which themselves take part directly in the hard interaction. Resolved photoproduction processes are those which can be described by modelling the photon as a composite hadronic particle. The concept of a photon being modelled as a composite particle may seem strange at first, given that a real photon has zero mass, no charge and does not have any intrinsic structure in the sense that the proton has. However, it is possible for a photon to split into a $q\bar{q}$ pair which themselves radiate gluons which in turn can split into further $q\bar{q}$ pairs. It is easy to therefore envisage a virtual photon, under certain circumstances, as a cloud of partons i.e. a composite hadronic particle. What makes such a concept realisable, in practice, is that at high energies and low photon virtualities the lifetime of the hadronic like state is similar to that of the hard interaction. Partons from the photon can then participate in the hard interaction.

Theoretically, resolved photoproduction is treated analogously to hadron-hadron interactions. The photon structure is described by a set of photon PDFs in

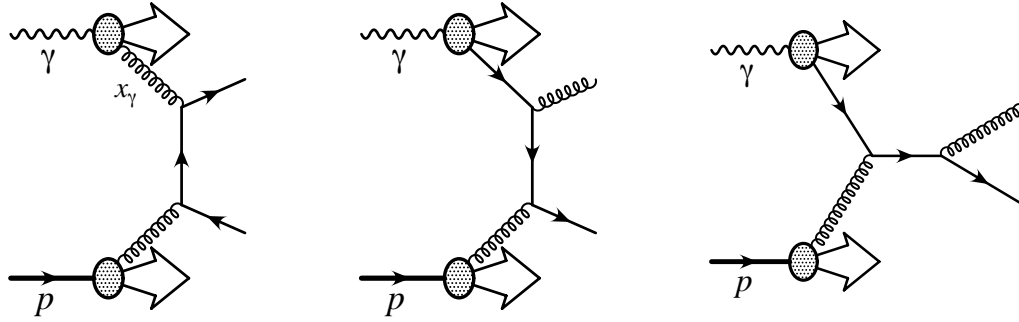


Figure 2.5: Some examples of LO resolved photoproduction processes: (a) Gluon-Gluon Fusion (b) & (c) Flavor excitation from the photon

exactly the same way as the proton is described by a set of proton PDFs. When discussing resolved photoproduction a new parameter is necessary to describe the fraction of the photons four momentum which is carried by the incident parton from the photon, which is given by

$$x_\gamma = \sum_i \frac{E_{T,i} e^{-\eta_i}}{y E_e}. \quad (2.17)$$

It can be seen that x_γ is the exact analog of x_p , that was discussed earlier, for partons which originate from the photon. Experimentally, the observable quantity, x_γ^{obs} , is defined, which is obtained by running the sum of equation 2.17 over the two highest transverse energy jets (see section 2.7 for the definition of a jet),

$$x_\gamma^{obs} = \sum_{i=1}^2 \frac{E_{T,i} e^{-\eta_i}}{y E_e}, \quad (2.18)$$

where once again, as in the case for x_p^{obs} , the sum is run over jet quantities instead of parton quantities.

The use of the observable, x_γ^{obs} , provides a simple way of differentiating between the two classes of photoproduction interactions. Direct photoproduction interactions are characterised by events such that $x_\gamma = 1$, whereas resolved photoproduction interactions are characterised by $x_\gamma < 1$. Although there is a close correspondence between x_γ^{obs} and x_γ , there is some smearing of the variable x_γ^{obs} about the value of x_γ (due to parton showering and hadronisation) so it is not possible to make an exact distinction between direct and resolved events using x_γ^{obs} . However, it is possible to divide the photoproduction sample into direct and

resolved enriched regions via the application of a suitable cut. In practice, events characterised by $x_\gamma^{obs} > 0.75$ are classified as direct events and those characterised by $x_\gamma^{obs} \leq 0.75$ are classified as resolved events.

One further point worth considering is that, in resolved photoproduction, only a fraction of the photon's energy takes part in the hard interaction. In direct photoproduction the entire energy of the exchanged photon takes part in the hard interaction. Therefore, higher energy photoproduction interactions tend to be dominated by direct photoproduction.

2.7 Definition of Jets

This thesis is concerned with the analysis of jets and therefore a discussion of the jet definition is fully warranted at this point. The main problem in comparing theoretical predictions to experimental data is that the partons that are predicted in the theory are not those which are detected in experiment. Outgoing partons hadronise into jets of outgoing hadrons and it is the job of a jetfinder to isolate these jets from a given hadronic final state. Thankfully, there is a close correspondence between the kinematic properties of the jets and those of the underlying outgoing partons from the interaction.

The actual jet finding routines need to fulfil certain conditions in order to allow the comparison of measured experimental distributions with those that are calculated theoretically. Calculations in perturbative QCD (pQCD) are subject to singularities which arise due to the emission of soft or collinear gluons. It is important that a jet finding algorithm is defined in such a way that the resulting jets are also infrared and collinear safe. More precisely, the algorithm is considered infrared and collinear safe if the jets obtained using an N and $N + 1$ configuration of input particles are identical under two limiting cases. The first been the case whereby the $(N + 1)^{th}$ momenta is collinear to one of the other N momenta and the second where the energies of the $(N + 1)^{th}$ momenta tend to zero. The results of the jet finder should also be independent of the number of input particles used. More details about the general aspects of jet finding algorithms can be found in [15].

2.7.1 The k_T Algorithm

The analysis presented in this thesis utilises the longitudinally invariant k_T -clustering algorithm (KTCLUS) [16], used in the inclusive mode [17]. This

algorithm is used instead of the more traditional cone jet finding algorithm to avoid problems associated with the latter that were highlighted in the previous section. The KTCLUS algorithm iteratively combines pairs of objects according to their transverse momentum and distance in $\eta - \phi$ space. The KTCLUS prescription is detailed below.

- For each pair of objects (partons, hadrons or calorimeter cells) in the final state, the distance parameter between the i^{th} and j^{th} object is defined as

$$d_{ij} = \min(E_{T,i}^2, E_{T,j}^2) R_{ij}^2, \quad (2.19)$$

where $R_{ij}^2 = \delta\eta_{ij}^2 + \delta\phi_{ij}^2$ is the distance between these objects in the $\eta - \phi$ plane.

- For each object i , the distance to the beam is defined as

$$d_i = E_{T,i}^2 R^2, \quad (2.20)$$

where R is a free parameter of the algorithm which is chosen to be 1.

- Next the list of numbers formed by $d_{i,j}$ and d_k is considered. If, for example, d_k is the smallest number in this list then object k is considered complete and removed from the list. If $d_{l,m}$ is the smallest number then objects l and m are merged into a single object and the list is updated. This process is repeated until a complete object is found.
- The result of the entire procedure is an E_T ordered list of complete objects. Objects above some threshold are accepted as jets.

When merging two objects, say the i^{th} and j^{th} , into the k^{th} merged object; the following formulae are used to calculate the merged object's kinematics:

$$E_{T,k} = E_{T,i} + E_{T,j}, \quad (2.21)$$

$$\eta_k = \frac{\eta_i E_{T,i} + \eta_j E_{T,j}}{E_{T,i} + E_{T,j}} \text{ and} \quad (2.22)$$

$$\phi_k = \frac{\phi_i E_{T,i} + \phi_j E_{T,j}}{E_{T,i} + E_{T,j}}. \quad (2.23)$$

This ensures that the final jet quantities are consistent with the Snowmass convention [18]:

$$E_{T,jet} = \sum_{i \in jet} E_{T,i} , \quad (2.24)$$

$$\eta_{jet} = \frac{\sum_{i \in jet} \eta_i E_{T,i}}{\sum_{i \in jet} E_{T,i}} \text{ and} \quad (2.25)$$

$$\phi_{jet} = \frac{\sum_{i \in jet} \phi_i E_{T,i}}{\sum_{i \in jet} E_{T,i}} . \quad (2.26)$$

Chapter 3

Monte Carlo Simulation and Data Correction

In this chapter the basic principles of Monte Carlo (MC) event simulation will be discussed. Before discussing particular event generators in detail a more general account will be given of the concept behind using simulated data in particle physics analyses. The chapter will finish with a discussion of hadronisation corrections and detector acceptance corrections.

3.1 Using Simulated Data in Particle Physics Analyses

Essentially, the concept of a particle physics analysis is rather simple. All one has to do is be able to observe a series of interactions and count the number of times a particular event occurs. In principle the exercise is little more than one of counting. The complexity is introduced because the instrumentation, used to observe a given interaction, gives us a distorted view of what we want to observe. Unless one can understand the effects of the instrumentation then one can not understand what is happening at the fundamental level at which one is trying to observe.

There are three distinct levels to consider in the observation of a typical interaction

- **Parton Level** This is the level at which individual partons from the colliding particles interact with each other. At this level there is no composite hadronic matter. It is the level at which theoretical calculations are performed.

- **Hadron Level** Individual partons from a given interaction are never observed directly because of the confinement property of QCD [11]. Outgoing partons from the hard interaction undergo a complex process of hadronisation which transforms the final state configuration of coloured partons into one consisting of colourless hadronic bound states. In particular, outgoing partons from the interaction are observed as jets of hadrons.
- **Detector Level** The hadronic final state is probed using a detector whose output consists of many complex electronic signals which are used to reconstruct the energies and momenta of the hadrons (jets) and leptons which comprise the final state.

Because of complex hadronisation effects the hadron level distributions will not correspond exactly to the parton level distributions. There does however tend to be a very close correlation between the two and determining the precise nature of this correlation allows you to infer one distribution from the other. Similarly due to complex detector effects, detector level distributions will not correspond exactly to the hadron level distributions. For example, hadrons traversing regions of dead material in front of the calorimeter will lose energy so that the energies of the hadrons, as measured in the calorimeter, tend to be lower than the true underlying hadronic energy. However, as long as one understands the nature of these detector effects, one may correct for them and derive the corresponding hadron level distribution for a given detector level distribution.

In particular, consider a parton level distribution in a variable x (which could be, for example, the p_T or η of the highest transverse momentum outgoing parton) denoted by $f_{part}(x)$. If the corresponding hadron level distribution is denoted by $f_{had}(x)$ then we define a function $g(x)$ such that

$$f_{had}(x) = g(x)f_{part}(x) , \quad (3.1)$$

where $g(x)$ is a function which maps $f_{part}(x)$ onto $f_{had}(x)$. Rearranging the above equation gives

$$f_{part}(x) = g^{-1}(x)f_{had}(x) , \quad (3.2)$$

where $g^{-1}(x)$ denotes the inverse of $g(x)$. Similarly, if the detector level distribution corresponding to a given hadronic distribution, $f_{had}(x)$, is denoted by $f_{det}(x)$ then we define a function $h(x)$ such that

$$f_{det}(x) = h(x)f_{had}(x) \text{ and} \quad (3.3)$$

$$f_{had}(x) = h^{-1}(x)f_{det}(x) . \quad (3.4)$$

If the detector was perfect then $h(x)$ and $h^{-1}(x)$ would be equal to unity. If $g(x)$ (or $g^{-1}(x)$) and $h(x)$ (or $h^{-1}(x)$) can be determined then all the different distributions can be mapped onto one another. This is shown schematically below

$$\begin{array}{ccccc} f_{part}(x) & \xrightarrow{g} & f_{had}(x) & \xrightarrow{h} & f_{det}(x) \\ f_{part}(x) & \xleftarrow{g^{-1}} & f_{had}(x) & \xleftarrow{h^{-1}} & f_{det}(x) . \end{array}$$

Simulated MC data is used to determine the functions g and h . A MC event generator manufactures events which produce final state configurations of partons. A hadronisation model is then applied to these partons to produce a hadronic final state. By calculating distributions at the parton and hadron levels, the function g (and g^{-1}) can be found. The second step involves feeding the hadronic final state into a detector simulator which predicts what the event looks like at the detector level and thus, allows h (and h^{-1}) to be found.

All cross-sections in this thesis will be shown at the hadron level. This means that the theoretical calculations (which at NLO are always calculated at the parton level) need to be corrected for hadronisation using the function g (this is termed the hadronisation correction) and all the detector level distributions need to be corrected for detector effects using the function h^{-1} (which is called the acceptance correction). This process allows theoretical calculations and experimental measurements to be compared on an equal footing.

3.2 Monte Carlo Event Generators

The MC generators that have been employed for the simulation of photoproduction events as part of the analysis presented in this thesis are HERWIG (version 6.505) and PYTHIA (version 6.2). The generation of the events takes place in the same general way for both generators and is outlined below (the specific implementation of each step however does differ between each generator):

- **Incoming partons** The incoming beam particles are characterised by a set of parton distribution functions (PDFs) which describe the fraction of 4-momentum associated with each flavour of parton. One parton from each incoming beam particle initiates the principal interaction, with the remainder of the partons, which make up the beam particles, taking part in secondary interactions (multi-parton interactions) or contributing to the beam remnants.
- **Initial-state parton showers** The two incoming partons go through a sequence of splittings (for example $q \rightarrow qg$) which are governed by the DGLAP evolution equations.
- **Hard scattering process** Both HERWIG and PYTHIA are often described as LO generators. This is because the calculation of the matrix elements for the relevant hard scattering process is performed at LO. One incoming parton from each initial-state shower takes part in the (LO) $2 \rightarrow 2$ hard sub-process.
- **Final-state parton showers** The outgoing partons from the hard interaction are characterised by a virtuality Q_{max}^2 which is determined from the nature of the hard interaction. The outgoing partons go through a sequence of splittings to create final-state parton showers, with the virtuality of the partons decreasing with each successive emission until some minimum virtuality Q_0^2 is obtained.
- **Hadronisation and decay of unstable particles** The final step involves the combination of the coloured partons from the final-state parton showers into colourless hadrons which subsequently decay into stable final state hadrons.

Some of the most important differences between HERWIG and PYTHIA are the treatment of the parton showers and the hadronisation process. The following sections give a more detailed description of each generator.

3.2.1 HERWIG Monte Carlo

The HERWIG (Hadron Emission Reactions With Interfering Gluons) program [20] is a general purpose LO MC generator whose aim is to describe the largest number of physical processes with the fewest possible free parameters giving it a large predictive power. It is capable of simulating a large number of physics processes. HERWIG produces final state configurations of particles (at the hadron level) which can then be run through the ZEUS detector simulator (see section 3.4) to produce simulated data which can be compared directly with experimentally measured data.

The hard sub-process sits at the heart of the event generation in HERWIG. As discussed above, the hard sub-process involves a (LO) hard interaction between partons from the two incoming parton showers (initiated by each beam particle). In HERWIG, the factorisation scale of the interaction is set to

$$\mu_F^2 = \frac{2stu}{s^2 + t^2 + u^2} , \quad (3.5)$$

where s , t and u are the Mandelstam variables (for a definition of these variables see, for example [11]). The resulting cross-sections are divergent as $p_T^2 \rightarrow 0 \text{ GeV}^2$ (where p_T is the outgoing parton transverse momenta) and it is therefore necessary to introduce a lower cut-off, p_T^{min} . The predictions of the generator are independent of the value of p_T^{min} as long as the transverse energy of the selected jets is significantly in excess of p_T^{min} . Setting the value of p_T^{min} to high values also provides a way of efficiently generating high transverse energy events.

The incoming and outgoing parton showers are generated by a coherent branching algorithm. Each individual parton is split into many partons according to the DGLAP splitting functions, thereby forming leading log parton showers. The partons are ordered in terms of the opening angle between them such that the angle decreases with each successive branching. This procedure leads to a more correct treatment of the effects of coherent radiation and interfering gluons [21]. For the outgoing partons, the evolution is continued down to some hadronic scale which is of the order of the mass of typical light mesons (in contrast to the initial state case where the parton showering is generated using the backward evolution scheme). At this stage, HERWIG uses a cluster model [26] to implement the

fragmentation of final state partons into hadrons. The cluster model is a non-perturbative model which exploits the pre-confinement property of QCD, where partons are grouped into colour neutral objects. Final state gluons from the parton showering are initially split into $q\bar{q}$ pairs. Next, the quarks and anti-quarks are grouped into colourless clusters, which fragment into hadrons. Light clusters are fragmented into a single hadron, whilst heavier clusters are decayed into two lighter hadrons. The clusters decay isotropically except for hadrons which contain a quark from the outgoing parton shower which are emitted in the same direction that these quarks are travelling.

The final point that will be mentioned regarding HERWIG is related to the implementation of multiple interactions (MI). Such interactions are those which occur between partons from the incident particles that are not involved in the primary interaction itself (so-called spectator partons). HERWIG implements MI via an independent plug-in called JIMMY [22]. The inclusion of a MI component in the simulation improves the description of the HERA resolved photoproduction data [23]. Nothing more shall be said on this matter, as MI are not expected to be significant in the analysis presented in this thesis, but it has been mentioned here because it is an area where PYTHIA and HERWIG differ significantly. The MI model implemented by PYTHIA (outlined in [29]) does not describe the HERA resolved photoproduction data as well as JIMMY.

3.2.2 PYTHIA Monte Carlo

The PYTHIA Monte Carlo program shares many features with HERWIG. Like HERWIG, it is a general purpose generator which allows the user to simulate a wide variety of physics processes, using LO matrix elements to generate the hard sub-process. However, PYTHIA uses detailed models for the simulation of non-perturbative components of the event which leads to a significant increase in the number of free parameters in the program. The general layout of the event simulation is similar for both generators but there are significant differences between the specific implementations of each aspect of the event.

Regarding the perturbative part of the event simulation, PYTHIA uses a different definition of the factorisation scale than HERWIG. In PYTHIA, the factorisation scale is defined as

$$\mu^2 = \frac{1}{2}(m_1^2 + p_{T,1}^2 + m_2^2 + p_{T,2}^2), \quad (3.6)$$

where m_i and $p_{T,i}$ are the mass and transverse momentum of parton i , respectively. The major difference between PYTHIA and HERWIG in the parton showering stage is that with PYTHIA, the evolution is ordered, not in terms of the opening angle, as was the case for HERWIG, but in terms of the virtuality of the radiated partons. This ordering does not imply coherence, which has to be treated separately.

The treatment of hadronisation differs considerably from HERWIG. In PYTHIA, the Lund Symmetric String Fragmentation Model [30], implemented via the JETSET routines [31, 32], is used to make the transition between partons and hadrons. In this model, strings, which correspond to the QCD field lines, are connected between the quarks and gluons. These strings have a string constant of about 1 GeVfm^{-1} . As the distance between the partons increases the energy in the string increases and $q\bar{q}$ pairs are formed which fragments the string. Consequently, lower energy segments are created. Once the energy of the individual strings is small enough, mesons and baryons are formed from the quarks at the end of the strings. Mesons are formed when a short string connects a quark on one end to an antiquark on the other and a baryon is formed when a quark or antiquark is connected to a diquark. The final step involves the decay of unstable hadrons.

3.3 AMADEUS (aka ZDIS)

Amadeus [33] is a Fortran based software framework, which has been developed by the ZEUS collaboration, for producing hadron level MC events. Both HERWIG and PYTHIA are run within AMADEUS. Running MC generators, from within the AMADEUS framework offers a number of attractive features:

- AMADEUS is used as a standardised interface to many different MC generators, including HERWIG and PYTHIA.
- Additional functionality within the AMADEUS framework to support the production of hadron level MC eg event filters.
- Hadron level information from the underlying MC generator is written out and stored in a format which can be read directly by the ZEUS detector and trigger simulators (see section 3.4).

Run Period	E_T cut	p_T^{min} cut	Direct Evt	Resolved Evt	\mathcal{L}_{dir}	\mathcal{L}_{res}
98 – 99 e^-p	9.0	4.0	220000	710000	77.1	96.2
Target Luminosity				16.7		
Total number of events generated				0.93 million		
99 – 00 e^+p	9.0	4.0	1000000	3270000	353.5	443.3
Target Luminosity				65.9		
Total number of events generated				4.27 million		

Table 3.1: HERWIG MC generated for the analysis presented in this thesis. Luminosity values are quoted in pb. The jet E_T cut and p_T^{min} cut are quoted in GeV. The jet E_T cut is applied to the two highest E_T jets i.e. if the E_T cut is 9 GeV then we require a dijet whereby both jets have $E_T > 9$ GeV. All jets are subject to the requirement that $-1.5 < \eta_{jet} < 4.0$

In this particular analysis, hadron level HERWIG and PYTHIA MC is produced using AMADEUS and funnelled through the ZEUS detector and trigger simulators to produce simulated detector level MC events which can be compared directly with experimental data and more importantly allows hadron level distributions to be extracted from the corresponding detector level distributions.

Event filters within the AMADEUS software allow specific samples of MC to be produced. For example, this analysis is concerned with measuring high- E_T dijets. Thus one can choose event filters within AMADEUS such that only MC events with at least two high- E_T jets are written out. The event filters can also be used to select the pseudorapidity range of the jets. Jets are identified by running the k_T clustering algorithm (see section 2.7.1) on the final state hadrons. Tables 3.1 and 3.2 detail the kinematic properties of the MC events that have been generated for the analysis presented in this thesis. For each running period the PYTHIA MC events are produced in five distinct regions of E_T . The samples are then combined by weighting the higher- E_T samples to the lower- E_T sample using the respective luminosities. The reason for doing this is to minimise the statistical error on the acceptance corrections (see section 3.6) in high- E_T regions. This was not done in the HERWIG case which was only used to perform a systematic check in the present analysis.

3.4 FUNNEL and the ZEUS MC Chain

The aim of the ZEUS MC chain is to simulate the entire data taking process from $e^\pm p$ interaction to reconstruction. The chain consists of four principal programs and is shown schematically in figure 3.1

Run Period	E_T cut	p_T^{min} cut	Direct Evts	Resolved Evts	\mathcal{L}_{dir}	\mathcal{L}_{res}
98 – 99 e^-p	9.0	4.0	220000	710000	58.8	56.4
98 – 99 e^-p	19.0	14.0	120000	190000	590.9	580.0
98 – 99 e^-p	29.0	24.0	90000	90000	2933.5	2940.6
98 – 99 e^-p	39.0	34.0	60000	50000	8635.6	10557.9
98 – 99 e^-p	49.0	44.0	30000	20000	15799.1	20754.5
Target Luminosity				16.7		
Total number of events generated				1.58 million		
99 – 00 e^+p	9.0	4.0	1000000	3270000	267.0	260.1
99 – 00 e^+p	19.0	14.0	570000	850000	2796.0	2602.1
99 – 00 e^+p	29.0	24.0	430000	430000	14054.2	14053.0
99 – 00 e^+p	39.0	34.0	280000	210000	40357.1	43968.6
99 – 00 e^+p	49.0	44.0	140000	70000	73724.9	73979.6
Target Luminosity				65.9		
Total number of events generated				7.25 million		

Table 3.2: PYTHIA MC generated for the analysis presented in this thesis. Luminosity values are quoted in pb. The jet E_T cut and p_T^{min} cut are quoted in GeV. The jet E_T cut is applied to the two highest E_T jets i.e. If the E_T cut is 9 GeV then we require a dijet whereby both jets have $E_T > 9$ GeV. All jets are subject to the requirement that $-1.5 < \eta_{jet} < 4.0$

Generators relevant to the the ZEUS experiment have been collected together in the software framework AMADEUS (or ZDIS as it was previously known). This has already been discussed in section 3.3. AMADEUS produces lists of hadrons and their corresponding 4-momenta, which are produced by generators such as HERWIG or PYTHIA.

The output of AMADEUS is then fed into the detector simulator, MOZART [34], which simulates the response of the ZEUS detector to the input event. Each component of the ZEUS detector is simulated separately within MOZART and it is of vital importance that any changes made to the detector set-up are modelled correspondingly in MOZART.

The output of MOZART is then fed into CZAR [35] which simulates the ZEUS trigger system. It is based on the FLT and SLT simulations in ZGANNA [35] and the TLT simulation in TLT-ZGANNA [35].

Finally, the output of CZAR is fed into the ZEUS physics reconstruction program, ZEPHYR. This is the same reconstruction program that reconstructs real (as opposed to simulated) data events. After reconstruction, the event information is written to tape and can be analysed in the same way that one would analyse the real data.

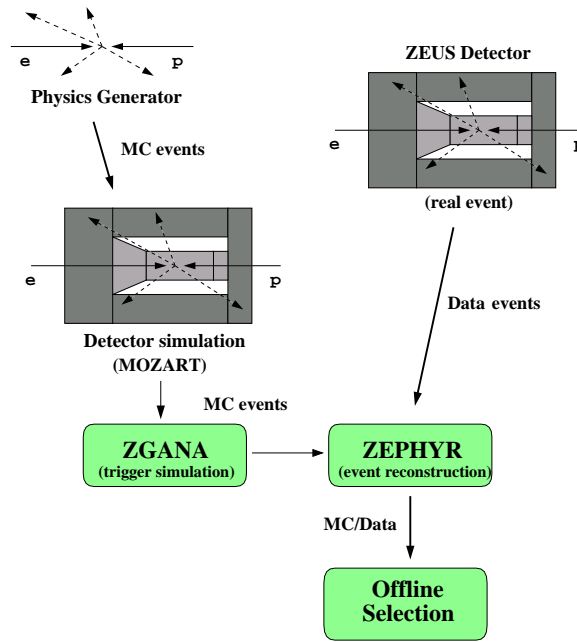


Figure 3.1: The ZEUS MC chain and its various software components

The entire process from the moment that the output files from AMADEUS are read into MOZART to the moment when the corresponding reconstructed files are written to tape is known as funnelling. And the various components of the process are collectively known as FUNNEL [36]

3.5 Hadronisation Corrections

The first major use of a MC event generator, such as PYTHIA or HERWIG, is in the estimation of the hadronisation correction. The defining equation (3.1) for the hadronisation correction, which was discussed in section 3.1, is

$$f_{had}(x) = g(x)f_{part}(x) ,$$

where $g(x)$ is the hadronisation correction. In actual fact, discretized versions of the above continuous functions (histograms) are measured in practice. So, for a given set of bin points, $\{x_k\}_{k=0}^n$, the following is written instead:

$$f_{had,i}(x) = g_i(x)f_{part,i}(x) , \quad (3.7)$$

for $i = 1, 2, \dots, n$ and the i^{th} bin is defined by $x_{i-1} < x \leq x_i$. Naturally, the binning is identical for each of the three histograms.

To calculate the hadronisation correction for a given distribution $f_{part,i}(x)$ all one has to do is perform the jet finding in two different modes. The jet finding is performed once over the final state partons (to determine $f_{part,i}(x)$) and once over the final state hadrons (to determine $f_{had,i}(x)$). The hadronisation correction is then determined by

$$g_i(x) = \frac{f_{had,i}(x)}{f_{part,i}(x)}, \quad (3.8)$$

for $i = 1, 2, \dots, n$. In this thesis, all hadronisation corrections have been calculated by running PYTHIA and HERWIG from within the program HZTOOL [37].

3.6 Acceptance Corrections

The second major use for a MC generator, such as HERWIG or PYTHIA, when combined with the ZEUS detector simulation software, is that it allows the relationship between detector level and hadron level quantities to be quantified. This relationship is illustrated via equation 3.4, whose discretized form is

$$f_{had,i}(x) = h_i^{-1}(x) f_{det,i}(x), \quad (3.9)$$

for $i = 1, 2, \dots, n$. As stated earlier, the goal of a particle physics analysis (as far as measuring cross-sections is concerned) is to measure some hadronic level distribution (cross-section), defined by some hadronic level kinematic cuts. The analysis begins, however, by measuring some detector level distribution (cross-section), defined by some detector level kinematic cuts. Calculating acceptance corrections involves calculating the mapping ($h_i^{-1}(x)$ in equation 3.9 above) between the measured detector level distributions and the corresponding hadronic level distributions. Once this mapping has been quantified, one can extract the hadronic level distribution underlying a given detector level distribution. The reasons why the detector level distributions and underlying hadronic distributions do not coincide exactly are numerous. Some of the main reasons include,

- The cuts used at the detector level, to isolate the hadronic sample of interest, are not 100% efficient.

- The sample, selected by the detector level cuts, is not 100% pure.
- The detector is imperfect. For a whole host of reasons (e.g. energy losses from dead material in the detector), detector level physical quantities do not coincide with the true underlying hadronic level variables.
- The triggers, used to reject background events, are not 100% efficient.
- The samples, which consist of all events which pass the triggers, are not 100% pure.

Once $h_i^{-1}(x)$ has been measured from the MC, it can be applied to the data distribution to extract the underlying hadronic distribution. The process of applying $h_i^{-1}(x)$ to the data level distribution is known as unfolding the distribution.

3.7 Bin-By-Bin Correction

In the bin-by-bin method the unfolded number of events in bin i , denoted by $f_{unf,i}(x)$ is given by

$$f_{unf,i}(x) = h_i^{-1}(x) f_{meas,i}(x), \quad (3.10)$$

where $f_{meas,i}(x)$ is the number of measured events in bin i . In the bin-by-bin method $h_i^{-1}(x)$ is

$$h_i^{-1}(x) = \frac{f_{had,i}(x)}{f_{det,i}(x)}. \quad (3.11)$$

It is important to distinguish between $f_{meas,i}(x)$ and $f_{det,i}(x)$. The former pertains to the real data whereas the latter is measured from the MC.

Two useful quantities, in the analysis of acceptance corrections, are the efficiency and purity of a bin. The efficiency is defined as

$$\epsilon_i(x) = \frac{f_{had,i}(x) \cap f_{det,i}(x)}{f_{had,i}(x)}, \quad (3.12)$$

where $f_{had,i}(x) \cap f_{det,i}(x)$ denotes the number of events which are both generated and detected in bin i . Therefore, $\epsilon_i(x)$ is the fraction of generated events in bin i that are also detected in bin i . Thus, if N events are generated in bin i then

one would expect $\epsilon_i(x)N$ of these events to be detected in this bin. The purity is defined as

$$p_i(x) = \frac{f_{had,i}(x) \cap f_{det,i}(x)}{f_{det,i}(x)}. \quad (3.13)$$

The purity is the fraction of detected events in bin i that were also generated in that bin. Thus, if N events are detected in bin i then one would expect $p_i(x)N$ of these events to have also been generated in this bin. From the definitions of the purity and efficiency it follows immediately that

$$h_i^{-1}(x) = \frac{p_i(x)}{\epsilon_i(x)}. \quad (3.14)$$

Clearly, if we have

$$\epsilon_i(x) = 1 \text{ and } p_i(x) = 1,$$

for $i = 1, 2, \dots, n$ then we must have

$$h^{-1}(x) = 1 \Rightarrow f_{had,i}(x) = f_{det,i}(x),$$

for $i = 1, 2, \dots, n$, and there would be a perfect reconstruction of the hadronic distribution. Thus, in any cross-section measurement it is desirable to have high efficiencies and purities, and acceptance corrections which are close to one.

The error on the acceptance correction can be shown (see appendix B) to be given by

$$\delta h_i^{-1}(x) = \sqrt{\frac{f_{had,i}(x)}{f_{det,i}^3(x)} [f_{had,i}(x) + f_{det,i}(x) - 2f_{had,i}(x) \cap f_{det,i}(x)]}. \quad (3.15)$$

As can be seen from this equation, the values of $h_i^{-1}(x)$ can be more precisely estimated if the numbers of events generated and measured in the same bin are large. This is equivalent to requiring high bin efficiencies and purities. This can be achieved by using bins which are at least twice the resolution of the physical quantity whose distribution is being measured. To define the resolution, suppose that a given physical quantity whose value lies in the range $a < x_{had} \leq b$ at the hadronic level is considered along with all its corresponding detector level values. The resolution is defined as the spread on the distribution of x_{det} (i.e. the probability density of x_{det} given x_{had}). Very often, this distribution can be approximated by a normal distribution.

It should be noted that when using the bin-by-bin technique to unfold cross-sections, correlations between adjacent bins are neglected and so differences between modelled and real migrations¹ can lead to inaccuracies in $h_i^{-1}(x)$. By using the bin-by-bin method an implicit assumption is being made that the migrations in the data are well modelled by the MC. To assess the model dependence of the unfolding procedure it is conducted using two different Monte Carlo generators. Both HERWIG and PYTHIA are used to unfold the distributions and an average of the two is taken as the central unfolded value (with half the difference between the two unfolded values being taken as the uncertainty).

¹If an event is generated in bin i , detected in bin j and $i \neq j$ then it is said to have migrated from bin i to bin j . If $|i - j|$ is large then the migration is termed long-range.

Chapter 4

Determination of Parton Densities

NLO QCD analyses of ZEUS data have been performed by the ZEUS collaboration for a number of years. The purpose of such analyses have been to extract the quark and gluon densities, or parton distribution functions (PDFs), of the proton by performing multidimensional fits to both ZEUS and world data. The principal objective of the present analysis is to make experimental measurements which are designed to further constrain the gluon distribution from the ZEUS QCD fits. A discussion of the ZEUS QCD fits is therefore warranted. This chapter will begin with an introduction to the QCD fits which are performed by the ZEUS collaboration before going on to discuss the most recent development of such fits, the incorporation of jet data into the fitted data set, the ramifications of which provide the motivation for the present analysis.

4.1 Introduction

As was seen in chapter 2, the kinematics of DIS lepton-proton scattering is described in terms of the variables Q^2 , Bjorken x and Bjorken y . The differential cross-section for the NC DIS process is given in terms of structure functions by equation 2.6, shown again below:

$$\frac{d^2\sigma^{NC}(e^\pm p)}{dx dQ^2} = \frac{2\pi\alpha^2}{xQ^4} [Y_+ F_2(x, Q^2) \mp Y_- xF_3(x, Q^2) - y^2 F_L(x, Q^2)] \quad . \quad (4.1)$$

The structure functions F_2 and xF_3 are directly related to the quark distributions and their Q^2 dependence (scaling violation) is predicted by perturbative QCD.

At $Q^2 \lesssim 10^3 \text{ GeV}^2$ the NC cross-section is dominated by photon exchange and the structure function F_2 . For $x \lesssim 10^{-2}$, F_2 is sea quark dominated and its Q^2 dependence is driven by the gluon contribution. HERA data is therefore sensitive to, and provides crucial information on, both the quark and gluon densities. The longitudinal structure function, F_L , is only important at high y , otherwise it is suppressed by the y^2 factor which precedes its contribution in equation 4.1. In perturbative QCD, F_L can be calculated from the quark and gluon densities [39]. The structure function F_3 becomes increasingly important at high Q^2 , providing information on the valence quark distributions. The CC interactions, at high- x , are directly sensitive to the flavour of the valence quarks. This can be seen by looking at the LO expressions for the CC e^+ and e^- cross-sections:

$$\frac{d^2\sigma^{CC}(e^+p)}{dx dQ^2} = \frac{G_F^2 M_W^4}{2\pi x(Q^2 + M_W^2)^2} x [(\bar{u} + \bar{c}) + (1-y)^2(d+s)] , \quad (4.2)$$

$$\frac{d^2\sigma^{CC}(e^-p)}{dx dQ^2} = \frac{G_F^2 M_W^4}{2\pi x(Q^2 + M_W^2)^2} x [(u+c) + (1-y)^2(\bar{d} + \bar{s})] , \quad (4.3)$$

where u , d , s and c are functions of x and Q^2 and represent the up, down, strange and charm densities, respectively. For the e^+p CC cross section we therefore see that at high- x , where the contribution from the sea quarks is negligible (\bar{u}, \bar{c} and s), the cross-section is directly sensitive to the d valence quark. Similarly, the high- x e^-p CC cross section is directly sensitive to the u valence quark. This information, provided by the CC cross-sections, is very important as it relinquishes the need for external fixed target data which has traditionally been used in the ZEUS QCD fits to constrain the valence quark densities.

Inclusive cross-section data is directly dependent on the valence and sea quark densities. The gluon, on the other hand, only affects the cross-section indirectly through the scaling violations of the quark densities. This scaling (the rate of change of the density w.r.t Q^2) is predicted by perturbative QCD (see section 2.3) and is given by equation 2.10 which is repeated below:

$$\frac{dq_i(x, Q^2)}{d \log Q^2} = \frac{\alpha_s}{2\pi} \int_x^1 \frac{dy}{y} \left[q_i(y, Q^2) P_{qq} \left(\frac{x}{y} \right) + g(y, Q^2) P_{qg} \left(\frac{x}{y} \right) \right] . \quad (4.4)$$

The gluon density can therefore be obtained indirectly from the scaling violations of the quark densities. It should be noted, that without further information about the gluon density or α_s dependence, the parameters which describe the gluon density and the value of α_s are strongly correlated via the DGLAP equations.

The problem of large correlations between the gluon density parameters and α_s can, to a certain extent, be circumvented by the consideration of more exclusive processes. The two QCD processes of QCD-Compton (QCDC) and boson-gluon-fusion (BGF) (see section 2.5), consist of events with distinct jets in the final states. Such jet cross-sections can be measured and included in the fitted data set to further tie down the gluon density and the value of α_s . This can be understood by noting that the QCDC process is dependent on the value of α_s and the quark densities. For HERA kinematics, this process dominates at large scales. At such scales, the quark densities are well constrained from the inclusive data so that α_s can be extracted without strong correlation to the gluon density. Also, the cross-section for the BGF process depends directly on the gluon density and allows for a direct probe of the gluon distribution to be made.

4.2 Brief History of the ZEUS QCD Fits

Since 2002, three (two published, one unpublished) principal QCD fits have been made by the ZEUS collaboration. These analyses fit parameters which are related to the parton densities of the proton and will be discussed in section 4.3. The fitting method used in each case is very similar (again, see section 4.3). The main difference between the various analyses is the data which were used in the fitted data set which is discussed in the following subsections.

4.2.1 The ZEUS-S, ZEUS- α_s and ZEUS-O Fits

These (published) fits [40] were made in 2002 and used ZEUS NC DIS data from 1996 and 1997 [43] together with fixed-target data, to extract the gluon and quark densities of the proton. It was necessary to use fixed target data because the ZEUS 96-97 NC data constrains the low- x sea and gluon rather well but does not provide significant constraints on the valence densities (or on the higher- x sea and gluon densities). Various fits were performed. In the ZEUS-S fit (the ZEUS-Standard fit) the value of $\alpha_s(M_Z)$ was fixed to the world average value of 0.118 [44]. A fit was also performed to simultaneously extract both the value of $\alpha_s(M_Z)$ and the parton densities. This was called the ZEUS- α_s fit. The role of ZEUS data were investigated by making a fit to ZEUS data alone. The ZEUS CC e^+p data from 94-97 [45], and the CC and NC e^-p data from 98-99 [46, 47], together with the ZEUS 96-97 e^+p NC data were fitted to make an extraction of the parton densities independently of other experiments. This was called the ZEUS-O fit.

4.2.2 The ZEUS-Type5 Fit

The 2002 analysis made it clear that correlated systematic uncertainties from many different experiments make a significant contribution to the overall uncertainties on the extracted densities. As explained above, the fixed target data were needed in order to constrain valence densities. The ZEUS-O fit attempted to use the e^\pm CC data to constrain the valence densities, without including the fixed target data in the fitted data set. The precision of the sea and gluon densities extracted from this ZEUS-O fit was comparable to the ZEUS-S fit at small- x (which suggests that the information about the small- x sea and gluon densities is coming from the ZEUS data alone). However, the quality of the extracted valence densities in the ZEUS-O fit was noticeably inferior to the ZEUS-S fit across the entire x range. The ZEUS-Type5 fit [41] is an updated analysis of ZEUS only data which was performed in 2004 (unpublished). The ZEUS-Type5 fit is the same as the ZEUS-O fit except that the former uses an enlarged fitted data set. In particular, ZEUS e^+ CC and NC data from 99-00 [48, 49] were included in the fitted data set to further constrain the parton densities, especially the valence densities (with the new CC data). Indeed, the ZEUS-Type5 fit led to a considerable improvement in the precision of the extracted valence PDFs.

4.2.3 The ZEUS-Jets Fit

The most recent QCD fits performed by the ZEUS collaboration were the ZEUS-Jets and ZEUS-Jets- α_s fits [42] which, along with the data of the ZEUS-Type5 fit, included ZEUS 96-97 inclusive DIS jet data [50] and ZEUS 96-97 γp dijet data [51] in the fitted data set. In the ZEUS-Jets fit, the value of $\alpha_s(M_z)$ was set to the world average of 0.118 [44], whereas in the ZEUS-Jets- α_s fit the value of $\alpha_s(M_z)$ was simultaneously fitted along with the PDFs. After a brief introduction, presented in the following section, to the method of performing the fits, the bulk of the remainder of this chapter will be devoted to a discussion of the incorporation of the ZEUS 96-97 γp dijet data into the fitted data set of the ZEUS QCD fit. The chapter will be concluded with a discussion of the results of this procedure.

4.3 Fitting Method

A brief outline of the fitting procedure used in the ZEUS QCD fits will now be presented. For in-depth details the reader is referred to [40].

4.3.1 Parameterisation of the PDFs

The PDFs are parameterised at some input scale Q_0^2 (in the fits that are considered in this thesis, $Q_0^2 = 7 \text{ GeV}^2$) by the form

$$xf(x) = p_1 x^{p_2} (1-x)^{p_3} (1+p_4 x). \quad (4.5)$$

Not all the individual proton PDFs are parameterised but instead the following distributions are considered: u valence, $xu_v(x)$; d valence, $xd_v(x)$; total sea, $xS(x)$; gluon, $xg(x)$; and the difference between the d and u contributions to the sea, $x\Delta = x(\bar{d} - \bar{u})$. The PDFs are evolved to an arbitrary Q^2 scale using the DGLAP equations (see section 4.1) implemented in the QCDNUM program [61]. At first glance it appears that there are 20 free parameters but in actual fact almost half of these parameters are fixed by theoretical and experimental constraints. In the ZEUS-Jets fit the parameters are constrained in the following manner:

- the normalisation parameters p_1 , for the d and u valence and for the gluon, were constrained by imposing the number sum-rules and momentum sum-rule, respectively.
- the p_2 parameters, which constrain the low- x behaviour of the valence distributions, were set equal for u and d , since there is insufficient information to constrain any difference;
- there is also no information on the flavour structure of the light-quark sea in a fit to ZEUS data alone. Thus, the normalisation of the $\bar{d} - \bar{u}$ distribution was fixed to be consistent with the measured violation of the Gottfried sum-rule [52, 53] and its shape was fixed to be consistent with the Drell-Yan data [54].
- A suppression of the strange sea by a factor of two at Q_0^2 was imposed in accordance with neutrino induced dimuon data from CCFR-NuTeV [55, 56].

The ZEUS inclusive data are statistics limited at large x , where the sea and gluon distributions are small. This leads to sizeable uncertainties in the mid-to-high- x sea and gluon shapes if a fit is made to inclusive cross-section data alone. The ZEUS jet data constrain the gluon distribution in this kinematic region. In order to constrain the sea distribution a simpler parameterisation was used by setting $p_4 = 0$. After the application of the above constraints, there are 11 free parameters describing the input PDF distributions.

4.3.2 Definition of the χ^2 and the Determination of PDF Errors

The definition of the χ^2 used in the ZEUS QCD fits is given below:

$$\chi^2 = \sum_i \frac{[F_i(p, s) - F_i(meas)]^2}{(\sigma_{i,stat}^2 + \sigma_{i,unc}^2)} + \sum_\lambda s_\lambda^2, \quad (4.6)$$

where

$$F_i(p, s) = F_i^{NLOQCD}(p) + \sum_\lambda s_\lambda \Delta_{i\lambda}^{sys}. \quad (4.7)$$

The actual χ^2 minimisation and the calculation of the covariance matrices are based on MINUIT [57]. The symbol $F_i(meas)$ represents a measured data point (structure function, reduced cross-section or cross-section) with statistical uncertainty $\sigma_{i,stat}$ and uncorrelated systematic uncertainty $\sigma_{i,unc}$. The symbol $F_i^{NLOQCD}(p)$ represents the theoretical NLO QCD prediction for data point i which is a function of the unknown parameters to be fitted for. This prediction is actually modified, as in equation 4.7, to include the effect of the correlated systematic uncertainty on data point i . The one-standard-deviation correlated systematic uncertainty, on data point i , due to the λ^{th} source is denoted by $\Delta_{i\lambda}^{sys}$. The parameters s_λ represent independent Gaussian standard random variables i.e. with mean 0, variance 1; for each source of systematic uncertainty. These parameters are fixed to zero to obtain the central values for the parameters \vec{p} but allowed to vary in the error analysis. In addition to the usual Hessian matrix, M_{jk} , given by

$$M_{jk} = \frac{1}{2} \frac{\partial^2 \chi^2}{\partial p_j \partial p_k}, \quad (4.8)$$

a second Hessian matrix, $C_{j\lambda}$, given by

$$C_{j\lambda} = \frac{1}{2} \frac{\partial^2 \chi^2}{\partial p_j \partial s_\lambda}, \quad (4.9)$$

was calculated. The correlated systematic covariance matrix is given by $V^{ps} = M^{-1} C C^T M^{-1}$ [58] and the total covariance matrix by $V^{tot} = V^p + V^{ps}$ where $V^p = M^{-1}$. This method of treating systematic uncertainties results in a more conservative error estimate than alternative methods (see [40] for a detailed

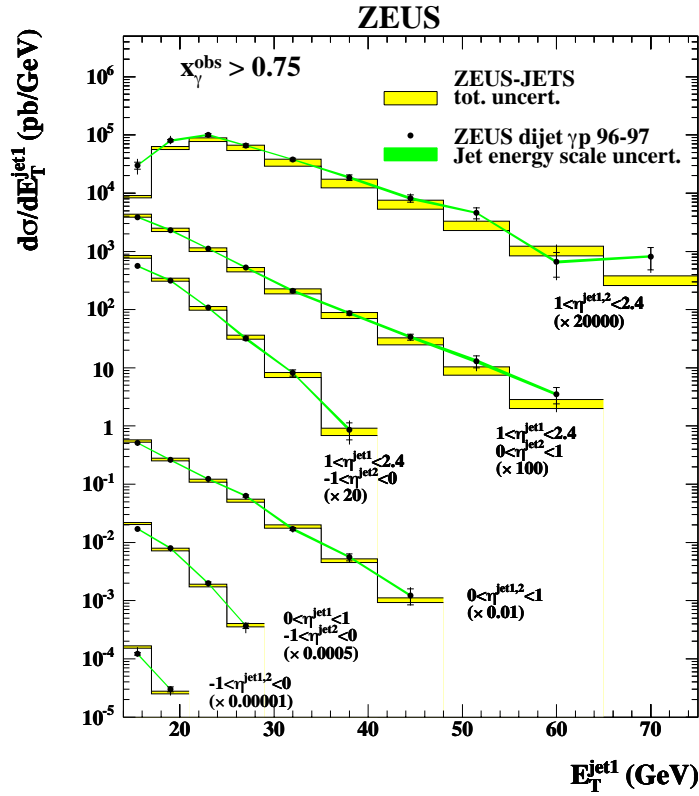


Figure 4.1: The six high- x_γ^{obs} dijet γp differential cross-sections as a function of the transverse energy of the leading jet, $E_{T,1}$, that were included in the fitted data set of the ZEUS-Jets fit. The cross-sections shown have been symmetrised with respect to the pseudorapidities of the jets. For example, the cross-section labelled $0 < \eta^{jet1} < 1$, $-1 < \eta^{jet2} < 0$ consist of events where either $0 < \eta^{jet1} < 1$ and $-1 < \eta^{jet2} < 0$ or $-1 < \eta^{jet1} < 0$ and $0 < \eta^{jet2} < 1$. This matter is discussed in more detail in section 5.4. Figure taken from [42]

discussion of the various methods that can be utilised). The uncertainty on any distribution, F , which is derived from the parameters \vec{p} is then given by

$$\langle \Delta F^2 \rangle = \sum_j \sum_k \frac{\partial F}{\partial p_j} V_{jk} \frac{\partial F}{\partial p_k} . \quad (4.10)$$

4.4 Adding γp Dijet Data into the Fit: Part 1

What distinguished the ZEUS-Jets fit from earlier ZEUS fits, and indeed other global fits, is that it incorporated jet data into the fitted data set, in a rigorous

manner, for the first time ever. As stated earlier, two sets of jet measurements were incorporated into the fit: ZEUS 96-97 inclusive DIS jet data [50] and ZEUS 96-97 γp dijet data [51]. The author was responsible for the incorporation of the γp dijet data and, therefore, the rest of this chapter will be devoted to a discussion of this work.

4.4.1 An Outline of the Problem

The ZEUS-Jets fit included, in its fitted data set, six high- x_γ^{obs} (> 0.75) γp dijet cross-sections as a function of the transverse energy of the most energetic jet, E_T^{jet1} , for different jet-pseudorapidity ranges [51]. These six cross-sections are shown in figure 4.1¹. Firstly, let us consider the contribution to the total χ^2 (equation 4.6) which comes from the γp dijet data,

$$\chi_{\gamma p}^2 = \sum_{i=1}^{38} \frac{[F_i^{NLOQCD}(p) - F_i(meas)]^2}{(\sigma_{i,stat}^2 + \sigma_{i,unc}^2)}, \quad (4.11)$$

where the sum runs over the 38 data points of figure 4.1. Some simplifications are made in order to arrive at the above equation. We have assumed, in order to keep the explanation tidy, that we are performing the fit to determine the central values of the parameters \vec{p} in which case the s_λ are fixed to zero. The points $F_i(meas)$ (for $i \in \{1, 2, \dots, 38\}$) are the data points of figure 4.1 and the $F_i^{NLOQCD}(p)$ are the NLO QCD theoretical predictions for these data points. These theoretical points are calculated using the NLO γp jet production code of Frixione and Ridolfi [19]. Given a certain input PDF the theoretical calculations take a relatively long time to calculate using the author's original code. In the ZEUS QCD fit, initially, a trial set of parameters is chosen. Cross-section predictions are computed based on the corresponding PDFs for these parameters. The parameters are then varied and cross-section predictions are recomputed. These steps are repeated until a minimum value of χ^2 is found. The number of steps required varies from fit to fit but is of the order of 100. Using the NLO jet production code, in its original guise, to calculate the relevant predictions at each stage of the fit is time consuming and a quicker method for calculating the cross-sections is sought to ensure that the method of fitting jet cross-sections is practical.

¹The figure uses slightly different notation for the transverse energy of the leading jet, $E_T^{jet1} \equiv E_{T,1}$.

Parameter	Meaning
x_{min}	Minimum value of x in the grid
x_{max}	Maximum value of x in the grid
N_x	Number of bins in x
$\mu_{F,min}^2$	Minimum value of μ_F^2 in the grid
$\mu_{F,max}^2$	Maximum value of μ_F^2 in the grid
$N_{\mu_F^2}$	Number of bins in μ_F^2

Table 4.1: Table showing the parameters which characterise the cross-section grids

4.4.2 Derivation of the Cross-Section Grid

In a nutshell, cross-section grids involve factoring a particular cross-section calculation into two parts: a PDF dependent part and a PDF independent part. The PDF dependent part can be calculated solely from a set of PDFs. Once the PDF independent part is calculated then the cross-section can be reconstructed quickly using any arbitrary PDF. This section describes how this is done.

We shall begin by considering the general expression for the NLO cross-section for γp processes which is

$$\sigma^{(\gamma p)} = \sum_{a_p, a_\gamma} \int f_{a_p}^{(p)}(x_1, \mu_F^2) f_{a_\gamma}^{(\gamma)}(x_2, \mu_F^2) \hat{\sigma}_{a_p, a_\gamma}(x_1, x_2, \mu_F^2) dx_1 dx_2 d\mu_F^2, \quad (4.12)$$

where $f_{a_p}^{(p)}(x_1, \mu_F^2)$ is the PDF for parton a_p , from the proton; $f_{a_\gamma}^{(\gamma)}(x_2, \mu_F^2)$ is the PDF for parton a_γ from the photon; x_1 is the proton momentum fraction of the struck parton from the proton, x_2 is the photon momentum fraction of the struck parton from the photon and μ_F is the kinematic variable which is taken to be the factorisation scale. For example, in DIS $\mu_F = Q$ but in photoproduction some other suitable definition has to be found (see section 2.4). The quantity $\hat{\sigma}_{a_1, a_2}(x_1, x_2, \mu_F^2)$ represents the NLO matrix element calculated by pQCD. The existence of another very important scale should also be noted, that of the renormalisation scale, μ_R , which α_s depends upon. In equation 4.12 we have made the assumption that $\mu_R = \mu_F$ and absorbed the $\alpha_s(\mu_F^2) (\equiv \alpha_s(\mu_R^2))$ term into the matrix element. It should also be noted that for direct γp processes, $f_{a_\gamma}^{(\gamma)}(x_2, \mu_F^2) = \delta_{\gamma a_\gamma} \delta(x_2 - 1)$.

First of all, a two-dimensional grid is defined in x - μ_F^2 space. This grid is defined with the parameters shown in table 4.1. These parameters are used to define the

individual grid points of the grid, the knot points. A uniform grid could be used (a grid with uniform spacing between the knots) but in the present situation and due to the form of the PDFs it is far more sensible to use a logarithmic binning. The grid knots in the x dimension are given by

$$\text{Log}(x_i) = \text{Log}(x_{min}) + \left[\frac{\text{Log}(x_{max}) - \text{Log}(x_{min})}{N_x} \right] (i - 1), \quad (4.13)$$

for $i = \{1, 2, \dots, N_x + 1\}$. And similarly, the grid knots in the μ_F^2 dimension are given by

$$\text{Log}(\mu_{F,j}^2) = \text{Log}(\mu_{F,min}^2) + \left[\frac{\text{Log}(\mu_{F,max}^2) - \text{Log}(\mu_{F,min}^2)}{N_{\mu_F^2}} \right] (j - 1), \quad (4.14)$$

for $j = \{1, 2, \dots, N_{\mu_F^2} + 1\}$. This produces a grid with $N_x \times N_{\mu_F^2}$ bins defined by $(N_x + 1) \times (N_{\mu_F^2} + 1)$ knots. Next, a 2D pulse function is defined across each bin. The ij^{th} pulse function is defined as

$$\Pi_{ij}(x, \mu_F^2) = \begin{cases} 1 & \text{if } x_i < x \leq x_{i+1} \text{ and } \mu_{F,i}^2 < \mu_F^2 \leq \mu_{F,i+1}^2 \\ 0 & \text{otherwise} \end{cases}, \quad (4.15)$$

for $i = \{1, 2, \dots, N_x\}$ and $j = \{1, 2, \dots, N_{\mu_F^2}\}$. The next step is to approximate $f_{a_p}^{(p)}(x, \mu_F^2)$ as a linear combination of 2D pulse functions as follows:

$$f_{a_p}^{(p)}(x, \mu_F^2) \approx \sum_i \sum_j c_{a_p,ij} \Pi_{ij}(x, \mu_F^2), \quad (4.16)$$

where the $c_{a_p,ij}$ are just constants which are found by evaluating the function $f_{a_p}^{(p)}(x, \mu_F^2)$ at a suitable point within the ij^{th} bin. A reasonable definition is

$$c_{a_p,ij} = f_{a_p}^{(p)}(\langle x \rangle_i, \langle \mu_F^2 \rangle_j), \quad (4.17)$$

where

$$\langle x \rangle_i = \frac{1}{2}(x_i + x_{i+1}), \quad (4.18)$$

for $i = \{1, 2, \dots, N_x\}$, and

$$\langle \mu_F^2 \rangle_j = \frac{1}{2}(\mu_{F,j}^2 + \mu_{F,j+1}^2), \quad (4.19)$$

for $j = \{1, 2, \dots, N_{\mu_F^2}\}$. In other words, the $c_{a_p,ij}$ are found by just evaluating the function $f_{a_p}^{(p)}(x, \mu_F^2)$ at the midpoint of the ij^{th} bin. Next, equation 4.16 is substituted into equation 4.12 to yield

$$\sigma^{(\gamma p)} = \sum_{a_p} \sum_{a_\gamma} \int \int \int \left[\sum_i \sum_j c_{a_p,ij} \Pi_{ij}(x_1, \mu_F^2) \right] f_{a_\gamma}^{(\gamma)}(x_2, \mu_F^2) \hat{\sigma}_{a_p, a_\gamma}(x_1, x_2, \mu_F^2) dx_1 dx_2 d\mu_F^2, \quad (4.20)$$

where the summations and integrals have, this time, been written out in full. This can be re-written as

$$\sigma^{(\gamma p)} = \sum_{a_p} \sum_i \sum_j c_{a_p,ij} \left[\sum_{a_\gamma} \int \int \int \Pi_{ij}(x_1, \mu_F^2) f_{a_\gamma}^{(\gamma)}(x_2, \mu_F^2) \hat{\sigma}_{a_p, a_\gamma}(x_1, x_2, \mu_F^2) dx_1 dx_2 d\mu_F^2 \right], \quad (4.21)$$

but the ij^{th} pulse function is only defined across the ij^{th} bin, where it has a value of unity. At all other points outside the ij^{th} bin it is zero, so we may write equation 4.21 as

$$\sigma^{(\gamma p)} = \sum_{a_p} \sum_i \sum_j c_{a_p,ij} \left[\sum_{a_\gamma} \int \int \int f_{a_\gamma}^{(\gamma)}(x_2, \mu_F^2) \hat{\sigma}_{a_p, a_\gamma}(x_1, x_2, \mu_F^2) dx_1 dx_2 d\mu_F^2 \right], \quad (4.22)$$

where the integrations w.r.t x_1 and μ_F^2 are understood to be carried out just over the ij^{th} bin. Writing equation 4.22 in a slightly different form yields

$$\sigma^{(\gamma p)} = \sum_{a_p} \sum_i \sum_j c_{a_p,ij} W_{a_p,ij}, \quad (4.23)$$

where

$$W_{a_p,ij} = \sum_{a_\gamma} \int \int \int f_{a_\gamma}^{(\gamma)}(x_2, \mu_F^2) \hat{\sigma}_{a_p, a_\gamma}(x_1, x_2, \mu_F^2) dx_1 dx_2 d\mu_F^2. \quad (4.24)$$

It should be noted that the weights $W_{a_p,ij}$ are completely independent of the proton PDF. The cross-section has successfully been factored into a PDF dependent part (the $c_{a_p,ij}$) and a PDF independent part (the $W_{a_p,ij}$). The set of all $W_{a_p,ij} \forall i, j, a_p$ is termed the cross-section grid and is denoted by W .

4.4.3 Reconstructing the Cross-Section

In this section a prescription is presented for reconstructing a cross-section², with the method from the previous section, using a given cross-section grid and arbitrary PDF. Consider the case where we have any proton PDF set (CTEQ, MRST etc), $\{f_{a_p}^{(p)}(x, \mu_F^2) : a_p \in \{-N_{a_p}, \dots, 0, \dots, N_{a_p}\}\}$ (where N_{a_p} is the number of active flavours); and a cross-section grid W . Below is the series of steps needed to be taken to reconstruct the cross section. Note, that the existence of a grid (in x - μ_F^2 space), defined by the parameters in table 4.1, is assumed (this is necessary to define W in the first place!).

- Calculate the coefficients $c_{a_p, ij}$ using equation 4.17.
- Use equation 4.23 to reconstruct the cross section.

4.4.4 Calculation of the Cross-Section Grid

Attention is now turned to the calculation of W (equation 4.24). This is done using the NLO γp jet production code of Frixione and Ridolfi [19]. There is one elegant method which immediately springs to mind. By comparing equation 4.24 with equation 4.12 it can be seen that $W_{a_p, ij}$ is the contribution of parton a_p to the cross-section calculated using a hypothetical PDF which consists of a pulse function situated at the ij^{th} bin. To calculate $W_{a_p, ij}$, one simply needs to feed the pulse-function PDF as input into the program. This must be done individually for each flavour i.e. the cross-section must be calculated with just the PDF for parton a_p (not the whole proton set) as the contributions to the cross-section from different flavours must be kept separate. What is attractive about this method is that it involves no modification to be made to the actual code. All one has to do is feed in a different PDF each time the program is run and to store the cross-section numbers produced. The trouble is, is that given that the number of active flavours in the calculation is 5 (the top contribution is neglected at HERA) and that the grids used are typically of the order of 150×150 , the code would have to be run 247,500 times! This is however a very conservative figure. If this approach was used in practice there would undoubtedly be ways of reducing the

²Reconstructing the cross-section in this sense refers to the reconstruction (determination) of the theoretical prediction using the cross-section grid method.

computational burden. The attraction of this approach, to reiterate, is that no modification to the code is necessary.

Instead, an alternative approach will be outlined which involves running the relevant program only once to produce the entire grid, W . Like the set-up of many other programs, the NLO γp jet production code of Frixione and Ridolfi [19] incorporates a user routine where the person running the code can place cuts on the kinematic variables of the events and fill histograms with an appropriate weight: the event weight, $w^{(evt)}$ (calculated by the program).

It should be noted at this point that, in practice, cross-sections are calculated using binned histograms. In this case equation 4.23 needs to be modified as follows

$$\sigma_k^{(\gamma p)} = \sum_{a_p} \sum_i \sum_j c_{a_p,ij} W_{a_p,ijk} , \quad (4.25)$$

where $\sigma_k^{(\gamma p)}$ is the cross-section in bin k i.e. there is a separate grid, W_k , for each bin of the cross section.

The event weight, $w^{(evt)}$, can be broken down into smaller components. The event weight is simply the integrand of equation 4.12, namely

$$\sum_{a_p} \sum_{a_\gamma} f_{a_p}^{(p)}(x_1, \mu_F^2) f_{a_\gamma}^{(\gamma)}(x_2, \mu_F^2) \hat{\sigma}_{a_p, a_\gamma}(x_1, x_2, \mu_F^2) , \quad (4.26)$$

where the sums have been written out in full and taken inside the integral. Rewriting this in a slightly different form gives

$$\sum_{a_p} f_{a_p}^{(p)}(x_1, \mu_F^2) \left[\sum_{a_\gamma} f_{a_\gamma}^{(\gamma)}(x_2, \mu_F^2) \hat{\sigma}_{a_p, a_\gamma}(x_1, x_2, \mu_F^2) \right] . \quad (4.27)$$

Thus,

$$w^{(evt)} = \sum_{a_p} f_{a_p}^{(p)}(x_1, \mu_F^2) w_{a_p}^{(evt)} , \quad (4.28)$$

where

$$w_{a_p}^{(evt)} = \sum_{a_\gamma} f_{a_\gamma}^{(\gamma)}(x_2, \mu_F^2) \hat{\sigma}_{a_p, a_\gamma}(x_1, x_2, \mu_F^2) . \quad (4.29)$$

So, somewhere in the code, the PDF weights, $f_{a_p}^{(p)}(x_1, \mu_F^2)$ are being convoluted together with the matrix element weights $w_{a_p}^{(evt)}$ (which themselves are convoluted

with the photon PDF weights) as per equation 4.28. To calculate the cross-section grids, W_k , the user must firstly find where in the code this convolution is being done and then to store the matrix element weights, $w_{a_p}^{(evt)}$, in a separate array. The deconvolution of the event weight in this way can be quite tricky depending on how the code the user is working with is written. But with careful work and constant checking of the modified code against a version of the original, untouched, code the task is more than feasible.

A general prescription for calculating the cross-section grids,

$$W = \{W_k : k \in \{1, 2, \dots, N_{bins}\}\}, \quad (4.30)$$

corresponding to a given cross-section histogram with N_{bins} bins can now be given.

1. Define a 2D grid in $x-\mu_F^2$ space according to the method outlined in section 4.4.2. Store the knot points along the x and μ_F^2 axis in appropriate arrays.
2. Define a cross-section grid array (W) which is dimensioned as $N_{bins} \times N_{a_p} \times N_x \times N_{\mu_F^2}$.
3. Generate an event
4. Apply any kinematic cuts to the event.
5. Find the following
 - Which bin in the $x-\mu_F^2$ grid, the event falls into.
 - Which bin in the cross-section histogram the event falls into.
6. Loop over all active partons and fill W (at the location specified by step 5) with the deconvoluted $w_{a_p}^{(evt)}$ weights.
7. Repeat steps 3-7 until as many events have been generated as desired.

Once W has been calculated then the particular cross-section under consideration can be calculated using any arbitrary PDF using the method of section 4.4.3 but with equation 4.23 replaced with equation 4.25 (and the reconstruction performed for each bin of the cross-section histogram).

The result of going to all the trouble of producing the cross-section grids using this method is

- As many cross-section grids can be produced as one desires by running the appropriate program just once.
- The reconstruction of the cross-section, given any arbitrary proton PDF, is very fast.

The methods outlined in this section lead to a quick, powerful and rigorous method of including jet cross-sections in an iterative PDF fit.

4.4.5 Deconvolution of α_s

In fits such as the ZEUS-Jets- α_s fit, the cross-section grid W needs to be independent of, not only the proton PDF, but also α_s . To understand how this is done, equation 4.22 has to be rewritten slightly as

$$\sigma^{(\gamma p)} = \sum_{a_p} \sum_i \sum_j \sum_n c_{a_p,ij} \left[\sum_{a_\gamma} \int \int \int f_{a_\gamma}^{(\gamma)}(x_2, \mu_F^2) \alpha_s^{(n)}(\mu_F^2) \hat{\sigma}_{a_p, a_\gamma}^{(n)}(x_1, x_2) dx_1 dx_2 d\mu_F^2 \right], \quad (4.31)$$

where it must be remembered that the assumption has been made that the factorisation scale is equal to the renormalisation scale. It must also be remembered that the integrations w.r.t x_1 and μ_F^2 are understood to be carried out over the ij^{th} bin. We see that all that has been done in the above equation is that the contributions from the various orders of the calculation have been separated. It is assumed that there are N_n orders contributing. In practice, the calculations are carried out to NLO ($N_n = 2$) but a more general notation is used as the actual powers of α_s contributing vary depending on whether the calculation is for direct or resolved γp . Next, the assumption is made that the value of $\alpha_s^{(n)}(\mu_F^2)$ is constant across the ij^{th} bin

$$\alpha_s^{(n)}(\mu_F^2) \approx \alpha_s^{(n)}(\langle \mu_F^2 \rangle_j), \quad (4.32)$$

allowing equation 4.31 to be rewritten as

$$\sigma^{(\gamma p)} = \sum_{a_p} \sum_i \sum_j \sum_n c_{a_p,ij} \alpha_s^{(n)}(\langle \mu_F^2 \rangle_j) \left[\sum_{a_\gamma} \int \int \int f_{a_\gamma}^{(\gamma)}(x_2, \mu_F^2) \hat{\sigma}_{a_p, a_\gamma}^{(n)}(x_1, x_2) dx_1 dx_2 d\mu_F^2 \right], \quad (4.33)$$

or

$$\sigma^{(\gamma p)} = \sum_{a_p} \sum_i \sum_j \sum_n c_{a_p,ij}^{(n)} W_{a_p,ij}^{(n)}, \quad (4.34)$$

where

$$c_{a_p,ij}^{(n)} = f_{a_p}^{(p)}(\langle x \rangle_i, \langle \mu_F^2 \rangle_j) \alpha_s^{(n)}(\langle \mu_F^2 \rangle_j) \text{ and} \quad (4.35)$$

$$W_{a_p,ij}^{(n)} = \sum_{a_\gamma} \int \int \int f_{a_\gamma}^{(\gamma)}(x_2, \mu_F^2) \hat{\sigma}_{a_p, a_\gamma}^{(n)}(x_1, x_2) dx_1 dx_2 d\mu_F^2. \quad (4.36)$$

The weights $W_{a_p,ij}^{(n)}$ are now completely independent of the proton PDF and α_s . The cross-section has successfully been factored into a PDF and α_s dependent part (the $c_{a_p,ij}^{(n)}$) and a PDF and α_s independent part (the $W_{a_p,ij}^{(n)}$).

4.4.6 Calculation of the α_s Independent Cross-Section Grid

The event weight of equation 4.28 can be rewritten as

$$w^{(evt)} = \sum_{a_p} \sum_n f_{a_p}^{(p)}(x_1, \mu_F^2) \alpha_s^{(n)}(\mu_F^2) w_{a_p}^{(evt),(n)}, \quad (4.37)$$

where

$$w_{a_p}^{(evt),(n)} = \sum_{a_\gamma} f_{a_\gamma}^{(\gamma)}(x_2, \mu_F^2) \hat{\sigma}_{a_p, a_\gamma}^{(n)}(x_1, x_2). \quad (4.38)$$

In section 4.4.4 a prescription was presented for the calculation of the cross-section grid. The challenge facing the programmer in the α_s case is that they must find in the code where the event weight is being multiplied by α_s , as per equation 4.37 and the relevant weights, $w_{a_p}^{(evt),(n)}$, must be stored in a separate array. The following updated prescription can then be used to calculate the cross-section grid

1. Define a 2D grid in $x\text{-}\mu_F^2$ space according to the method outlined in section 4.4.2. Store the knot points along the x and μ_F^2 axis in appropriate arrays.
2. Define a cross-section grid array (W) which is dimensioned as $N_{bins} \times N_{a_p} \times N_x \times N_{\mu_F^2} \times N_n$.

3. Generate an event
4. Apply any kinematic cuts to the event.
5. Find the following
 - Which bin in the $x\text{-}\mu_F^2$ grid, the event falls into.
 - Which bin in the cross-section histogram the event falls into.
6. Loop over all active partons and all orders of the calculation and fill W (at the location specified by step 5) with the deconvoluted $w_{a_p}^{(evt),(n)}$ weights.
7. Repeat steps 3-7 until as many events have been generated as desired.

4.4.7 Cross-Section Grids: Summary

Sections 4.4.1-4.4.6 have highlighted how jet data can be incorporated into the ZEUS QCD fits in a rigorous manner. This final subsection will summarise what has been covered and also discuss a few additional points.

The complete definition of the cross-section grid, W , for a given cross-section histogram is defined by

$$W = \{W_{a_p,ijk}^{(n),proc} \forall i, j, k, a_p, n, proc\}, \quad (4.39)$$

where the symbol $proc$ is yet another label which is introduced to take into account that a separate grid needs to be calculated for direct and resolved γp processes. The symbol k , as before, refers to which bin of the cross-section histogram is being reconstructed (remember a separate grid is required for each bin of the cross-section histogram). The total grid, W , can be calculated using the prescription of section 4.4.6. If the direct process is labelled by $proc = 1$ and the resolved by $proc = 2$ then the k^{th} bin of the cross-section histogram can be reconstructed using any arbitrary proton PDF and any value of $\alpha_s(\mu_F^2)$ with the following:

$$\sigma_k^{(\gamma p)} = \sum_{a_p} \sum_i \sum_j \sum_n c_{a_p,ij}^{(n)} \left[W_{a_p,ijk}^{(n),1} + W_{a_p,ijk}^{(n),2} \right]. \quad (4.40)$$

In practice it is not really very tidy to store so many weights in one file. It is a good idea to break the files up by the process and the order of the calculation i.e. the weights $W_{a_p,ijk}^{(1),1}$ (direct,LO), $W_{a_p,ijk}^{(2),1}$ (direct,NLO), $W_{a_p,ijk}^{(1),2}$ (resolved,LO), $W_{a_p,ijk}^{(2),2}$ (resolved,NLO) are stored in separate files.

Another important point is that for direct processes not all the weights $W_{a_p,ijk}^{(n),1}$ are unique w.r.t the parton flavour a_p . Table 4.2 summarises the numerical values of a_p and their corresponding parton flavours.

Flavour	b	\bar{c}	\bar{s}	d	\bar{u}	g	u	d	s	c	b
a_p	-5	-4	-3	-2	-1	0	1	2	3	4	5

Table 4.2: Parton flavour codes

In fact, for direct processes, we have

$$W_{1,ijk}^{(n),1} = W_{-1,ijk}^{(n),1} = W_{4,ijk}^{(n),1} = W_{-4,ijk}^{(n),1} \text{ and} \quad (4.41)$$

$$W_{2,ijk}^{(n),1} = W_{-2,ijk}^{(n),1} = W_{3,ijk}^{(n),1} = W_{-3,ijk}^{(n),1} = W_{5,ijk}^{(n),1} = W_{-5,ijk}^{(n),1}, \quad (4.42)$$

which comes from the fact that the calculation (in the case of Frixiene and Ridolfi's) is a massless one and the matrix elements for partons with the same charge are equal. There are therefore only 3 unique weights, namely $W_{0,ijk}^{(n),1}$, $W_{1,ijk}^{(n),1}$ and $W_{2,ijk}^{(n),1}$. This fact can save a fair amount of storage space. For the resolved case the symmetry between the partons is broken because of the convolution of the matrix elements with the photon PDF but there is, nevertheless, still symmetry between particle and antiparticle. In the resolved case there are therefore six unique weights, namely $W_{0,ijk}^{(n),2}$, $W_{1,ijk}^{(n),2}$, $W_{2,ijk}^{(n),2}$, $W_{3,ijk}^{(n),2}$, $W_{4,ijk}^{(n),2}$ and $W_{5,ijk}^{(n),2}$.

4.5 Adding γp Dijet Data into the Fit: Part 2

In this section, all the techniques of the previous section are illustrated for the case where the γp dijet data of [51] were added to the ZEUS-Jets and ZEUS-Jets- α_s fit. The $x\text{-}\mu_F^2$ grid parameters for the grids that were used to reconstruct these cross-sections are shown in table 4.3

A crucial check which has to be made is that the grid method of reconstructing the cross-sections agrees with the cross-section predictions of an independent and untouched version of the original code.

Figures 4.2 and 4.3 show the comparison between the grid reconstructed cross-sections and those of the original code. Figure 4.2 illustrates the case where α_s has not been deconvoluted (ZEUS-Jets fit) whereas figure 4.3 illustrates the case where α_s has been deconvoluted (ZEUS-Jets- α_s). Figures 4.4 and 4.5 show the corresponding ratios. For the case where α_s is not deconvoluted (figure 4.4) 24%

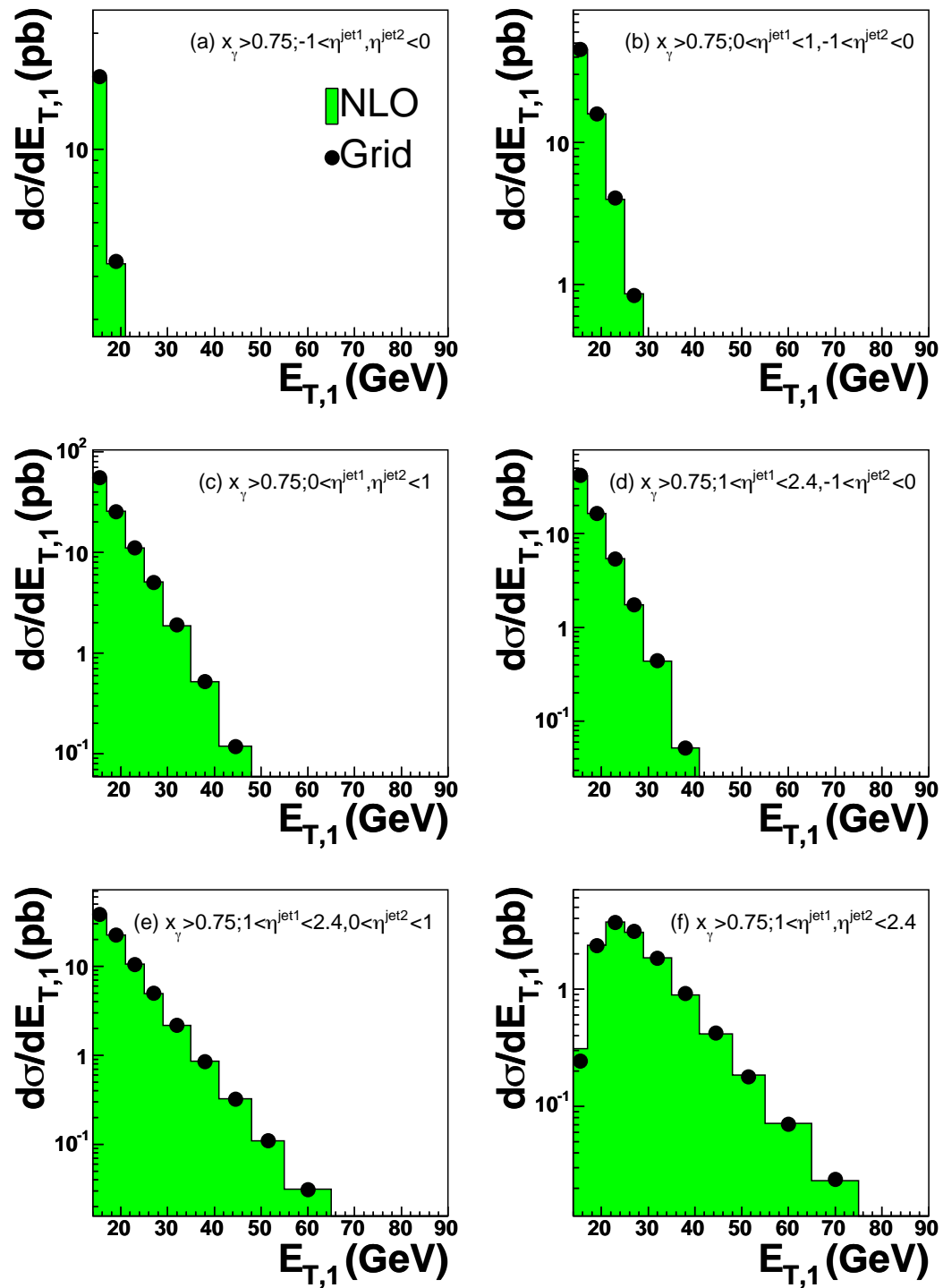


Figure 4.2: A comparison between the grid reconstructed cross-sections and the cross-section predictions of an independent version of the NLO γp jet production code of Frixione and Ridolfi [19]. A comparison has been made for each of the 6 high- x_γ^{obs} differential cross-sections w.r.t $E_{T,1}$ that were included in the ZEUS-Jets fit (α_s convoluted)

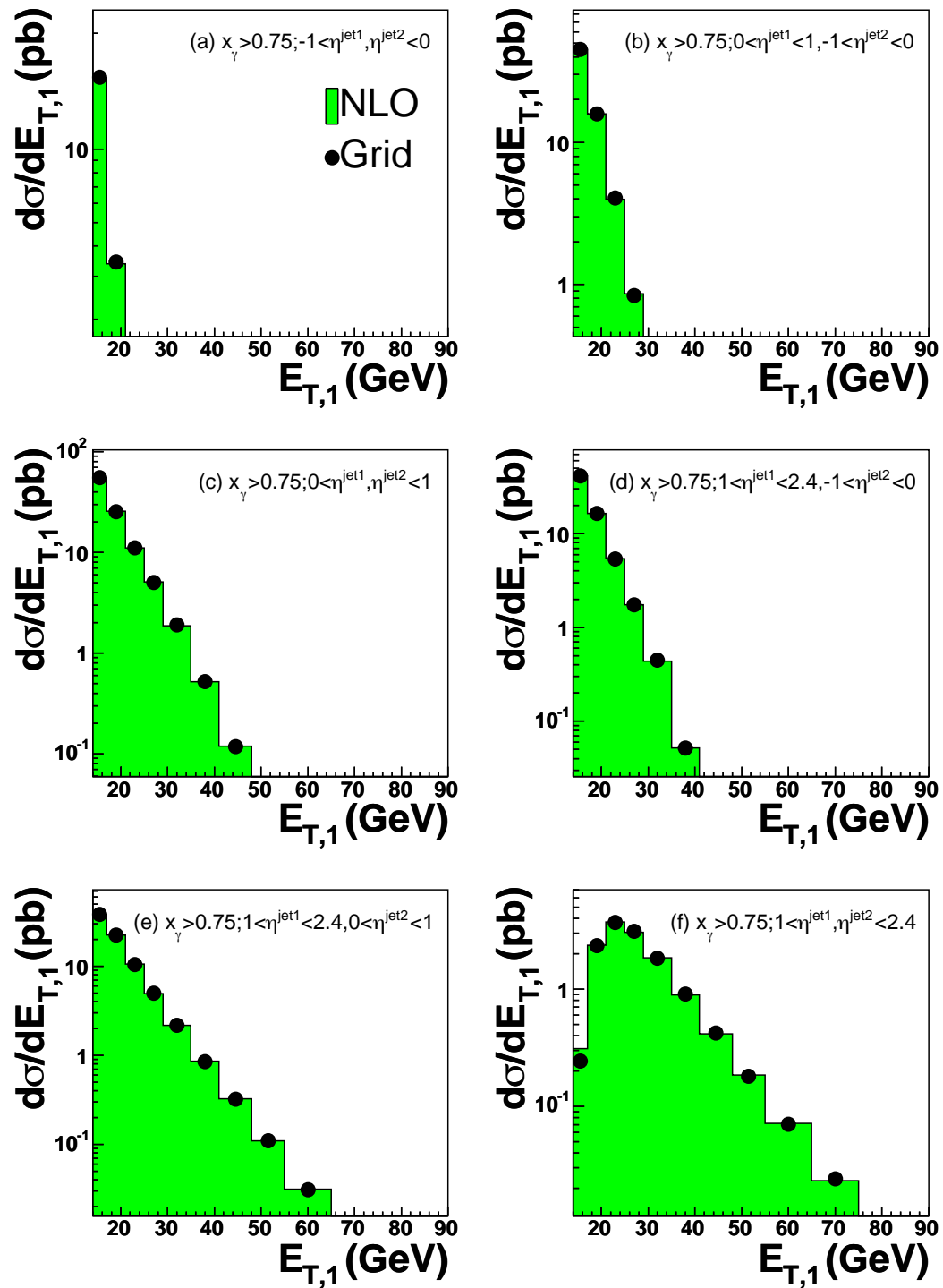


Figure 4.3: A comparison between the grid reconstructed cross-sections and the cross-section predictions of an independent version of the NLO γp jet production code of Frixione and Ridolfi [19]. A comparison has been made for each of the 6 high- x_γ^{obs} differential cross-sections w.r.t $E_{T,1}$ that were included in the ZEUS-Jets- α_s fit (α_s deconvoluted)

Parameter	Value
x_{min}	0.0001
x_{max}	1.0
N_x	150
$\mu_{F,min}^2$	1.0
$\mu_{F,max}^2$	19000.0
$N_{\mu_F^2}$	150

Table 4.3: Table showing the grid parameters used for the incorporation of the ZEUS 96-97 γp dijet data into the ZEUS-Jets and ZEUS-Jets- α_s fitted data sets

of the reconstructed points lie within 0.5% of the nominal theoretical points, 55% lie within 1.0% and 79% lie within 2%. For the α_s deconvoluted case (figure 4.5) 29% of the reconstructed points lie within 0.5% of the nominal theoretical points, 50% lie within 1.0% and 79% lie within 2%. So we see that in both cases the grid method does a reasonable job of reconstructing the cross-section, considering the approximations of the method. From figures 4.4 and 4.5 it can be seen that the far forward cross-section ($1 < \eta^{jet1}, \eta^{jet2} < 2.4$) is poorly reconstructed in the lowest $E_{T,1}$ bin. This is taken in to account in the ZEUS-Jets fit by performing a fit with the lowest $E_{T,1}$ bin excluded. This is then included as a source of model uncertainty which was included in the PDF uncertainty bands.

4.6 Results of Adding Jet Data into the Fit

In this section we briefly review the most relevant (as far as the present analysis is concerned) results of adding ZEUS jet data into the fitted data set of the QCD fits. In the preceding sections, the method of including jet data into the fitted data set was highlighted for the photoproduction case. The method used for the inclusion of the DIS jet data is the same.

The effect, on the precision of the extracted gluon PDF, of including jet data in the fitted data set can be seen from figure 4.6. The total uncertainty on the gluon PDF is reduced in comparison to the older fits. It should be noted that the bulk of this improvement is in the mid to high- x gluon (0.01-0.4). In the ZEUS-Jets- α_s fit, the additional constraint of the jet data on the gluon PDF allowed an accurate extraction of $\alpha_s(M_z)$ in NLO QCD,

$$\alpha_s(M_z) = 0.1183 \pm 0.0028(exp) \pm 0.0008(model) , \quad (4.43)$$

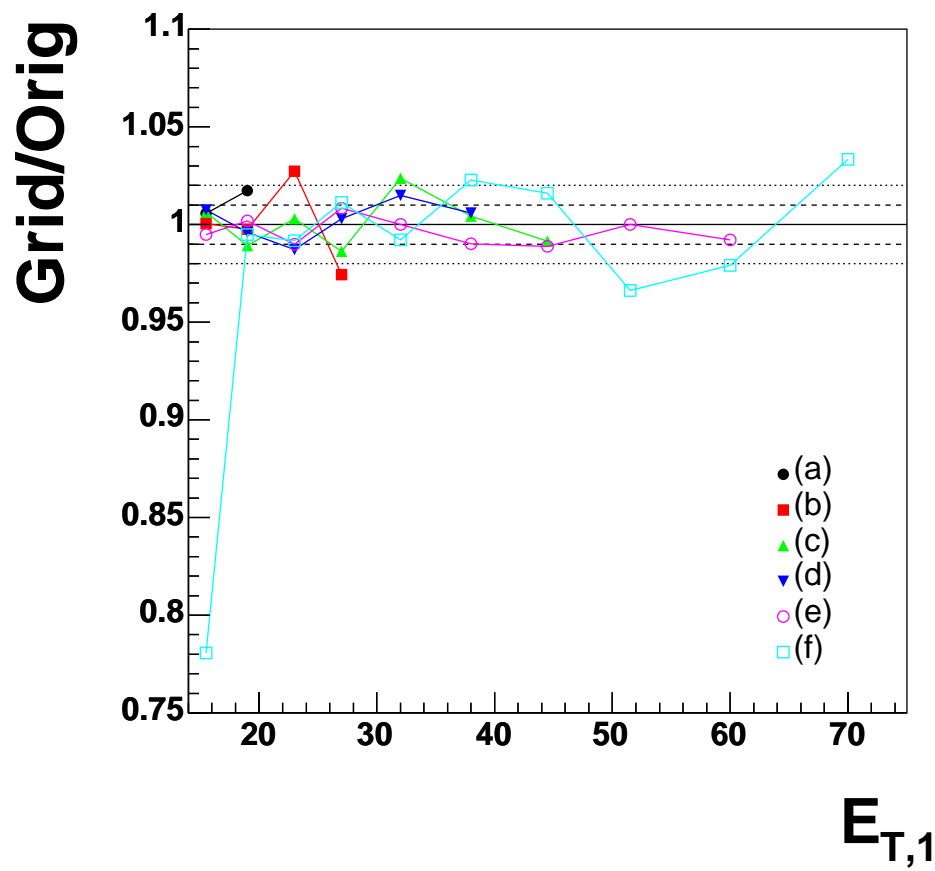


Figure 4.4: The ratio between the grid reconstructed cross-sections and the cross-section predictions of an independent version of the NLO γp jet production code of Frixione and Ridolfi [19] for the cross-sections of figure 4.2 (see this figure for an explanation of the labels (a)-(f)).

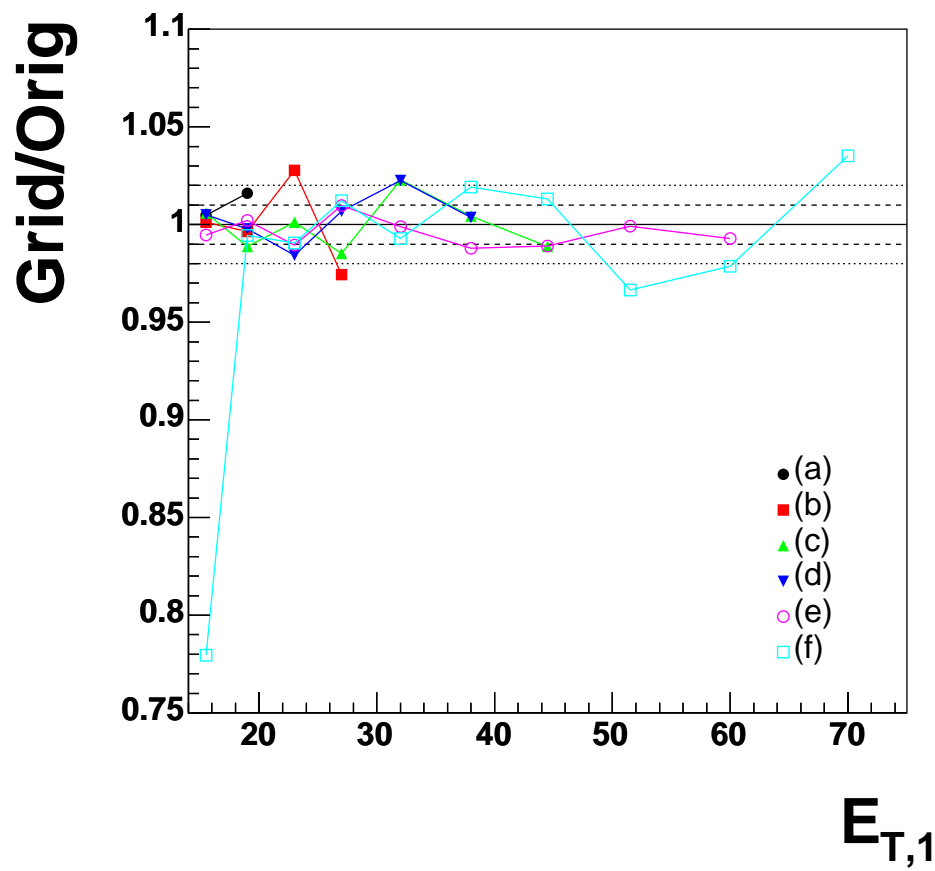


Figure 4.5: (i) The ratio between the grid reconstructed cross-sections and the cross-section predictions of an independent version of the NLO $\gamma\gamma$ jet production code of Frixione and Ridolfi [19] for the cross-sections of figure 4.3 (see this figure for an explanation of the labels (a)-(f)).

with an additional uncertainty of ± 0.005 coming from the choice of scale [42]. The effect that the jet data has in constraining $\alpha_s(M_z)$ can be clearly seen from figure 4.7. From this figure it can be seen that a much tighter χ^2 (see section 4.3) profile is obtained when jet data is included in the fitted data set compared with the older fits.

4.6.1 The Fitting of Resolved Cross-Sections

The ZEUS 1996-97 γp dijet data [51] included 6 low- x_γ^{obs} (resolved enriched) cross-sections in addition to the high- x_γ^{obs} cross-sections already discussed. The cross-section predictions for photoproduced dijets are sensitive to the choice of input photon PDF with the low- x_γ^{obs} cross sections showing particular sensitivity (see [51]). In the ZEUS-Jets fits only the direct enriched cross-sections were included in the fitted data set in order to minimise the sensitivity to this choice. Including the resolved enriched cross-sections in the fit leads to a sizable model uncertainty on the extracted PDFs. This uncertainty comes from the large uncertainty on the resolved enriched cross-sections due to the choice of photon PDF. This issue has been mentioned here because it has relevance to topics which will be discussed in later chapters. It is also worth discussing the uncertainty on the extracted parton densities in slightly more detail. The uncertainty on the parton densities is formed from two principal components. The first of these are the statistical, uncorrelated and correlated systematic uncertainties which are derived from the corresponding uncertainties on the extracted fit parameters. These uncertainties were discussed in section 4.3.2 and are determined from equation 4.10. This component of the total uncertainty is termed the experimental uncertainty. The second component is formed from variations of certain model parameters. The central values of the fit parameters are used to determine the central values of the extracted densities. Separate fits are then performed, making certain changes to model parameters. These may include changing the input photon PDF for example, or the input scale that the parton densities are parameterised at (see section 4.3.1). A full list of the various model uncertainties considered can be found in [42]. These model uncertainties are then added in quadrature with the experimental uncertainties to give the total experimental uncertainty (which correspond to the shaded bands in figure 4.6).

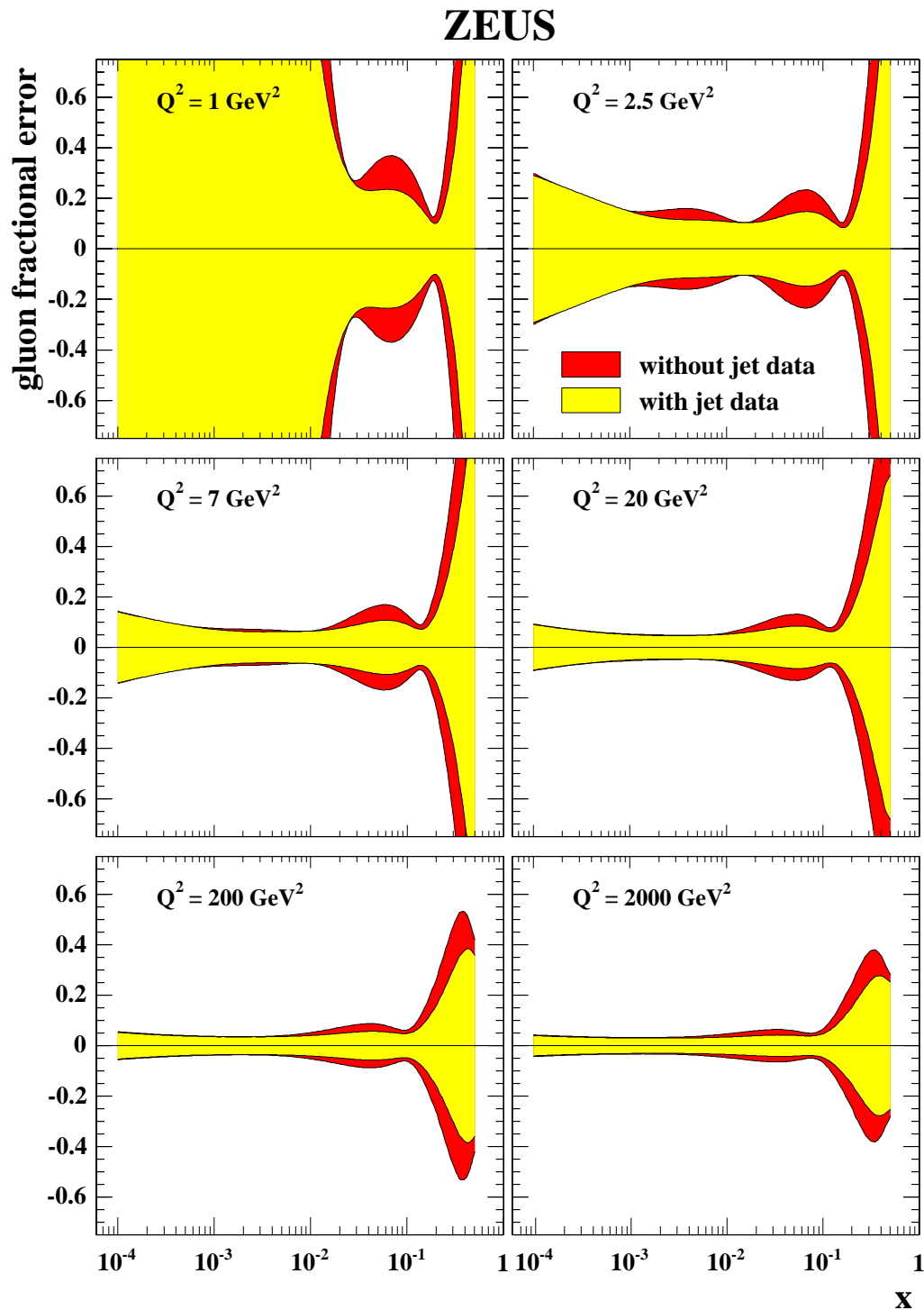


Figure 4.6: The total experimental uncertainty on the gluon PDF for the ZEUS-Jets fit (central error bands) compared to the total experimental uncertainty on the gluon PDF for a fit not including the jet data (outer error bands). The uncertainties are shown as fractional differences from the central values of the fits, for various values of Q^2 . The total experimental uncertainty includes the statistical, uncorrelated and correlated systematic uncertainties, for both fits. Figure taken from [42]

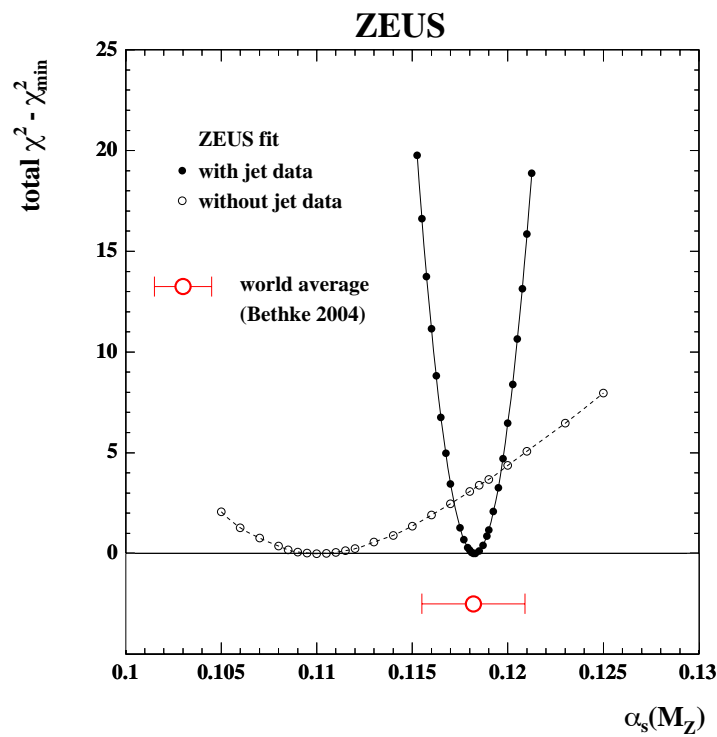


Figure 4.7: The χ^2 profile as a function of $\alpha_s(M_Z)$ for the ZEUS-Jets- α_s fit (black dots) and for a similar fit not including the jet data (clear dots). The ordinate is given in terms of the difference between the total χ^2 and the minimum χ^2 , for each fit. Figure taken from [42]

Chapter 5

Optimisation of γp Dijet Cross-Sections

In the last chapter we saw that the inclusion of jet data in the fitted data set of the ZEUS QCD fits leads to a considerable improvement in the precision of the extracted gluon PDF. In this chapter we will discuss the possibility of measuring γp dijet cross-sections which optimise this enhancement. The chapter will begin by discussing the reasons for measuring the gluon PDF to high precision, before discussing a method for optimising γp dijet cross-sections to the uncertainties of the underlying gluon PDF. The chapter culminates in the presentation of the γp dijet cross-sections which will be measured in this analysis.

5.1 Making Precise Measurements of the Gluon PDF

The ZEUS QCD fits [40–42], along with the fits of other groups such as CTEQ [59] and MRST [60] exhibit the common feature that the uncertainty on the extracted gluon PDF for high- x ($\gtrsim 0.1$) is large. For the case of the ZEUS QCD fits, this can be seen from figure 4.6. Appendix C shows some similar figures for the case of CTEQ and MRST. This uncertainty arises from the lack of high- x gluon data in the fitted data sets. Parton distribution functions play a central role in particle physics experiments, particularly at hadron colliders such as the Tevatron [66] and the LHC [67]. A precise knowledge of the PDFs of the proton over the entire range of x - Q^2 space is important in order for accurate theoretical predictions to be made for the various signal and background processes that take place at these experiments.

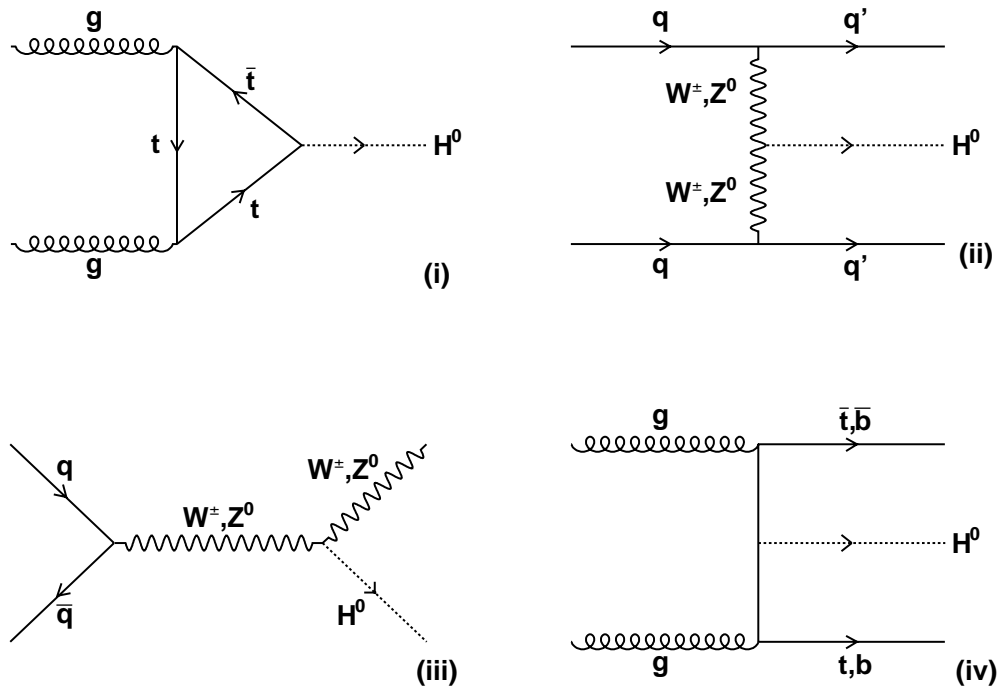


Figure 5.1: The most important processes for Higgs production at hadron colliders: (i) Gluon fusion (ii) vector boson fusion (iii) associated production with weak bosons and (iv) associated production with a t or b pair

The discovery of the Higgs boson is an important test of the standard model and attempts to measure it will be amongst the highest-priority issues at the LHC and Tevatron for many years to come. If the Higgs boson has a relatively low mass ($M_H \lesssim 200 \text{ GeV}$), as is suggested by precision electroweak measurements [68], then it could be discovered at the Tevatron Run II, provided sufficient luminosity is collected. At the LHC, the Higgs can be produced across its entire mass range, $M_H \lesssim \mathcal{O}(1\text{TeV})$. If the Higgs boson is found then the next step would be to explore all of its fundamental properties. This, in turn, would require the accurate measurement of all possible Higgs cross-sections, for different production processes, and also all branching ratios, for the various decay modes. At the same time, precise cross-section and branching ratio predictions are needed in addition to a good estimate of the theoretical uncertainties on these predictions.

The most important production processes for Higgs production at the LHC and Tevatron are shown in figure 5.1. The cross-sections for these various processes are shown in figure 5.2. The dominant Higgs production mechanism at the Tevatron

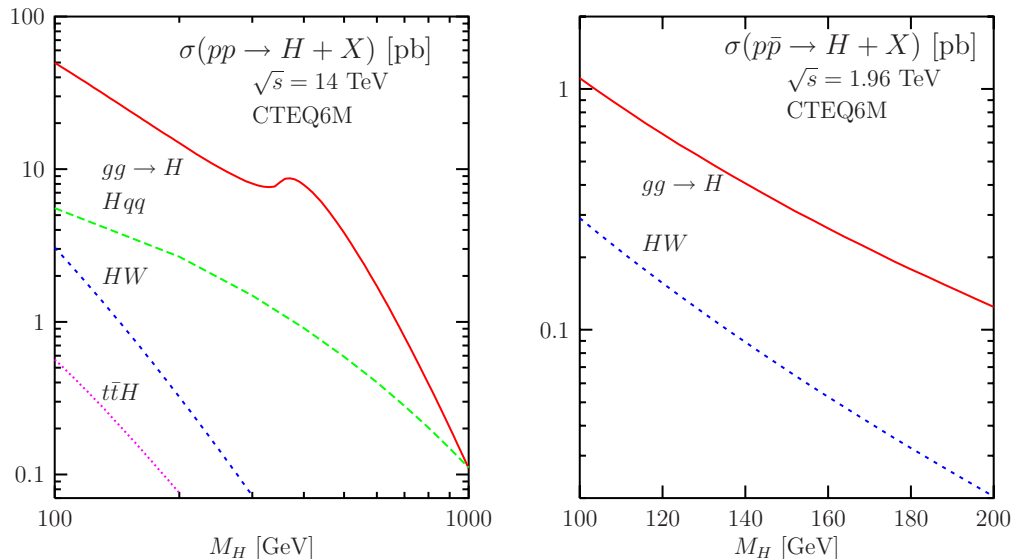


Figure 5.2: The NLO cross-section predictions for Higgs production at the LHC (left) and the Tevatron (right) as a function of the Higgs mass. The proton PDF used in this case has been CTEQ6M. Figure taken from [69].

and the LHC is the gluon fusion process. A pertinent question is how the gluon PDF uncertainties affect the cross-section predictions for the dominant gluon fusion process. Such a study was performed by Djouadi and Ferrag [69]. Figure 5.3 shows the uncertainties on the NLO cross-section predictions for the gluon fusion process which arise from the uncertainties on the underlying gluon PDF. At the LHC, for relatively low Higgs masses ($M_H \lesssim 300$ GeV) the predictions for the $gg \rightarrow H$ production cross-section is constrained at the 3-5% level. At higher masses ($M_H \gtrsim 300$ GeV) the uncertainty on the cross-section begins to increase, reaching the 10% level at a mass of about $1TeV$. This increase is attributed to the increasing participation of high- x gluons in the gluon fusion process. At the Tevatron, because of the smaller centre-of-mass energy, the high- x gluon regime is already reached for low Higgs masses ($M_H \lesssim 300$ GeV) and the uncertainties increase from $\sim 5\%$ to $\sim 15\%$.

It is seen, therefore, that a precise knowledge of the gluon PDF (particularly at high- x) is required for the accurate cross-section prediction of Higgs production at the LHC and Tevatron. Although a theoretical error (in the LHC case) of 5-10% (assuming a heavy Higgs) is not startling; it is, nevertheless, one of the most significant sources of theoretical uncertainty and is a serious hindrance on the ability to make precision Higgs cross-section predictions.

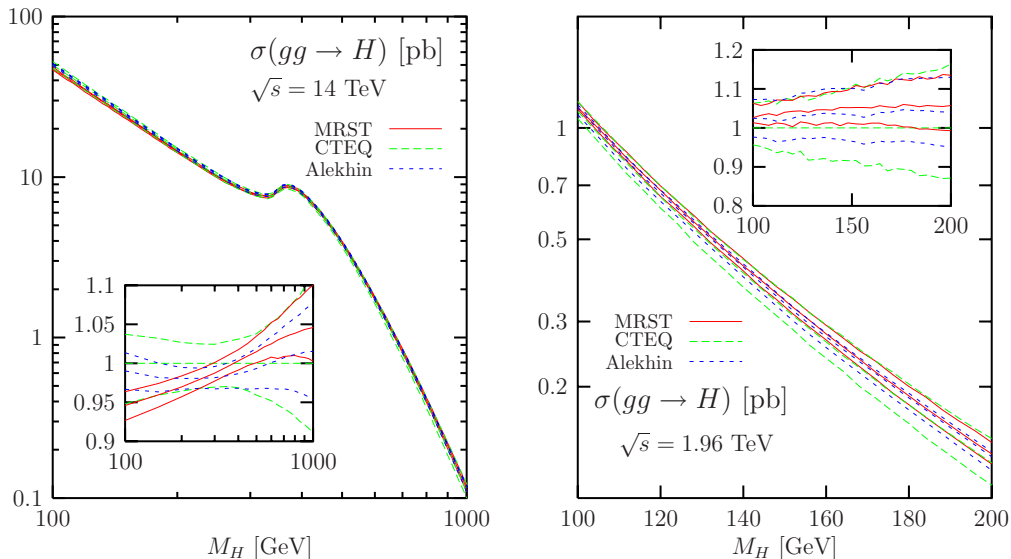


Figure 5.3: The CTEQ, MRST and Alekhin [70] PDF uncertainty bands for the NLO cross-section predictions for the production of the Higgs boson at the LHC (left) and at the Tevatron (right) in the $gg \rightarrow H$ channel. Figure taken from [69]

In this section we have used Higgs production as an illustrative example of the importance of having a precise knowledge of the gluon PDF. More generally, what is of great importance is that colliders such as the LHC, with their immense operating luminosities, will open up the way to performing statistically rich studies of high- x gluon physics processes. Without a precise knowledge of the gluon PDF at high- x the additional power of increased statistics will be impaired by large theoretical uncertainties on the theoretical predictions of such processes. Finally, it is necessary to introduce the very question that the analysis presented in this thesis has been designed to address. We saw in the previous chapter that the inclusion of jet data in the fitted data set of the ZEUS QCD fits significantly improved the precision of the extracted gluon PDF. Therefore,

- Is it possible to use ZEUS jet data to optimise this improvement in precision, especially at high- x ?

In other words, by somehow tuning the measurements to be sensitive to the high- x gluon and using more data (the data included in the ZEUS QCD fits was only the 96-97 subset of the ZEUS data set), is it possible to further constrain the (high- x) gluon PDF obtained from the ZEUS QCD fits. The rest of this chapter will discuss how this could be achieved.

5.2 Why γp Dijets?

Throughout this thesis, emphasis has been placed on the γp component of $e^\pm p$ interactions rather than DIS. Both types of process have their merits. In the analysis presented in this thesis γp was chosen for two main reasons. Firstly, the statistical abundance of the γp data set relative to DIS allows for more accurate (statistically speaking) measurements to be made in tighter pockets of phase space (pockets which may show enhanced sensitivity to the gluon). Secondly, in γp , the x_γ^{obs} observable (see section 2.6) may be used to discriminate between direct and resolved processes which may be important in isolating the physics processes which show enhanced sensitivity to the gluon. It is also necessary to justify the choice as to why γp dijet processes have been studied instead of, for example, inclusive γp jet processes. In the dijet case there is a wealth of additional variables which can be measured (x_γ^{obs} , x_p^{obs} etc) compared with the inclusive case. Certain variables may or may not show more sensitivity to the gluon. In summary, γp dijet provides a very rich and statistically abundant area of study, and it is for these reasons that it has been chosen for study in the present analysis.

5.3 Optimisation Study

The optimisation study conducted as part of the present analysis was designed to determine regions of phase space, in which cross-sections could be measured, which show particular sensitivity to the uncertainties on the underlying gluon PDF. If such cross-sections could then be measured to a sufficient accuracy then their inclusion in the fitted data set of the ZEUS QCD fit could lead to a more precise gluon PDF. The rest of this chapter will focus on the question of how to find regions of phase space, in which to make cross-section measurements, that show optimum (maximum) sensitivity to the uncertainties on the underlying gluon PDF. These cross-sections will be termed the optimised cross-sections.

5.3.1 Method of Optimisation

The general method of optimisation is quite simple and can be summarised as follows. A total of 9000 different cross-sections were chosen, each being defined by a unique set of cuts on the kinematic variables $E_{T,1}$, $E_{T,2}$, η_1 , η_2 , x_γ^{obs} and y (see chapter 2). In each of the 9000 regions defined, a differential cross-section

with respect to x_p^{obs} is measured as a function of x_p^{obs} . The variable x_p^{obs} was chosen as this is an estimator for the momentum fraction x_p . As the gluon PDF error increases sharply with increasing x_p then it is expected that this would be manifested most evidently in a cross-section as a function of $x_p \sim x_p^{obs}$. Each cross-section is calculated using the NLO γp jet production code of Frixione and Ridolfi [19]. Next, the uncertainty on the central prediction which arises from the uncertainty on the underlying PDFs is calculated. This is done in two ways

- Firstly, the uncertainty on the cross-section which arises collectively from the uncertainties on all the underlying PDFs is calculated (taking into account all correlations between the PDFs). These uncertainties are termed the total PDF errors.
- Secondly, the sea and valence PDFs are fixed at their central values and the uncertainty on the cross-section which arises purely from the uncertainty on the underlying gluon PDF is calculated. These uncertainties are termed the gluon PDF errors.

The optimised cross-sections are defined to be the cross-sections which are endowed with the largest gluon PDF errors. Appendix D details exactly how the PDF uncertainties on a particular cross-section are calculated.

5.3.2 Phase Space Regions Considered

The phase space regions which were considered in the optimisation study are shown in tables 5.1-5.4. By taking permutations of the different cuts, shown in the tables, one can determine all (9000) of the phase space regions considered in the optimisation study. An additional 36 cross-sections, defined using the cuts of [51], were also included in the study. This was done in order to determine exactly how sensitive the 96-97 γp dijet cross-sections were compared with the other cross-sections been considered in the study.

5.3.3 Considerations of the Study

Before continuing, a couple of important points about the study must be mentioned:

	$E_{T,1}$ cut (GeV)	$E_{T,2}$ cut (GeV)
1	$E_{T,1} > 15$	$E_{T,2} > 10$
2	$E_{T,1} > 20$	$E_{T,2} > 10$
3	$E_{T,1} > 25$	$E_{T,2} > 10$
4	$E_{T,1} > 30$	$E_{T,2} > 10$
5	$E_{T,1} > 35$	$E_{T,2} > 10$
6	$E_{T,1} > 20$	$E_{T,2} > 15$
7	$E_{T,1} > 25$	$E_{T,2} > 15$
8	$E_{T,1} > 30$	$E_{T,2} > 15$
9	$E_{T,1} > 35$	$E_{T,2} > 15$
10	$E_{T,1} > 25$	$E_{T,2} > 20$
11	$E_{T,1} > 30$	$E_{T,2} > 20$
12	$E_{T,1} > 35$	$E_{T,2} > 20$
13	$E_{T,1} > 30$	$E_{T,2} > 25$
14	$E_{T,1} > 35$	$E_{T,2} > 25$
15	$E_{T,1} > 35$	$E_{T,2} > 30$

Table 5.1: Classification of the $E_{T,1}$ and $E_{T,2}$ cuts

	η_1 cut	η_2 cut
1	$-1 < \eta_1 < 0$	$-1 < \eta_2 < 0$
2	$-1 < \eta_1 < 0$	$0 < \eta_2 < 1$
3	$-1 < \eta_1 < 0$	$1 < \eta_2 < 2$
4	$-1 < \eta_1 < 0$	$2 < \eta_2 < 3$
5	$0 < \eta_1 < 1$	$0 < \eta_2 < 1$
6	$0 < \eta_1 < 1$	$1 < \eta_2 < 2$
7	$0 < \eta_1 < 1$	$2 < \eta_2 < 3$
8	$1 < \eta_1 < 2$	$1 < \eta_2 < 2$
9	$1 < \eta_1 < 2$	$2 < \eta_2 < 3$
10	$2 < \eta_1 < 3$	$2 < \eta_2 < 3$

Table 5.2: Classification of the η_1 and η_2 cuts

	x_γ^{obs} cut
1	0.90
2	0.85
3	0.80
4	0.75
5	0.70
6	0.65
7	0.60
8	0.55
9	0.50
10	0.45

Table 5.3: Classification of the x_γ^{obs} cuts. The actual cuts considered are those which lie above and below the values shown in the table

	y cut
a	$0.20 < y < 0.40$
b	$0.40 < y < 0.60$
c	$0.60 < y < 0.80$

Table 5.4: Classification of the y cuts

- The study was completed using the ZEUS-Type5 PDFs. These are not the most recent fits but they were at the time the study was conducted.
- All calculations were performed using 820 GeV protons (only relevant to the 96-97 ZEUS data). However, a check was made using 920 GeV protons and the results of the optimisation study essentially remained the same.

5.3.4 Optimisation

Once the various cross-sections and their associated PDF errors have been calculated in each kinematic region, various quantities of interest can be found (see table 5.5) and interesting kinematic regions can be selected for further study. The CTEQ5M PDF set is used as a set of reference proton PDFs to compare the ZEUS-Type5 PDF set predictions against. The average gluon error, $\delta\sigma_{gluon}$, is the average value of the gluon PDF error taken over all bins of the cross-section. Likewise for the average total error, $\delta\sigma_{total}$. Optimisation with respect to the (average) gluon error and (average) total error are done separately. The ratio between the ZEUS-Type5 and CTEQ5M predictions was also considered to identify phase space regions where the two may disagree strongly (these regions

	Symbol	Quantity
1	$\delta\sigma_{gluon}$	Average gluon error
2	$\delta\sigma_{total}$	Average total error
3	$\sigma_{cteq}/\sigma_{zeus}$	Difference between ZEUS-O and CTEQ5M central values
4	ξ^{dir}	Fraction of direct events
5	ξ^{res}	Fraction of resolved events
6	σ_{cteq}	Total cross section (CTEQ5M)

Table 5.5: Main quantities of interest in the optimisation study

may or may not correspond to regions where the PDF errors themselves are large). The fraction, ξ^{dir} , represents the proportion of the cross-section attributable to direct events. Care has to be taken using such a definition because the notion of distinguishable direct and resolved processes is only valid at LO. The quantity, ξ^{dir} , is calculated by finding the proportion of the total theoretical prediction that is obtained by treating the photon as a point-like object and can be thought of as the component of the cross-section which is not dependent on the photon PDF parameterisation. Likewise, ξ^{res} , is calculated by finding the proportion of the total theoretical prediction that is obtained by treating the photon as a composite object and represents the component of the cross-section which is dependent on the choice of photon PDF. It is desirable (see section 4.6.1) to consider regions of phase space which show minimal sensitivity to the choice of photon PDF. The total cross-section, σ_{cteq} (as calculated using the CTEQ proton PDFs), is also considered in order to select regions of phase space which are statistically rich. The next stage of the optimisation study is to select a *ranking* quantity (either of quantities 1,2 or 3 in table 5.5) to rank each cross-section with. This ranking is done in parallel with the application of a set of selection criteria. This selection criteria can be used to rank interesting subsets of the 9036 principal kinematic regions. An example set of selection criteria is shown in table 5.6

Quantity	Selection cuts
ξ^{dir}	≥ 0.7
σ_{cteq}	$\geq 15 \text{ pb}$

Table 5.6: Example selection criteria

5.3.5 Optimisation Study Results

Table 5.7 shows the results of the optimisation when the ranking quantity is set to $\delta\sigma_{gluon}$ and the selection criteria is set to $\sigma_{cteq} \geq 1 \text{ pb}$. All cross-section

Rank	E_T cuts (GeV)	η^{jet} cuts	x_γ^{obs} cut	y cut	$\delta\sigma_{gluon}$	ξ_{direct}	σ_{cteq}
1	$E_{T,1} > 20, E_{T,2} > 15$	$2 < \eta_1 < 3, 2 < \eta_2 < 3$	$x_\gamma^{obs} < 0.45$	$0.4 < y < 0.6$	0.31	0.02	5.83
2	$E_{T,1} > 20, E_{T,2} > 15$	$2 < \eta_1 < 3, 2 < \eta_2 < 3$	$x_\gamma^{obs} < 0.5$	$0.4 < y < 0.6$	0.31	0.02	5.83
3	$E_{T,1} > 20, E_{T,2} > 15$	$2 < \eta_1 < 3, 2 < \eta_2 < 3$	$x_\gamma^{obs} < 0.55$	$0.4 < y < 0.6$	0.31	0.02	5.83
4	$E_{T,1} > 20, E_{T,2} > 15$	$2 < \eta_1 < 3, 2 < \eta_2 < 3$	$x_\gamma^{obs} < 0.6$	$0.4 < y < 0.6$	0.31	0.02	5.84
5	$E_{T,1} > 20, E_{T,2} > 15$	$2 < \eta_1 < 3, 2 < \eta_2 < 3$	$x_\gamma^{obs} < 0.65$	$0.4 < y < 0.6$	0.31	0.02	5.84
6	$E_{T,1} > 20, E_{T,2} > 15$	$2 < \eta_1 < 3, 2 < \eta_2 < 3$	$x_\gamma^{obs} < 0.7$	$0.4 < y < 0.6$	0.31	0.02	5.84
7	$E_{T,1} > 20, E_{T,2} > 15$	$2 < \eta_1 < 3, 2 < \eta_2 < 3$	$x_\gamma^{obs} < 0.75$	$0.4 < y < 0.6$	0.31	0.02	5.84
8	$E_{T,1} > 20, E_{T,2} > 15$	$2 < \eta_1 < 3, 2 < \eta_2 < 3$	$x_\gamma^{obs} < 0.9$	$0.4 < y < 0.6$	0.31	0.02	5.84
9	$E_{T,1} > 20, E_{T,2} > 15$	$2 < \eta_1 < 3, 2 < \eta_2 < 3$	$x_\gamma^{obs} < 0.85$	$0.4 < y < 0.6$	0.31	0.02	5.84
10	$E_{T,1} > 20, E_{T,2} > 15$	$2 < \eta_1 < 3, 2 < \eta_2 < 3$	$x_\gamma^{obs} < 0.8$	$0.4 < y < 0.6$	0.31	0.02	5.84
11	$E_{T,1} > 20, E_{T,2} > 15$	$2 < \eta_1 < 3, 2 < \eta_2 < 3$	$x_\gamma^{obs} < 0.45$	$0.2 < y < 0.4$	0.31	0.04	9.34
12	$E_{T,1} > 20, E_{T,2} > 15$	$2 < \eta_1 < 3, 2 < \eta_2 < 3$	$x_\gamma^{obs} < 0.5$	$0.2 < y < 0.4$	0.31	0.04	9.56
13	$E_{T,1} > 20, E_{T,2} > 15$	$2 < \eta_1 < 3, 2 < \eta_2 < 3$	$x_\gamma^{obs} < 0.55$	$0.2 < y < 0.4$	0.31	0.04	9.67
14	$E_{T,1} > 20, E_{T,2} > 15$	$2 < \eta_1 < 3, 2 < \eta_2 < 3$	$x_\gamma^{obs} < 0.6$	$0.2 < y < 0.4$	0.31	0.04	9.74
15	$E_{T,1} > 20, E_{T,2} > 15$	$2 < \eta_1 < 3, 2 < \eta_2 < 3$	$x_\gamma^{obs} < 0.65$	$0.2 < y < 0.4$	0.31	0.04	9.77
16	$E_{T,1} > 20, E_{T,2} > 15$	$2 < \eta_1 < 3, 2 < \eta_2 < 3$	$x_\gamma^{obs} < 0.7$	$0.2 < y < 0.4$	0.31	0.04	9.80
17	$E_{T,1} > 20, E_{T,2} > 15$	$2 < \eta_1 < 3, 2 < \eta_2 < 3$	$x_\gamma^{obs} < 0.75$	$0.2 < y < 0.4$	0.31	0.04	9.81
18	$E_{T,1} > 20, E_{T,2} > 15$	$2 < \eta_1 < 3, 2 < \eta_2 < 3$	$x_\gamma^{obs} < 0.8$	$0.2 < y < 0.4$	0.31	0.04	9.82
19	$E_{T,1} > 20, E_{T,2} > 15$	$2 < \eta_1 < 3, 2 < \eta_2 < 3$	$x_\gamma^{obs} < 0.85$	$0.2 < y < 0.4$	0.31	0.04	9.83
20	$E_{T,1} > 20, E_{T,2} > 15$	$2 < \eta_1 < 3, 2 < \eta_2 < 3$	$x_\gamma^{obs} < 0.9$	$0.2 < y < 0.4$	0.31	0.04	9.84
21	$E_{T,1} > 20, E_{T,2} > 10$	$2 < \eta_1 < 3, 2 < \eta_2 < 3$	$x_\gamma^{obs} < 0.75$	$0.2 < y < 0.4$	0.30	0.07	10.93
22	$E_{T,1} > 20, E_{T,2} > 10$	$2 < \eta_1 < 3, 2 < \eta_2 < 3$	$x_\gamma^{obs} < 0.8$	$0.2 < y < 0.4$	0.30	0.07	10.94
23	$E_{T,1} > 20, E_{T,2} > 10$	$2 < \eta_1 < 3, 2 < \eta_2 < 3$	$x_\gamma^{obs} < 0.85$	$0.2 < y < 0.4$	0.30	0.07	10.95
24	$E_{T,1} > 20, E_{T,2} > 10$	$2 < \eta_1 < 3, 2 < \eta_2 < 3$	$x_\gamma^{obs} < 0.9$	$0.2 < y < 0.4$	0.30	0.07	10.96
25	$E_{T,1} > 20, E_{T,2} > 15$	$2 < \eta_1 < 3, 2 < \eta_2 < 3$	$x_\gamma^{obs} < 0.45$	$0.6 < y < 0.8$	0.30	0.01	4.16

Table 5.7: Top 25 cross-sections with the ranking quantity set to $\delta\sigma_{gluon}$ and the selection criteria set to $\sigma_{cteq} \geq 1 pb$

Rank	E_T cuts (GeV)	η^{jet} cuts	x_γ^{obs} cut	y cut	$\delta\sigma_{gluon}$	ξ_{direct}	σ_{cteq}
1	$E_{T,1} > 20, E_{T,2} > 10$	$2 < \eta_1 < 3, 2 < \eta_2 < 3$	$x_\gamma^{obs} < 0.75$	$0.2 < y < 0.8$	0.31	0.04	22.26
2	$E_{T,1} > 20, E_{T,2} > 15$	$2 < \eta_1 < 3, 2 < \eta_2 < 3$	$x_\gamma^{obs} < 0.75$	$0.2 < y < 0.8$	0.31	0.02	19.81
3	$E_{T,1} > 15, E_{T,2} > 10$	$2 < \eta_1 < 3, 2 < \eta_2 < 3$	$x_\gamma^{obs} < 0.75$	$0.2 < y < 0.8$	0.29	0.02	90.02
4	$E_{T,1} > 25, E_{T,2} > 15$	$1 < \eta_1 < 2, 2 < \eta_2 < 3$	$x_\gamma^{obs} < 0.75$	$0.2 < y < 0.8$	0.28	0.10	14.23
5	$E_{T,1} > 25, E_{T,2} > 20$	$1 < \eta_1 < 2, 2 < \eta_2 < 3$	$x_\gamma^{obs} < 0.75$	$0.2 < y < 0.8$	0.27	0.06	12.09
6	$E_{T,1} > 25, E_{T,2} > 10$	$1 < \eta_1 < 2, 2 < \eta_2 < 3$	$x_\gamma^{obs} < 0.75$	$0.2 < y < 0.8$	0.27	0.10	14.59
7	$E_{T,1} > 20, E_{T,2} > 10$	$1 < \eta_1 < 2, 2 < \eta_2 < 3$	$x_\gamma^{obs} < 0.75$	$0.2 < y < 0.8$	0.25	0.08	43.46
8	$E_{T,1} > 20, E_{T,2} > 15$	$1 < \eta_1 < 2, 2 < \eta_2 < 3$	$x_\gamma^{obs} < 0.75$	$0.2 < y < 0.8$	0.25	0.05	38.63
9	$E_{T,1} > 25, E_{T,2} > 10$	$0 < \eta_1 < 1, 2 < \eta_2 < 3$	$x_\gamma^{obs} > 0.75$	$0.2 < y < 0.8$	0.25	0.46	12.70
10	$E_{T,1} > 25, E_{T,2} > 15$	$0 < \eta_1 < 1, 2 < \eta_2 < 3$	$x_\gamma^{obs} > 0.75$	$0.2 < y < 0.8$	0.24	0.45	12.86
11	$E_{T,1} > 25, E_{T,2} > 20$	$0 < \eta_1 < 1, 2 < \eta_2 < 3$	$x_\gamma^{obs} > 0.75$	$0.2 < y < 0.8$	0.24	0.43	12.05
12	$E_{T,1} > 20, E_{T,2} > 10$	$0 < \eta_1 < 1, 2 < \eta_2 < 3$	$x_\gamma^{obs} > 0.75$	$0.2 < y < 0.8$	0.19	0.42	31.90
13	$E_{T,1} > 20, E_{T,2} > 15$	$0 < \eta_1 < 1, 2 < \eta_2 < 3$	$x_\gamma^{obs} > 0.75$	$0.2 < y < 0.8$	0.19	0.40	31.23
14	$E_{T,1} > 15, E_{T,2} > 10$	$1 < \eta_1 < 2, 2 < \eta_2 < 3$	$x_\gamma^{obs} < 0.75$	$0.2 < y < 0.8$	0.17	0.05	143.33
15	$E_{T,1} > 30, E_{T,2} > 15$	$1 < \eta_1 < 2, 1 < \eta_2 < 2$	$x_\gamma^{obs} > 0.75$	$0.2 < y < 0.8$	0.17	0.69	14.25
16	$E_{T,1} > 30, E_{T,2} > 10$	$1 < \eta_1 < 2, 1 < \eta_2 < 2$	$x_\gamma^{obs} > 0.75$	$0.2 < y < 0.8$	0.17	0.69	14.43
17	$E_{T,1} > 30, E_{T,2} > 20$	$1 < \eta_1 < 2, 1 < \eta_2 < 2$	$x_\gamma^{obs} > 0.75$	$0.2 < y < 0.8$	0.17	0.69	13.96
18	$E_{T,1} > 30, E_{T,2} > 25$	$1 < \eta_1 < 2, 1 < \eta_2 < 2$	$x_\gamma^{obs} > 0.75$	$0.2 < y < 0.8$	0.17	0.68	13.62
19	$E_{T,1} > 25, E_{T,2} > 15$	$1 < \eta_1 < 2, 1 < \eta_2 < 2$	$x_\gamma^{obs} < 0.75$	$0.2 < y < 0.8$	0.15	0.14	19.12
20	$E_{T,1} > 25, E_{T,2} > 20$	$1 < \eta_1 < 2, 1 < \eta_2 < 2$	$x_\gamma^{obs} < 0.75$	$0.2 < y < 0.8$	0.15	0.10	16.34
21	$E_{T,1} > 15, E_{T,2} > 10$	$0 < \eta_1 < 1, 2 < \eta_2 < 3$	$x_\gamma^{obs} > 0.75$	$0.2 < y < 0.8$	0.13	0.35	77.42
22	$E_{T,1} > 15, E_{T,2} > 10$	$-1 < \eta_1 < 0, 1 < \eta_2 < 2$	$x_\gamma^{obs} > 0.75$	$0.2 < y < 0.8$	0.13	0.49	132.27
23	$E_{T,1} > 25, E_{T,2} > 15$	$1 < \eta_1 < 2, 1 < \eta_2 < 2$	$x_\gamma^{obs} > 0.75$	$0.2 < y < 0.8$	0.13	0.66	26.60
24	$E_{T,1} > 25, E_{T,2} > 10$	$1 < \eta_1 < 2, 1 < \eta_2 < 2$	$x_\gamma^{obs} > 0.75$	$0.2 < y < 0.8$	0.13	0.66	26.58
25	$E_{T,1} > 15, E_{T,2} > 10$	$0 < \eta_1 < 1, 2 < \eta_2 < 3$	$x_\gamma^{obs} < 0.75$	$0.2 < y < 0.8$	0.13	0.08	146.03

Table 5.8: Top 25 integrated cross-sections with the ranking quantity set to $\delta\sigma_{gluon}$ and the selection criteria set to $\sigma_{cteq} \geq 10 \text{ pb}$ and $x_\gamma^{obs} < 0.75$ or > 0.75

Rank	E_T cuts (GeV)	η^{jet} cuts	x_γ^{obs} cut	y cut	$\delta\sigma_{gluon}$	ξ_{direct}	σ_{cteq}
1	$E_{T,1} > 30, E_{T,2} > 15$	$1 < \eta_1 < 2, 1 < \eta_2 < 2$	$x_\gamma^{obs} > 0.75$	$0.2 < y < 0.8$	0.17	0.69	14.25
2	$E_{T,1} > 30, E_{T,2} > 10$	$1 < \eta_1 < 2, 1 < \eta_2 < 2$	$x_\gamma^{obs} > 0.75$	$0.2 < y < 0.8$	0.17	0.69	14.43
3	$E_{T,1} > 30, E_{T,2} > 20$	$1 < \eta_1 < 2, 1 < \eta_2 < 2$	$x_\gamma^{obs} > 0.75$	$0.2 < y < 0.8$	0.17	0.69	13.96
4	$E_{T,1} > 30, E_{T,2} > 25$	$1 < \eta_1 < 2, 1 < \eta_2 < 2$	$x_\gamma^{obs} > 0.75$	$0.2 < y < 0.8$	0.17	0.68	13.62
5	$E_{T,1} > 25, E_{T,2} > 15$	$1 < \eta_1 < 2, 1 < \eta_2 < 2$	$x_\gamma^{obs} > 0.75$	$0.2 < y < 0.8$	0.13	0.66	26.60
6	$E_{T,1} > 25, E_{T,2} > 10$	$1 < \eta_1 < 2, 1 < \eta_2 < 2$	$x_\gamma^{obs} > 0.75$	$0.2 < y < 0.8$	0.13	0.66	26.58
7	$E_{T,1} > 25, E_{T,2} > 20$	$1 < \eta_1 < 2, 1 < \eta_2 < 2$	$x_\gamma^{obs} > 0.75$	$0.2 < y < 0.8$	0.12	0.66	25.61
8	$E_{T,1} > 20, E_{T,2} > 10$	$-1 < \eta_1 < 0, 0 < \eta_2 < 1$	$x_\gamma^{obs} > 0.75$	$0.2 < y < 0.8$	0.12	0.73	22.97
9	$E_{T,1} > 20, E_{T,2} > 15$	$-1 < \eta_1 < 0, 0 < \eta_2 < 1$	$x_\gamma^{obs} > 0.75$	$0.2 < y < 0.8$	0.12	0.73	19.66
10	$E_{T,1} > 15, E_{T,2} > 10$	$0 < \eta_1 < 1, 0 < \eta_2 < 1$	$x_\gamma^{obs} > 0.75$	$0.2 < y < 0.8$	0.12	0.67	281.82
11	$E_{T,1} > 14, E_{T,2} > 11$	$0 < \eta_1 < 1, 0 < \eta_2 < 1$	$x_\gamma^{obs} > 0.75$	$0.2 < y < 0.8$	0.11	0.66	345.34
12	$E_{T,1} > 20, E_{T,2} > 10$	$0 < \eta_1 < 1, 0 < \eta_2 < 1$	$x_\gamma^{obs} > 0.75$	$0.2 < y < 0.8$	0.11	0.69	95.49
13	$E_{T,1} > 14, E_{T,2} > 11$	$1 < \eta_1 < 2.4, 0 < \eta_2 < 1$	$x_\gamma^{obs} > 0.75$	$0.2 < y < 0.8$	0.11	0.51	289.72
14	$E_{T,1} > 20, E_{T,2} > 15$	$0 < \eta_1 < 1, 0 < \eta_2 < 1$	$x_\gamma^{obs} > 0.75$	$0.2 < y < 0.8$	0.11	0.68	87.88
15	$E_{T,1} > 15, E_{T,2} > 10$	$0 < \eta_1 < 1, 1 < \eta_2 < 2$	$x_\gamma^{obs} > 0.75$	$0.2 < y < 0.8$	0.11	0.56	207.81
16	$E_{T,1} > 14, E_{T,2} > 11$	$1 < \eta_1 < 2.4, 1 < \eta_2 < 2.4$	$x_\gamma^{obs} > 0.75$	$0.2 < y < 0.8$	0.11	0.55	59.26
17	$E_{T,1} > 20, E_{T,2} > 15$	$-1 < \eta_1 < 0, 1 < \eta_2 < 2$	$x_\gamma^{obs} > 0.75$	$0.2 < y < 0.8$	0.11	0.54	25.56
18	$E_{T,1} > 15, E_{T,2} > 10$	$-1 < \eta_1 < 0, 0 < \eta_2 < 1$	$x_\gamma^{obs} > 0.75$	$0.2 < y < 0.8$	0.11	0.67	148.12
19	$E_{T,1} > 25, E_{T,2} > 10$	$0 < \eta_1 < 1, 0 < \eta_2 < 1$	$x_\gamma^{obs} > 0.75$	$0.2 < y < 0.8$	0.10	0.71	31.94
20	$E_{T,1} > 25, E_{T,2} > 15$	$0 < \eta_1 < 1, 0 < \eta_2 < 1$	$x_\gamma^{obs} > 0.75$	$0.2 < y < 0.8$	0.10	0.72	31.45
21	$E_{T,1} > 14, E_{T,2} > 11$	$0 < \eta_1 < 1, -1 < \eta_2 < 0$	$x_\gamma^{obs} > 0.75$	$0.2 < y < 0.8$	0.10	0.65	198.09
22	$E_{T,1} > 30, E_{T,2} > 15$	$0 < \eta_1 < 1, 1 < \eta_2 < 2$	$x_\gamma^{obs} > 0.75$	$0.2 < y < 0.8$	0.10	0.64	14.00
23	$E_{T,1} > 25, E_{T,2} > 20$	$0 < \eta_1 < 1, 0 < \eta_2 < 1$	$x_\gamma^{obs} > 0.75$	$0.2 < y < 0.8$	0.10	0.71	28.97
24	$E_{T,1} > 20, E_{T,2} > 15$	$1 < \eta_1 < 2, 1 < \eta_2 < 2$	$x_\gamma^{obs} > 0.75$	$0.2 < y < 0.8$	0.09	0.62	42.98
25	$E_{T,1} > 15, E_{T,2} > 10$	$1 < \eta_1 < 2, 1 < \eta_2 < 2$	$x_\gamma^{obs} > 0.75$	$0.2 < y < 0.8$	0.09	0.55	51.37

Table 5.9: Top 25 integrated cross-sections with the ranking quantity set to $\delta\sigma_{gluon}$ and the selection criteria set to $\sigma_{cteq} \geq 10 \text{ pb}$, $x_\gamma^{obs} < 0.75$ or > 0.75 and $\xi^{dir} > 0.5$

figures shown in this, and subsequent tables regarding the optimisation study, are quoted in pb. It is seen that the most sensitive cross-sections are characterised by a gluon error of $\sim 30\%$. They are also dominated by resolved events and all lie in the forward η regions. It can also be seen that there is not much sensitivity of the cross-sections to the cut on x_γ^{obs} or y so it is more constructive to integrate the cross-sections over the entire y region and to just consider one x_γ^{obs} cut. A standard x_γ^{obs} cut of 0.75 is chosen.

Table 5.8 shows the results of the optimisation when the above changes are made. To obtain more statistically significant cross-sections the requirement that $\sigma_{cteq} \geq 10$ pb has also been included in the selection criteria. The general results of this optimisation procedure are much the same as those illustrated by table 5.7. The most sensitive cross-sections appear to be resolved cross-sections, which lie in the forward region. In an effort to find more direct enriched optimised cross-sections, optimisation was performed using the additional constraint that $\xi^{dir} > 0.5$. The results of this procedure are shown in table 5.9. We see that the direct enriched cross-sections do not exhibit the same degree of sensitivity to the uncertainties on the underlying gluon PDF as the resolved enriched cross-sections. To see more clearly how the 96-97 γp dijet cross-sections of [51] perform in the optimisation, table 5.10 shows the results of the optimisation procedure when only these cross-sections are considered. It's seen that these cross-sections are characterised by a gluon PDF error of the order of $\sim 10\%$. The most sensitive cross-sections found from the optimisation study are about 3 times as sensitive as this.

Only a snapshot of the entire optimisation study has been presented here. For the full details of all the results the reader is referred to [71].

5.3.6 Discussion

Tables 5.8 and 5.9 were employed to choose 8 optimised cross-sections for measurement (4 direct enriched and 4 resolved enriched). Before showing the 8 chosen cross-sections, a number of important points need to be discussed. The optimisation study made it clear that in order to measure cross-sections which show a lot of sensitivity to the uncertainties on the underlying gluon PDF, it is necessary to go forward in η . This is quite easy to understand if one looks at the formula used to calculate x_p^{obs}

Rank	E_T cuts (GeV)	η^{jet} cuts	x_γ^{obs} cut	y cut	$\delta\sigma_{gluon}$	ξ_{direct}	σ_{cteq}
1	$E_{T,1} > 14, E_{T,2} > 11$	$1 < \eta_1 < 2.4, -1 < \eta_2 < 0$	$x_\gamma^{obs} > 0.75$	$0.2 < y < 0.8$	0.12	0.44	207.40
2	$E_{T,1} > 14, E_{T,2} > 11$	$1 < \eta_1 < 2.4, -1 < \eta_2 < 0$	$x_\gamma^{obs} < 0.75$	$0.2 < y < 0.8$	0.12	0.09	69.48
3	$E_{T,1} > 14, E_{T,2} > 11$	$0 < \eta_1 < 1, 0 < \eta_2 < 1$	$x_\gamma^{obs} < 0.75$	$0.2 < y < 0.8$	0.12	0.11	129.32
4	$E_{T,1} > 14, E_{T,2} > 11$	$0 < \eta_1 < 1, 0 < \eta_2 < 1$	$x_\gamma^{obs} > 0.75$	$0.2 < y < 0.8$	0.11	0.66	345.34
5	$E_{T,1} > 14, E_{T,2} > 11$	$1 < \eta_1 < 2.4, 0 < \eta_2 < 1$	$x_\gamma^{obs} > 0.75$	$0.2 < y < 0.8$	0.11	0.51	289.72
6	$E_{T,1} > 14, E_{T,2} > 11$	$0 < \eta_1 < 1, -1 < \eta_2 < 0$	$x_\gamma^{obs} < 0.75$	$0.2 < y < 0.8$	0.11	0.14	23.19
7	$E_{T,1} > 14, E_{T,2} > 11$	$1 < \eta_1 < 2.4, 0 < \eta_2 < 1$	$x_\gamma^{obs} < 0.75$	$0.2 < y < 0.8$	0.11	0.07	281.08
8	$E_{T,1} > 14, E_{T,2} > 11$	$1 < \eta_1 < 2.4, 1 < \eta_2 < 2.4$	$x_\gamma^{obs} > 0.75$	$0.2 < y < 0.8$	0.11	0.55	59.26
9	$E_{T,1} > 14, E_{T,2} > 11$	$1 < \eta_1 < 2.4, 1 < \eta_2 < 2.4$	$x_\gamma^{obs} < 0.75$	$0.2 < y < 0.8$	0.10	0.04	408.21
10	$E_{T,1} > 14, E_{T,2} > 11$	$0 < \eta_1 < 1, -1 < \eta_2 < 0$	$x_\gamma^{obs} > 0.75$	$0.2 < y < 0.8$	0.10	0.65	198.09
11	$E_{T,1} > 14, E_{T,2} > 11$	$-1 < \eta_1 < 0, -1 < \eta_2 < 0$	$x_\gamma^{obs} < 0.75$	$0.2 < y < 0.8$	0.09	0.34	0.63
12	$E_{T,1} > 14, E_{T,2} > 11$	$-1 < \eta_1 < 0, -1 < \eta_2 < 0$	$x_\gamma^{obs} > 0.75$	$0.2 < y < 0.8$	0.08	0.78	57.27

Table 5.10: The 12 cross sections of [51] integrated over $0.20 < y < 0.8$

$$x_p^{obs} = \frac{E_{T,1}e^{\eta_1} + E_{T,2}e^{\eta_2}}{2E_p}, \quad (5.1)$$

where it is easy to see that for any given values of $E_{T,1}$ and $E_{T,2}$, x_p^{obs} , which is closely correlated with x_p , increases rapidly as a function of η_1 and η_2 . Isolated forward regions therefore tend to be dominated by interactions involving relatively high x_p partons. Provided there is a significant contribution to the cross-section from gluon interactions then, because of the uncertainty on the high- x_p gluon, it is expected that the uncertainty on the corresponding cross-section will be large. A γp measurement has never been conducted as far forward as $\eta = 3$ (previous measurements have only been taken as far forward as $\eta = 2.5$ [51],[72]) so the measurement of the optimised cross-sections will utilise regions of the detector never used in previous γp analyses. It will be seen later (see chapter 7) that it is not actually possible to trigger efficiently on a dijet event whereby both jets lie in the far forward region ($2.5 < \eta < 3.0$). The best one can do is to measure events whereby both jets satisfy $2 < \eta < 3$ but with at least one jet satisfying $2 < \eta < 2.5$.

It also turns out (see chapter 7) that if cuts on the transverse energy of the leading and trailing jets of 15 GeV and 10 GeV are used then an inadequate description of the data by the MC is obtained in the forward region. In order to remedy this, the E_T cuts are increased to 20 GeV and 15 GeV for the leading and trailing jets respectively.

Rank	E_T cuts (GeV)	η^{jet} cuts	x_γ^{obs} cut	y cut	$\delta\sigma_{gluon}$	ξ_{direct}	σ_{cteq}
1	$E_{T,1} > 20, E_{T,2} > 15$	$2 < \eta_1 < 2.5, 2 < \eta_2 < 3$	$x_\gamma^{obs} < 0.75$	$0.2 < y < 0.8$	0.31	0.02	19.81
2	$E_{T,1} > 25, E_{T,2} > 15$	$1 < \eta_1 < 2, 2 < \eta_2 < 3$	$x_\gamma^{obs} < 0.75$	$0.2 < y < 0.8$	0.28	0.10	14.23
3	$E_{T,1} > 20, E_{T,2} > 15$	$1 < \eta_1 < 2, 2 < \eta_2 < 3$	$x_\gamma^{obs} < 0.75$	$0.2 < y < 0.8$	0.25	0.05	38.63
4	$E_{T,1} > 25, E_{T,2} > 15$	$0 < \eta_1 < 1, 2 < \eta_2 < 3$	$x_\gamma^{obs} > 0.75$	$0.2 < y < 0.8$	0.24	0.45	12.86
5	$E_{T,1} > 20, E_{T,2} > 15$	$0 < \eta_1 < 1, 2 < \eta_2 < 3$	$x_\gamma^{obs} > 0.75$	$0.2 < y < 0.8$	0.19	0.40	31.23
6	$E_{T,1} > 30, E_{T,2} > 15$	$1 < \eta_1 < 2, 1 < \eta_2 < 2$	$x_\gamma^{obs} > 0.75$	$0.2 < y < 0.8$	0.17	0.69	14.25
7	$E_{T,1} > 25, E_{T,2} > 15$	$1 < \eta_1 < 2, 1 < \eta_2 < 2$	$x_\gamma^{obs} < 0.75$	$0.2 < y < 0.8$	0.15	0.14	19.12
8	$E_{T,1} > 20, E_{T,2} > 15$	$-1 < \eta_1 < 0, 0 < \eta_2 < 1$	$x_\gamma^{obs} > 0.75$	$0.2 < y < 0.8$	0.12	0.73	19.66

Table 5.11: The 8 optimised cross-sections chosen for measurement

Name	E_T cuts (GeV)	η^{jet} cuts	x_γ^{obs} cut	y cut
OptA	$E_{T,1} > 20, E_{T,2} > 15$	$2 < \eta_1 < 2.5, 2 < \eta_2 < 3$	$x_\gamma^{obs} < 0.75$	$0.2 < y < 0.85$
OptB	$E_{T,1} > 25, E_{T,2} > 15$	$1 < \eta_1 < 2, 1 < \eta_2 < 2$	$x_\gamma^{obs} < 0.75$	$0.2 < y < 0.85$
OptC	$E_{T,1} > 20, E_{T,2} > 15$	$1 < \eta_1 < 2, 2 < \eta_2 < 3$	$x_\gamma^{obs} < 0.75$	$0.2 < y < 0.85$
OptG	$E_{T,1} > 25, E_{T,2} > 15$	$1 < \eta_1 < 2, 2 < \eta_2 < 3$	$x_\gamma^{obs} < 0.75$	$0.2 < y < 0.85$
OptD	$E_{T,1} > 25, E_{T,2} > 15$	$0 < \eta_1 < 1, 2 < \eta_2 < 3$	$x_\gamma^{obs} > 0.75$	$0.2 < y < 0.85$
OptE	$E_{T,1} > 20, E_{T,2} > 15$	$0 < \eta_1 < 1, 2 < \eta_2 < 3$	$x_\gamma^{obs} > 0.75$	$0.2 < y < 0.85$
OptF	$E_{T,1} > 30, E_{T,2} > 15$	$1 < \eta_1 < 2, 1 < \eta_2 < 2$	$x_\gamma^{obs} > 0.75$	$0.2 < y < 0.85$
OptH	$E_{T,1} > 20, E_{T,2} > 15$	$-1 < \eta_1 < 0, 0 < \eta_2 < 1$	$x_\gamma^{obs} > 0.75$	$0.2 < y < 0.85$

Table 5.12: The nomenclature used for the 8 optimised cross-sections chosen for measurement

With these caveats in mind it is now possible to present the 8 optimised cross-sections chosen for measurement. These are shown in table 5.12 (and ranked in table 5.11) which also details the nomenclature which will be used to refer to these optimised cross-sections throughout the rest of this thesis. Note the small change of the upper limit of the y cut from 0.8 to 0.85. This is a more standard cut on y , made in photoproduction analyses.

The optimised cross-sections of table 5.12 are plotted in figures 5.4-5.7. An interesting feature of these plots is the shape of the gluon PDF error across the whole range of x_p^{obs} . At low- x_p^{obs} ($\lesssim 0.1$) the cross-sections are relatively well constrained by the uncertainties on the gluon PDF. Between $0.1 \lesssim x_p^{obs} \lesssim 0.3$ there is a rise in the gluon PDF error. The gluon PDF error reaches a maximum in the range $0.3 \lesssim x_p^{obs} \lesssim 0.4$ before falling off quite rapidly with increasing x_p^{obs} . It is also interesting to note that the total PDF error in the region $0.0 \lesssim x_p^{obs} \lesssim 0.5$ is dominated by the gluon PDF error. However, this is not true over the entire range of x_p^{obs} . To see why this is so it is necessary to take a closer look at the region between $0.5 < x_p^{obs} < 1.0$. Figure 5.8 shows a more enhanced plot of the

optimised cross-section, OptG (only one of the optimised cross-sections has been shown, but the trend is similar for the other cross-sections). It can be seen that the total PDF error has a bow-tie shape whereby the initially large error in the region $0.1 \lesssim x_p^{obs} \lesssim 0.4$ falls to a minimum at between $0.5 \lesssim x_p^{obs} \lesssim 0.6$ before finally increasing as x_p^{obs} gets closer to unity. The gluon PDF error dominates the total PDF error in the region $x_p^{obs} \lesssim 0.5$.

One might expect, from the shape of the uncertainties on the underlying gluon PDF (see figure 4.6, C.1 or C.2), that the gluon PDF error should be much more substantial at high- x_p^{obs} ($\gtrsim 0.5$) but this is not the case and in fact it drops off to a negligible level as $x_p^{obs} \rightarrow 1$. This effect can be understood if one looks at the contribution to the cross-section from the individual parton flavours. This is shown, for the optimised-cross sections of table 5.12, in figures 5.9 and 5.10, where the gluon, up valence, down valence and sea contributions to the cross-section are all shown separately. It can be seen that the gluon provides the most significant contribution to the cross-section at low- x_p^{obs} which leads to a large gluon PDF error on the cross-section but as x_p^{obs} is increased the gluon contribution falls off and the contribution from the valence quarks begin to take over. Because the valence quark distributions are much better constrained than the gluon at higher- x_p^{obs} (see [40–42]) the total PDF error begins to decrease even though the error on the gluon component of the cross-section increases. In other words the effect of the large gluon PDF uncertainty on the gluon component of the cross-section is suppressed by the fact that the much better constrained valence distributions (particularly the up valence distribution) dominates the cross-section. Finally, as $x_p^{obs} \rightarrow 1$ the total PDF error begins to increase as a consequence of the fact that even the valence distributions are poorly constrained at very high- x_p (see [40–42]).

5.4 Final Cross-Section Definitions

In the last section of this chapter the cross-sections that will be measured in the present analysis are summarised. The optimisation study discussed in this chapter has shown that it could be possible to further constrain the gluon PDF up to $x_p^{obs} \sim 0.4$ with (precisely measured) ZEUS data. By measuring optimised cross-sections it is possible to consider γp dijet cross-sections which show up to three times the sensitivity to the uncertainties on the underlying gluon PDF than those already measured. These cross-sections are summarised in table 5.12. A key

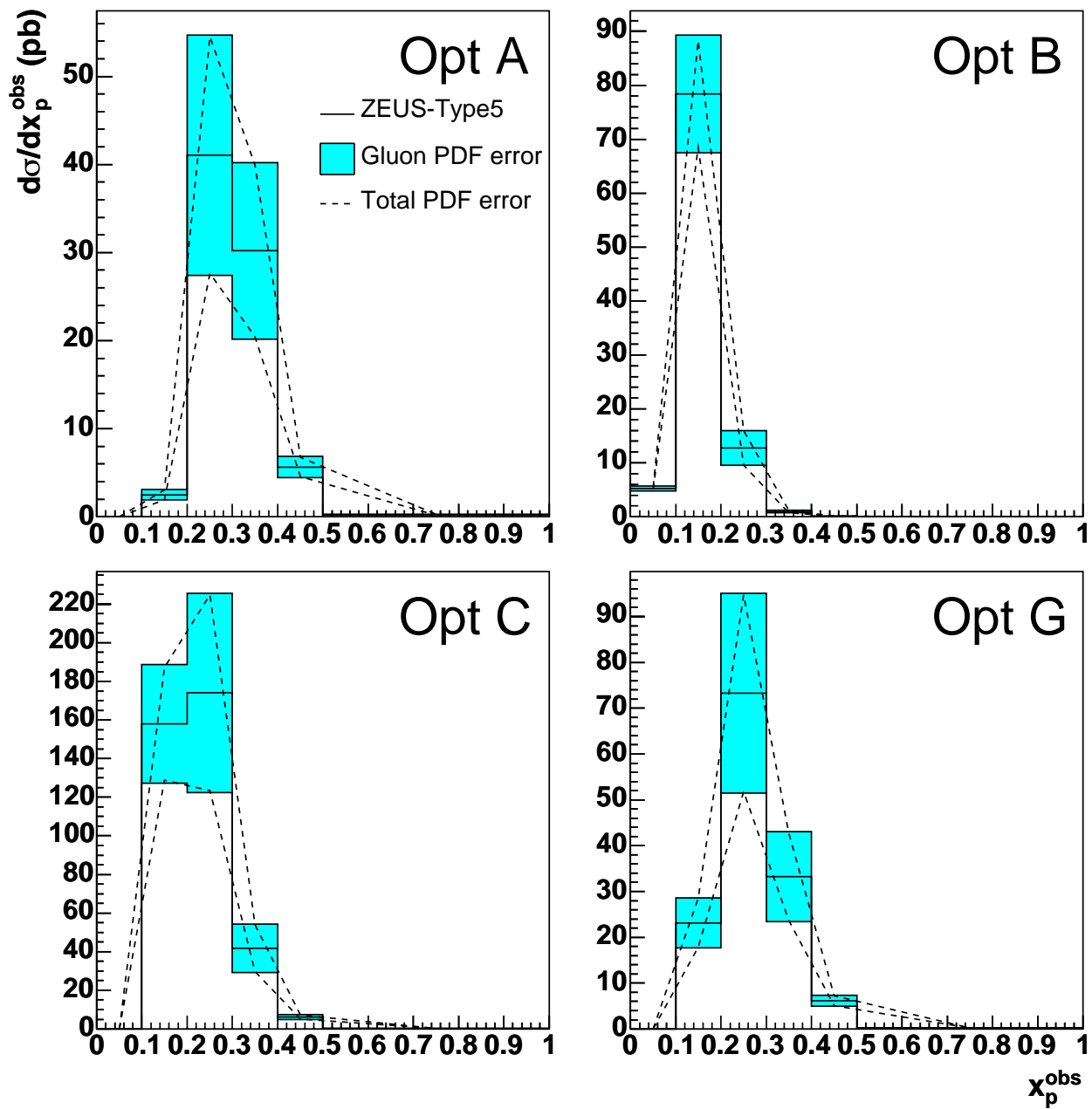


Figure 5.4: The total PDF errors (dashed) and gluon PDF errors (blue) for the low- x_γ^{obs} optimised cross-sections of table 5.12

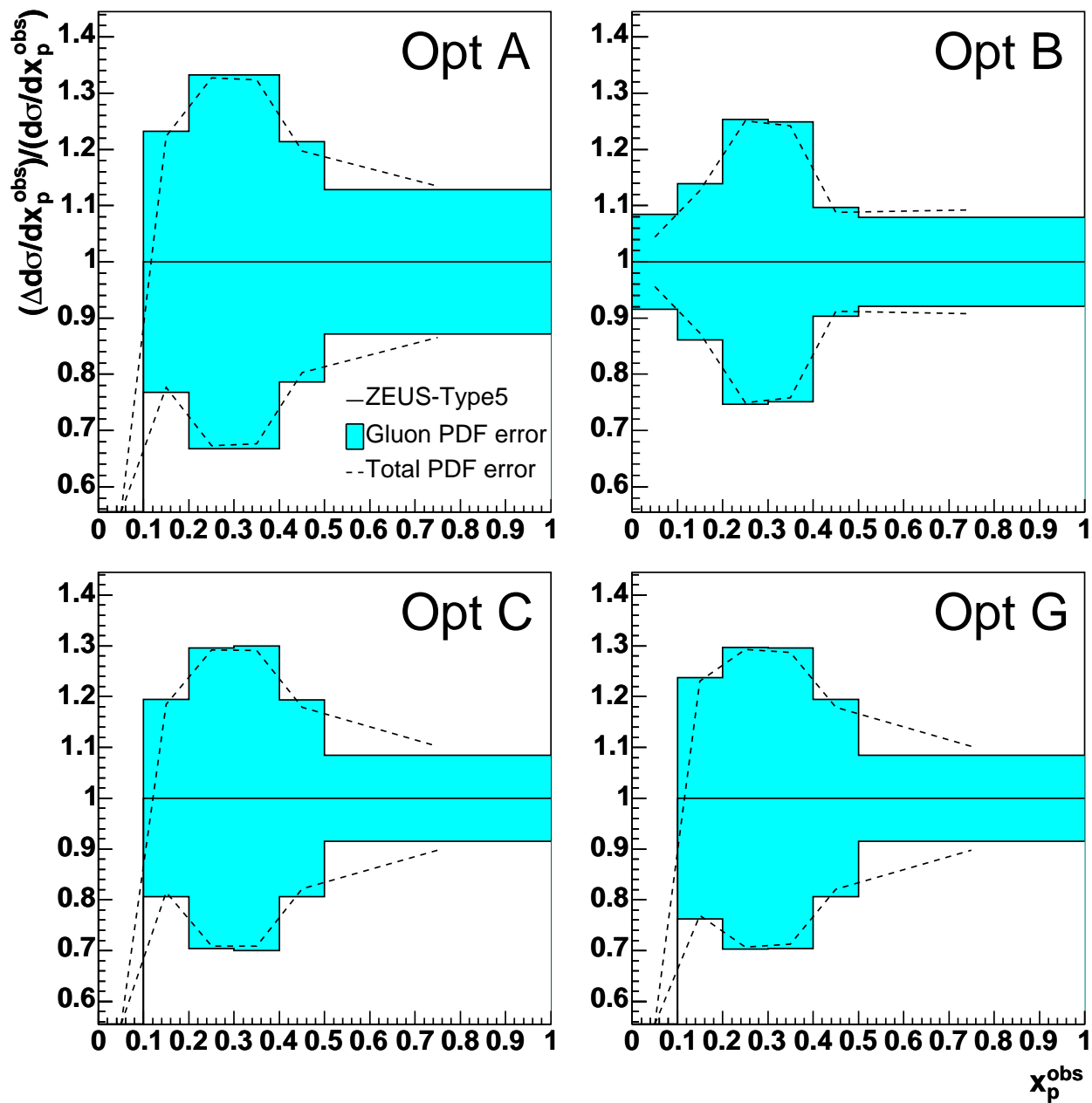


Figure 5.5: The total PDF errors (dashed) and gluon PDF errors (blue) for the low- x_p^{obs} optimised cross-sections of table 5.12 ($\Delta d\sigma/dx_p^{obs}$) shown as a fraction of the nominal prediction ($d\sigma/dx_p^{obs}$)

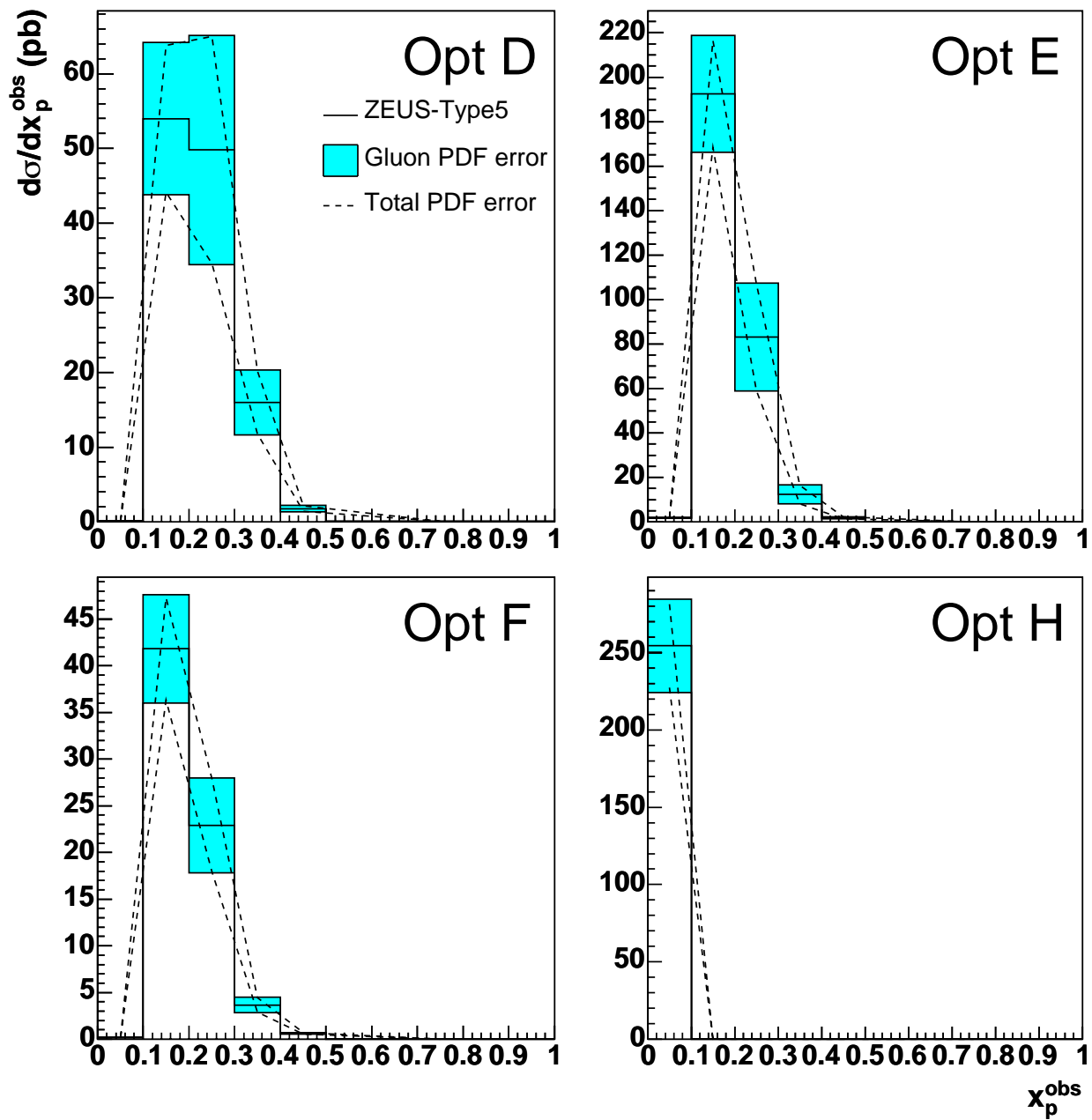


Figure 5.6: The total PDF errors (dashed) and gluon PDF errors (blue) for the high- x_p^{obs} optimised cross-sections of table 5.12

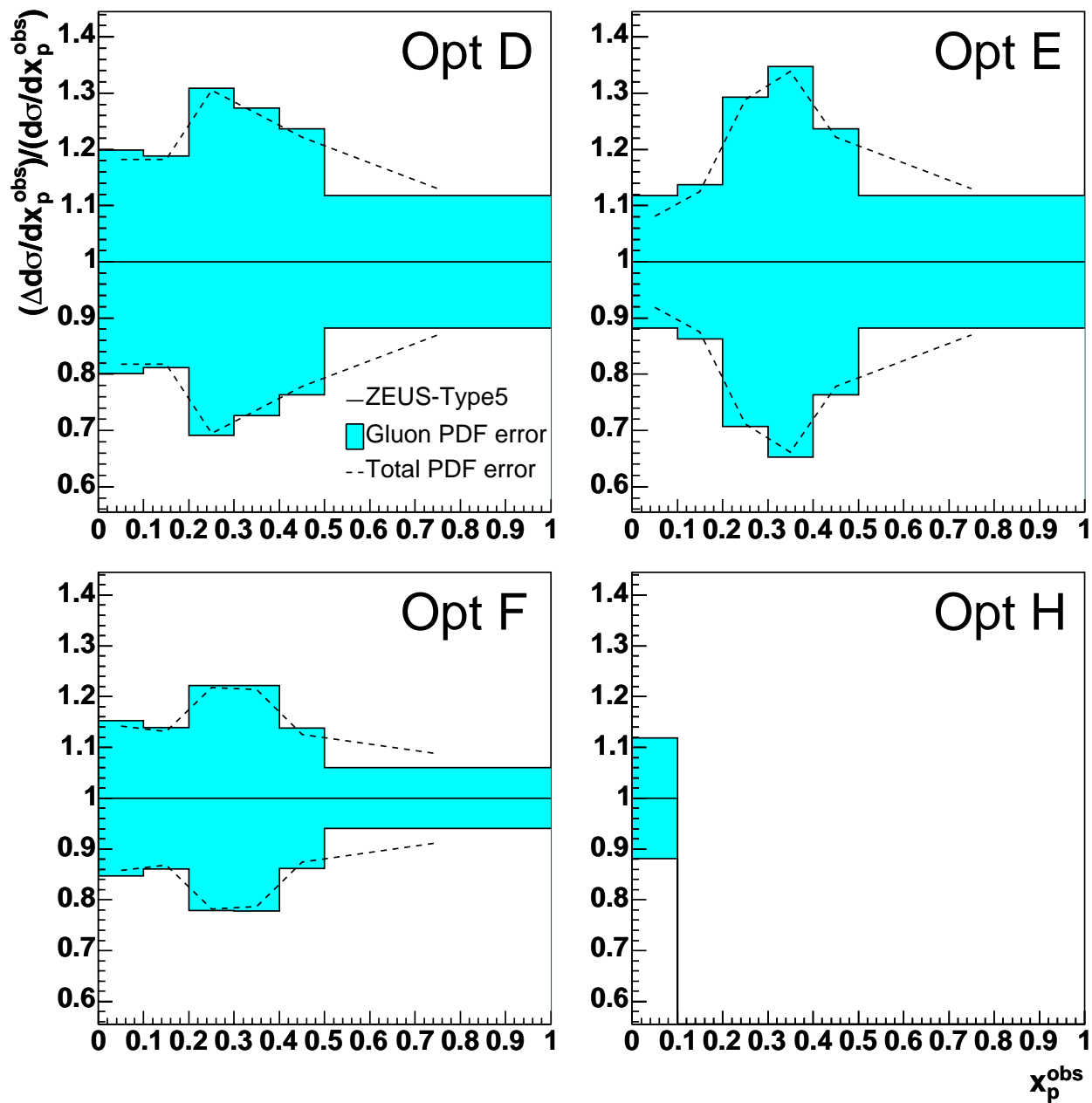


Figure 5.7: The total PDF errors (dashed) and gluon PDF errors (blue) for the high- x_p^{obs} optimised cross-sections of table 5.12 ($\Delta d\sigma/dx_p^{obs}$) shown as a fraction of the nominal prediction ($d\sigma/dx_p^{obs}$)

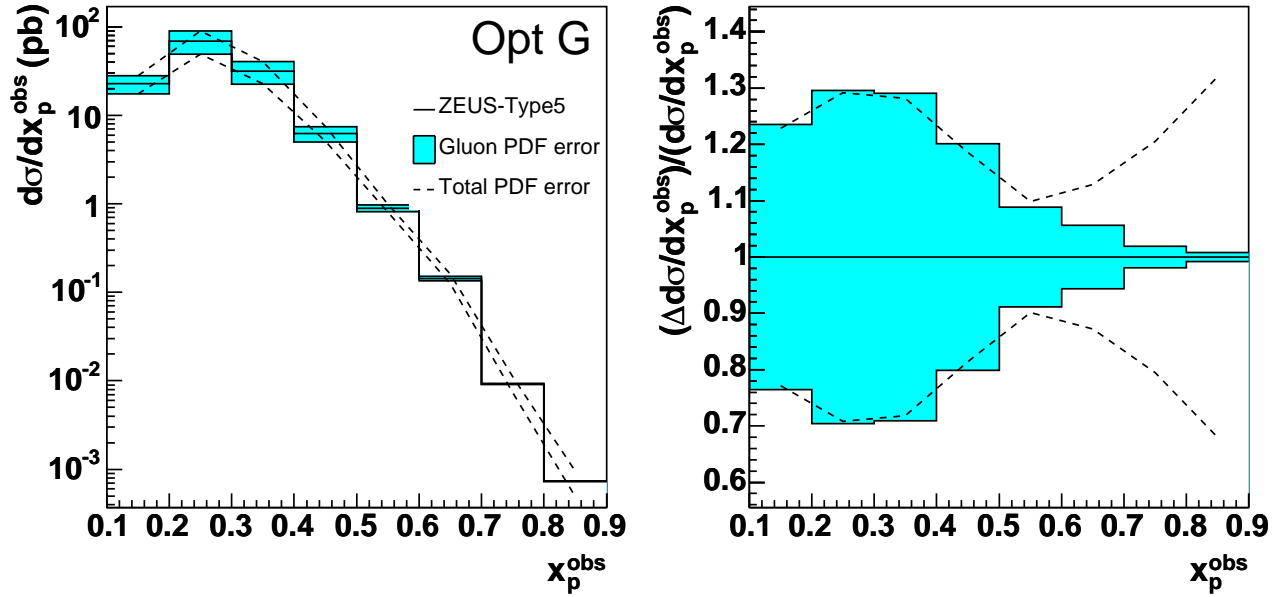


Figure 5.8: An enhanced plot of optimised cross-section, OptG, showing the bow-tie shaped total PDF error and the suppression of the gluon PDF error at high- x_p^{obs} .

requirement of these measurements is that they be made at high jet transverse energies in the forward region of the ZEUS detector.

In summary, the required conditions on the γp dijet events for the determination of the cross-sections presented in this thesis are:

- At least two jets in the event. The transverse energies, $E_{T,1}$ and $E_{T,2}$, of the two highest E_T jets, must exceed 20 GeV and 15 GeV respectively. This is known as an asymmetric cut and improves the stability of NLO QCD calculations in the case that both jets meet the minimum transverse energy requirements. Previous γp dijet analyses [51, 73] have utilised cuts of $E_{T,1} > 14$ GeV and $E_{T,2} > 11$ GeV for the leading and trailing jets, where it was shown that by making such cuts the data was in better agreement with NLO QCD calculations. Lower E_T cuts resulted in the data lying significantly above the calculations when $x_\gamma^{\text{obs}} < 0.75$. The even harder cuts in the present case will be justified in chapter 7 and is related to obtaining a reasonable agreement between data and MC events in the forward region of the ZEUS detector. The increase in the cuts results in a significantly harder scale suitable for pQCD calculations. In addition, the comparison of the data with a QCD calculation that neglects quark masses is better justified (which is the case for the calculation of Frixione and Ridolfi [19]). The

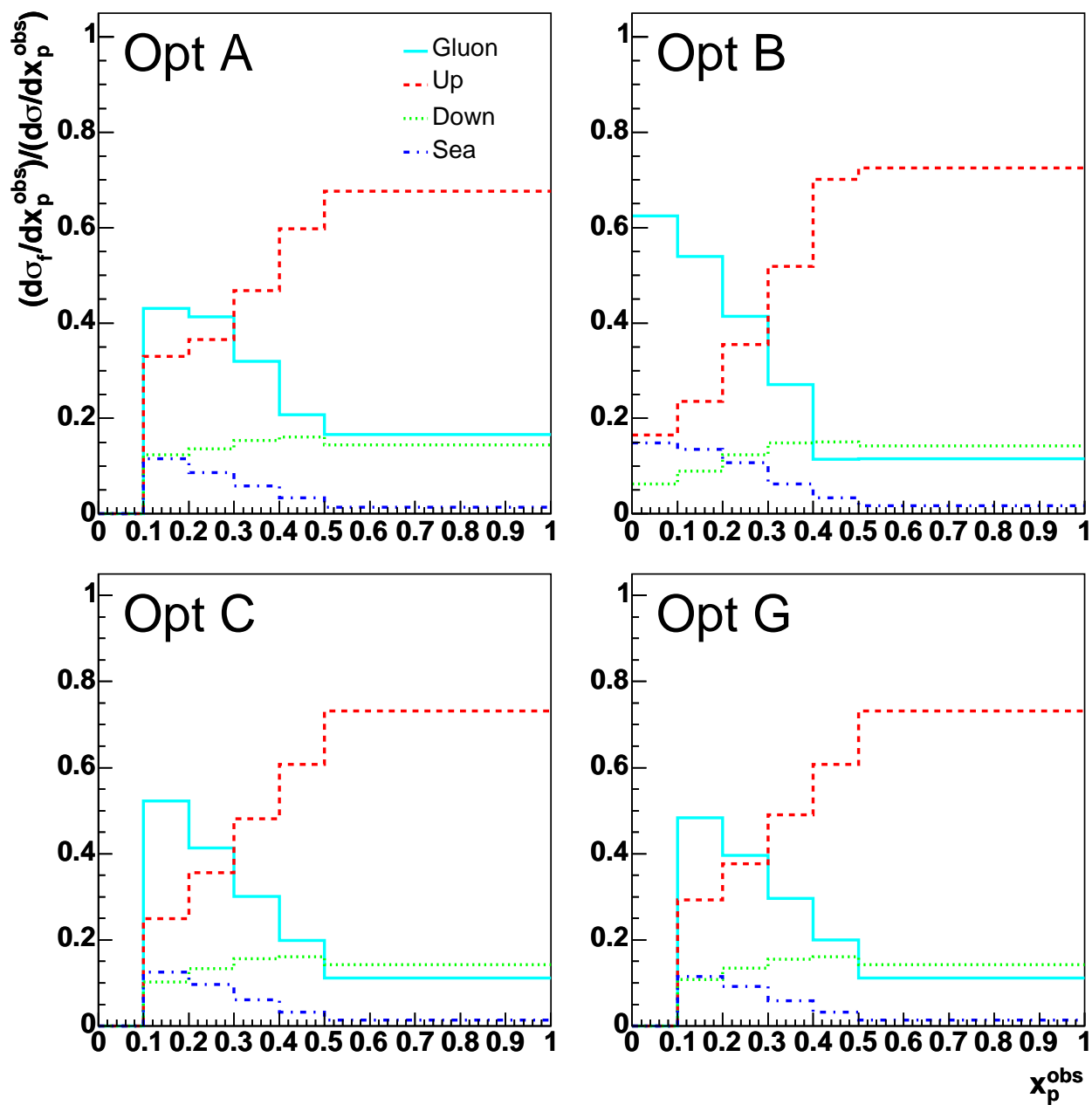


Figure 5.9: The fractional contribution to the low- x_γ^{obs} optimised cross-sections from the various parton flavours.

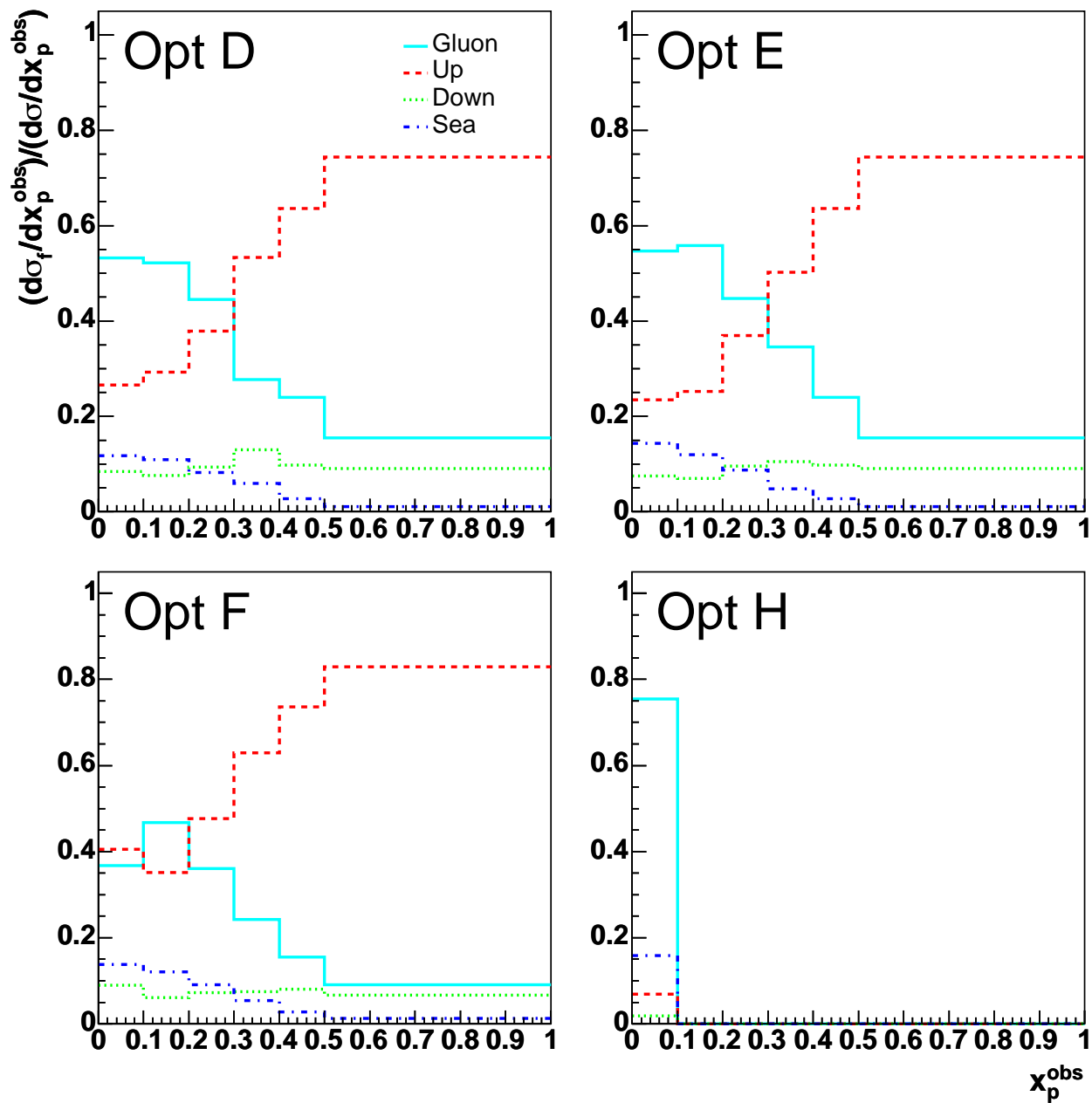


Figure 5.10: The fractional contribution to the high- x_p^{obs} optimised cross-sections from the various parton flavours.

asymmetric cuts on the transverse energies of the jets is required because they improve the stability of the NLO QCD calculations, in cases where both jets meet the minimum transverse energy requirements.

- The two jets fulfilling the above E_T requirements must have pseudorapidities in the range of -1 to 3 with at least one of the jets lying in the range -1 to 2.5 . The lower limit is due to a lack of events in the rear regions of the ZEUS detector. The upper cut has never been attempted in a previous γp dijet analysis. Previous analyses have only gone up to 2.4 in pseudorapidity. The forward region is a challenging region of the detector to investigate because of the presence of the proton remnant and the possibility that the Monte Carlo may not be able to adequately describe the data in this region. It's also important to note here that differential cross-sections in specific regions of the pseudorapidities of the two highest transverse energy jets (such as the aforementioned optimised cross-sections) must be symmetrised with respect to the pseudorapidities. In NLO processes, unlike LO, the transverse energies of the jets do not balance. The equality in the jet transverse energies is approached in events when one of the partons is soft. The assignment of which jet is the hardest therefore depends on the soft partons of the events and is not infrared safe. By symmetrisation of the cross-sections with respect to the pseudorapidities of the two highest transverse energy jets, the problem can be avoided [74].
- The kinematic region is taken to be $Q^2 < 1 \text{ GeV}^2$ and $0.20 < y < 0.85$.

Various differential dijet cross-sections will be measured in addition to the optimised cross-sections presented in this chapter. The optimised cross-sections will subsequently be included in a new ZEUS QCD fit to see if it is possible to further improve the precision of the extracted gluon PDF.

5.5 Remaining issues

The optimisation study presented in this chapter is not absolute and there are many ways in which it could be adjusted or modified. One of the main drawbacks of the study is that it fails to properly take into account the accuracy with which the various cross-sections can actually be measured. One of the main

assumptions being made is that the statistical errors on the cross-sections are small (hence the minimum cross-section cut used in the optimisation procedure). If the systematic errors of the cross-section measurement using data are small in relation to the size of the gluon PDF errors then there is potential for such cross-section data to further constrain the PDF. However, no estimate of the likely size of systematic errors is made and taken account of during the study. Another point worth noting is that throughout the procedure attention is focused entirely on the differential cross-section as a function of x_p^{obs} . This cross-section may not be the most accurate cross-section to measure (in relation to systematics). No investigation was performed as to the relative merit of measuring the cross-section relative to x_p^{obs} as opposed to some other kinematic variable.

Chapter 6

Event Reconstruction

This chapter describes how the hadronic final state is reconstructed in the ZEUS detector. The reconstruction of some general event kinematics will be discussed as well as the reconstruction of the specific jet and dijet variables used in this thesis. Certain correction procedures for the reconstructed jet transverse energies will also be discussed.

6.1 Tracking and Vertex Reconstruction

Tracking information is not so important for the analysis presented in this thesis. In the present case it is used only to assist the identification of electrons in the ZEUS detector and for the study of the calorimeter jet energy scale. Both of these topics will be discussed in due course. Vertex information, on the other hand, is crucial as all the calorimeter cell positions are measured with respect to it. The colliding particles do not always interact at the nominal interaction point (the origin of the ZEUS coordinate system) but have a characteristic spread about this point determined by the finite size of the colliding particle bunches. The vertex finding is integrated into the track reconstruction procedure [75], which the reader is referred to for all the relevant details.

6.2 Calorimeter Cell Energy Reconstruction

All the jet variables relevant to the analysis presented in this thesis are reconstructed using calorimeter cell information. The calorimeter cells are constructed from (amongst other materials) Uranium which produces a background signal from β decay. This background signal leads to an energy deposit which is referred

to as the noise of the cell. Only cells which contain energy deposits above some characteristic threshold are used in the subsequent reconstruction of the event. Such thresholds are determined from calibration procedures which are performed when no beams are inside the detector (between successive data runs). There can be other additional sources of noise in the calorimeter cells which originate from factors such as sparks and noise in the photomultiplier tubes or readout electronics. Noisy cells are removed from consideration using the NOISE02S routine [76]. From the beginning of ZEUS it has been noticed that the measured spectrum of electron energies in NC DIS ZEUS data is not well described by MC [77]. Studies have been performed under the main assumption that the discrepancy arises due to the absolute energy response of the calorimeter. The results of the study presented in [78] were used to correct the calorimeter energy scale of the data in the present analysis. Table 6.1 shows the correction factors that were applied to the calorimeter cells (data only). As can be seen from the table, different corrections were applied depending on the region of the calorimeter been considered and the type of calorimeter cell. These corrections were applied via the application of the ESCALE03 routine [79].

	EMC	HAC
FCAL	1.024	0.941
BCAL	1.053	1.096
RCAL	1.022	1.022

Table 6.1: Cell energy corrections used for the electromagnetic (EMC) and hadronic (HAC) cells in the forward (FCAL), barrel (BCAL) and rear (RCAL) calorimeters.

6.3 Definition of Jets

The corrected calorimeter cell energies and the cell positions (corrected for the position of the event vertex) are fed into a jet finding algorithm. The algorithm used to define jets in this analysis is the k_T algorithm which was described in section 2.7.1. It should be noted here that an additional jet finder, the cone algorithm, is used for the definition and selection of jets in the online software of the TLT. The Cone algorithm will not be discussed further here but the reader is referred to [23] for further details. The output of the jet finding algorithm are the reconstructed variables $E_{T,i}$, η_i and ϕ_i for each i^{th} reconstructed jet.

6.4 Electron Identification

The identification of electrons is important in the present analysis because it is used to discriminate between γp and DIS events. In DIS events the electron is scattered through a significant angle and for values of $Q^2 \gtrsim 1.0 \text{ GeV}^2$ a deposit is left in the RCAL¹. The identification of the scattered electron is important for the reconstruction of event kinematics. A number of different electron finders are available but in the present analysis the SINISTRA electron finder is employed. For details the reader is referred to [80].

6.5 The Reconstruction of y and Q^2

In this section, two methods, out of the many possible ways [81], of reconstructing y and Q^2 are discussed, the electron method and the Jacquet-Blondel method.

6.5.1 The Electron Method

The electron method is the first method used in the reconstruction of y and Q^2 . These variables are reconstructed from the energy and polar angle of the scattered electron, E'_e and θ_e respectively:

$$y_e = 1 - \frac{E'_e}{2E_e}(1 - \cos\theta_e) \text{ and} \quad (6.1)$$

$$Q_e^2 = 2E_e E'_e(1 + \cos\theta_e), \quad (6.2)$$

where E_e is the initial (beam) energy of the electron. Events for which no scattered electron is found in the calorimeter are used to define γp events. In such cases the electron is scattered down the beam pipe and is not recorded in the detector ($\theta_e \approx 180^\circ$). From equation 6.2 it can be seen that $Q_e^2 \rightarrow 0$ as $\theta_e \rightarrow 180^\circ$. Events in which the electron is scattered down the beam pipe of the ZEUS detector ² therefore correspond to low values of Q^2 . In this thesis (and indeed previous γp analyses) Q^2 is restricted to be less than 1 GeV^2 .

¹90% of DIS electrons are scattered into the RCAL.

²The electron is lost down the beam pipe if $\theta_e \gtrsim 177^\circ$ which roughly corresponds to $Q^2 < 1 \text{ GeV}^2$.

6.5.2 The Jacquet-Blondel Method

The electron method relies on the presence of an electron in the final state. However, in γp events, in which the scattered electron is lost down the beam pipe, an alternative method has to be used to reconstruct y . The Jacquet-Blondel method [82] uses the hadronic final state to reconstruct y . The reconstruction is performed by summing over all the final state particles except the scattered electron,

$$y_{JB} = \frac{\sum_i (E_i - p_{z,i})}{2E_e} . \quad (6.3)$$

In practise, the sum is performed over all calorimeter cells except those associated with the scattered electron. The SINISTRA routine, like other electron finding routines, is not 100% efficient and sometimes the energy deposit of the scattered electron can enter into the above equations which typically yields large values of $y_{JB} \approx 1$. By cutting out events characterised by high values of y_{JB} this DIS contamination can be removed from the γp sample. Just as in the case of jet finding, before the calorimeter cell information is used in the above equations, account must be taken of the position of the event vertex in calculating the various momentum components of each cell.

6.6 Reconstruction of Other Dijet Variables

Using the jet variables which are output from the jet finding algorithm, a number of dijet variables which are relevant to this thesis can be defined. We concern ourselves with events where there are at least two jets found. The leading transverse energy jet is denoted using a 1 subscript and the trailing jet by a 2 subscript so for example, $E_{T,1}$ denotes the transverse energy of the leading jet, ϕ_2 denotes the azimuthal angle of the trailing jet etc. Using these variables, along with the reconstructed electron variables, a number of dijet quantities can be defined. The variable x_γ^{obs} is related to the fraction of the photon's momentum carried by the struck parton from the photon, x_γ , and is given by

$$x_\gamma^{obs} = \frac{E_{T,1}e^{-\eta_1} + E_{T,2}e^{-\eta_2}}{2E_e y_{JB}} . \quad (6.4)$$

The variable x_p^{obs} is related to the fraction of the proton's momentum carried by the struck parton from the proton, x_p , and is given by

$$x_p^{obs} = \frac{E_{T,1}e^{\eta_1} + E_{T,2}e^{\eta_2}}{2E_p}. \quad (6.5)$$

The following additional variables can also be defined:

$$\bar{E}_T = \frac{E_{T,1} + E_{T,2}}{2}, \quad (6.6)$$

the mean transverse energy of the dijet,

$$\bar{\eta} = \frac{\eta_1 + \eta_2}{2}, \quad (6.7)$$

the mean pseudorapidity of the dijet and,

$$|\Delta\phi| = |\phi_1 - \phi_2|, \quad (6.8)$$

the absolute separation in ϕ of the jets.

6.7 Jet Energy Corrections

6.7.1 Jet Resolutions

The calorimeter and hadron level jet quantities deviate from one another due to energy losses in the dead material in front of the calorimeter, the finite resolution of the calorimeter and particles which do not deposit energy in the calorimeter, such as neutrinos. Monte Carlo³ simulated data can be used to account for these discrepancies.

To investigate the relationship between hadron and calorimeter level jets, jet finding is performed at both the hadron and calorimeter levels. Calorimeter and hadronic level jet quantities are denoted using the appropriate subscripts. A hadron jet is considered matched to a calorimeter level jet if the quantity

$$\Delta R(\eta, \phi) = \sqrt{(\eta^{Had} - \eta^{Cal})^2 + (\phi^{Had} - \phi^{Cal})^2}, \quad (6.9)$$

which is the separation of the pair in η - ϕ space, is a minimum and satisfies $\Delta R_{min}(\eta, \phi) < 1.0$. There is an additional constraint imposed that each calorimeter level jet must be matched to at most one hadron level jet. When a sample of matched jets has been obtained, jet variables at the hadron and

³PYTHIA MC is used for the resolutions and correction factors discussed in this section.

calorimeter level may be compared. The MC sample used to perform the jet resolutions study presented here (and to derive the energy corrections discussed in the next section) is defined as all events which contain at least one dijet where both jets satisfy $E_T^{Cal} > 10$ GeV and $-1 < \eta^{Cal} < 3$. Jet matching is then performed on all the jets in the event.

Figures 6.1 and 6.2 show the relationship between the quantities $(E_T^{Had} - E_T^{Cal})/E_T^{Cal}$, $\eta^{Had} - \eta^{Cal}$ and $\phi^{Had} - \phi^{Cal}$ with each of the quantities E_T^{Cal} , η^{Cal} and ϕ^{Cal} in turn. These figures help us to understand the possible correlations which exist between the hadron and calorimeter level jet variables.

There is a good correlation between ϕ^{Had} and ϕ^{Cal} for all values of the calorimeter level jet quantities, E_T^{Cal} , η^{Cal} and ϕ^{Cal} . There is also a good correlation between η^{Had} and η^{Cal} for most values of the calorimeter level jet quantities. The value of $\eta^{Had} - \eta^{Cal}$ increases steadily in the forward region of the detector which follows from the geometry of the detector but no attempt to correct this feature was made in the present analysis. The application of an η correction was investigated but did not significantly benefit the quality of the reconstruction. The fractional difference between the transverse energies of the hadron and calorimeter level jets shows a marked dependence on both E_T^{Cal} and η^{Cal} with a mean difference between the transverse energies of about 11.5% i.e. the calorimeter level jets tend to lose 11.5% of their true underlying hadron level transverse energy. This is corrected for using the method presented in the next section. As an additional point of interest it can be seen from figures 6.1 and 6.2 that the resolutions of all the jet quantities improves as E_T^{Cal} increases. Also, the resolution of the jet quantities tends to be poorer in the forward region of the detector.

6.7.2 Correction of the Jet Transverse Energies

From figure 6.1 it can be seen that the mean difference in transverse energy of a calorimeter level jet and its matched hadron level jet is a function of both the transverse energy, E_T^{Cal} , and pseudorapidity, η^{Cal} of the calorimeter level jet. One way of expressing this is as follows:

$$\left\langle \frac{E_T^{Had}}{E_T^{Cal}} \right\rangle = f(E_T^{Cal}, \eta^{Cal}), \quad (6.10)$$

where the angle brackets denote the mean of the enclosed quantity. The function $f(E_T^{Cal}, \eta^{Cal})$ is termed the jet energy correction function. The purpose of the

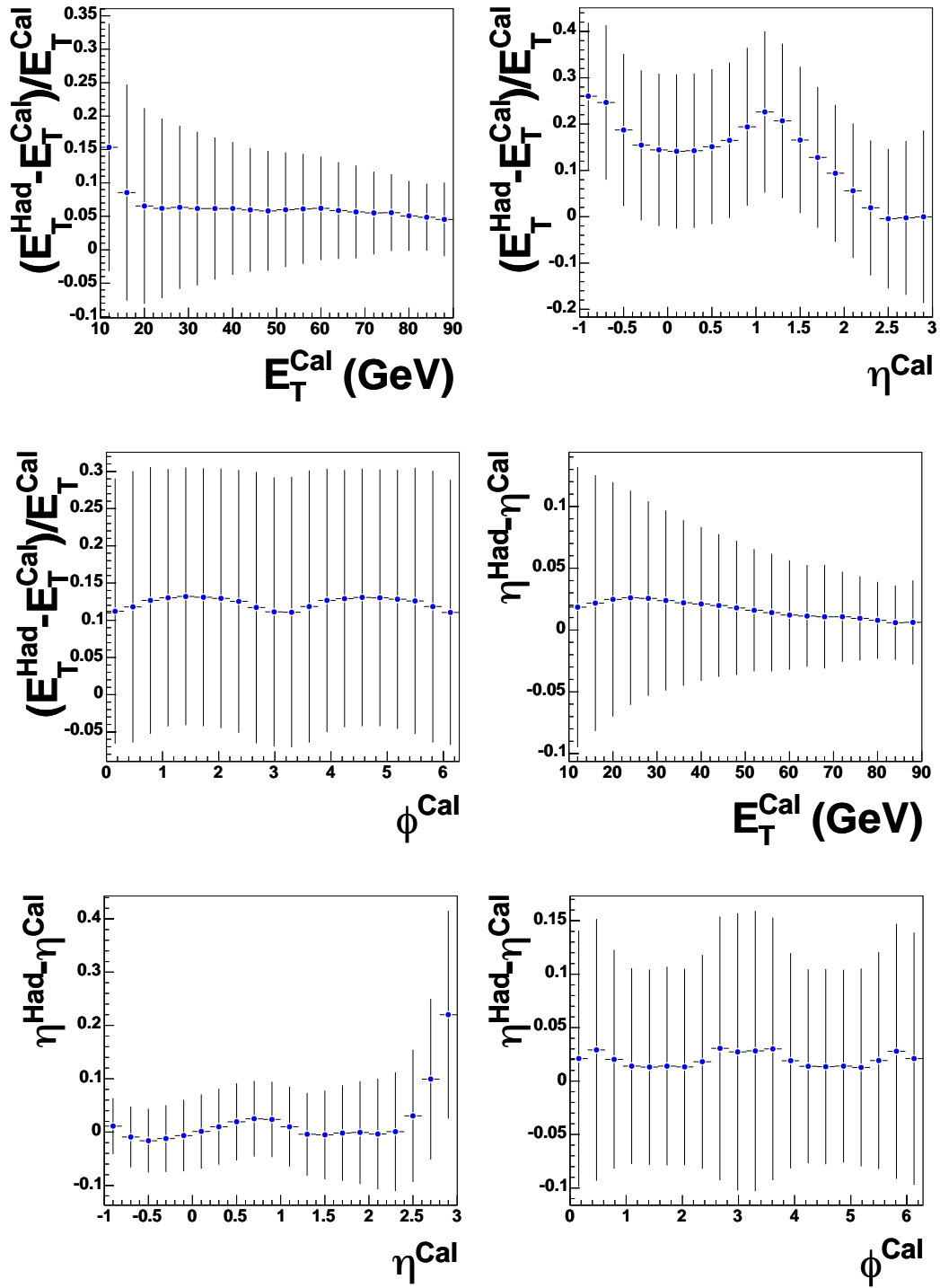


Figure 6.1: Various jet resolutions for calorimeter jets with $E_T^{\text{Cal}} > 10 \text{ GeV}$ and $-1 < \eta^{\text{Cal}} \leq 3$. The error bars represent the standard deviation of the relevant quantities in each bin.

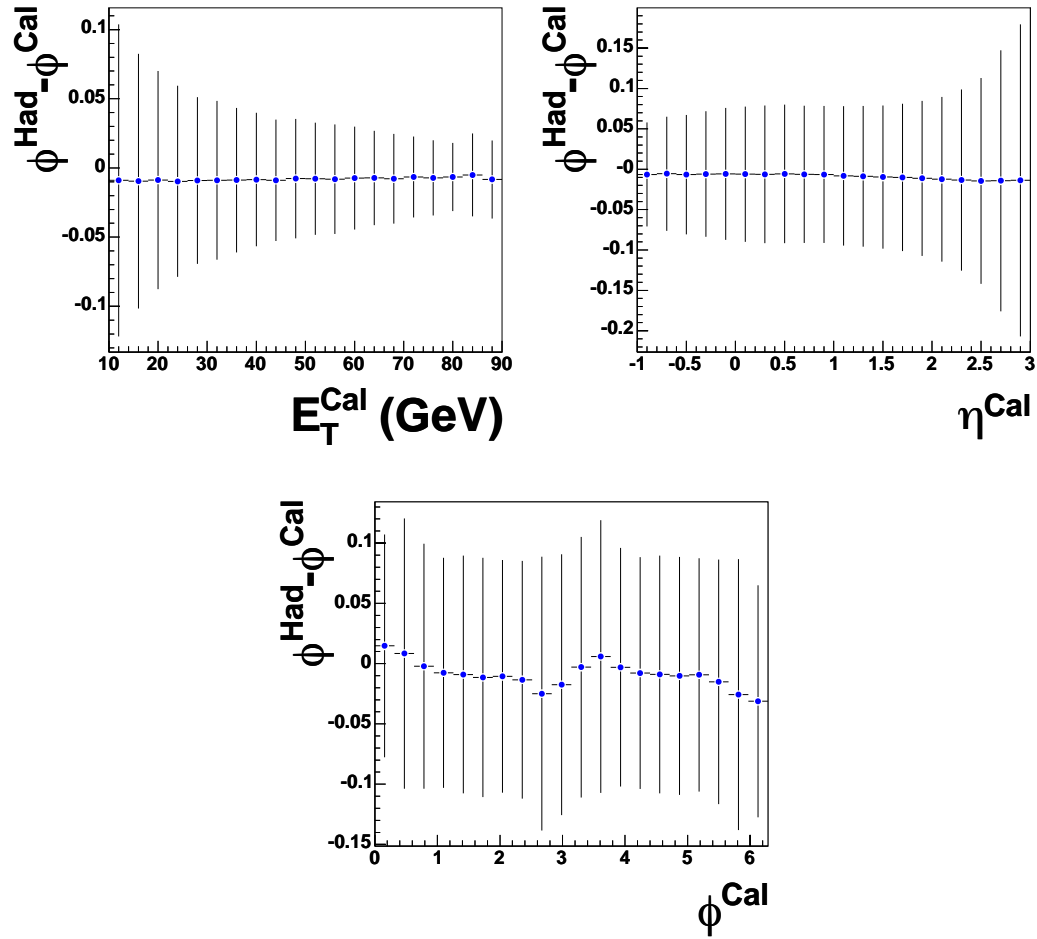


Figure 6.2: Various jet resolutions for calorimeter jets with $E_T^{\text{Cal}} > 10 \text{ GeV}$ and $-1 < \eta^{\text{Cal}} \leq 3$. The error bars represent the standard deviation of the relevant quantities in each bin

correction procedure is to correct the calorimeter level jets in such a way that the mean transverse energy of the calorimeter level jets is equal to the mean transverse energy of the hadron level jets so that

$$\left\langle \frac{E_T^{\text{Had}} - E_T^{\text{Corr}}}{E_T^{\text{Corr}}} \right\rangle = 0, \quad (6.11)$$

where

$$E_T^{\text{Corr}} = \alpha E_T^{\text{Cal}} \quad (6.12)$$

is the corrected calorimeter jet transverse energy with a correction factor of α applied. Substituting equation 6.12 into equation 6.11 gives

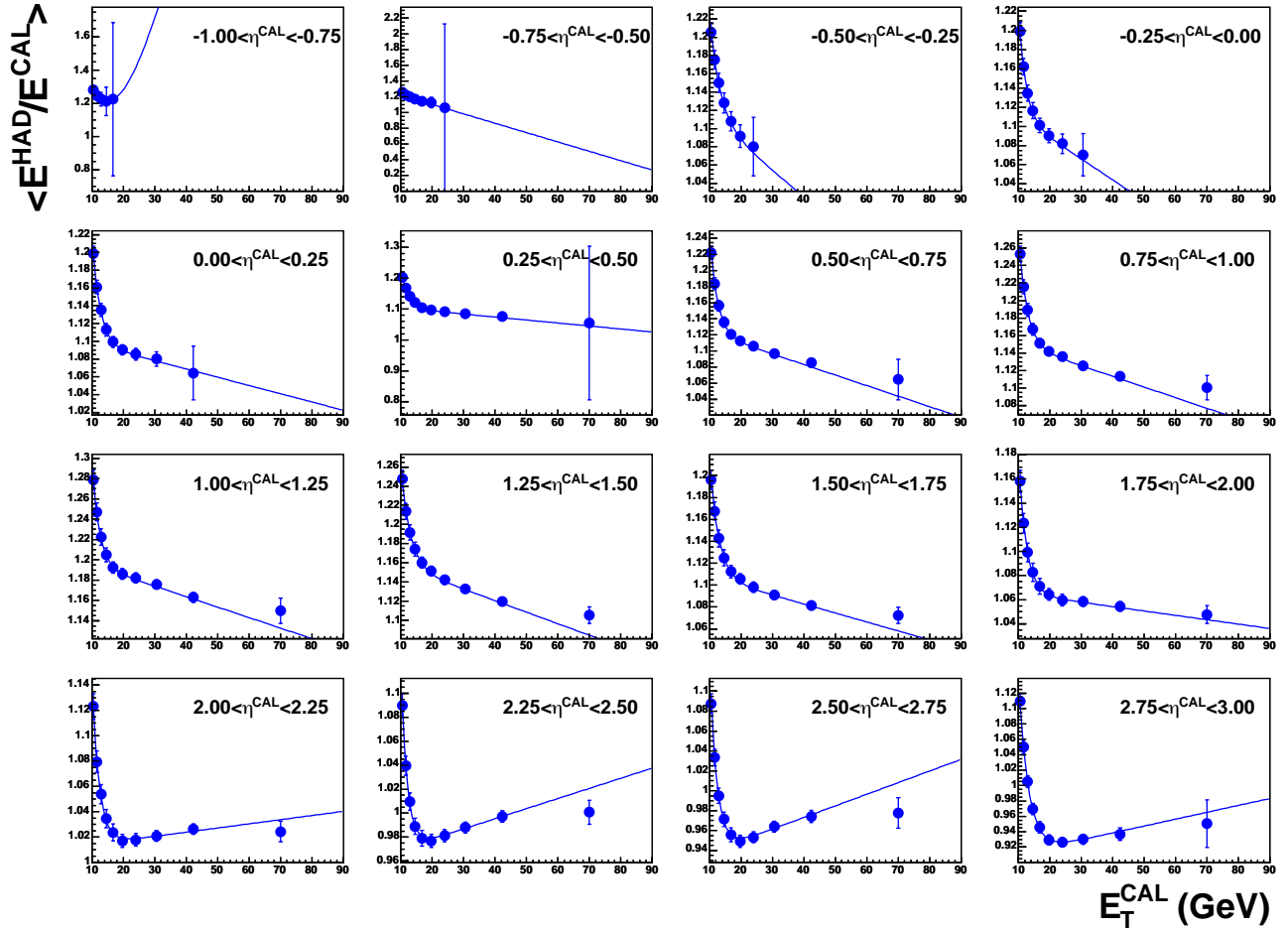


Figure 6.3: Jet transverse energy correction functions. The error shown is the statistical error on $\langle E_T^{HAD}/E_T^{CAL} \rangle$ in each bin.

$$\left\langle \frac{E_T^{HAD} - \alpha E_T^{CAL}}{\alpha E_T^{CAL}} \right\rangle = \left\langle \frac{E_T^{HAD}}{\alpha E_T^{CAL}} - 1 \right\rangle = \left\langle \frac{E_T^{HAD}}{\alpha E_T^{CAL}} \right\rangle - 1 = 0, \quad (6.13)$$

which can be solved to find α ,

$$\left\langle \frac{E_T^{HAD}}{\alpha E_T^{CAL}} \right\rangle = 1 \Rightarrow \frac{1}{\alpha} \left\langle \frac{E_T^{HAD}}{E_T^{CAL}} \right\rangle = 1 \Rightarrow \alpha = \left\langle \frac{E_T^{HAD}}{E_T^{CAL}} \right\rangle. \quad (6.14)$$

So we see that $\alpha = f(E_T^{CAL}, \eta^{CAL})$ and consequently

$$E_T^{Corr} = f(E_T^{CAL}, \eta^{CAL}) E_T^{CAL}. \quad (6.15)$$

Attention is now turned to the determination of the transverse energy correction function. To do this, $\langle E_T^{HAD}/E_T^{CAL} \rangle$ was plotted as a function of E_T^{CAL} in 16 uniform bins between $-1 < \eta^{CAL} < 3$. Within each region of η^{CAL} the relationship between $\langle E_T^{HAD}/E_T^{CAL} \rangle$ and E_T^{CAL} was parameterised as

i	η region	$p_{0,i}$	$p_{1,i}$	$p_{2,i}$	$p_{3,i}$
1	$-1.00 < \eta < -0.75$	-1.729	0.095	1.344	-0.062
2	$-0.75 < \eta < -0.50$	1.340	-0.012	3.421	-0.633
3	$-0.50 < \eta < -0.25$	1.142	-0.003	0.875	-0.309
4	$-0.25 < \eta < 0.00$	1.131	-0.002	2.246	-0.443
5	$0.00 < \eta < 0.25$	1.106	-0.001	1.887	-0.398
6	$0.25 < \eta < 0.50$	1.114	-0.001	1.703	-0.382
7	$0.50 < \eta < 0.75$	1.136	-0.001	2.068	-0.417
8	$0.75 < \eta < 1.00$	1.162	-0.001	1.707	-0.379
9	$1.00 < \eta < 1.25$	1.205	-0.001	2.175	-0.442
10	$1.25 < \eta < 1.50$	1.169	-0.001	1.122	-0.338
11	$1.50 < \eta < 1.75$	1.116	-0.001	1.201	-0.345
12	$1.75 < \eta < 2.00$	1.069	-0.000	1.828	-0.402
13	$2.00 < \eta < 2.25$	1.011	0.000	2.435	-0.444
14	$2.25 < \eta < 2.50$	0.962	0.001	3.265	-0.513
15	$2.50 < \eta < 2.75$	0.926	0.001	2.631	-0.432
16	$2.75 < \eta < 3.00$	0.903	0.001	1.761	-0.323

Table 6.2: Fitted parameters for the correction functions of figure 6.3

$$\left\langle \frac{E_T^{Had}}{E_T^{Cal}} \right\rangle = p_{0,i} + p_{1,i} E_T^{Cal} + e^{p_{2,i} + p_{3,i} E_T^{Cal}}, \quad (6.16)$$

for $i = \{1, 2, \dots, 16\}$ ($-1 + 0.25(i - 1) < \eta^{Cal} < -1 + 0.25i$). Figure 6.3 shows the results of this procedure along with the fitted correction functions obtained. The fitted parameters are shown in table 6.2.

The effectiveness of these correction factors is seen by applying them to the same MC sample that was used to derive the corrections (all events that contain a dijet where both jets satisfy $E_T^{Cal} > 10$ GeV and $-1 < \eta^{Cal} < 3$) and re-plotting the jet resolutions. The corrected resolutions are shown in figure 6.4. After the correction of the calorimeter level jets, the mean difference between the transverse energy of the hadron and calorimeter level jets is less than 1%. Also, the E_T^{Cal} and η^{Cal} dependence has been almost completely removed.

6.8 Energy Scale Uncertainty for Jets

One of the largest, if not dominant, sources of uncertainty on a measured cross-section is that which arises from the calorimeter energy scale uncertainty. Such uncertainty arises from the difference in the response of the calorimeter in MC

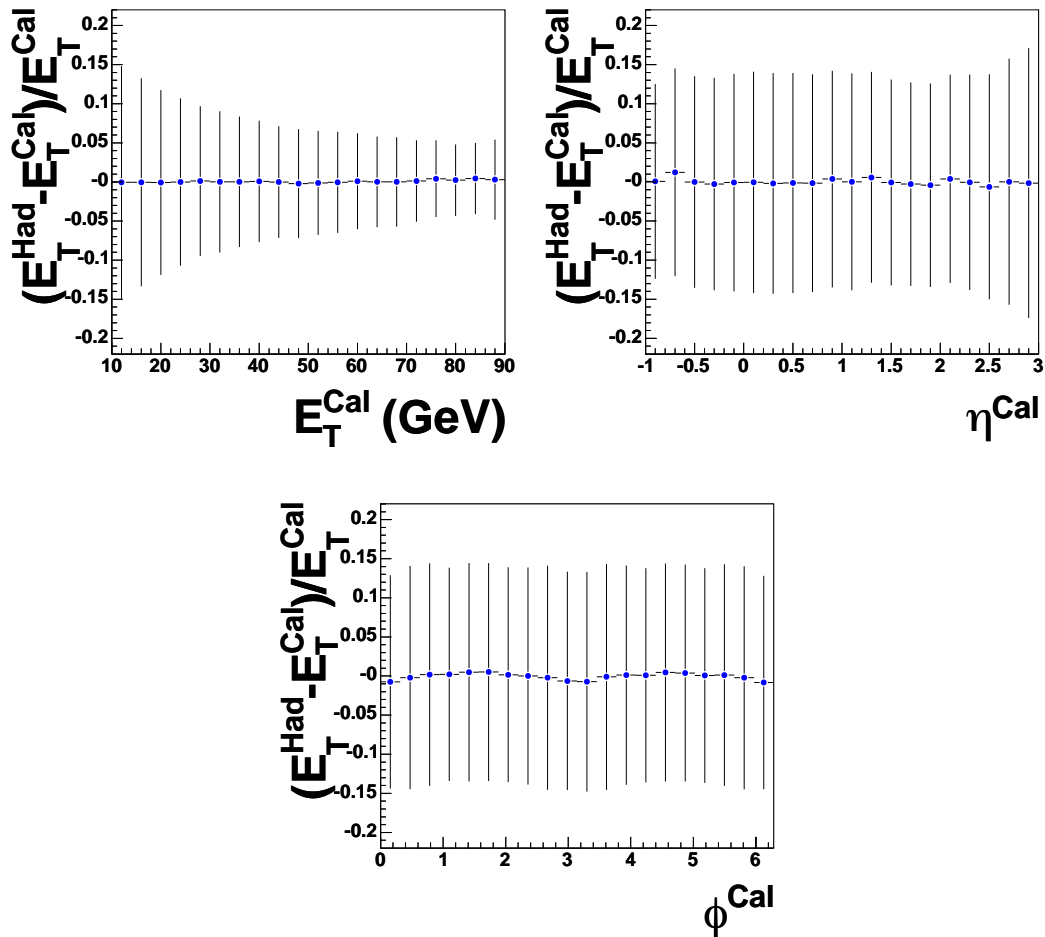


Figure 6.4: Jet resolutions, after the application of energy corrections, for calorimeter jets with $E_T^{Cal} > 10$ GeV and $-1 < \eta^{Cal} \leq 3$

and data. This was discussed earlier in the context of individual calorimeter cells where the correction factors in table 6.1 were applied to the calorimeter cell energy deposits, before jet-finding was performed, in order to correct for the differences in the energy scales between data and MC. However, the methods used in [78] attempt to model these differences for single electrons and differences in the calorimeter energy response for jets are not expected to match those for single electrons. How well do these cell corrections correct the energy scale differences between jets in MC and data? This was checked in [78] and a typical shift of $\pm 1\%$ was observed. This shift is termed the jet energy scale uncertainty and the corresponding uncertainty on the measured cross-section is derived by varying the energies in the data or MC (but not both) up and down by this amount. As will be seen later, a jet energy scale uncertainty of $\pm 1\%$ typically leads to

an uncertainty on the measured cross-section of the order of 5 – 10%. Thus, it is important that the jet energy scale uncertainty is known as accurately as possible and attempts are made to correct for it so that the differences between the energy scales in MC and data (and consequently the resulting uncertainty on the cross-section) are minimised. Numerous studies of the jet energy scale uncertainty have been made in the past and the generally accepted value for this uncertainty is $\pm 1\%$. But previous studies have not explored beyond an η of 2.5. As this analysis is also concerned with the region of η between 2.5 and 3.0 it was necessary to extend previous studies to the forward region of the detector.

The study of the jet energy scale uncertainty used in this thesis is modelled on those studies used in [78, 83, 84]. All the details of the study are omitted here but a comprehensive discussion is presented in Appendix E. The general method involves using a high Q^2 NC DIS sample of well isolated single jet events. In such events it is known that the p_T of the scattered electron should balance that of the jet. Using this fact, the energy scale differences between MC and data can be investigated. To summarise the results of the study, no additional correction to the energy scale of the jets is necessary beyond the calorimeter cell corrections presented in section 6.2. Furthermore, a jet energy scale uncertainty of $\pm 1\%$ is quoted for all jets in the range $-1 < \eta < 3$.

Chapter 7

Event Selection

This chapter will describe the criteria which are employed to select the data used for the analysis presented in this thesis. The selection consists of two principal parts: an online (trigger) selection and an offline selection. We discuss each of these selections in turn. The data, upon which the selection criteria is applied, is the ZEUS 98-00 data set (81.8 pb^{-1}) which is comprised of both e^-p data (16.7 pb^{-1}) and e^+p data (65.1 pb^{-1}). There were no significant changes in the experimental apparatus during this period and data taking was generally stable and well understood. It should be noted here that the ZEUS 96-97 data set was not included in this analysis. Although there is nothing technically complicated about its inclusion, doing so would have resulted in correlations, in the ZEUS QCD fit, between the cross-sections measured in this analysis and those 96-97 cross-sections already included in the fit. To avoid such correlations it was felt that it was best to restrict the measurement to just the 98-00 data set.

7.1 Trigger Selection

As discussed in section 1.7 the ZEUS experiment employs a three level trigger system which selects physics events online (in real-time as the data is being collected). The trigger system can be thought of as a complicated system of filters which are designed to filter out unwanted (background) events and select only the events which are of interest to the experimenter. With a bunch crossing occurring every 96 ns and assuming an interaction rate of once per bunch crossing then if every event that occurred in the ZEUS detector was written out to tape then over 10^7 events would have to be stored every second. Only about ~ 10 of these events are considered to be of interest. The ZEUS trigger system is designed to select these events and reject the remaining events that are not of interest.

7.1.1 First Level Trigger Selection

There are four slots¹ involved in the first level trigger (FLT) selection used in the present analysis. They are named FLT 40,41,42 and 43, and will be discussed below.

FLT 40 requires

- $E_{EMC}^{CAL} \geq 15$ GeV, where E_{EMC}^{CAL} is the total energy deposited in the EMC.
- **AND** The event is not rejected by veto counters which use timing measurements to classify events as background.

FLT 41 requires

- $E_T^{CAL} \geq 21$ GeV, where E_T^{CAL} is the total transverse energy deposited in the calorimeter.
- **AND** The event is not rejected by veto counters which use timing measurements to classify events as background.

FLT 42 requires

- $E^{CAL} \geq 15$ GeV or $E_{EMC}^{CAL} \geq 10.1$ GeV or $E_{EMC}^{BCAL} \geq 3.4$ GeV or $E_{EMC}^{RCAL} \geq 2.0$ GeV where E^{CAL} denotes the total energy deposited in the calorimeter, E_{EMC}^{BCAL} denotes the total energy deposited in the barrel part of the EMC and E_{EMC}^{RCAL} denotes the total energy deposited in the rear part of the EMC.
- **AND** At least one track is found with $-50 \text{ cms} < z_{vtx} < 80 \text{ cms}$ in the first superlayer of the CTD.
- **AND** The event is not rejected by veto counters which use timing measurements to classify events as background.

FLT 43 requires

- $E_T^{CAL} \geq 11.6$ GeV
- **AND** The event is not rejected by veto counters which use timing measurements to classify events as background.

It is required that at least one of these slots is passed.

¹A slot is an individual filter with its own set of selection criteria.

7.1.2 Second Level Trigger Selection

There are three slots involved in the second level trigger (SLT) selection. The three SLT slots are named SLT Hi- E_T 1, SLT Hi- E_T 3 and SLT Special, and are discussed below.

SLT Hi- E_T 1 requires

- A vertex to be found satisfying $|z_{vtx}| < 60$ cms.
- **AND** At least one track associated with the vertex.
- **AND** $\sum_i (E_i - p_{z,i}) > 8$ GeV, where the sum is over all the calorimeter cells.
- **AND** $E_T^{cone} > 8$ GeV, where E_T^{cone} is the summed transverse energy (over all calorimeter cells), excluding the inner ring of the FCAL.
- **AND** If $\sum_i (E_i - p_{z,i}) < 12$ GeV then $(\sum_i p_{z,i})/(\sum_i E_i) < 0.95$.

SLT Hi- E_T 3 is the same as SLT Hi- E_T 1 except for the additional requirements that

- $N_{EMC}^{CAL} > 0$, where N_{EMC}^{CAL} is the number of calorimeter SLT EMC clusters with energy greater than 0.7 GeV.
- $N_{trks}^{vtx}/N_{trks} > N$, where N_{trks}^{vtx} is the number of vertex matched tracks, N_{trks} is the total number of tracks and N is a function of the total number of tracks (see [89]).

SLT Special is the same as SLT Hi- E_T 1 except for some additional requirements for certain FLT slots to be passed (see [89]).

It is required that at least one of these slots is passed. In addition to the requirements above, there are certain timing requirements which have to be satisfied at the SLT level. The timing of the ZEUS components is synchronised in such a way that interactions which occur at the nominal interaction point are measured at $t = 0$. Events are detected in the FCAL, BCAL and RCAL at times t_{FCAL}, t_{BCAL} and t_{RCAL} respectively. The requirements on the timing of events at the SLT level are given below

- $t_{BCAL}^{lower} - t_{BCAL}^{upper} > 10$ ns, where t_{BCAL}^{lower} and t_{BCAL}^{upper} are the timings of the lower and upper halves of the BCAL respectively. This requirement is designed to reject cosmic muons entering the detector from above.
- $t_{FCAL} - t_{RCAL} > 8$ ns, which is designed to reject proton beam gas interactions.
- $t_{RCAL} > 8$ ns or $t_{FCAL} > 8$ ns

7.1.3 Third Level Trigger Selection

At the third level trigger (TLT) the full event information from all components is available to support the decision making process. The event is fully reconstructed and appropriate physics variables are calculated. In particular, at the TLT, a modified version of the EUCELL [23] jet finding algorithm is applied in order to identify events containing jets. In this analysis the inclusive jet TLT slot (HPP02 or DST65) is used. Details are given below.

TLT HPP02 (DST65) requires

- At least one jet is found satisfying $E_T > 10$ GeV and $\eta < 2.5$.
- The event has a vertex satisfying $|z_{vtx}| < 60$ cms
- $\sum_i (E_i - p_{z,i}) < 75$ GeV
- The number of bad tracks is less than 6 where a bad track is defined as a track which fails to satisfy the following criteria

The number of degrees of freedom of the track exceeds 20

AND $P_T \geq 0.2$ GeV

AND $0.35 < \eta < 3.13$

AND Number of CTD axial hits exceeds 5

AND Number of CTD stereo hits exceeds 5

AND z at distance of closest approach (to the vertex) is less than -75 cms.

It is required that this slot is passed.

7.2 Offline Event Selection

In addition to the online selection discussed, an additional set of selection criteria is applied to the data to optimise the reduction of non- γp events in the sample. The various offline selection cuts are discussed in this section and follow from those used in previous γp dijet measurements (see, for example, [51]).

- To minimise the contribution from beam-gas and cosmic muon events a tighter vertex cut of $|z_{vtx}| < 40$ cm was applied. The motivation for this cut is based on the z-vertex distribution as shown in figure 7.1. The simulation of the Monte Carlo z-vertex distribution contains information from the experimentally measured vertex distribution for the given year and compares well with the vertex distribution from data. The distribution is well fitted by a gaussian plus a constant. The width of the gaussian is about 12 cm. The distribution starts to deviate from a pure gaussian at about $\pm 30 \sim 35$ cm. The cut of ± 40 cm ensures that more than 3σ of the distribution coming from nominal ep physics is contained in the selected region, while keeping non- ep background events out of the sample.
- As discussed in [91], a discrepancy in the distribution of the ratio of tracks fitted to the primary vertex over all tracks found in an event between data and MC exists. This can be seen in figure 7.1. The origin of this discrepancy is the existence of a large number of ghost tracks in the data. A cut of $N_{trks}^{vtx}/N_{trks} > 0.1$ was imposed, where N_{trks} is the number of tracks in the event and N_{trks}^{vtx} is the number of primary vertex fitted tracks, in order to remove events where the tracks are dominated by ghost tracks.
- Events are classed as γp in two ways. Firstly, if no positron was found in the event then the event was classed as γp (subject to the constraint on y_{JB} discussed below). Secondly, if a positron with an energy of $E'_e > 5$ GeV and $y_e > 0.7$ was found in the final state then it is classed as a misidentified positron and the event was accepted as γp . For all other events containing a positron the event was rejected. The justification for this cut comes from figure 7.1 where good agreement between data and the photoproduction Monte Carlo is found for values above approximately 0.7. At lower values of y_e the NC DIS events dominate. The photoproduction events tend to have a high value of y_e peaking at 1.

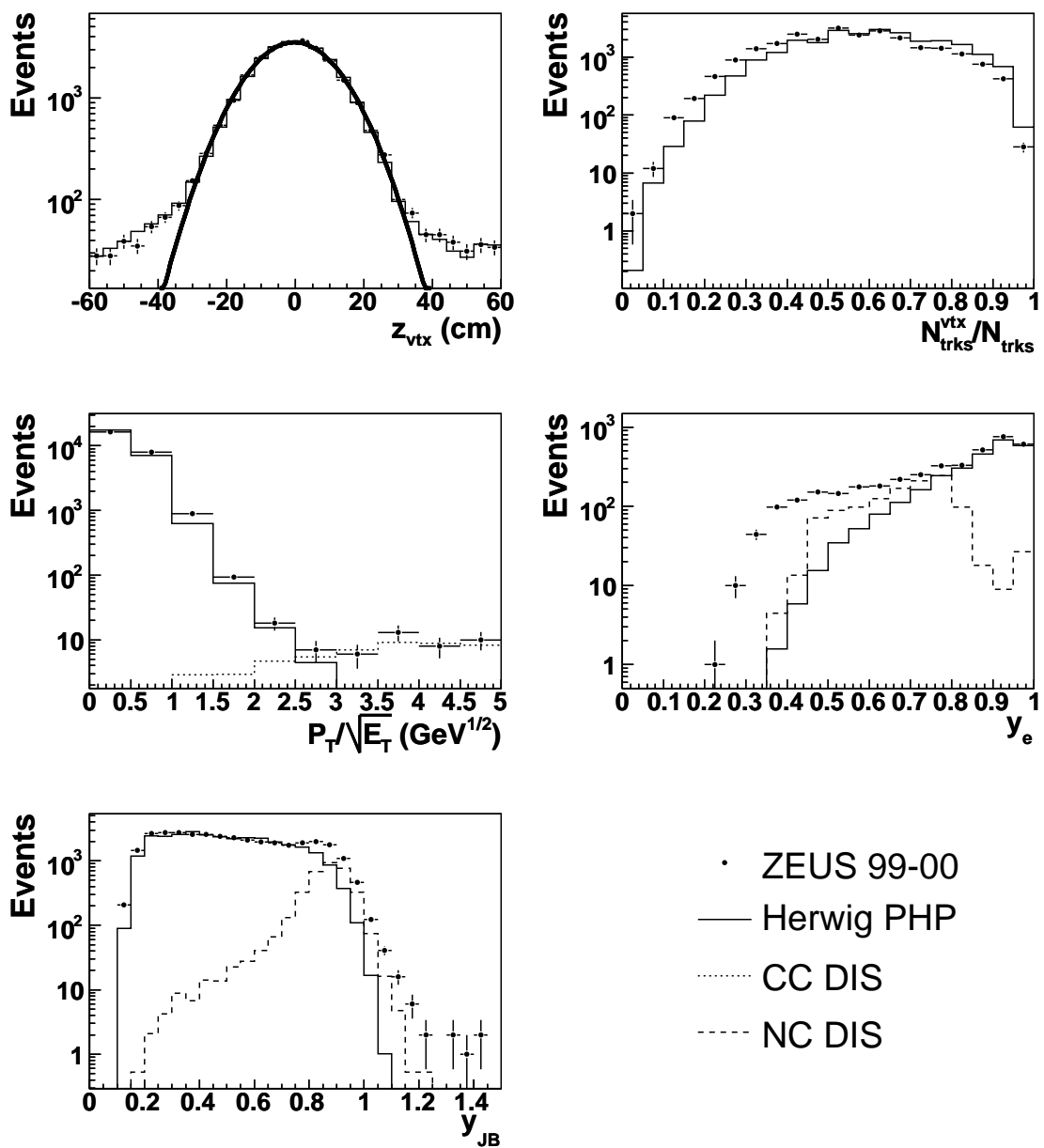


Figure 7.1: Comparison of various distributions as seen in data (99-00) and Monte Carlo (Herwig)

- To reject NC DIS events without a reconstructed electron in the final state, a cut on the variable y_{JB} was applied. Shown in figure 7.1 are the distributions for data, photoproduction and NC DIS Monte Carlos for y_{JB} . A cut on y_{JB} of $0.15 < y_{JB} < 0.7$ was imposed. The lower cut on y_{JB} was designed to reject beam-gas events where as the upper cut was designed to reduce the contribution from NC-DIS events which peak at about 1 for these events. The implementation of these cuts places a constraint on the virtuality of the exchanged photon $Q^2 < 1 \text{ GeV}^2$.
- CC DIS events are rejected by considering the missing transverse momentum, \cancel{P}_T , carried away by the undetected neutrino (see figure 7.1). Events were rejected as CC DIS if $\frac{\cancel{P}_T}{\sqrt{E_T}} > 1.5 \text{ GeV}^{0.5}$. The missing transverse energy was scaled with the square root of the sum of the deposited transverse energy to take into account the energy resolution of the calorimeter.

7.3 Subsample selection

Having selected a sample of γp events the following cuts were applied to select the subsample of events to be used for analysis.

- After application of the jet energy corrections detailed in section 6.7 events were selected for analysis by requiring the presence of two jets with $E_{T,1} > 20 \text{ GeV}$ and $E_{T,2} > 15 \text{ GeV}$.
- The two jets fulfilling the above E_T requirements were required to have pseudorapidities in the range of -1 to 3 with at least one of the jets lying in the range -1 to 2.5 .

After the online, offline and subsample selections had been carried out, a total of 31,203 events remained for analysis. From the above Monte Carlo studies there is a $< 1\%$ contribution from NC DIS events and a $< 0.1\%$ from CC DIS events.

7.4 Trigger Efficiencies

The trigger efficiency was studied using a sample of PYTHIA MC events. The efficiency of the trigger is defined as the proportion of events which pass the hadron level cross-section cuts (as defined in section 5.4) that are accepted by the

trigger. Of particular concern in this analysis is the trigger efficiency as a function of η_1 and η_2 , the pseudorapidity of the leading and trailing jets respectively. Chapter 5 illustrated the need to make confined measurements in the forward region of the ZEUS detector. Such measurements show considerable sensitivity to the uncertainties of the underlying gluon PDF. However, trigger restraints limit our ability to make such measurements.

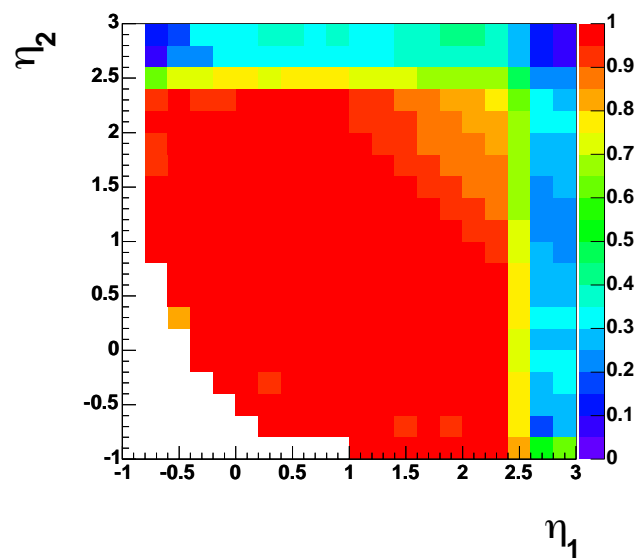
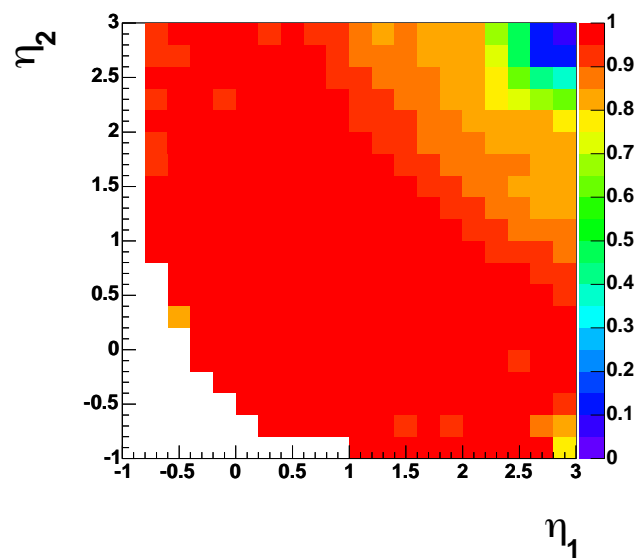
Previous γp dijet measurements, performed by the ZEUS collaboration, have utilised the specialised dijet triggers at the TLT, for example HPP14, the low- E_T dijet trigger. This trigger accepts events which contain at least two jets which satisfy $E_{T,1}, E_{T,2} > 4 \text{ GeV}$ (4.5 GeV from June 1999) and $\eta_1, \eta_2 < 2.5$. Therefore, using this trigger does not allow any dijet measurement to be made for $\eta > 2.5$. The inclusive jet trigger, HPP02, which was discussed in the previous section is not quite as restrictive as the low- E_T dijet trigger because it only has a single jet requirement. This jet has to satisfy $\eta < 2.5$ but the second jet which makes up a particular dijet is able to lie anywhere. The use of the inclusive jet trigger is the best that can be done if one wishes to make forward γp dijet measurements. No trigger exists which allows one to select dijet events where both jets satisfy $\eta > 2.5$ ². The preceding discussion is illustrated in figures 7.2(a) and 7.2(b) which show the trigger efficiency in the η_1 - η_2 plane for the low- E_T dijet and inclusive jet triggers respectively. Within the relevant η ranges the trigger efficiencies are very good.

Figure 7.3 shows the trigger efficiencies at the FLT, SLT and TLT levels separately, for distributions of η_2 and $E_{T,1}$ at both high and low x_γ^{obs} . Once again the trigger efficiencies are very good and tend to lie well above 90%.

The trigger efficiency, as defined above, is not defined for the data. To see how well the trigger efficiencies in the data are modelled by the MC it is necessary to define the trigger efficiency in an alternative way. A sample of events was chosen which satisfied the FLT and SLT criteria of section 7.1, the offline selection criteria of section 7.2, the subsample selection criteria of section 7.3 and the criteria of an independent TLT slot. The chosen slot was HPP01, the so-called High- E_T trigger, defined below.

TLT HPP01 (DST64) requires

²The η limit of the low- E_T dijet trigger has been increased to 3 for new ZEUS data, at the request of the author.

(a) HPP14 low- E_T dijet trigger slot

(b) HPP02 inclusive jet trigger slot

Figure 7.2: Trigger efficiencies in the η_1 - η_2 plane for (a) the HPP14 low- E_T dijet slot and (b) the HPP02 inclusive jet slot

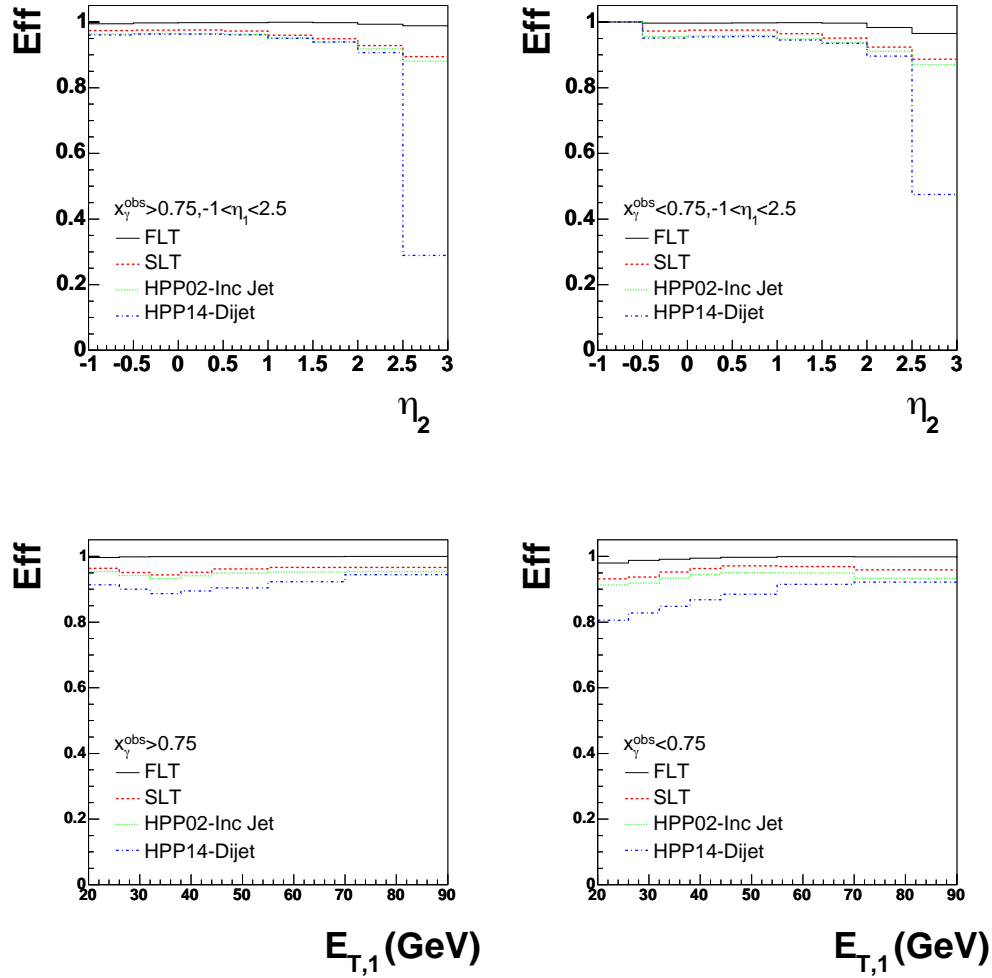


Figure 7.3: Trigger efficiencies at the FLT, SLT and TLT levels for distributions of $E_{T,1}$ and η_2 at both low and high- x_γ^{obs}

- $E_T^{cone} > 25 \text{ GeV}$, where E_T^{cone} is the summed transverse energy (over all calorimeter cells), excluding the inner ring of the FCAL.
- $\sum_i (E_i - p_{z,i}) > 8 \text{ GeV}$
- $\frac{\sum_i p_{z,i}}{\sum_i E_i} < 0.95$ or $\sum_i (E_i - p_{z,i}) > 12 \text{ GeV}$

The trigger efficiency was then defined as the proportion of events which pass the above selection that are accepted by the inclusive jet (HPP02) trigger slot (the trigger used as part of the present analysis). This quantity can be calculated in both data and MC and can be used to see how well the MC describes the trigger efficiencies in the data. The resulting comparison is shown in figure 7.4. The description of the data trigger efficiencies is generally good. Most of the efficiencies are close to 100% and the largest discrepancy between data and MC (the most forward bin of η_2 at low- x_γ^{obs}) is only of the order of 0.4%.

7.5 Monte Carlo Description of Data

This section looks at the description of the data by the PYTHIA and HERWIG MC models. The MC events used in the present analysis, along with the parameters used to generate them, were described in chapter 3.

7.5.1 Weighting the MC

In the present analysis, MC events were weighted in two ways. Firstly, high- E_T dijet MC events were combined with low- E_T dijet MC events by weighting the high- E_T events with respect to the luminosities of the two respective samples. All in all, five regions of E_T were considered. These regions were illustrated in tables 3.1 and 3.2 from which the relevant luminosity weighting factors can be calculated. The purpose of this treatment of the MC is to produce acceptance corrections which are statistically accurate at high transverse energies (where statistics would otherwise be poor).

As discussed in chapter 2, γp interactions consist of two distinct processes, direct and resolved. These processes are generated separately by both PYTHIA and HERWIG and so the second method of weighting the MC involves weighting the direct and resolved components in a suitable manner. The method chosen in the present analysis is outlined below.

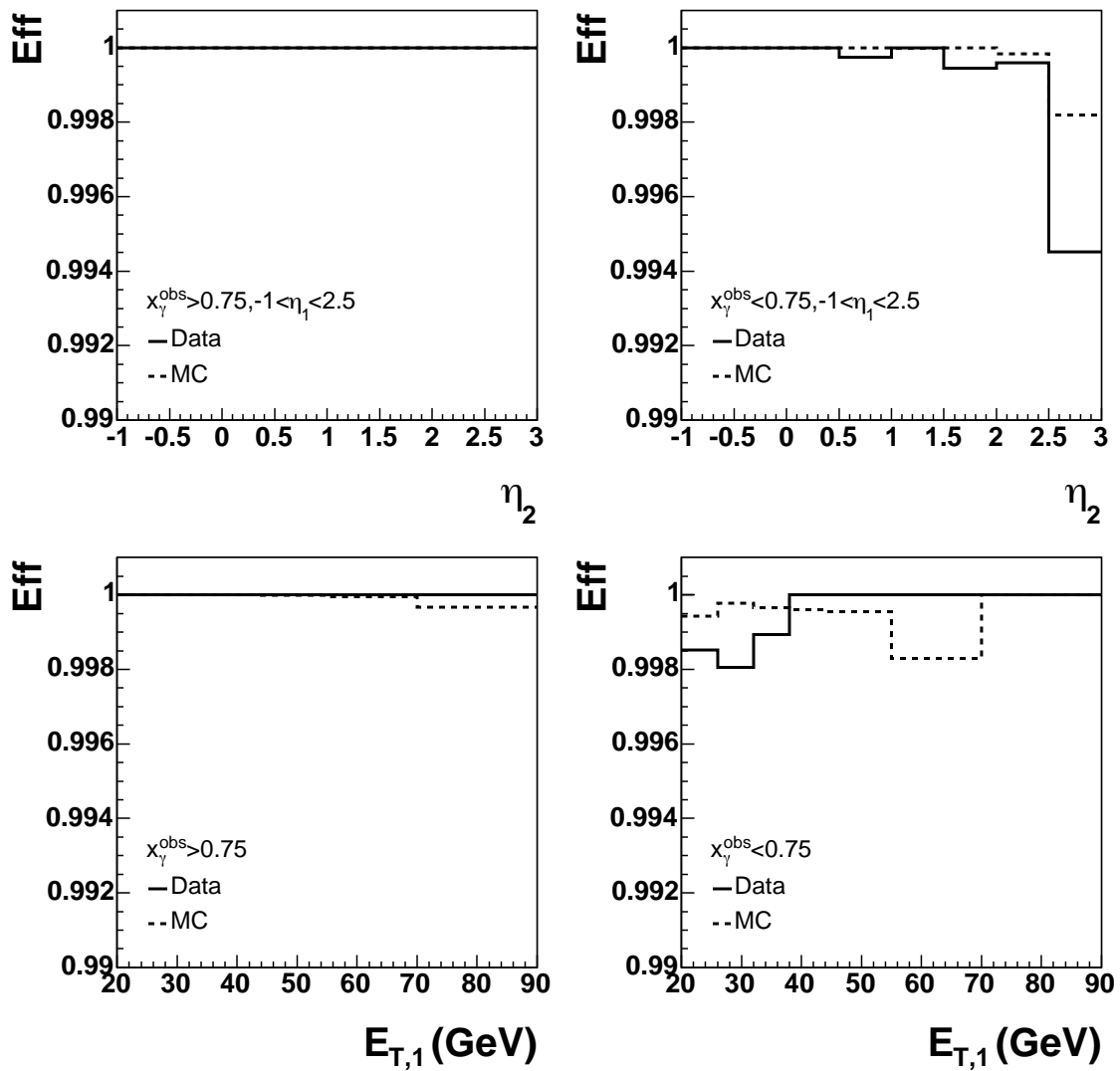


Figure 7.4: Comparison between data and MC trigger efficiencies for distributions of $E_{T,1}$ and η_2 at both low and high- x_γ^{obs}

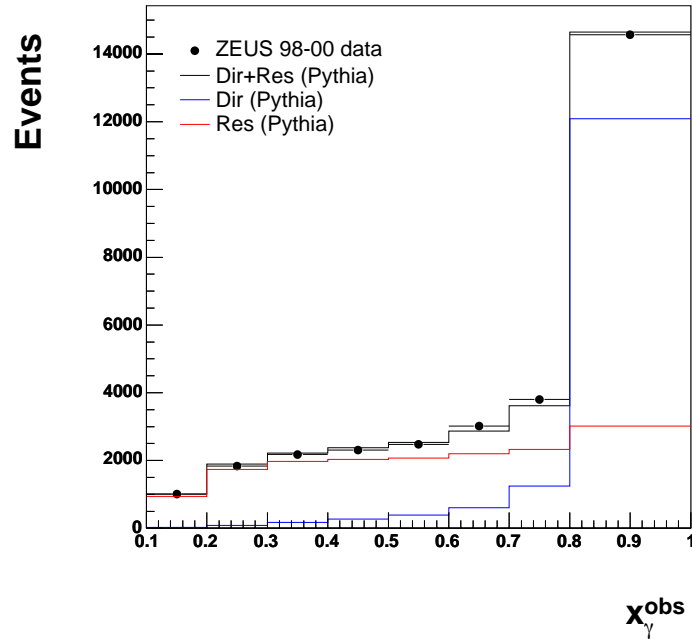


Figure 7.5: The result of fitting the direct and resolved PYTHIA MC x_γ^{obs} distributions to the corresponding data distribution. A direct weight of 0.48 and a resolved weight of 0.52 have been used

- All data and MC events passing the online, offline and subsample selections, presented in this chapter, are considered.
- An x_γ^{obs} distribution is plotted for each of data, direct MC and resolved MC.
- The direct and resolved MC distributions are normalised to the number of data events.
- The direct MC is weighted by a factor α , where $0 < \alpha < 1$, and the resolved MC is weighted by a factor of $1 - \alpha$. The parameter, α is chosen such that the description of the data by the combined MC samples is optimised. This parameter is determined by a fit of the MC distributions to the data using MINUIT [57].

The results of this process are shown, for the case of PYTHIA, in figure 7.6. The PYTHIA and HERWIG direct and resolved weights that are obtained using the above method are shown in table 7.1.

	Direct	Resolved
PYTHIA	0.48	0.52
HERWIG	0.58	0.42

Table 7.1: PYTHIA and HERWIG direct and resolved MC weights

It was mentioned at the end of chapter 5 that the original plans for the present analysis involved using transverse energy cuts of $E_{T,1} > 15$ GeV and $E_{T,2} > 10$ GeV. Figure 7.6 shows the x_γ^{obs} control plot (data-MC comparison plot) with these lower transverse energy cuts. There is a poorer description of the data by the MC in the resolved enriched region ($x_\gamma^{obs} \leq 0.75$). This corresponds to more forward regions of the detector. Analyses have been performed with transverse energy cuts as low (and indeed lower) than $E_{T,1} > 15$ GeV and $E_{T,2} > 10$ GeV but none have gone as far forward in η as the present analysis. Although a lower E_T analysis is not completely unfeasible in the present case, as the description is far from woeful, it was felt that the poorer description of the data by the MC would lead to higher systematic errors on any subsequent cross-section measurement. As one of the objectives of the present analysis is to make as accurate measurements as possible it was decided to increase the transverse energy requirements so that regions of phase space which were well described by MC were being dealt with.

7.5.2 Control Plots

In this section, the main dijet distributions derived from the data are compared with those derived from the MC. The data and MC events considered are those passing the online, offline and subsample selections, presented earlier in the chapter.

Figures 7.7 and 7.8 show the comparison between data and MC for an assortment of dijet kinematic variables relevant to the present analysis. Both MC programs describe the data reasonably well for all variables. A notable exception is the description of η_1 in the region $1.0 < \eta_1 < 1.5$ which is rather poor. This region corresponds to the boundary between the BCAL and FCAL (the so-called crack region) which is known to be poorly described. The poor statistics of the HERWIG sample at high- E_T are due to the fact that only one sample of HERWIG MC was generated (events were not generated in different regions of jet transverse energy as was the case for PYTHIA). In this analysis PYTHIA was chosen to

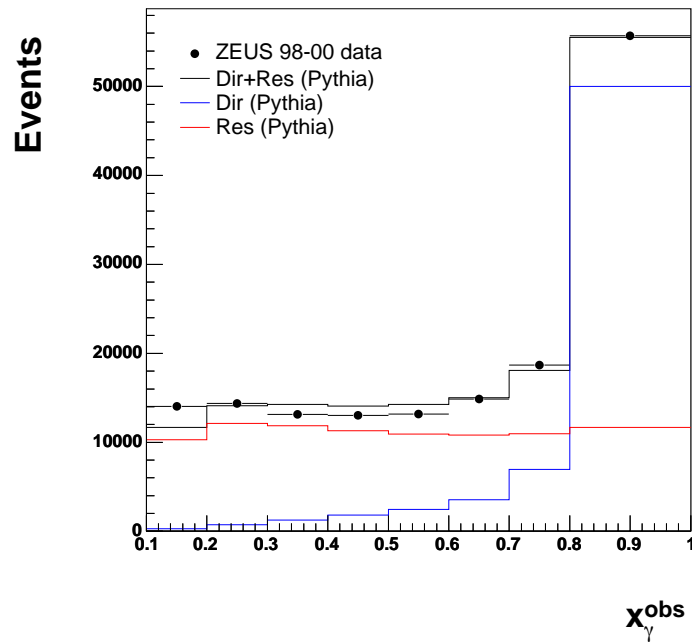


Figure 7.6: The result of fitting the direct and resolved PYTHIA MC x_γ^{obs} distributions to the corresponding data distribution with transverse energy cuts of $E_{T,1} > 15$ GeV and $E_{T,2} > 10$ GeV

correct the data (jet E_T corrections, acceptance corrections etc) with HERWIG used as a systematic check.

7.5.3 Underlying event

Previous dijet analyses conducted at lower transverse energy [73] have shown that the comparison between data and Monte Carlo distributions is sensitive to the model used for the underlying event. This is illustrated in figure 7.9. In particular the underlying event may have an influence on resolved interactions. In the present analysis, due to the high transverse energy cuts and the fact that the MC (which has been generated with out multiparton interactions included) describes the data, it is assumed that the effects of the underlying event are negligible.

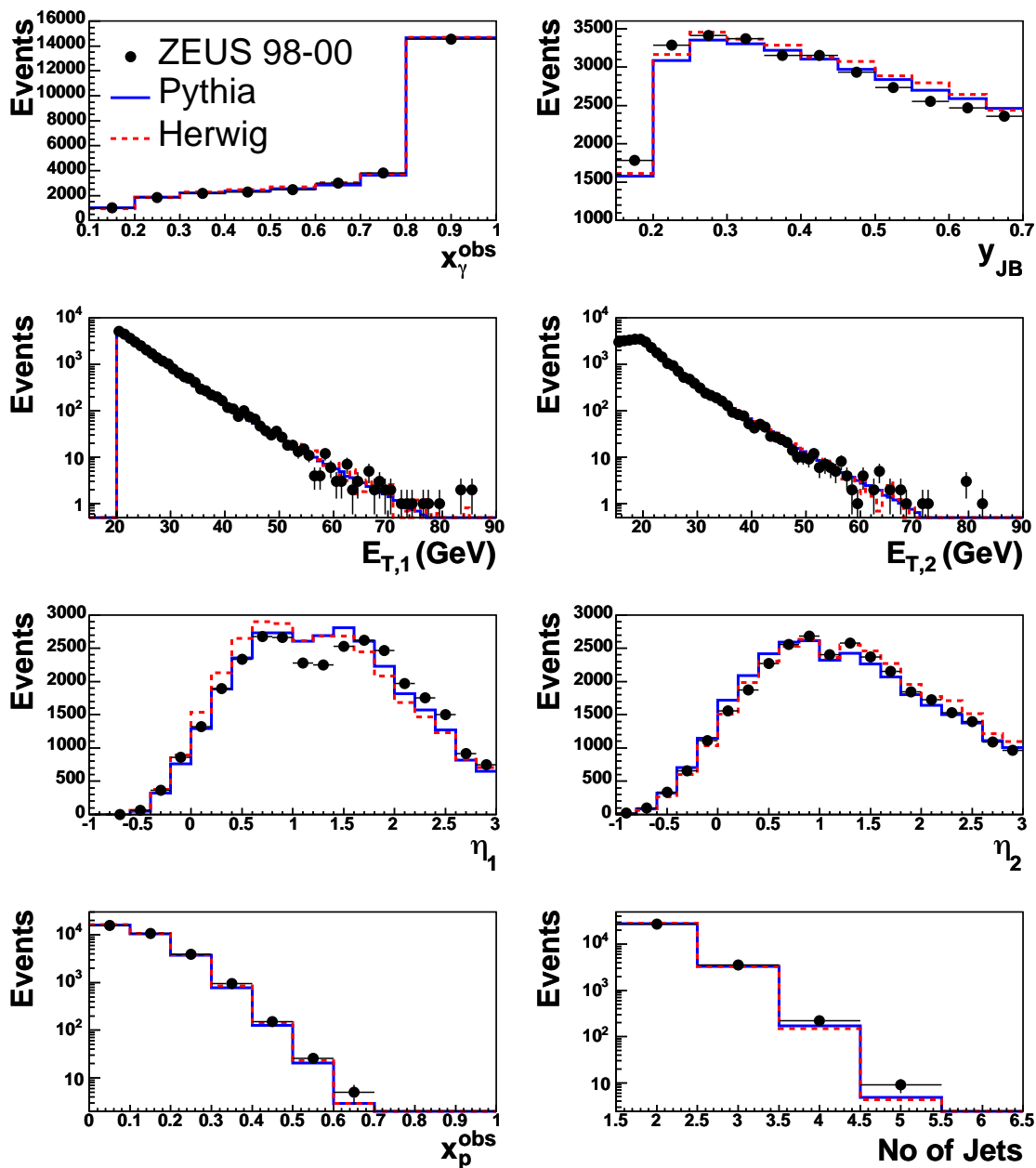


Figure 7.7: Comparison of data and PYTHIA and HERWIG MC for various dijet distributions. The direct and resolved MC distributions are normalised to the data and combined according to the values in table 7.1.

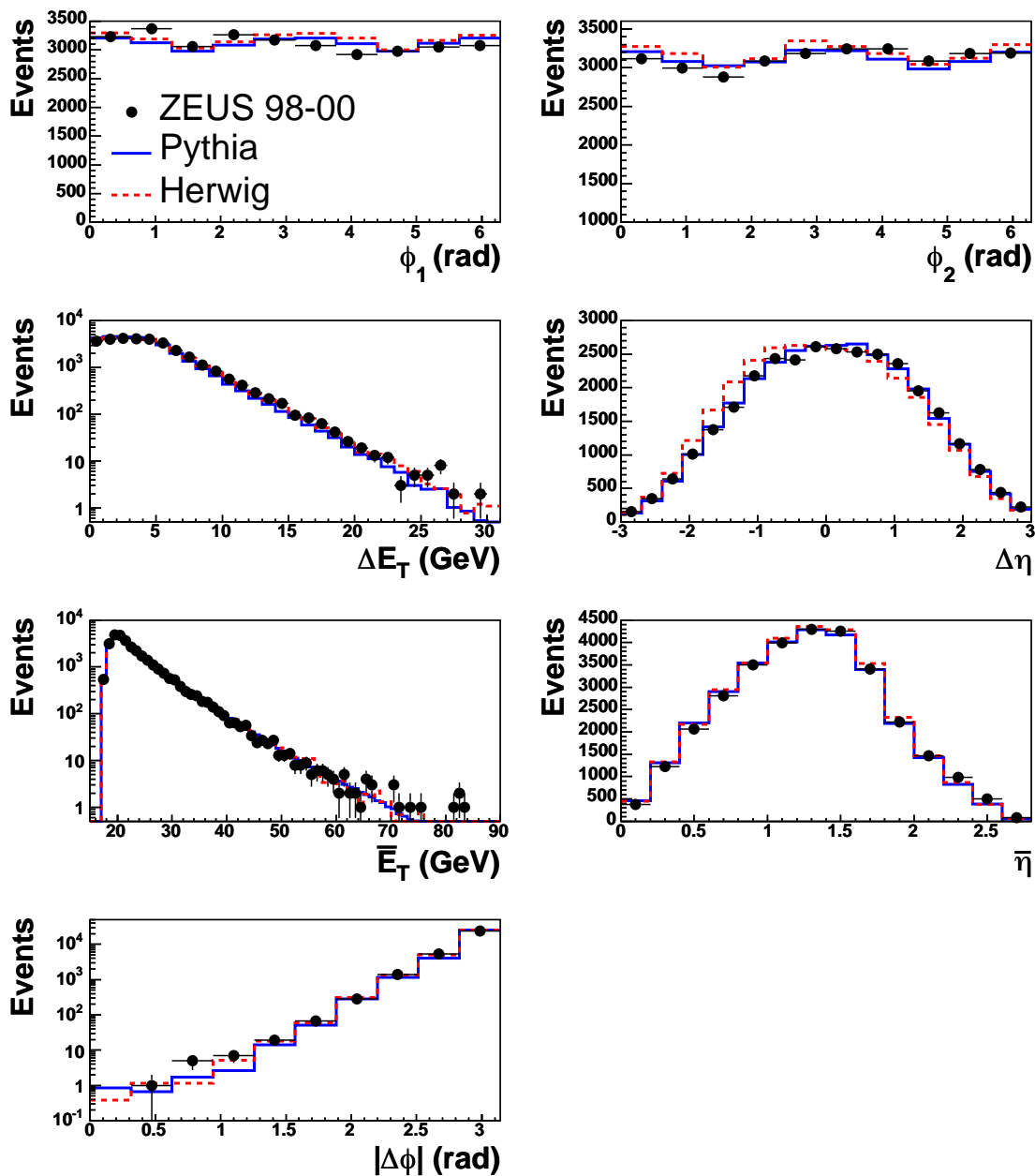


Figure 7.8: Comparison of data and PYTHIA and HERWIG MC for various dijet distributions. The direct and resolved MC distributions are normalised to the data and combined according to the values in table 7.1.

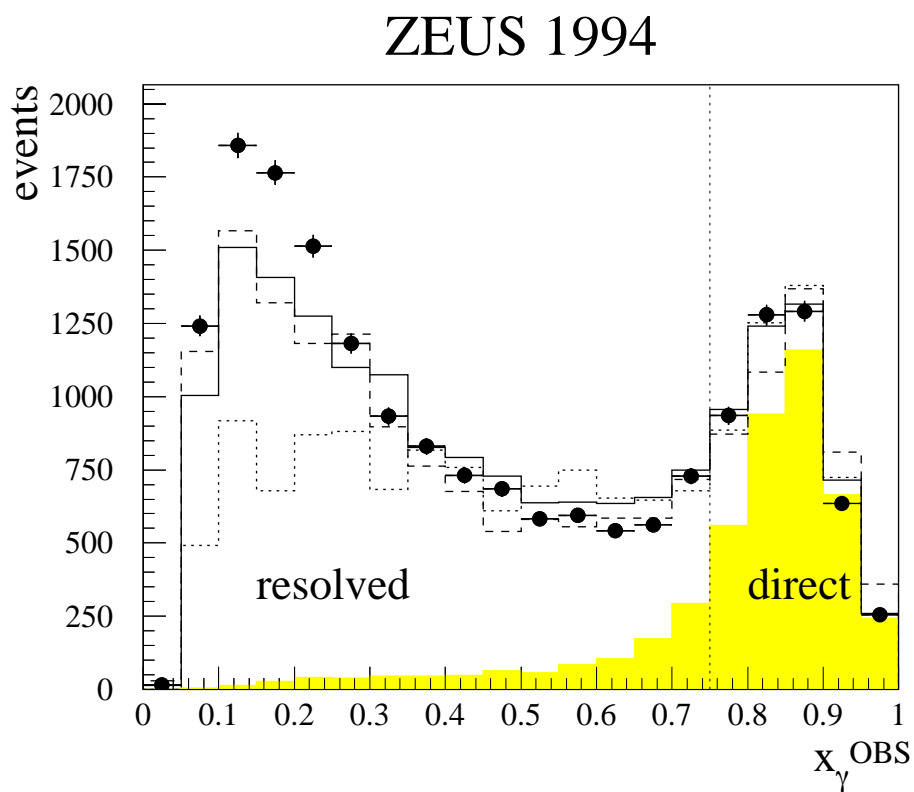


Figure 7.9: x_γ^{obs} distribution for jets with $E_T > 6$ GeV, $-1.375 < \eta < 1.875$ and $|\Delta\eta| < 0.5$. The ZEUS 1994 data (black dots) are compared to the results of the HERWIG with multiparton interactions (MI, solid line) and without (dotted line) and PYTHIA with MI (dashed line). Figure taken from [73].

Variable	μ	σ
E_T	0.017	0.105
η	0.009	0.048
ϕ	-0.008	0.051
$E_{T,1}$	-0.014	0.088
η_1	0.009	0.044
ϕ_1	-0.008	0.048
$E_{T,2}$	0.054	0.115
η_2	0.009	0.052
ϕ_2	-0.008	0.055
x_γ^{obs}	-0.020	0.053
x_p^{obs}	0.010	0.010
\bar{E}_T	0.017	0.079
$\bar{\eta}$	0.012	0.039
y_{JB}	0.070	0.060
$y_{JB} : 0.15 < y_{JB} \leq 0.35$	0.041	0.036
$y_{JB} : 0.50 < y_{JB} \leq 0.70$	0.108	0.077

Table 7.2: Dijet resolutions for various quantities of relevance to the present analysis

7.6 Dijet Resolutions

One aspect of the systematic error study on any particular cross-section measurement involves varying each quantity, upon which a cut is made (for example the transverse energy of the leading jet, $E_{T,1} > 20$ GeV), by the resolution of that quantity in order to obtain an estimate of the uncertainty on the measured cross-section due to the choice of the cut (the cut is varied in both data and Monte Carlo). It is therefore necessary to calculate the resolutions of various dijet quantities relevant to the present analysis. For all PYTHIA MC events passing the online, offline and subsample selections the dijet at the calorimeter level was matched to a dijet at the hadron level in the manner outlined in section 6.7.1. A calorimeter level dijet was considered matched if each of the constituent jets was matched to one, and only one, distinct hadron level jet. By using the resulting hadron level dijet, the difference between various dijet quantities at the calorimeter and hadron level could be considered.

The resulting resolutions are shown in figures 7.10 and 7.11. We see that the resolution of the jet transverse energy is about 10.5%, being slightly lower for the leading jet (8.8%) than the trailing jet (11.5%). This is expected as the resolution in jet transverse energy tends to decrease with increasing energy and the leading

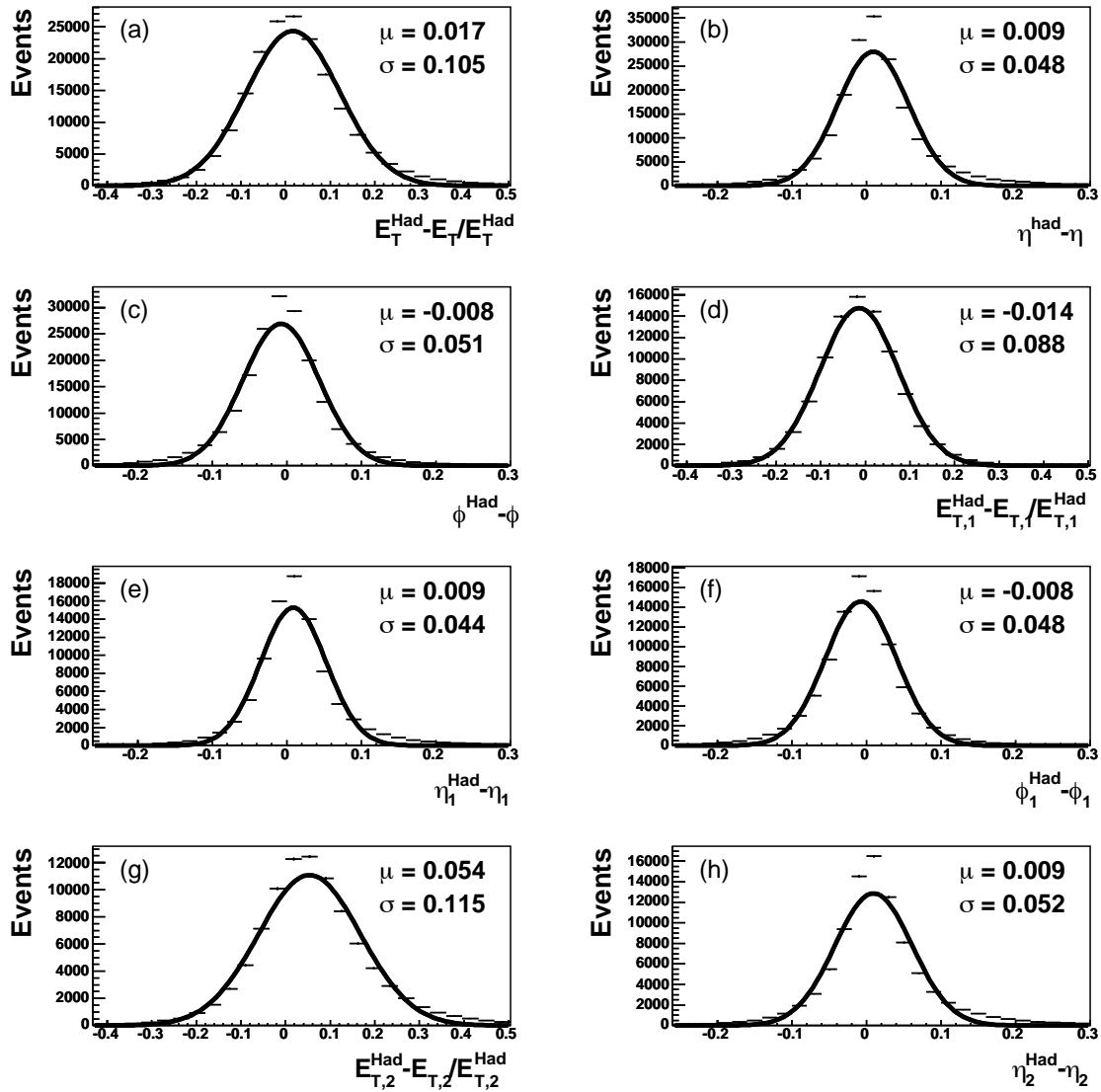


Figure 7.10: Various dijet resolutions (a) E_T (b) η (c) ϕ (d) $E_{T,1}$ (e) η_1 (f) ϕ_1 (g) $E_{T,2}$ (h) η_2

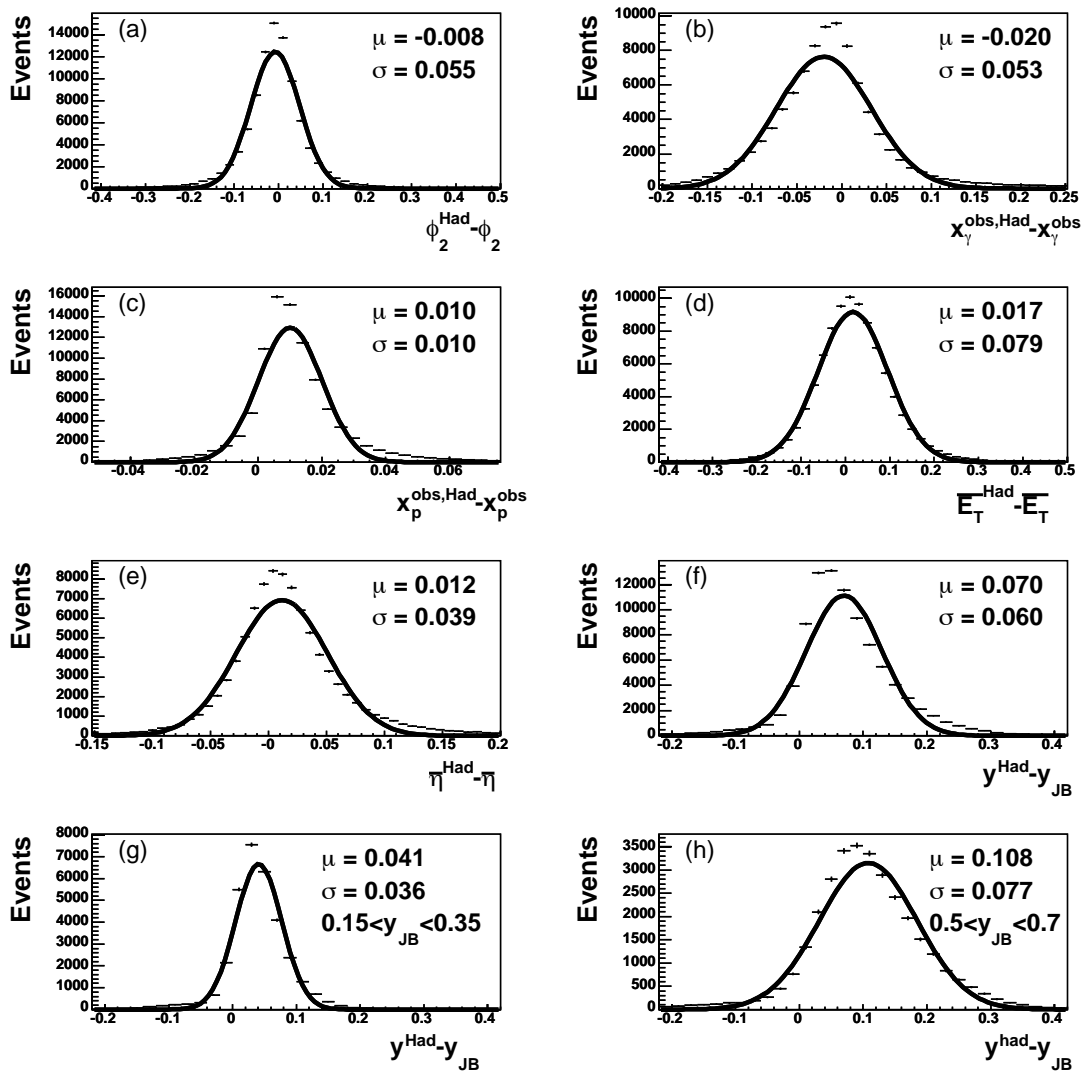


Figure 7.11: Various dijet resolutions (continued) (a) ϕ_2 (b) x_γ^{obs} (c) x_p^{obs} (d) \bar{E}_T (e) $\bar{\eta}$ (f) y_{JB} (g) y_{JB} for $0.15 < y_{JB} < 0.35$ (h) y_{JB} for $0.5 < y_{JB} < 0.7$

jet is harder in transverse energy than the trailing jet. The resolution in η and ϕ is quite low at 0.048 and 0.051 respectively. Although both x_γ^{obs} and x_p^{obs} are defined using similar quantities the resolution of x_γ^{obs} (0.053) is noticeably worse than x_p^{obs} (0.010) due to the fact that x_γ^{obs} is calculated using y_{JB} which has a relatively large resolution of 0.060. Not all of the resolutions determined in this section will be used further in the analysis (for example ϕ or x_p^{obs}) but have been included for completeness.

Chapter 8

Cross-Section Measurement

In this chapter the measured cross-sections and their comparison with the predictions of NLO QCD will be discussed. A total of 19 cross-section measurements were performed as part of the present analysis. Due to the large amount of cross-sections measured it would be rather cumbersome to discuss the specific details of the measurement of each one. Instead, this chapter will present, in detail, the measurement of one cross-section in particular, to illustrate the general method involved. Having highlighted the measurement of this one cross-section, the results for all other cross-sections will be presented in the next chapter. However, the specific details of the measurement of these remaining cross-sections will be deferred to the appendices.

8.1 Data Cross-Section Measurement

This section discusses the measurement of the differential cross-section with respect to x_γ^{obs} .

8.1.1 Unfolding the Cross-Section

The first step in the measurement is to consider all events which pass the online, offline and subsample selections introduced in chapter 7. The analysis begins with a measurement of the x_γ^{obs} distribution for events reconstructed in the ZEUS detector (see figure 8.1). The next step, involves calculating the efficiencies and purities, which was outlined in section 3.7. The efficiencies and purities for the x_γ^{obs} measurement presented in this section are shown in figure 8.1. The efficiencies and purities are relatively flat apart from the last bin where they are about twice

the size as the other bins. This is mainly attributable to the fact that the highest bin width is twice the size of the lower bin widths. As detailed in section 3.7, the acceptance corrections, which relate the hadron level distribution to the detector level distribution, are found by taking the ratio of the purity and efficiency (which is equivalent to taking the ratio of the hadron and detector level distributions in the MC). The x_γ^{obs} acceptance corrections are shown in figure 8.1. The corrections are relatively constant at ~ 1.2 . Ideally, these correction factors should be ~ 1 but are not due to the fact that both the efficiencies and purities are below 1, with the purity of the selected events being slightly greater than the efficiency of the cuts used to define the selection.

The final step in the unfolding procedure is to apply the acceptance corrections to the reconstructed x_γ^{obs} distribution and calculate the differential cross-section. This is done by using the formula below,

$$\frac{d\sigma(i)}{dx}(i) = \frac{N(i)C(i)}{\mathcal{L}\Delta x(i)}, \quad (8.1)$$

where $\frac{d\sigma(i)}{dx}(i)$ is the differential cross with respect to some quantity x (in the present case this is of course x_γ^{obs}) in bin i , $N(i)$ is the number of reconstructed events that fall in bin i , $C(i)$ is the acceptance correction for bin i , \mathcal{L} is the integrated luminosity of the data set (in the present case the ZEUS 98-00 data set was used which corresponds to 81.7pb^{-1}) and $\Delta x(i)$ is the bin width of bin i . The differential cross-section is plotted in figure 8.1.

Having measured the central values of the differential cross-section attention is now turned to the error analysis.

8.1.2 Jet Energy Scale Uncertainty

As discussed in section 6.8 there exists an uncertainty in the calorimeter jet energy scale of the order of $\pm 1\%$. To assess the uncertainty on the measured cross-section which arises from the uncertainty of the jet energy scale the energies of the jets in the data (but not the MC) are varied by $\pm 1\%$. Figure 8.2 shows the resulting uncertainty on the measured cross-section which is of the order of $\pm 5\%$ for this particular distribution.

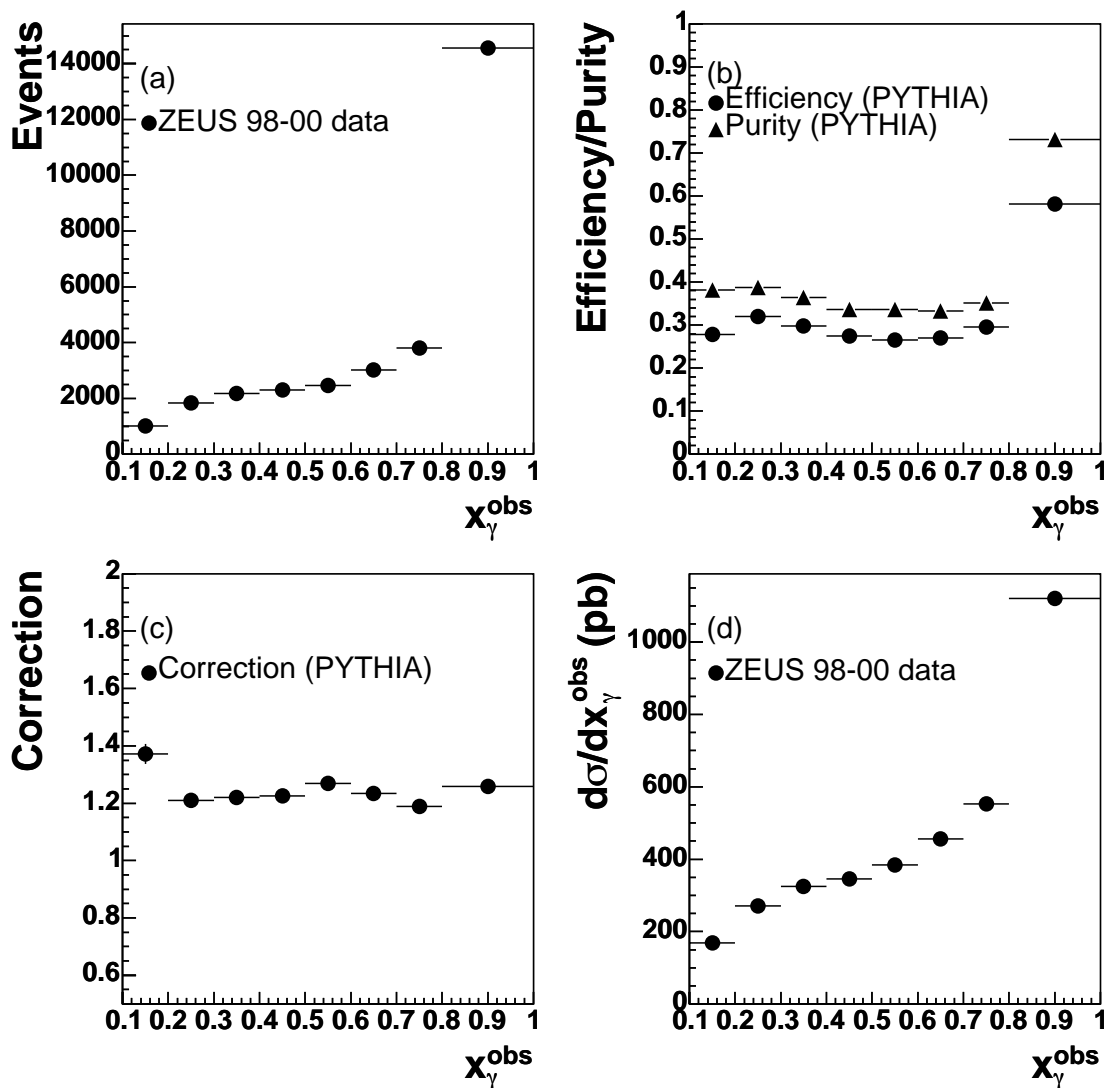


Figure 8.1: The various stages of the differential cross-section measurement, highlighted by the following steps (a) reconstructed distribution (b) computation of efficiencies and purities (c) calculation of the acceptance corrections (d) unfolding the hadron level distribution and calculation of the differential cross-section

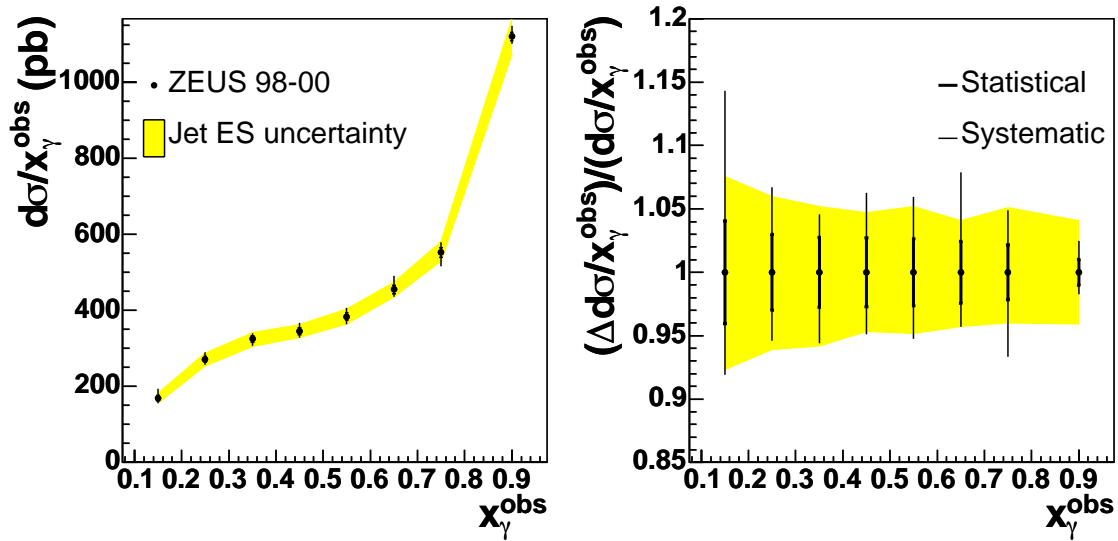


Figure 8.2: The statistical errors, systematic errors and jet energy scale uncertainty on the measured differential cross-section with respect to x_γ^{obs} .

8.1.3 Systematic Uncertainties

A detailed study of the sources of systematic uncertainty on the cross-section measurements presented in this thesis was performed. The study included making the following variations

- (Hrw E_T) HERWIG derived jet energy corrections were applied to the jets instead of the nominal PYTHIA corrections.
- ($\eta + \sigma$ & $\eta - \sigma$) All pseudorapidity cuts were varied by $\pm\sigma$ (0.05).
- ($E_T + \sigma$ & $E_T - \sigma$) All transverse energy cuts were varied by $\pm\sigma$ (10.5%).
- ($y_{JB} + \sigma$) The upper and lower y_{JB} cuts were varied by $+\sigma$ (0.036 and 0.077 respectively).
- ($y_{JB} - \sigma$) The upper and lower y_{JB} cuts were varied by $-\sigma$ (0.036 and 0.077 respectively).
- ($x_\gamma^{obs} + \sigma$ & $x_\gamma^{obs} - \sigma$) All x_γ^{obs} cuts were varied by $\pm\sigma$ (0.053).
- (MC weights) Direct/Resolved MC weights varied from those that are obtained by a fit to the x_γ^{obs} distribution (0.476659,0.523341), which are the nominal weights, to those obtained by a fit to the y_{JB} distribution (0.57746,0.42254).

- (Herwig) Unfolding of the cross-section performed using HERWIG instead of PYTHIA.
- (Vtx up) Looser vertex cut ($|z_{vtx}| < 50$ cms).
- (Vtx dn) Tighter vertex cut ($|z_{vtx}| < 30$ cms).
- (Trks up) $N_{trks}^{vtx}/N_{trks} > 0.1$ changed to $N_{trks}^{vtx}/N_{trks} > 0.15$.
- (Trks dn) $N_{trks}^{vtx}/N_{trks} > 0.1$ changed to $N_{trks}^{vtx}/N_{trks} > 0.05$.
- (Miss E_T up) $\frac{P_T}{\sqrt{E_T}} > 1.5$ GeV^{0.5} changed to $\frac{P_T}{\sqrt{E_T}} > 1.75$ GeV^{0.5}.
- (Miss E_T dn) $\frac{P_T}{\sqrt{E_T}} > 1.5$ GeV^{0.5} changed to $\frac{P_T}{\sqrt{E_T}} > 1.25$ GeV^{0.5}.
- (E_e up) E_{el} cut changed from 5 GeV to 6 GeV.
- (E_e dn) E_{el} cut changed from 5 GeV to 4 GeV.
- (y_{el} up) y_{el} cut changed from 0.7 to 0.75.
- (y_{el} dn) y_{el} cut changed from 0.7 to 0.65.
- (CTEQ4L) Proton PDF changed (in MC used to unfold the cross-section) from CTEQ5L [63] to CTEQ4L [64].
- (WHIT2) Photon PDF changed (in MC used to unfold the cross-section) from GRV [28] to WHIT2 [97].

All the above systematics were added in quadrature¹ and are shown, together with the jet energy scale uncertainty and the statistical errors, in figure 8.2. Table 8.1 shows the systematic shifts in each bin for each of the above variations.

¹This procedure is only strictly valid if the individual sources of systematic variation are uncorrelated. Although no formal check has been made, it has (and often is in analyses of this nature [51, 73]) been anticipated that this assumption of no correlation and the procedure of adding the individual sources of systematic uncertainty in quadrature are reasonable.

Systematic	1	2	3	4	5	6	7	8
ES up	7.5	5.9	5.1	4.7	5.2	4.1	5.1	4.1
ES dn	-7.6	-6.1	-5.8	-4.6	-4.8	-4.2	-4.0	-4.0
Hrw E_T corrs	0.3	0.1	-0.1	-0.5	-0.0	-0.5	-0.3	-0.0
$\eta + \sigma$	-0.5	-0.7	-0.5	-0.3	-0.0	-0.1	0.0	0.1
$\eta - \sigma$	-0.8	0.3	0.6	-0.3	0.7	0.4	-0.1	-0.1
$E_T + \sigma$	0.5	0.0	2.1	3.3	4.8	5.6	2.9	0.6
$E_T - \sigma$	1.3	2.5	1.2	-0.2	1.1	0.9	1.5	1.8
$y_{jb} + \sigma$	-5.6	-3.8	-3.8	-3.7	-3.6	-2.7	-2.8	0.7
$y_{jb} - \sigma$	6.9	2.9	2.6	3.0	1.7	2.3	1.2	-0.1
$x_\gamma^{obs} + \sigma$	0.0	0.0	0.0	0.0	0.0	0.0	0.0	0.0
$x_\gamma^{obs} - \sigma$	0.0	0.0	0.0	0.0	0.0	0.0	0.0	0.0
MC weights	-0.4	-0.6	-1.0	-1.4	-1.4	-2.1	-2.8	0.8
Herwig	11.7	4.6	0.3	2.4	1.1	1.1	1.0	0.2
Vtx up	0.7	-0.2	0.0	-0.1	-0.2	0.1	0.0	-0.1
Vtx dn	0.6	0.0	-0.4	0.3	-0.1	0.0	0.3	0.0
Trks up	-0.1	-0.3	-0.2	-0.2	-0.4	-0.3	-0.3	-0.2
Trks dn	-0.0	-0.0	0.0	0.1	0.0	0.0	0.0	0.0
Miss E_T up	-0.1	0.0	-0.0	0.2	0.1	0.1	-0.1	0.2
Miss E_T dn	-0.4	0.2	-0.2	0.0	-0.3	-0.4	-0.3	-0.5
E_e up	0.0	0.0	-0.0	-0.0	-0.0	-0.0	0.0	0.0
E_e dn	0.0	0.0	0.0	0.0	0.0	0.0	0.0	0.0
y_{el} up	-0.5	0.3	-0.1	-0.2	-0.5	-0.2	-0.2	-0.6
y_{el} dn	0.2	0.3	0.3	0.4	0.4	0.1	0.3	0.6
CTEQ4L	1.0	-0.5	-2.8	0.9	-1.7	2.7	2.5	-0.4
WHIT2	-4.0	-2.2	-0.5	2.2	-1.5	3.1	-4.9	-1.0

Table 8.1: Systematic shifts in each bin of the measured x_γ^{obs} cross-section (shown as a percentage of the nominal value). The jet energy scale uncertainty is also shown (ES up and ES dn).

8.2 Theoretical Predictions

All theoretical predictions for the cross-sections considered in the present analysis are produced using the NLO jet production code of Frixione and Ridolfi [19]. The nominal predictions are produced by setting the renormalisation scale equal to the factorisation scale, which is given by

$$\mu_R = \mu_F = \mu = \frac{1}{2} \sum_{i=1}^3 E_T^{part,i}, \quad (8.2)$$

where $E_T^{part,i}$ is the transverse energy of parton i . The nominal predictions are produced using the CTEQ5M1 proton PDF set [27] and AFG04 [95] photon PDF set. A range of additional PDF sets were also considered. For the proton, the MRST99 [60] set was also considered. For the photon, the GRVHO [92], AFG [93], CJK [94] and SAL [96] sets were also considered. The AFG04, CJK and SAL photon PDFs are new since the previous dijet measurements, performed by the ZEUS collaboration, and will be considered in more detail during the discussion about photon structure in the next chapter. The number of active flavours in the calculation was set to 5 and a value of $\alpha_s(M_Z) = 0.118$ was adopted. The nominal prediction for the differential cross-section with respect to x_γ^{obs} is shown in figure 8.3.

The theoretical predictions presented so far are valid at the parton level. In order to compare the theory to the data it is necessary to correct the NLO predictions to the hadron level. This was discussed in section 3.5. The method of determining the hadronisation correction is to use a LO MC generator, which has an inbuilt hadronisation model (such as PYTHIA [29] or HERWIG [20]), to calculate the cross-section at both the parton and the hadron levels. The hadronisation correction is then given by

$$C(i) = \frac{H(i)}{P(i)}, \quad (8.3)$$

where $C(i)$, the hadronisation correction in bin i , is given by the ratio of the hadron level cross-section, $H(i)$, in bin i to the parton level cross-section, $P(i)$, in bin i . These correction factors are then applied to the NLO prediction to determine the hadron level cross-section. In this analysis, PYTHIA and HERWIG (implemented within the HZTOOL [37] framework) were used to calculate the hadronisation corrections. Both PYTHIA and HERWIG use

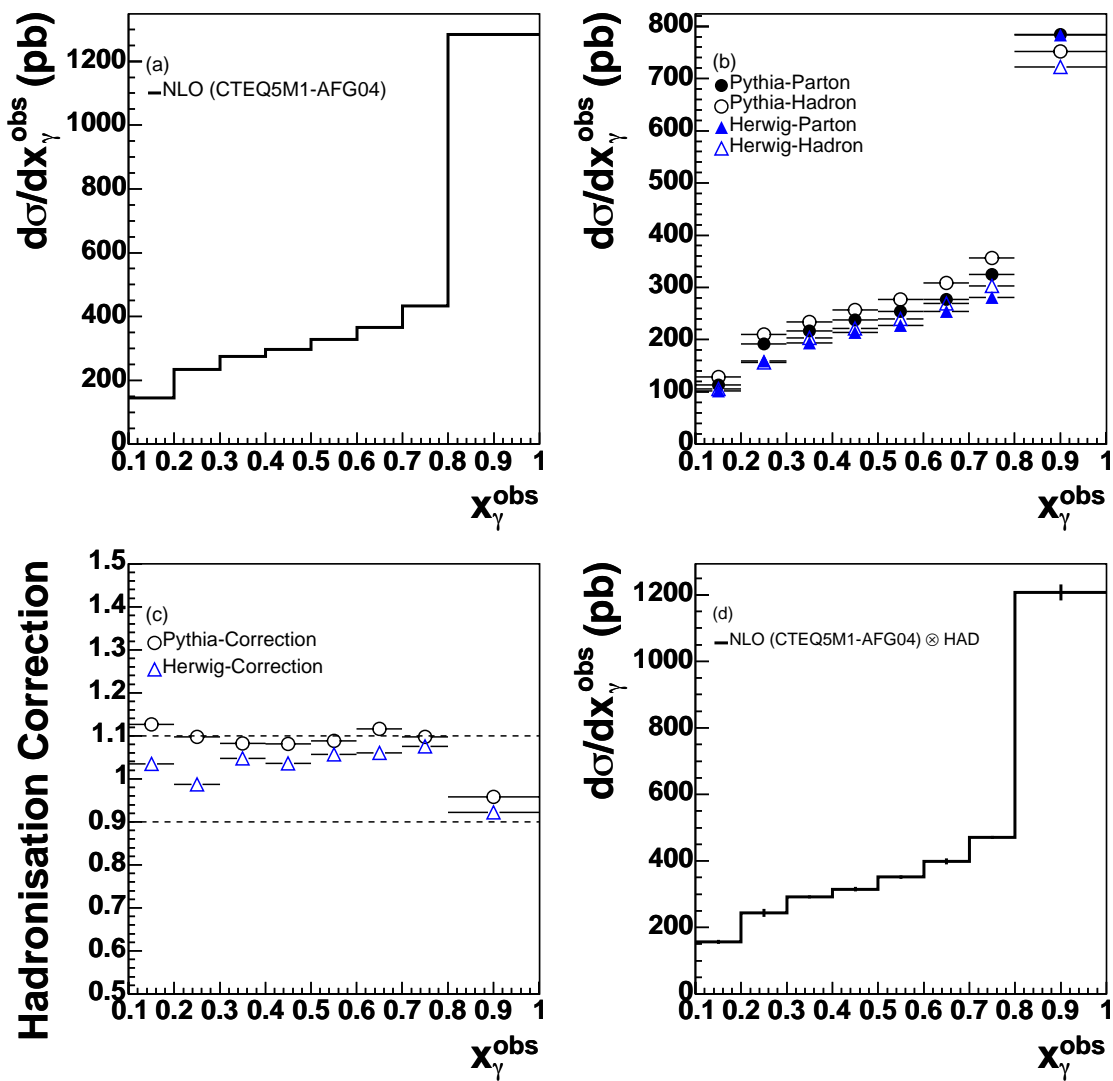


Figure 8.3: The series of steps taken to calculate the hadron level theoretical prediction (a) calculation of the parton level prediction (b) calculation of the LO parton and hadron level cross-sections (c) computation of the hadronisation correction (d) the hadron level prediction (corrected parton level prediction)

different hadronisation models and therefore the corrections that are obtained from each generator differ slightly. The PYTHIA and HERWIG parton and hadron level cross-sections, for the differential cross-section with respect to x_γ^{obs} , are shown in figure 8.3 and the corresponding hadronisation corrections are shown in figure 8.3. The final corrections, applied to the parton level NLO predictions, are the average of the PYTHIA and HERWIG corrections. The difference between the corrections predicted by each generator is used as an estimate for the error on the hadronisation correction. The corrected parton level x_γ^{obs} cross-section is shown in figure 8.3.

To estimate the uncertainty on the NLO prediction which arises from the value of $\alpha_s(M_Z)$, the predictions are generated using the CTEQ4 series of PDFs which provide separate PDF sets that are fitted using the values of $\alpha_s(M_Z) = 0.113, 0.116$ and 0.119 [64]. This is shown in figure 8.4. The resulting uncertainty on the predicted cross-section is $\sim 5\%$.

To estimate the uncertainty on the NLO prediction which arises from the choice of scale a number of approaches were considered. The first approach was to vary both the renormalisation and factorisation scales simultaneously. The cross-sections were produced once with the respective scales set to $2^{0.5}\mu$ (with μ as defined in equation 8.2) and once with the respective scales set to $2^{-0.5}\mu$. Figure 8.4 shows the resulting predictions (the upper values in the figure correspond to the prediction with the lowered scale and vice versa). The second approach used to investigate the scale dependence of the cross-section prediction was to vary the renormalisation and factorisation scales separately by the same factors as used for the simultaneous case. These scale uncertainties are also shown in figure 8.4. Varying the scales simultaneously produces an uncertainty on the cross-section prediction which is approximately 0.5 of that produced by varying the renormalisation scale alone. Varying the factorisation scale, by a given factor, therefore produces a shift in the cross-section which is in the opposite direction to that produced by varying the renormalisation scale. Previous analyses have used a method, of estimating the scale uncertainty on the cross-section, whereby the scales are simultaneously varied by a factor of 2. In this analysis the total scale uncertainty is defined to be the uncertainty from varying the renormalisation scale by a factor of $2^{\pm 0.5}$ added in quadrature to the uncertainty from varying the factorisation scale by a factor of $2^{\pm 0.5}$. By adopting this method, it is not been suggested that the shifts in the cross-section, that result from each scale variation,

are independent; this approach is used merely in order to make a conservative estimate of the variation in the cross-section which arises from the choice of the scales. The same approach has been used in the past to estimate the scale uncertainty of the extracted PDFs of the ZEUS QCD fits.

The systematic uncertainties presented in this section were added in quadrature² to give the total uncertainty on the theoretical prediction of the cross-section. Differences between parameterisations of the proton and photon PDF were not included in the total uncertainty as these will be discussed in the comparison of the measured data to the theoretical predictions in the next chapter.

This chapter has highlighted, in quite some detail, the exact steps which are taken in making a cross-section measurement and calculating the corresponding theoretical prediction. This has been done specifically for the case of the differential cross-section with respect to x_γ^{obs} . In the next chapter the results of all cross-sections measured as part of this thesis will be presented. However, only the final cross-sections will be presented with all supporting plots (efficiencies and purities, hadronisation corrections etc) placed into the appendices at the end of this thesis.

²This procedure is only strictly valid if the individual sources of variation are uncorrelated but adopting such a procedure is in line with previous analyses [51, 73] and results in a more conservative error estimate.

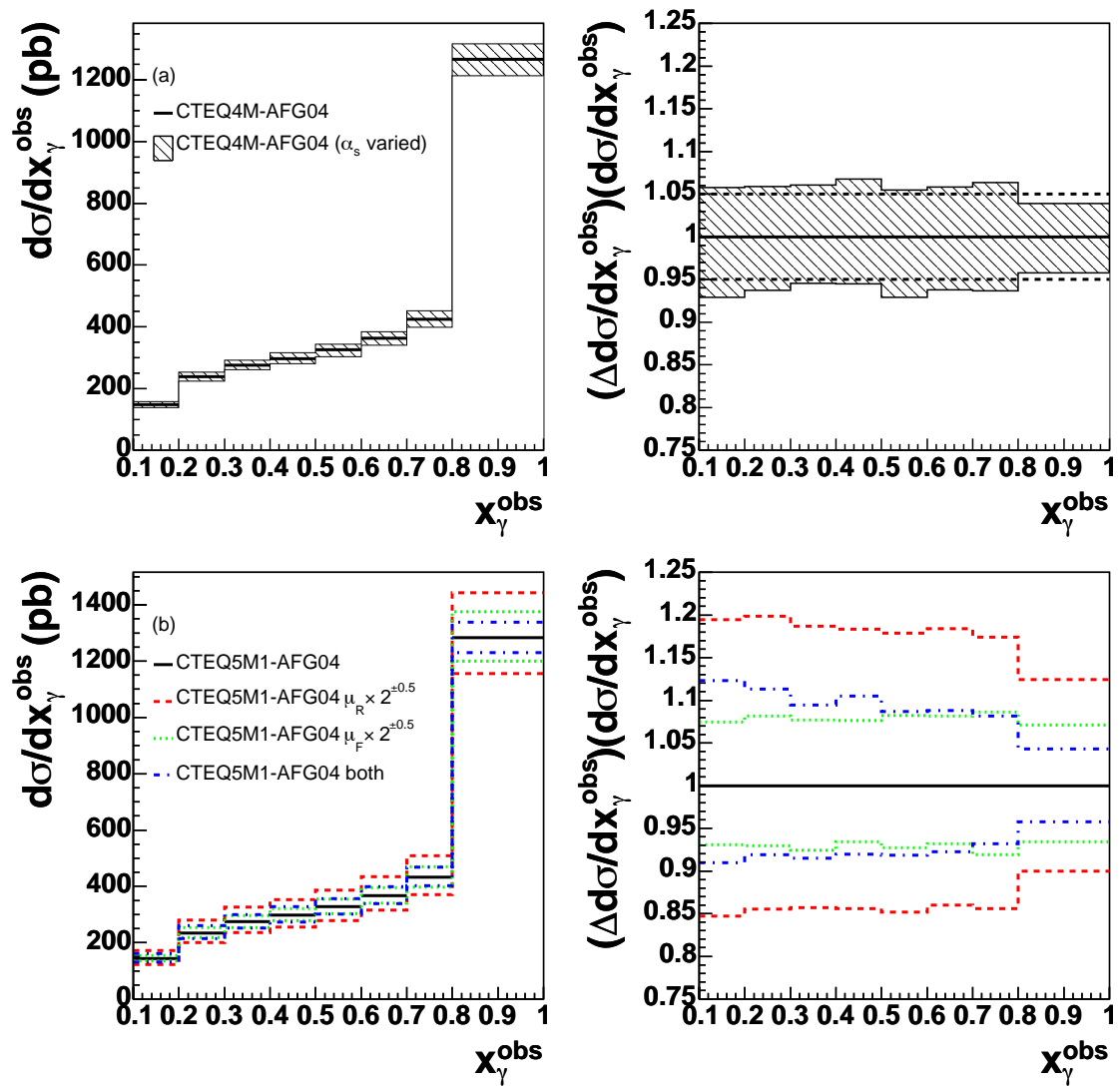


Figure 8.4: The two dominant sources of uncertainty on the theoretical cross-section predictions (a) the uncertainty due to the value of $\alpha_s(M_Z)$ and (b) the uncertainty due to the choice of scale

Chapter 9

Results and Discussion - Part I

In this chapter cross-sections are presented, and their comparison to the NLO predictions of QCD are discussed.

9.1 Differential Cross-Section with respect to x_γ^{obs}

The differential cross-section with respect to x_γ^{obs} is shown in figure 9.1 and table J.1. The plot on the right side of figure 9.1 also shows the ratio of the data to the theory. As can be seen from the figures the size of the highest x_γ^{obs} bin is twice that of the other bins. The reason for this is to average over the erratic hadronisation corrections in this region (at the parton level there is just a single peak at $x_\gamma^{obs} = 1$ for direct events).

The measured data are consistent with the predictions using the AFG04 photon parameterisation (and agreement is very good within the quoted experimental and theoretical uncertainties) across all x_γ^{obs} . However, for the case of the CJK parameterisation there is an increasing trend, as x_γ^{obs} decreases, for the prediction to lie above the data. For $0.5 < x_\gamma^{obs} < 0.8$ the data lies about 0 – 20% below the prediction and for $0.0 < x_\gamma^{obs} < 0.5$ the data lies about 20 – 30% below the prediction and so the shape of the data is poorly described by the CJK prediction. On the other hand, the AFG04 prediction describes the shape of the distribution very well, with the data for $x_\gamma^{obs} < 0.8$ lying typically 10% above the prediction. The AFG04 and CJK parameterisations were only two out of a total of five photon parameterisations considered. The comparison of the measured data with all five photon parameterisations is shown in figure 9.2. The predictions of AFG,

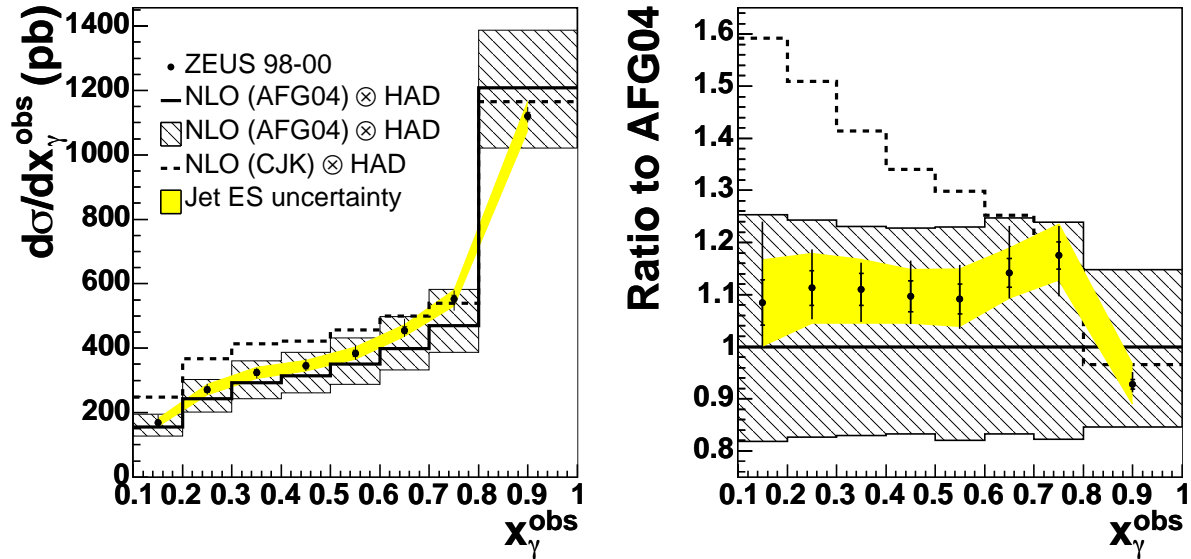


Figure 9.1: Measured differential cross-section with respect to x_γ^{obs} compared to NLO predictions. The data are shown with statistical errors (inner bars) and statistical and systematic errors added in quadrature (outer bars). The uncertainty due to that of the jet energy scale is shown as the yellow shaded band. The NLO prediction corrected for hadronisation effects is shown calculated using the CTEQ5M1 and AFG04 (solid line) PDFs for the proton and photon respectively. The scale is set to μ (see equation 8.2) for the central value of the prediction. The hatched band represents the quadratic sum of the theoretical uncertainties discussed in section 8.2. The prediction calculated using the CJK photon PDF is also shown (dashed line). The plot on the right shows the ratio of the data points to the predicted points. The dashed line on the right-hand plot shows the ratio of the CJK predicted points to the AFG04 predicted plots

GRV and SAL are similar to those using AFG04 lying between -10% and 20% of the AFG04 prediction. The shapes of the AFG and GRV predictions are very similar to the AFG04 prediction, with the former typically lying ($0 - 10\%$) above the AFG04 prediction and the latter ($15 - 20\%$) above, and are consistent with the measured data. The shape of the SAL prediction describes the data very well for $x_\gamma^{obs} > 0.4$ but below this value the prediction appears to fall off slightly more rapidly than the data suggests. The CJK prediction lies ($20 - 60\%$) above the AFG04 prediction and falls off much less rapidly than AFG04 with decreasing x_γ^{obs} . The data falls off with decreasing x_γ^{obs} in a manner which is more consistent with AFG04 (and indeed AFG, GRV and, to the extent discussed above, SAL) than CJK. For the moment the various differences between the photon parameterisations are just noted and will be discussed in more detail later on in this chapter.

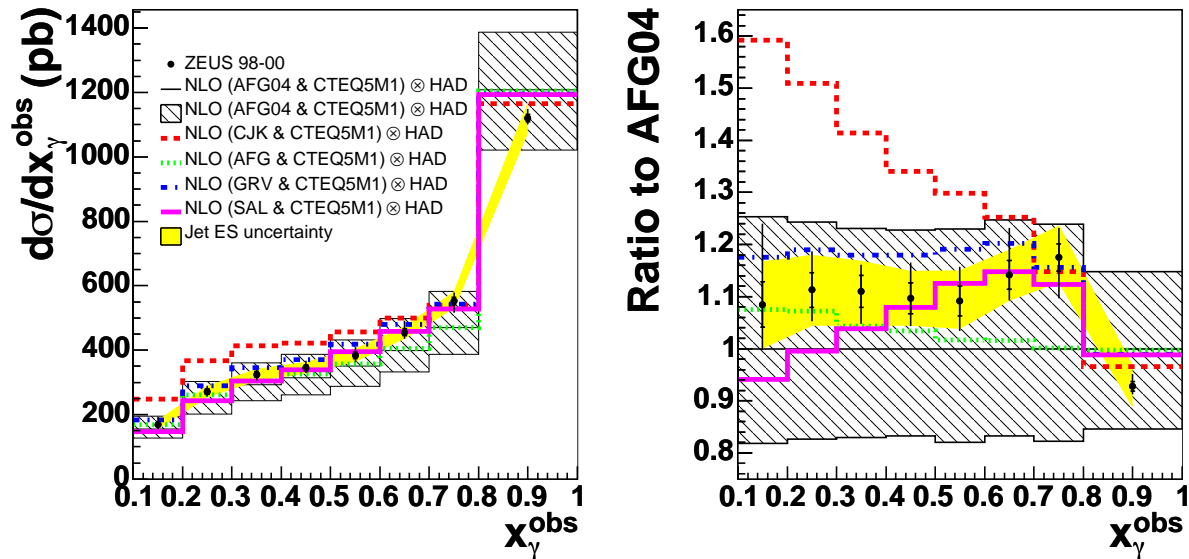


Figure 9.2: Measured differential cross-section with respect to x_γ^{obs} compared to NLO predictions. Exactly as figure 9.1 except that the predictions using the photon PDFs AFG, GRV and SAL are also shown. The right-hand plot shows the ratio of the predicted points to the AFG04 predicted points

9.2 Differential Cross-Section with respect to x_p^{obs}

The differential cross-section with respect to x_p^{obs} for both high (> 0.75) and low (≤ 0.75) x_γ^{obs} is shown in figure 9.3 and tables J.2 and J.3. Within the relevant uncertainties the measured data are consistent with the predicted points at both high and low- x_γ^{obs} across most values of x_p^{obs} . At low- x_γ^{obs} the data lies above the predicted values for $x_p^{obs} > 0.3$. However, the statistical errors on the measured points in this region are significant. The cross-sections fall by three orders of magnitude and exhibit a turn over at the lowest values of x_p^{obs} . This turnover is attributable to the cuts used in the analysis. The high- E_T cuts used, combined with the lack of events in the rear direction lead to a relatively low number of events in the lowest x_p^{obs} bin. The turnover is more pronounced in the case of resolved events because such events tend to lie more forward in the detector leading to them being characterised by relatively high values of x_p^{obs} . For an illustration of these points see figure 9.4. For values of $x_p^{obs} \gtrsim 0.1$ the measured data, at both high and low- x_γ^{obs} , does not appear to fall off with increasing x_p^{obs} as quickly as the prediction suggests. However, despite the difference in shapes

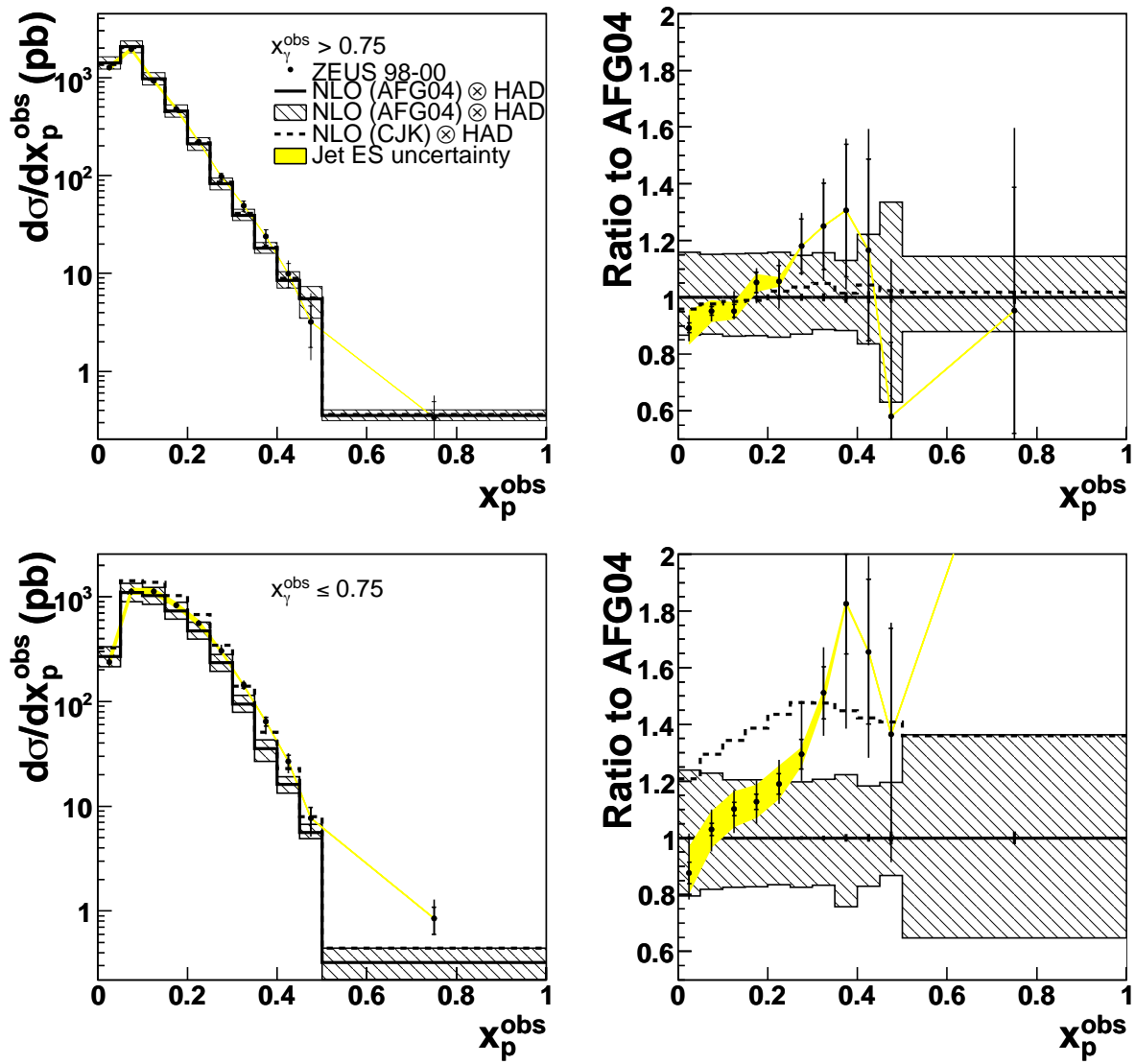


Figure 9.3: Measured differential cross-section with respect to x_p^{obs} for $x_\gamma^{obs} > 0.75$ (top) and $x_\gamma^{obs} \leq 0.75$ (bottom) compared to NLO predictions. For further details, see the caption to figure 9.1

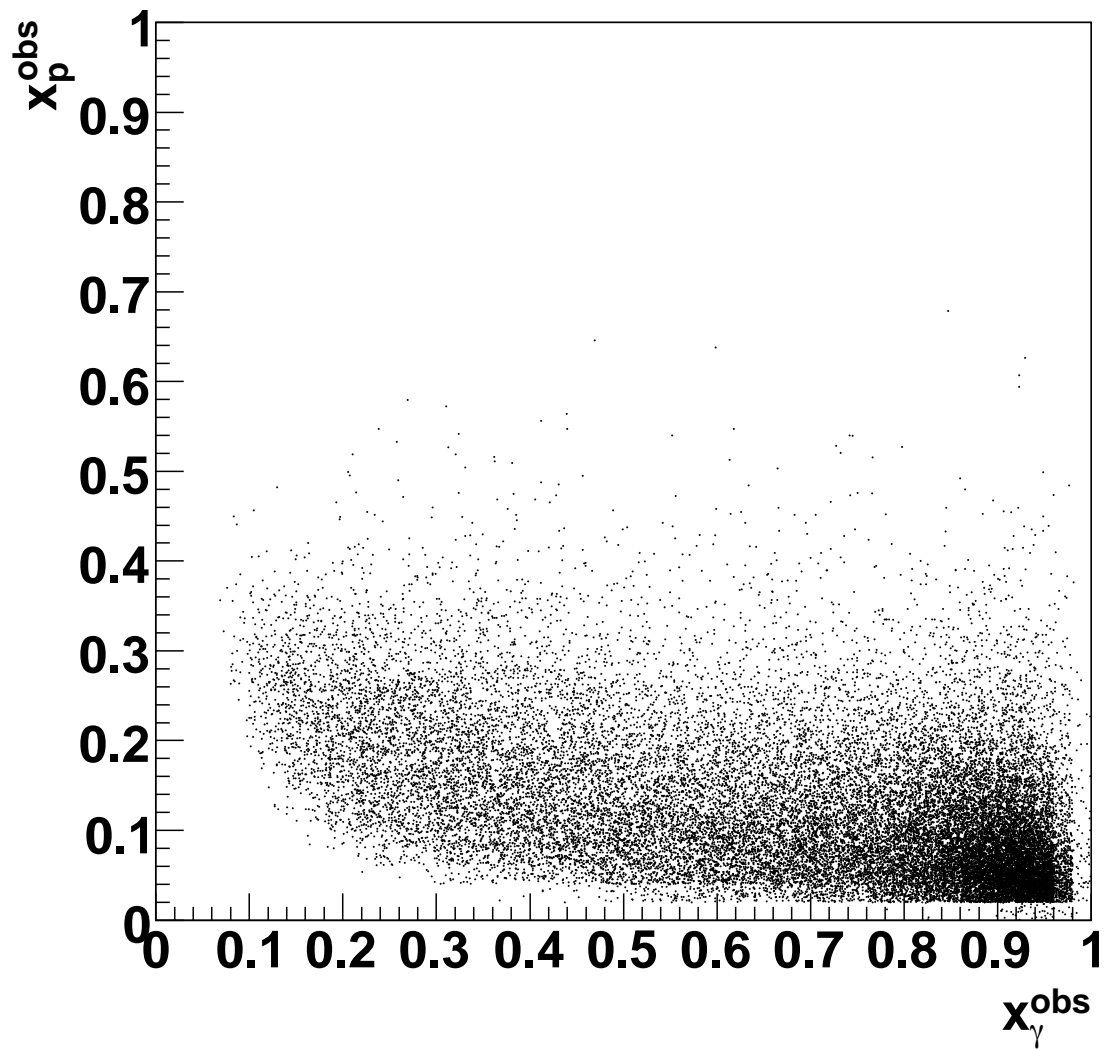


Figure 9.4: A plot of x_p^{obs} versus x_γ^{obs} for data events

the measured data are still consistent with the predictions within the relevant uncertainties.

9.3 Differential Cross-Sections with respect to $E_{T,1}$ and \bar{E}_T

The differential cross-sections with respect to $E_{T,1}$ and \bar{E}_T , for both high and low- x_γ^{obs} , are shown in figures 9.5 and 9.6 and also given in tables J.4-J.7. The measurement at both high and low- x_γ^{obs} extends to transverse energies of ~ 90 GeV. However, the measurement has statistical significance only for transverse energies $\lesssim 70$ GeV. The $E_{T,1}$ data at high- x_γ^{obs} is well described by the prediction. At low- x_γ^{obs} the $E_{T,1}$ data are well described in the first $E_{T,1}$ bin but at higher transverse energies tends to lie significantly above the prediction. This trend was also observed in the previous dijet measurement [51]. At low- x_γ^{obs} the $E_{T,1}$ data are poorly described by the CJK calculation in the first $E_{T,1}$ bin but there is an improvement in the description of the higher transverse energy regions. For the cross-section with respect to \bar{E}_T a similar picture is seen with the predictions describing the data reasonably well at high- x_γ^{obs} but falling significantly below the data at low- x_γ^{obs} . This latter observation is more apparent in the \bar{E}_T case than for the previous $E_{T,1}$ case. Once again it is seen that the data are poorly described by the CJK calculation in the first \bar{E}_T bin but described very well at higher transverse energies (more so than the $E_{T,1}$ case).

9.4 Differential Cross-Section with respect to $\bar{\eta}$

The differential cross-section with respect to $\bar{\eta}$ is shown in figure 9.7 and also given in tables J.8 and J.9. At high- x_γ^{obs} a good description of the data are seen for all statistically significant bins. In the low- x_γ^{obs} AFG04 case a good description of the data are seen for $\bar{\eta}$ values less than ~ 2 . However, the description of the data becomes progressively poorer in the more forward regions with the data lying 80% above the prediction in the most forward bin though it should be noted that both statistical and systematic uncertainties are appreciable in this region. The CJK prediction describes the most forward point well but underestimates the normalisation of the cross-section by $\sim 20\%$ for $\bar{\eta} \lesssim 2.5$ (although the shape is well described).

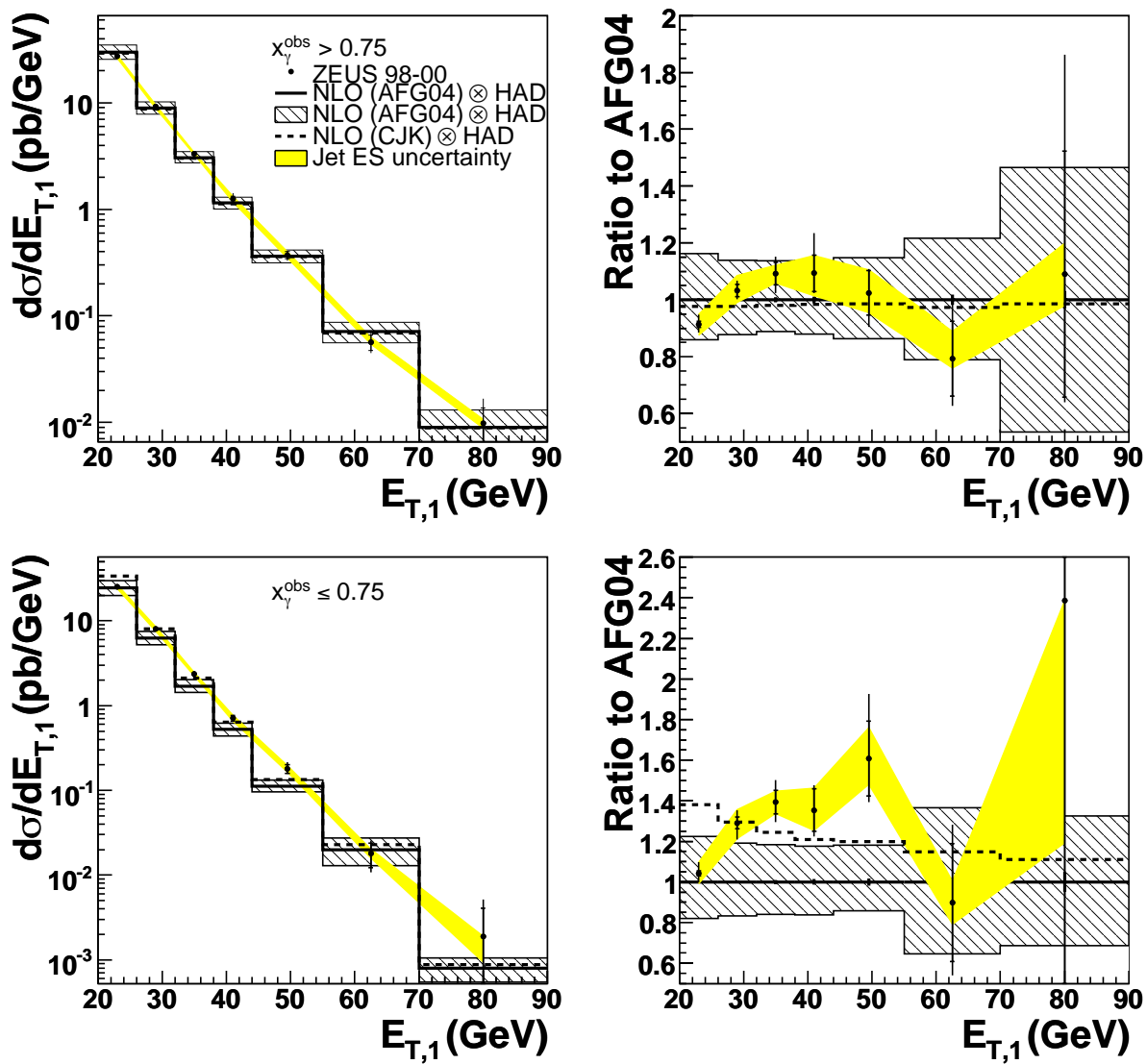


Figure 9.5: Measured differential cross-section with respect to $E_{T,1}$ for $x_\gamma^{obs} > 0.75$ (top) and $x_\gamma^{obs} \leq 0.75$ (bottom) compared to NLO predictions. For further details, see the caption to figure 9.1

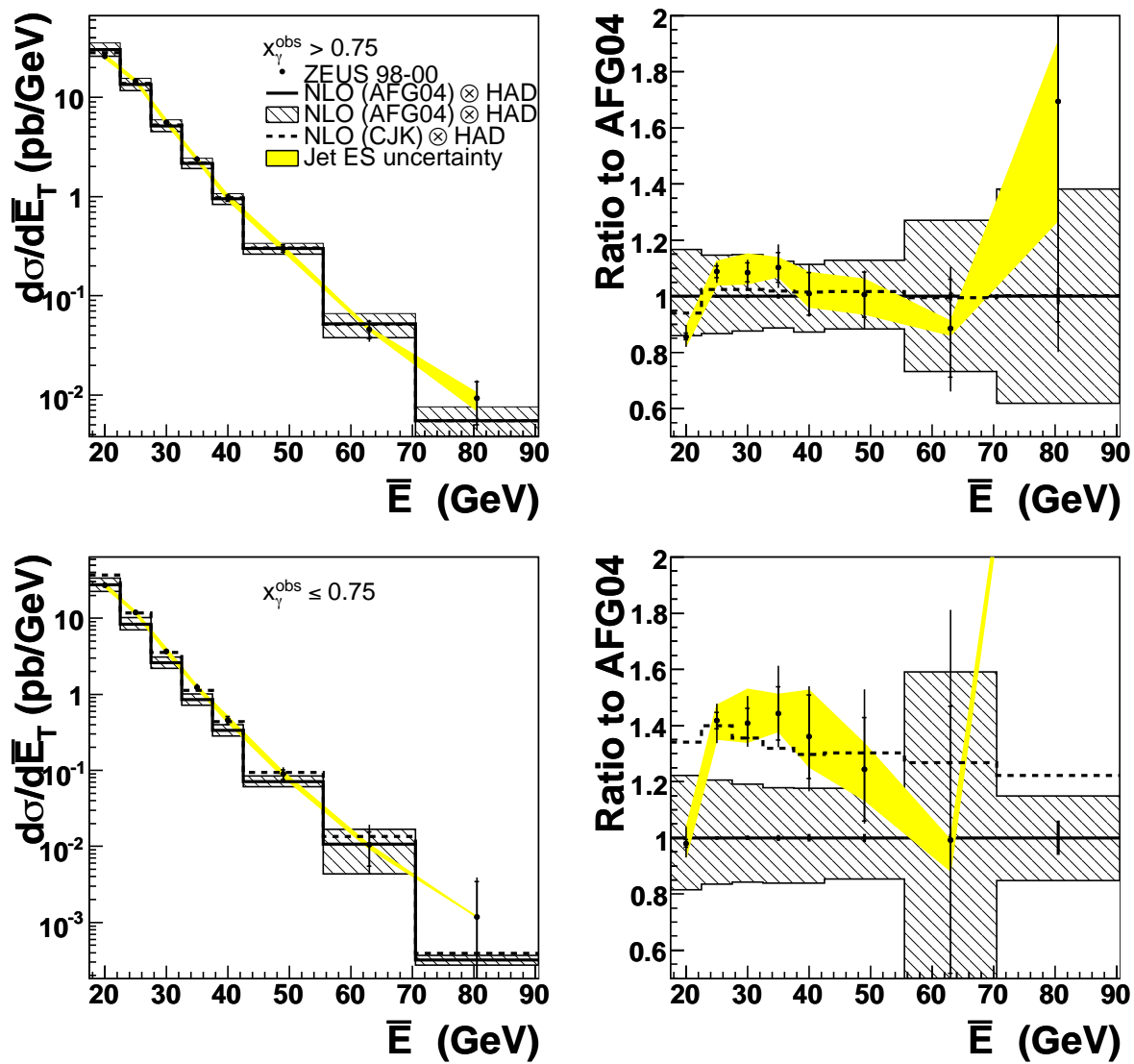


Figure 9.6: Measured differential cross-section with respect to \bar{E}_T for $x_\gamma^{obs} > 0.75$ (top) and $x_\gamma^{obs} \leq 0.75$ (bottom) compared to NLO predictions. For further details, see the caption to figure 9.1

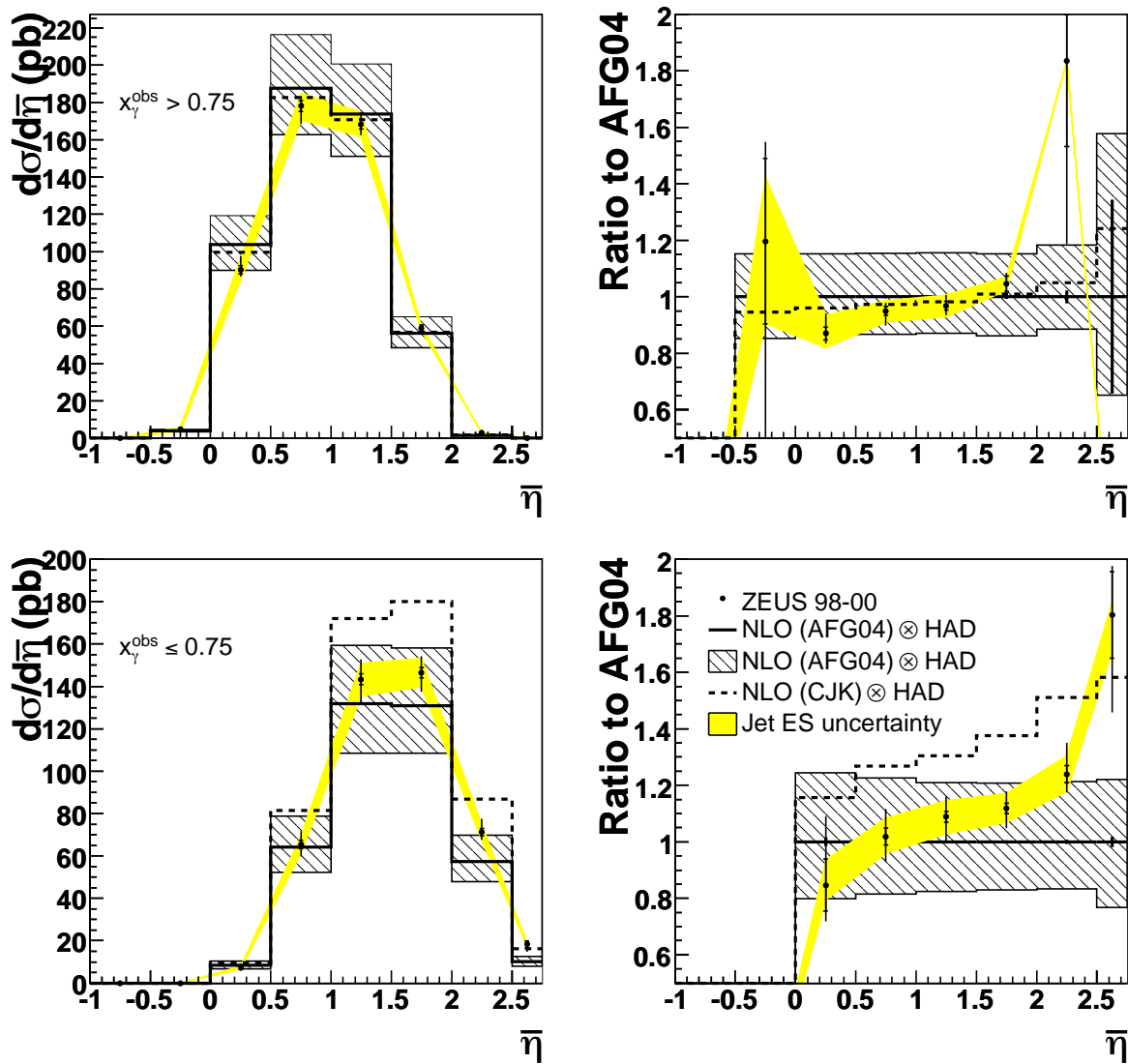


Figure 9.7: Measured differential cross-section with respect to $\bar{\eta}$ for $x_{\gamma}^{obs} > 0.75$ (top) and $x_{\gamma}^{obs} \leq 0.75$ (bottom) compared to NLO predictions. For further details, see the caption to figure 9.1.

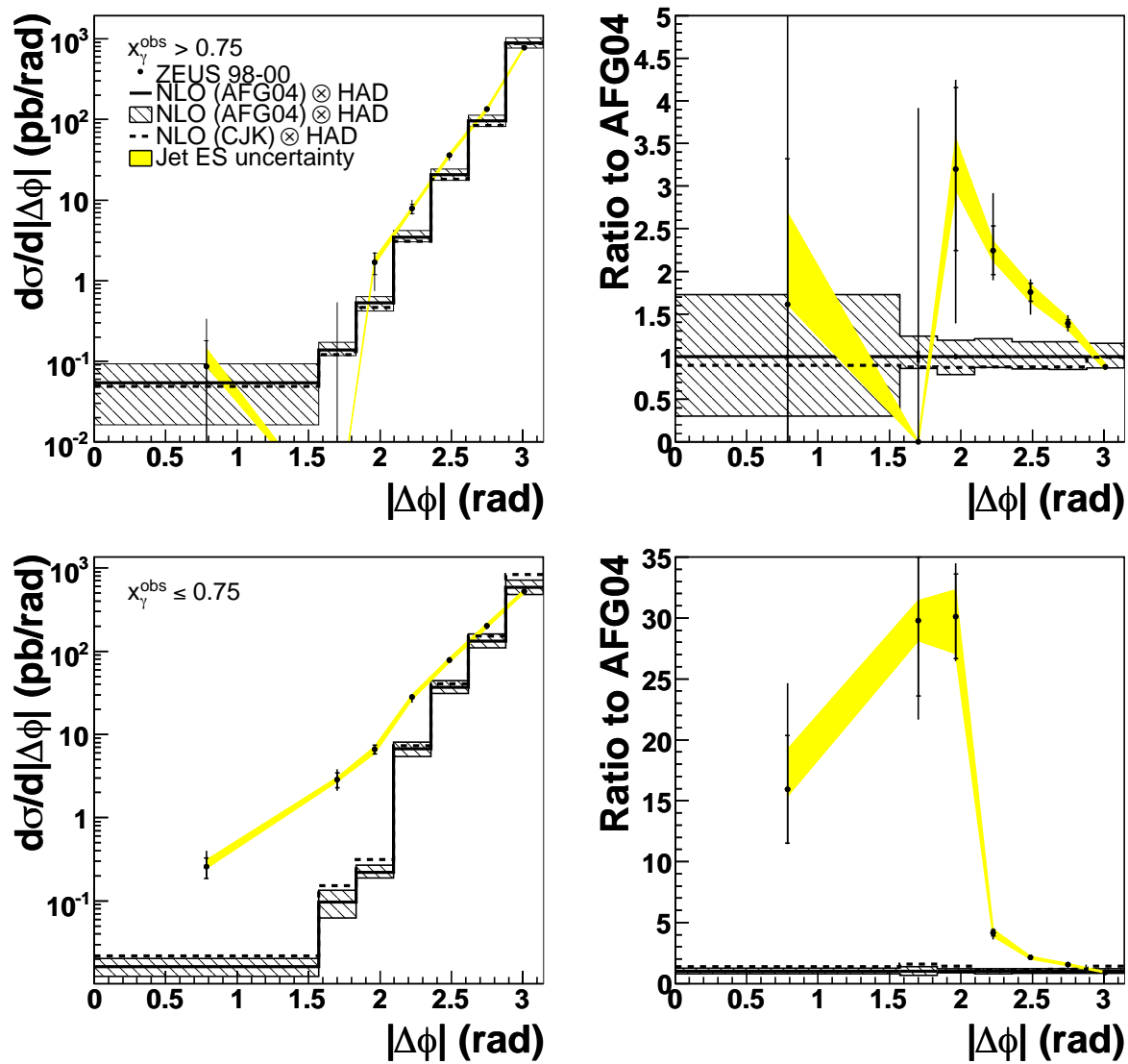


Figure 9.8: Measured differential cross-section with respect to $|\Delta\phi|$ for $x_\gamma^{obs} > 0.75$ (top) and $x_\gamma^{obs} \leq 0.75$ (bottom) compared to NLO predictions. For further details, see the caption to figure 9.1

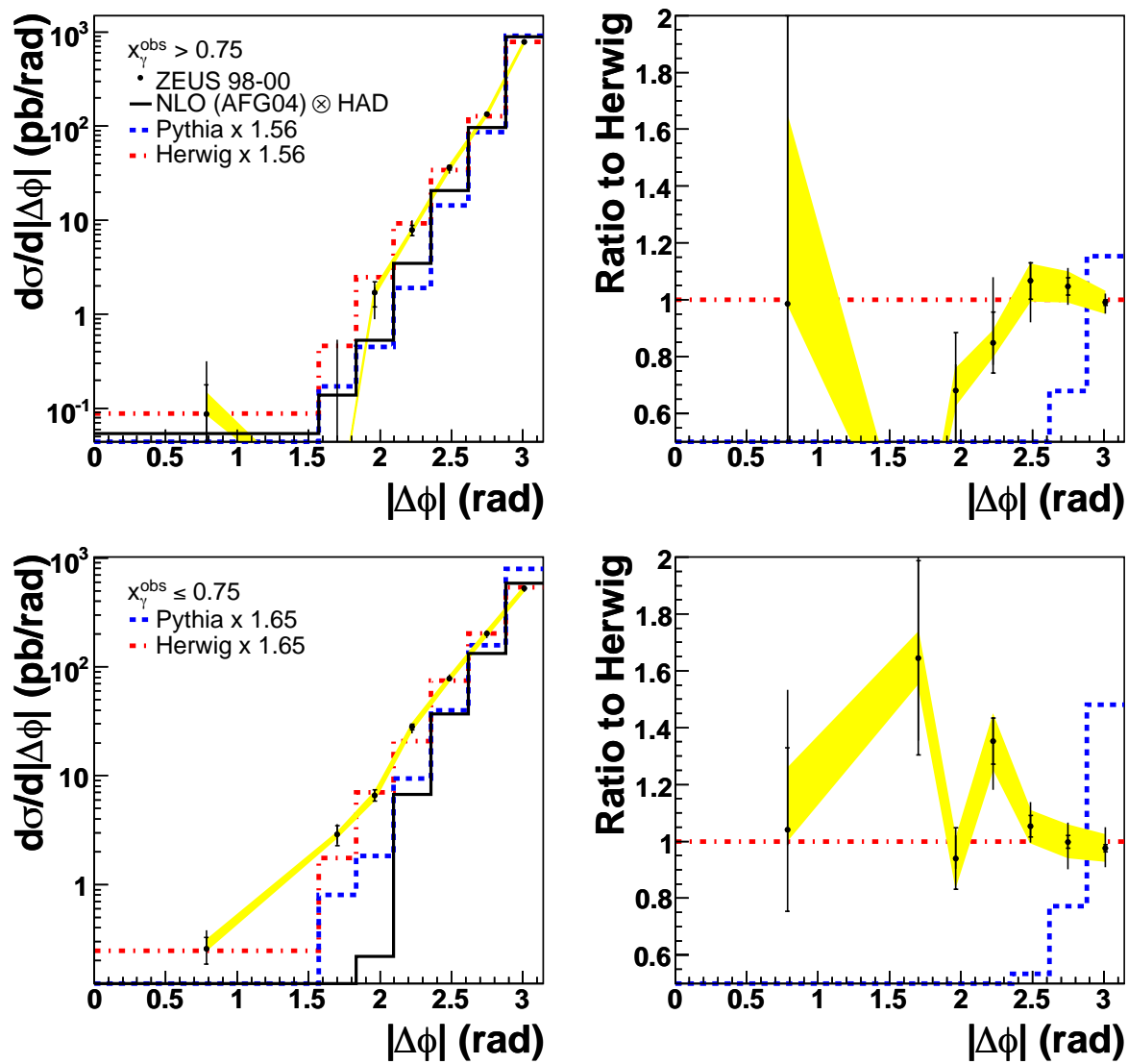


Figure 9.9: Measured differential cross-section with respect to $|\Delta\phi|$ for $x_\gamma^{obs} > 0.75$ (top) and $x_\gamma^{obs} \leq 0.75$ (bottom) compared to the predictions of NLO (black), HERWIG (red) and PYTHIA (blue).

9.5 Differential Cross-Section with respect to $|\Delta\phi|$

Amongst the most interesting cross-sections measured as part of the present analysis are those with respect to $|\Delta\phi|$ which are shown in figure 9.8 and also given in tables J.10 and J.11. The LO prediction for this cross-section would simply be a single peak at 180° , since only two partons are emitted and by conservation of energy and momentum they must be emitted back to back in ϕ leading to every event been characterised by a $|\Delta\phi|$ value of 180° . The presence of higher order effects results in the emission of additional partons in the final state and values of $|\Delta\phi|$ between $0 - 180^\circ$. The form of the cross-section with respect to $|\Delta\phi|$ is therefore directly sensitive to higher-order topologies and provides an excellent test of whether or not NLO QCD truly is a sufficient level of approximation for making QCD predictions for the data presented here. From figure 9.8 it can be seen that at high- x_γ^{obs} the data has a significantly harder spectrum than the NLO prediction. The effect is even more apparent at low- x_γ^{obs} with the data lying up to 30 times above the NLO prediction. At both high and low- x_γ^{obs} both the normalisation and the shape of the data are poorly described by the NLO predictions. The fact that the NLO predictions describe the data so poorly is indicative of the need to include higher orders in the QCD calculation. In figure 9.9 the data have also been compared against the cross-section predictions of HERWIG and PYTHIA. Both of these programs are leading order generators which have parton shower models incorporated. The predictions of neither PYTHIA or HERWIG describe the normalisation of the data. However, after multiplication by an appropriate normalisation factor (found by normalising the relevant MC histogram to the data histogram), HERWIG describes the shape of the data well. The description of the shape of the data is poor using PYTHIA. Similar findings to those presented in this section have also been made for the more exclusive case of dijet photoproduction for events which contain a D^* meson [99]. The fact that a LO MC program incorporating parton shower models can describe the data well, whereas the NLO QCD prediction describes the data poorly is further indication that the QCD calculation requires higher orders. Such higher order calculations are not yet available for the processes discussed here. However, work has been underway for a number of years on the development of NLO MC generators which incorporate parton shower models [100]. Predictions

from such generators would possibly improve the description of the data but again, unfortunately, these generators are not yet available for the processes discussed here.

9.6 Optimised Cross-Sections

9.6.1 Low- x_γ^{obs} Optimised Cross-Sections

The low- x_γ^{obs} optimised differential cross-sections with respect to x_p^{obs} are shown in figures 9.10 and 9.11, and also given in tables J.12-J.15. Statistically significant data points are yielded in the region $0.1 < x_p^{obs} \leq 0.4$. There are a negligible number of events in the region $0.5 < x_p^{obs} \leq 1$. To illustrate more clearly the precision to which these measurements are made, table 9.1 illustrates the various uncertainties on the measured cross-sections expressed as a percentage of the nominal cross-section values. All cross-sections are characterised by fairly large statistical errors (3 – 10% for the most significant bins) due to the reason that, despite the large 98-00 data set used in the present case, the analysis is conducted at high transverse energies and the optimised cross-sections are made in relatively small pockets of phase space. For bins with a statistical uncertainty of 10% or less (10 bins altogether) the average systematic error is ${}^{+9.3}_{-7.5}\%$. The average jet energy scale uncertainty for such bins is ${}^{+4.3}_{-4.7}\%$.

The measured data has a tendency to lie systematically above the AFG04 predicted points. Although, within the relevant uncertainties the predictions are still roughly consistent with the data. With the exception of optimised cross-section C (OptC) the CJK predicted points provide an improved description of both the shape and the normalisation of the data. It is worth discussing this point in more detail. Optimised cross-section A (OptA) is the most forward cross-section measured in the present analysis. It represents the cross-section whereby both jets lie in the the region of pseudorapidity between $2 < \eta \leq 3$ (with at least one jet lying in the region between $2 < \eta \leq 2.5$). The fact that the CJK cross-section describes the data in this region better than AFG04 should come as no surprise as this has already been seen, in the case of the differential cross-section with respect to $\bar{\eta}$ (see figure 9.7), that CJK provides a better description in the far-forward region. Optimised cross-section C (OptC) has the same transverse energy cuts as OptA (namely $E_{T,1} > 20$ GeV and $E_{T,2} > 15$ GeV) but different pseudorapidity cuts ($1 < \eta_1 \leq 2, 2 \leq \eta_2 \leq 3$). Such events will be characterised

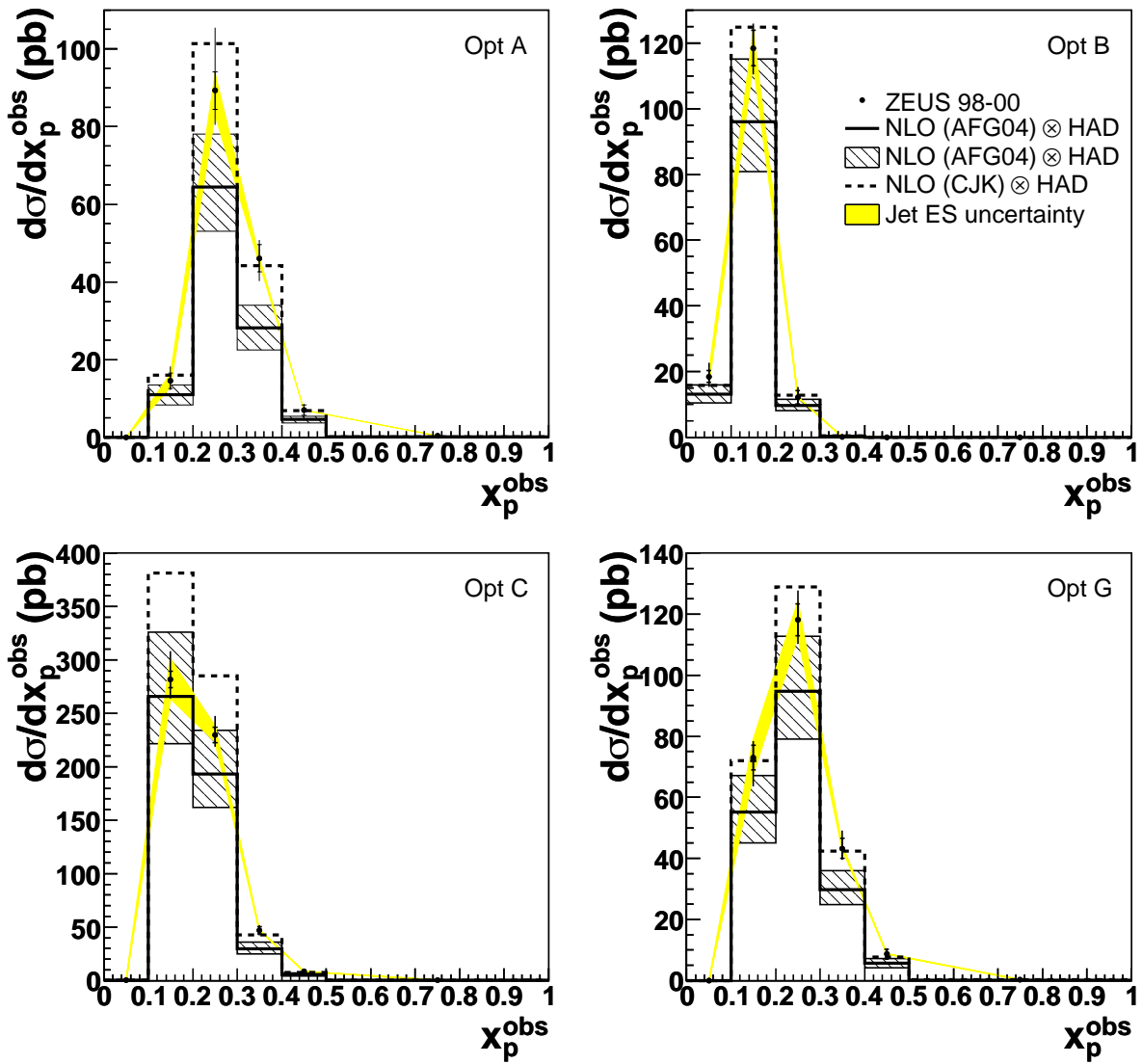


Figure 9.10: Low- x_γ^{obs} optimised cross-sections. For further details, see the cross-section definitions in table 5.12 and the caption to figure 9.1.

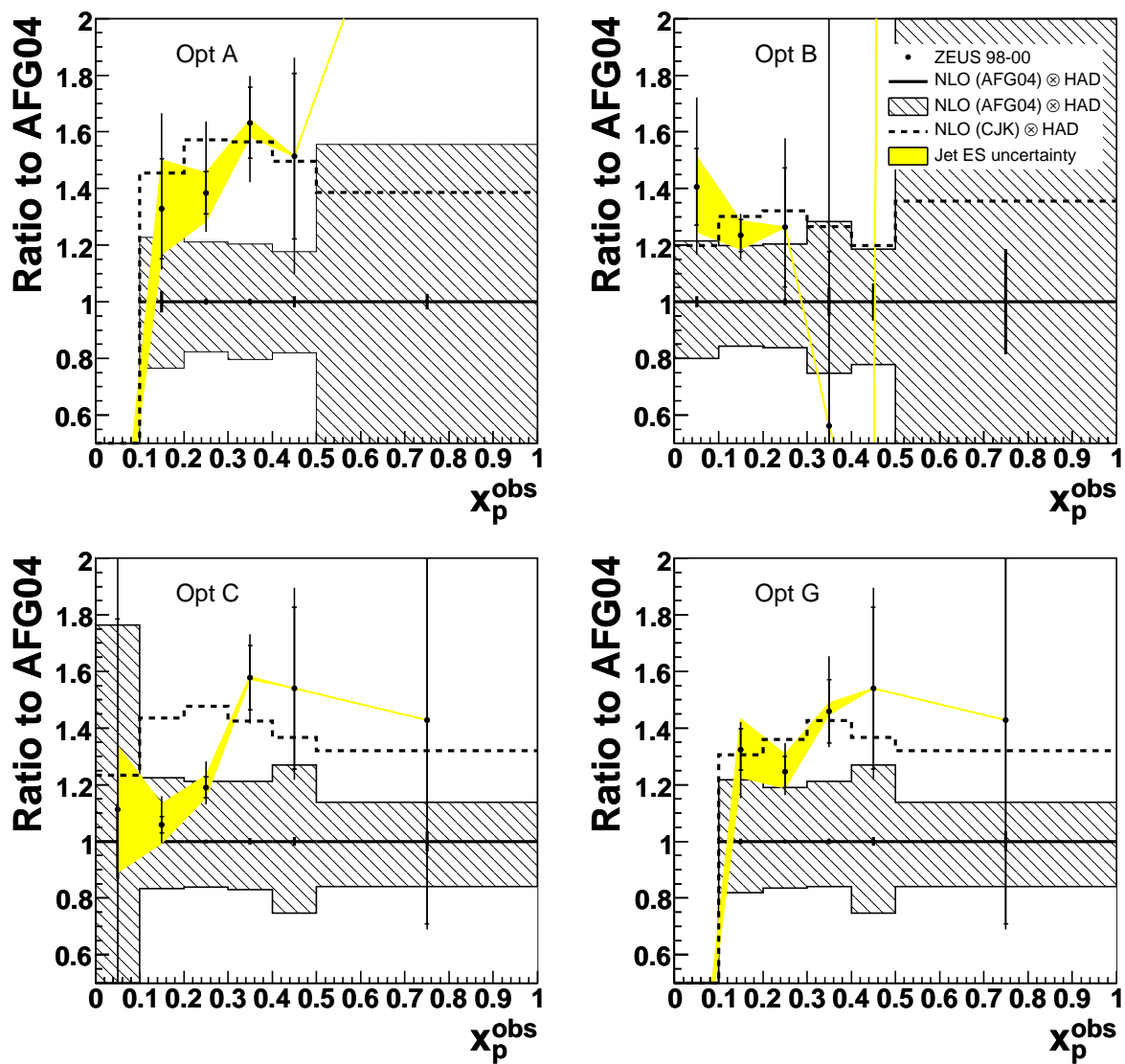


Figure 9.11: Low- x_γ^{obs} optimised cross-sections (continued). For further details, see the cross-section definitions in table 5.12 and the caption to figure 9.1.

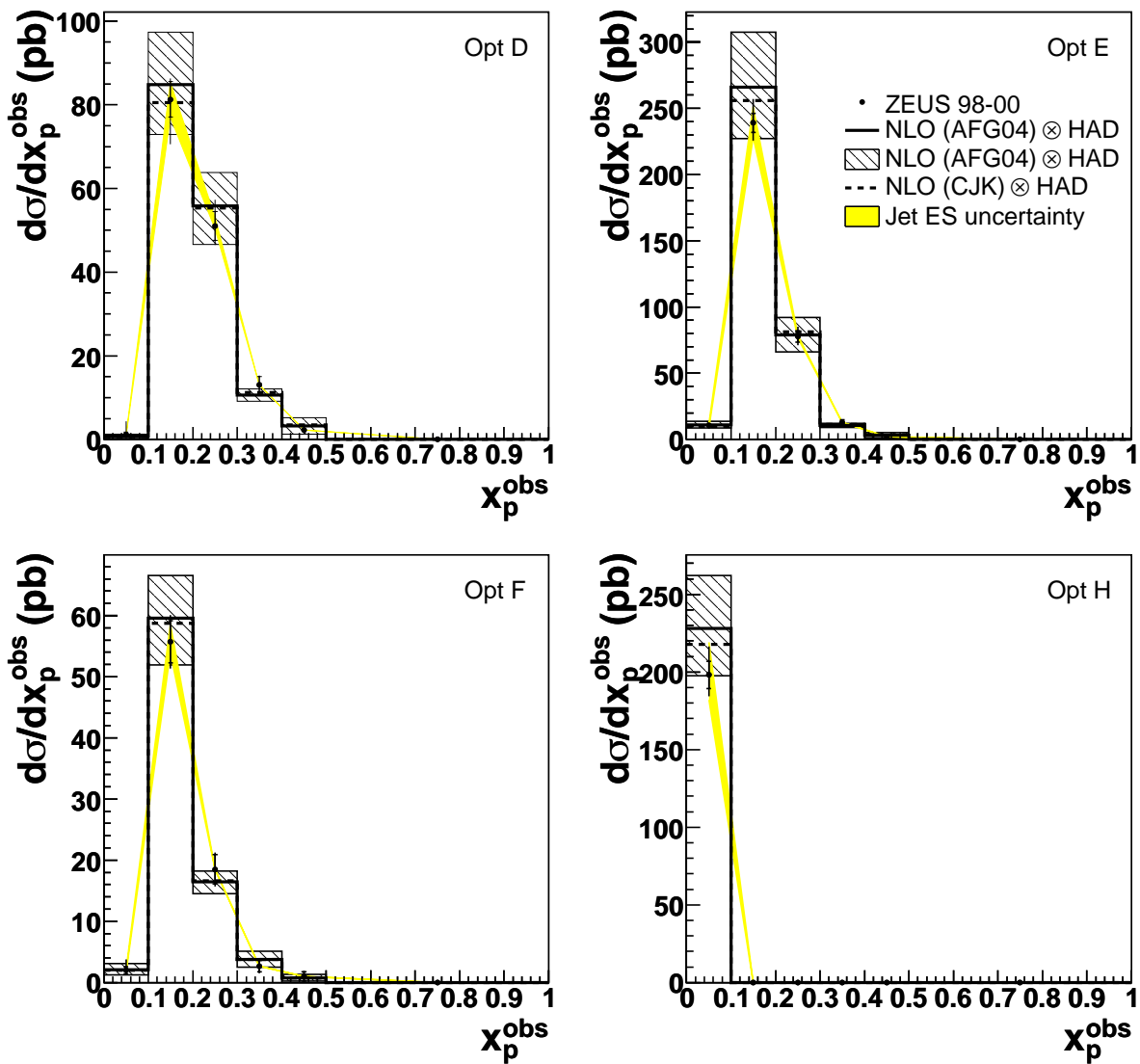


Figure 9.12: High- x_γ^{obs} optimised cross-sections. For further details, see the cross-section definitions in table 5.12 and the caption to figure 9.1.

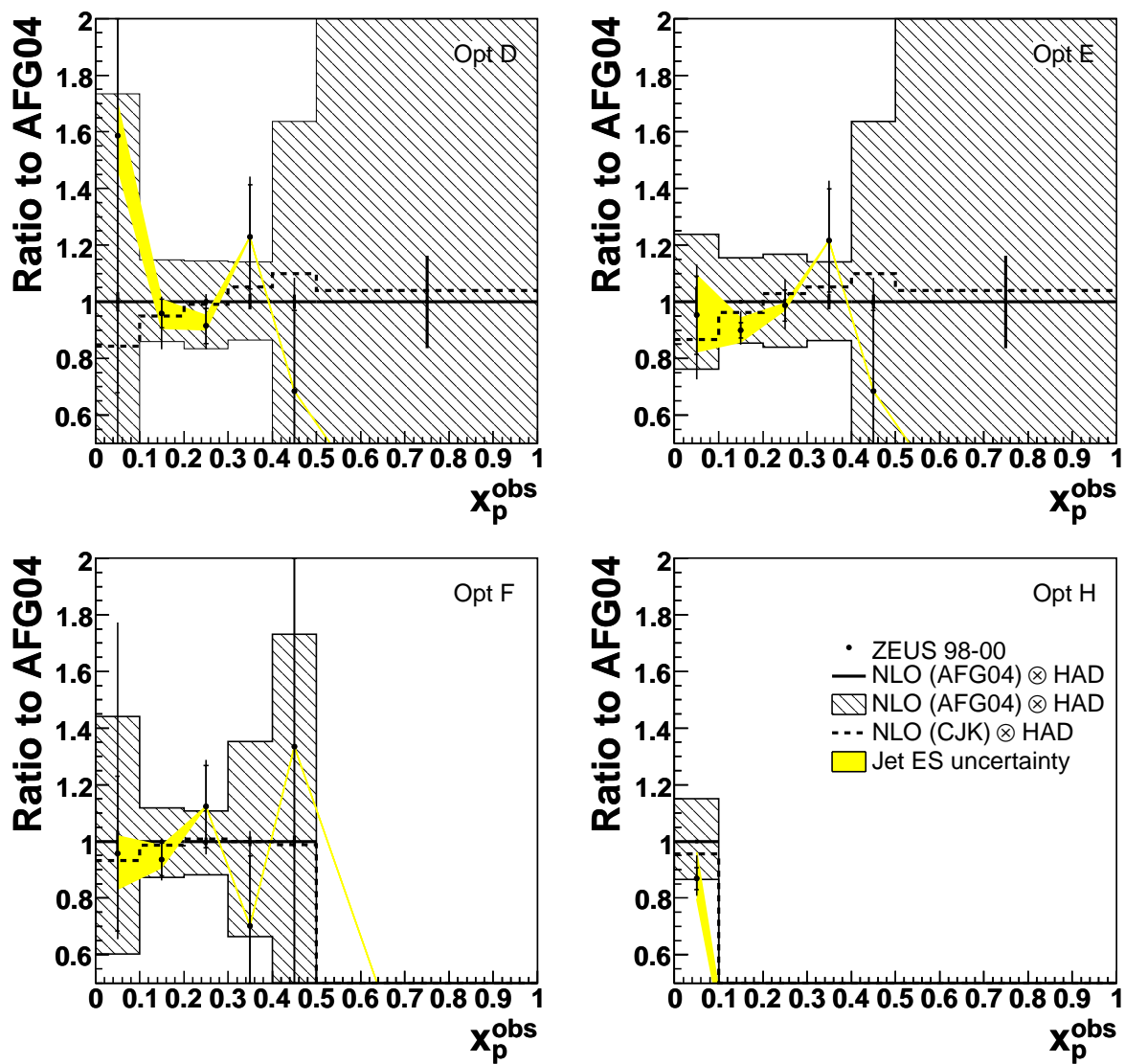


Figure 9.13: High- x_γ^{obs} optimised cross-sections (continued). For further details, see the cross-section definitions in table 5.12 and the caption to figure 9.1.

Bin	$\frac{d\sigma}{dx_p^{obs}}$ (pb)	δ_{stat}	δ_{syst}	δ_{ES}
0.00,0.10	0.0	± 0.0	0.0 0.0	0.0 0.0
0.10,0.20	14.6	± 13.3	21.6 -9.1	12.9 -12.1
0.20,0.30	89.3	± 5.4	17.3 -8.3	5.0 -7.2
0.30,0.40	46.1	± 7.7	6.6 -10.3	0.6 -3.0
0.40,0.50	7.0	± 19.3	12.4 -19.6	0.0 0.0
0.50,1.00	0.5	± 38.8	22.9 -15.6	0.0 0.0

(a) OptA

Bin	$\frac{d\sigma}{dx_p^{obs}}$ (pb)	δ_{stat}	δ_{syst}	δ_{ES}
0.00,0.10	18.6	± 9.7	20.2 -14.1	7.5 -11.3
0.10,0.20	118.4	± 4.6	4.3 -5.0	4.2 -3.9
0.20,0.30	12.2	± 16.7	18.6 -12.8	0.0 0.0
0.30,0.40	0.2	± 109.2	247.1 -101.0	0.0 0.0
0.40,0.50	0.0	± 0.0	0.0 0.0	0.0 0.0
0.50,1.00	0.1	± 526.7	184.2 -209.6	0.0 0.0

(b) OptB

Bin	$\frac{d\sigma}{dx_p^{obs}}$ (pb)	δ_{stat}	δ_{syst}	δ_{ES}
0.00,0.10	0.2	± 60.4	90.6 -116.5	20.0 -20.0
0.10,0.20	281.5	± 2.7	9.1 -5.5	6.9 -6.2
0.20,0.30	230.0	± 3.2	6.9 -3.9	3.5 -2.9
0.30,0.40	47.1	± 7.2	6.5 -7.3	0.3 -0.3
0.40,0.50	8.6	± 18.5	13.6 -10.0	0.0 0.0
0.50,1.00	0.2	± 50.4	107.6 -11.9	0.0 0.0

(c) OptC

Bin	$\frac{d\sigma}{dx_p^{obs}}$ (pb)	δ_{stat}	δ_{syst}	δ_{ES}
0.00,0.10	0.0	± 0.0	0.0 0.0	0.0 0.0
0.10,0.20	73.0	± 5.5	4.8 -11.7	8.1 -7.4
0.20,0.30	118.1	± 4.4	6.8 -5.0	5.0 -4.5
0.30,0.40	43.3	± 7.7	10.9 -4.0	2.0 -0.7
0.40,0.50	8.6	± 18.5	13.6 -10.0	0.0 0.0
0.50,1.00	0.2	± 50.4	107.6 -11.9	0.0 0.0

(d) OptG

Table 9.1: The statistical, systematic and jet energy scale uncertainties for the low- x_γ^{obs} cross-sections, shown as a percentage of the nominal cross-section prediction

Bin	$\frac{d\sigma}{dx_p^{obs}}$ (pb)	δ_{stat}	δ_{syst}	δ_{ES}
0.00,0.10	1.1	± 57.2	$^{269.4}_{-68.2}$	$^{7.1}_{-7.1}$
0.10,0.20	81.3	± 5.2	$^{3.3}_{-12.1}$	$^{5.1}_{-5.4}$
0.20,0.30	51.0	± 6.9	$^{10.1}_{-5.8}$	$^{4.0}_{-1.4}$
0.30,0.40	13.1	± 15.0	$^{8.9}_{-10.3}$	$^{0.0}_{0.0}$
0.40,0.50	2.2	± 41.7	$^{41.1}_{-19.9}$	$^{0.0}_{0.0}$
0.50,1.00	0.0	± 0.0	$^{0.0}_{0.0}$	$^{0.0}_{0.0}$

(a) OptD

Bin	$\frac{d\sigma}{dx_p^{obs}}$ (pb)	δ_{stat}	δ_{syst}	δ_{ES}
0.00,0.10	10.6	± 14.4	$^{12.1}_{-18.9}$	$^{14.9}_{-13.5}$
0.10,0.20	239.1	± 3.0	$^{6.9}_{-4.8}$	$^{4.9}_{-4.5}$
0.20,0.30	77.8	± 5.6	$^{7.5}_{-6.3}$	$^{0.7}_{-1.6}$
0.30,0.40	12.9	± 15.0	$^{8.9}_{-9.6}$	$^{0.0}_{0.0}$
0.40,0.50	2.2	± 41.7	$^{41.1}_{-19.9}$	$^{0.0}_{0.0}$
0.50,1.00	0.0	± 0.0	$^{0.0}_{0.0}$	$^{0.0}_{0.0}$

(b) OptE

Bin	$\frac{d\sigma}{dx_p^{obs}}$ (pb)	δ_{stat}	δ_{syst}	δ_{ES}
0.00,0.10	2.0	± 28.5	$^{80.4}_{-13.8}$	$^{6.6}_{-13.1}$
0.10,0.20	55.7	± 6.2	$^{4.9}_{-4.7}$	$^{5.2}_{-3.1}$
0.20,0.30	18.5	± 12.9	$^{7.0}_{-7.8}$	$^{0.0}_{0.0}$
0.30,0.40	2.6	± 35.0	$^{32.1}_{-27.9}$	$^{0.0}_{0.0}$
0.40,0.50	1.0	± 73.4	$^{45.3}_{-73.1}$	$^{0.0}_{0.0}$
0.50,1.00	0.0	± 0.0	$^{0.0}_{0.0}$	$^{0.0}_{0.0}$

(c) OptF

Bin	$\frac{d\sigma}{dx_p^{obs}}$ (pb)	δ_{stat}	δ_{syst}	δ_{ES}
0.00,0.10	198.2	± 4.4	$^{8.2}_{-5.4}$	$^{10.6}_{-8.1}$
0.10,0.20	0.0	± 0.0	$^{0.0}_{0.0}$	$^{0.0}_{0.0}$
0.20,0.30	0.0	± 0.0	$^{0.0}_{0.0}$	$^{0.0}_{0.0}$
0.30,0.40	0.0	± 0.0	$^{0.0}_{0.0}$	$^{0.0}_{0.0}$
0.40,0.50	0.0	± 0.0	$^{0.0}_{0.0}$	$^{0.0}_{0.0}$
0.50,1.00	0.0	± 0.0	$^{0.0}_{0.0}$	$^{0.0}_{0.0}$

(d) OptH

Table 9.2: The statistical, systematic and jet energy scale uncertainties for the high- x_γ^{obs} cross-sections, shown as a percentage of the nominal cross-section prediction

by a mean pseudorapidity between $1.5 < \bar{\eta} \leq 2.5$ which has already been seen from the differential cross-section with respect to $\bar{\eta}$ to be poorly described by the CJK prediction. It is constructive to compare optimised cross-section G (OptG) directly with OptC. The only difference between OptC and OptG is that OptG is conducted with harder transverse energy cuts ($E_{T,1} > 25$ GeV and $E_{T,2} > 15$ GeV). For the case of OptG the CJK prediction provides a good description of both the shape and normalisation of the data, in contrast to the OptC case. This point is reinforced by looking at optimised cross-section B (OptB) which is also conducted with harder transverse energy cuts of $E_{T,1} > 25$ GeV and $E_{T,2} > 15$ GeV but in the more central pseudorapidity region given by $1 < \eta_1, \eta_2 \leq 2$. Once again the CJK prediction provides a better description of the shape and normalisation of the measured data.

9.6.2 High- x_γ^{obs} Optimised Cross-Sections

The high- x_γ^{obs} optimised differential cross-sections with respect to x_p^{obs} are shown in figures 9.12 and 9.13, and also given in tables J.16-J.19. Statistically significant data points are yielded in the region $0 < x_p^{obs} \leq 0.3$. There are a negligible number of events in the region $0.4 < x_p^{obs} \leq 1$. The high- x_γ^{obs} cross-sections are therefore less sensitive to high- x_p^{obs} events than the low- x_γ^{obs} cross-sections, as expected. To illustrate more clearly the precision to which these measurements are made, table 9.2 illustrates the various uncertainties on the measured cross-sections expressed as a percentage of the nominal cross-section values. For bins with a statistical uncertainty of 10% or less (6 bins altogether) the average systematic error is ${}^{+6.8}_{-6.5}\%$. The average jet energy scale uncertainty for such bins is ${}^{+5.1}_{-4.0}\%$. A good description of both the normalisation and the shape of the data are obtained using the NLO predictions.

9.7 Photon Structure

The cross-sections presented in this thesis have provided a good test of the different photon parameterisations currently available. The predictions from five different parameterisations (AFG04, CJK, AFG, GRV and SAL) were compared to the measured data. Figure 9.2 showed the comparison for the case of the differential cross-section with respect to x_γ^{obs} and figures 9.14 and 9.15 show the comparison for the low- x_γ^{obs} cross-sections (excluding $|\Delta\phi|$) measured as part of

this analysis. It must firstly be noted that the predictions of AFG04 and AFG are very similar and will be discussed collectively as just AFG04 in the following discussion. It must also be noted that the predictions of SAL are similar in shape and normalisation to AFG04. The GRV predictions tend to be similar in shape to the AFG04 predictions but differ in normalisation and typically lie about 15 – 20% above AFG04. The CJK parameterisation differs most from AFG04, both in terms of shape and normalisation and so the following discussion will focus on these two particular photon PDFs.

By referring to figure 9.2 it can be seen that the measured data (with respect to x_γ^{obs}) is well described by the AFG04, AFG, GRV and SAL predictions but poorly described by the CJK prediction. In particular, CJK predicts the shape of the measured x_γ^{obs} cross-section poorly, with the data falling off with decreasing x_γ^{obs} quicker than the calculation. It has also been seen from the consideration of the low- x_γ^{obs} optimised cross-sections (section 9.6.1) that at higher transverse energies CJK provides an improved description of the data (surpassing the prediction of AFG04). This was also seen for the x_γ^{obs} cross-sections measured in the previous dijet analysis (see figure 9.18). Consideration of the cross-sections with respect to $E_{T,1}$ and \bar{E}_T (see figures 9.5 and 9.6), particularly \bar{E}_T , also suggest that whereas the description of the data by the CJK prediction is poor at low transverse energies, at higher transverse energies it is much improved compared with the AFG04 prediction. The factorisation scale, used for the nominal predictions, is equal to half the sum of the transverse energies of the outgoing partons from the hard interaction (see equation 8.2). This loosely corresponds to half of the sum of the transverse energies of the outgoing jets. This quantity itself is therefore closely correlated with \bar{E}_T and consideration of figure 9.6 implies that the CJK prediction describes the data poorly for relatively low values of μ_F^2 ($\lesssim 500 \text{ GeV}^2$) but describes the data relatively well at high values of the factorisation scale ($\gtrsim 500 \text{ GeV}^2$). Armed with this observation it is now worth considering the CJK and AFG04 parameterisations in slightly more detail.

The AFG04 and CJK photon PDFs are obtained by fits to LEP F_2^γ data. It is important to note that neither group includes any HERA photoproduction data in their fitted data sets. For exact details of the fitted data sets and the fitting methods used, the reader is referred to [92–96]. Only the results of the fit shall be considered here. Figure 9.19 shows the comparison of the NLO parton densities predicted by the CJK, AFG and GRV fits at $\mu_F^2 = 10 \text{ GeV}^2$. The CJK fit predicts

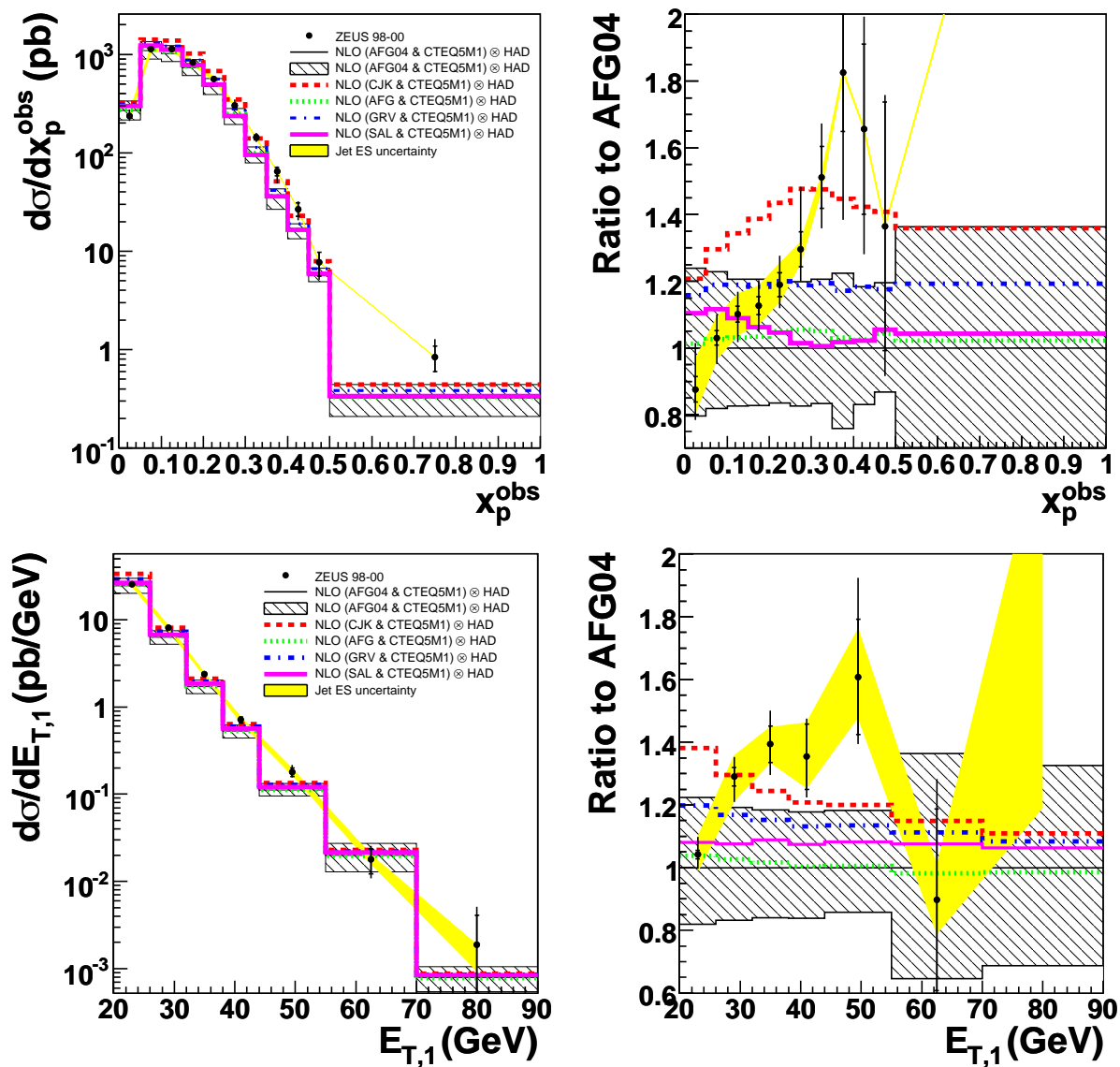


Figure 9.14: Measured Low- x_γ^{obs} differential cross-sections with respect to x_p^{obs} (top) and $E_{T,1}$ (bottom) compared to the predictions of the AFG04, CJK, AFG, GRV and SAL photon parameterisations. The right-hand plots show the ratios of the data and the predictions of each respective parameterisation, relative to the AFG04 predicted points.

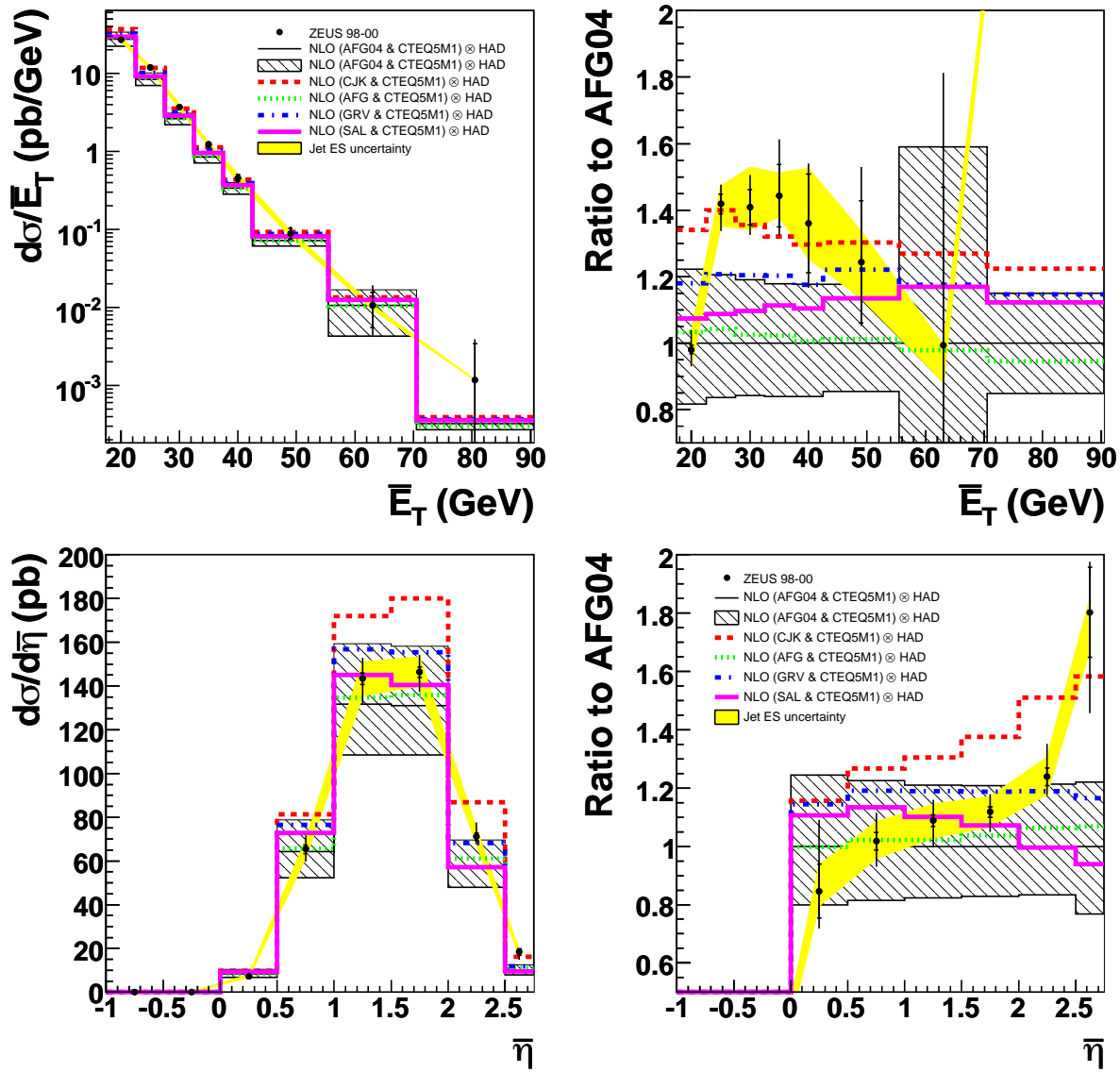


Figure 9.15: Measured Low- x_γ^{obs} differential cross-sections with respect to \bar{E}_T (top) and $\bar{\eta}$ (bottom) compared to the predictions of the AFG04, CJK, AFG, GRV and SAL photon parameterisations. The right-hand plots show the ratios of the data and the predictions of each respective parameterisation, relative to the AFG04 predicted points.

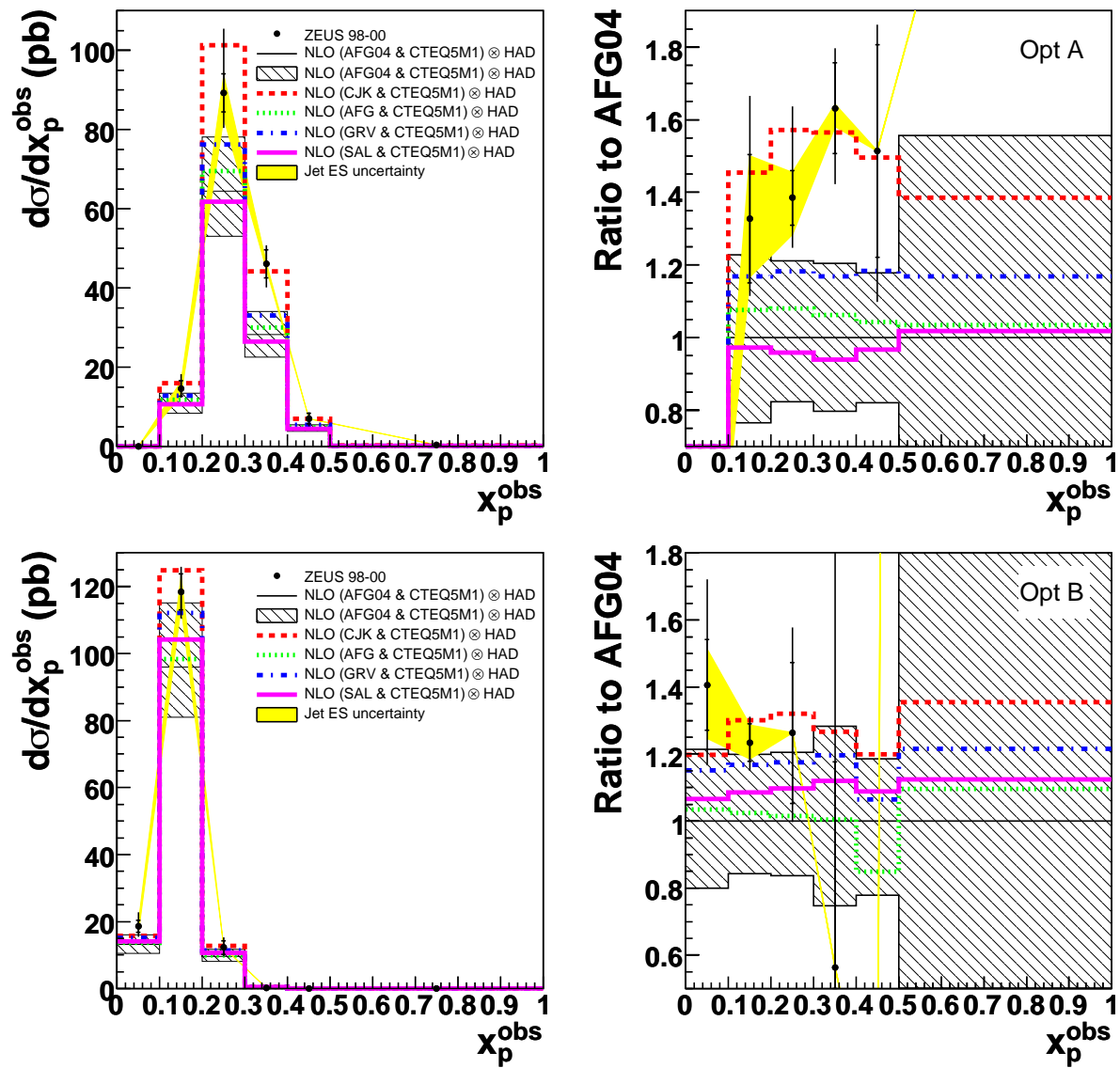


Figure 9.16: Measured Low- x_γ^{obs} optimised cross-sections compared to the predictions of the AFG04, CJK, AFG, GRV and SAL photon parameterisations. The right-hand plots show the ratios of the data and the predictions of each respective parameterisation, relative to the AFG04 predicted points.

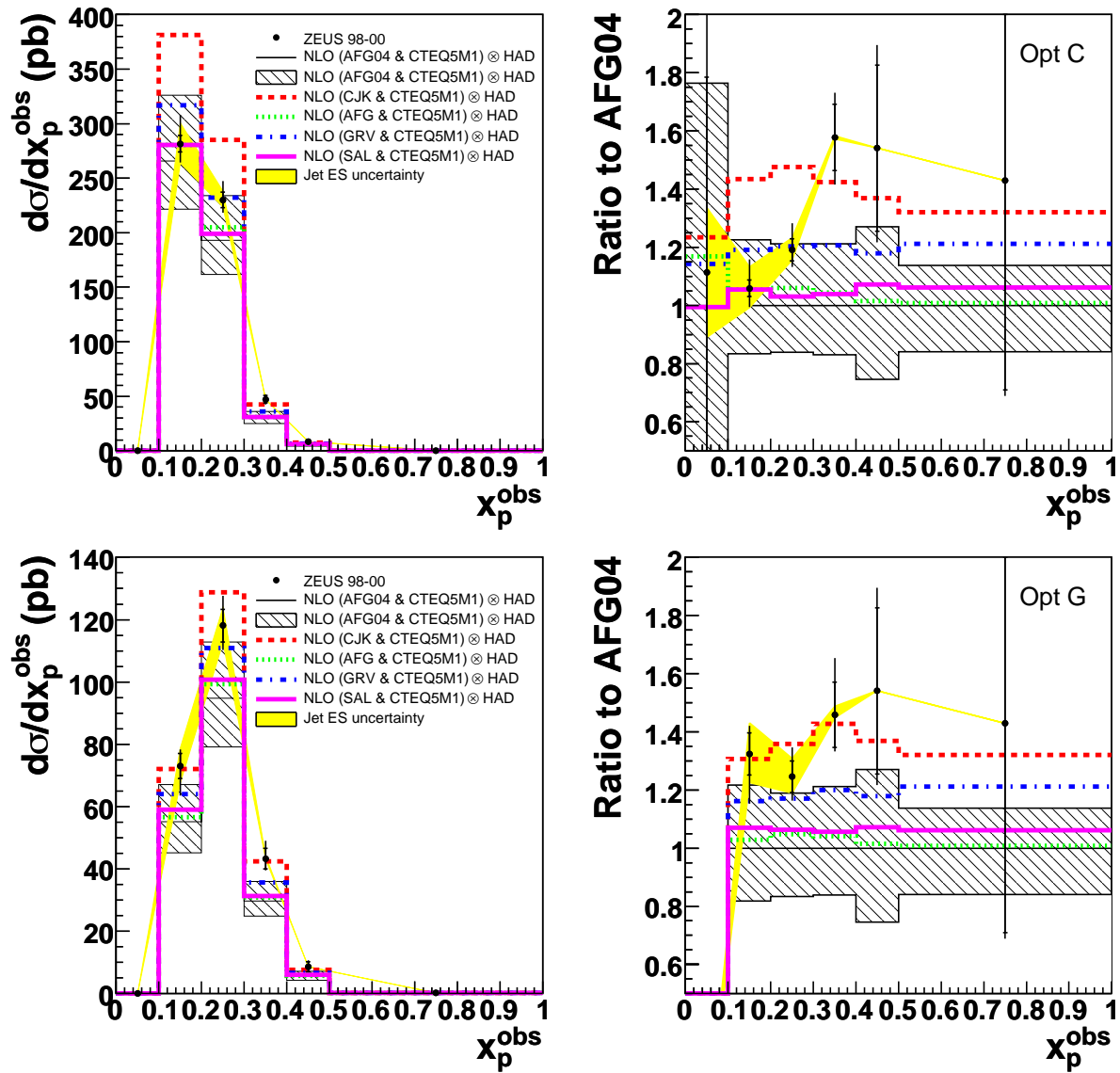


Figure 9.17: Measured Low- x_γ^{obs} optimised cross-sections (continued) compared to the predictions of the AFG04, CJK, AFG, GRV and SAL photon parameterisations. The right-hand plots show the ratios of the data and the predictions of each respective parameterisation, relative to the AFG04 predicted points.

HERA dijet photoproduction

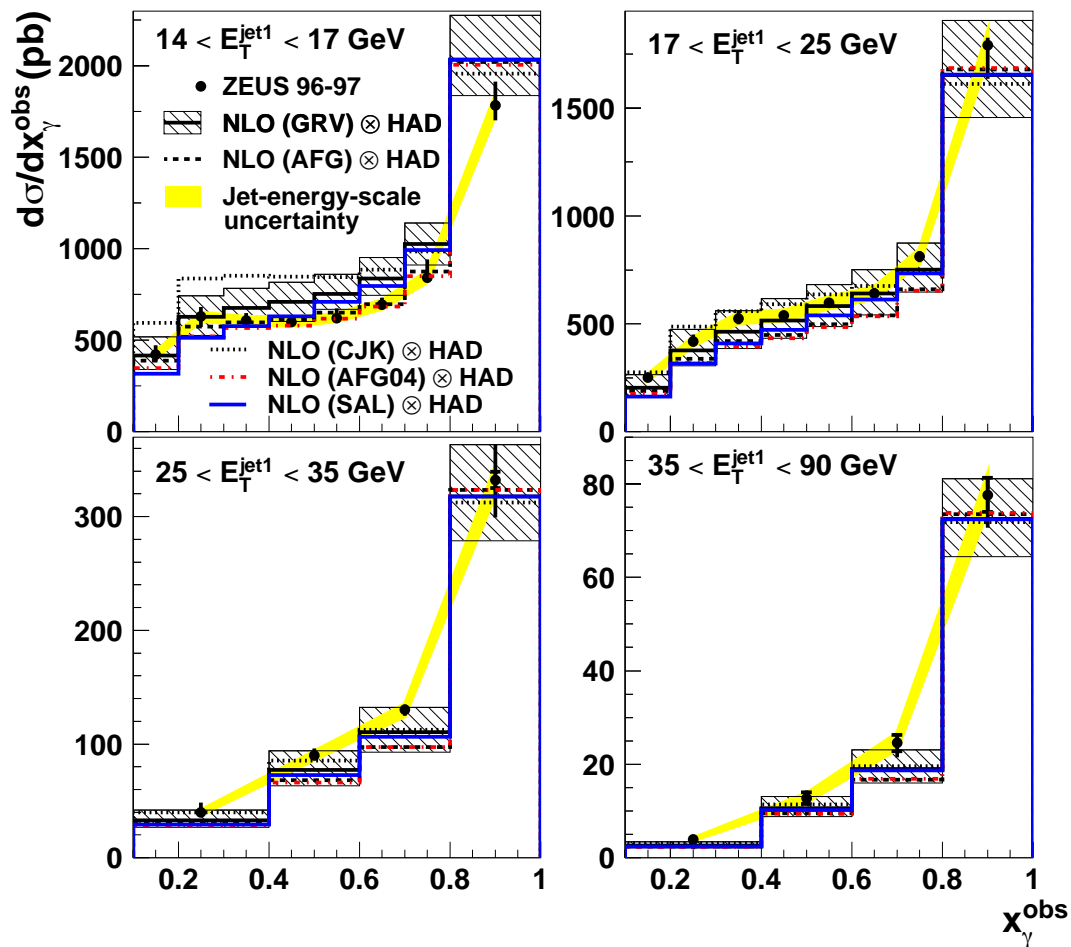


Figure 9.18: The differential cross-section with respect to x_γ^{obs} , from the previous dijet analysis [51], in four regions of $E_{T,1}$ compared to NLO predictions using a variety of photon parameterisations. Figure taken from [98]

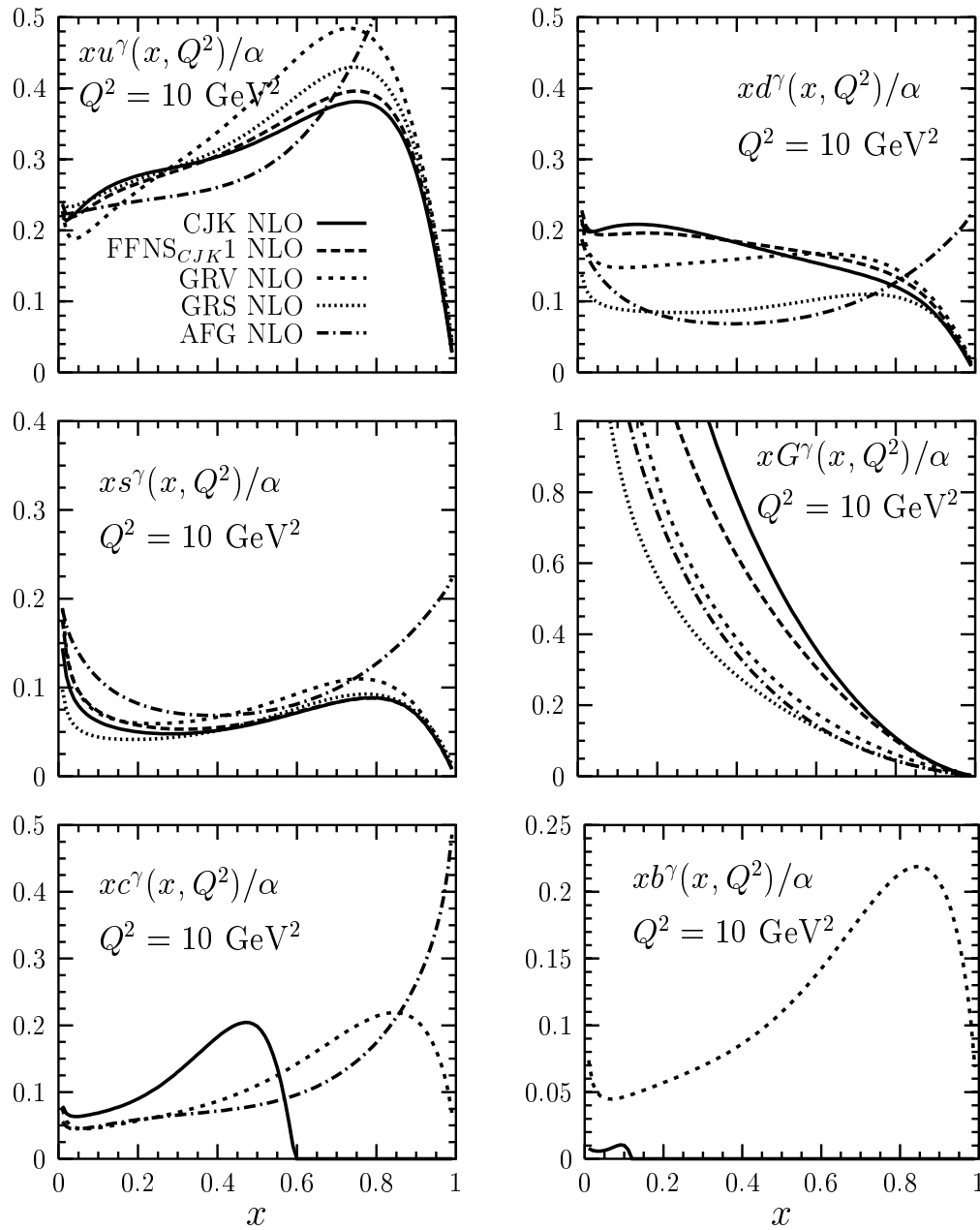


Figure 9.19: Comparison of the NLO parton densities predicted by the CJK, GRV and AFG parameterisations at $Q^2 (\equiv \mu_F^2) = 10 \text{ GeV}^2$, as a function of x . Figure taken from [101].

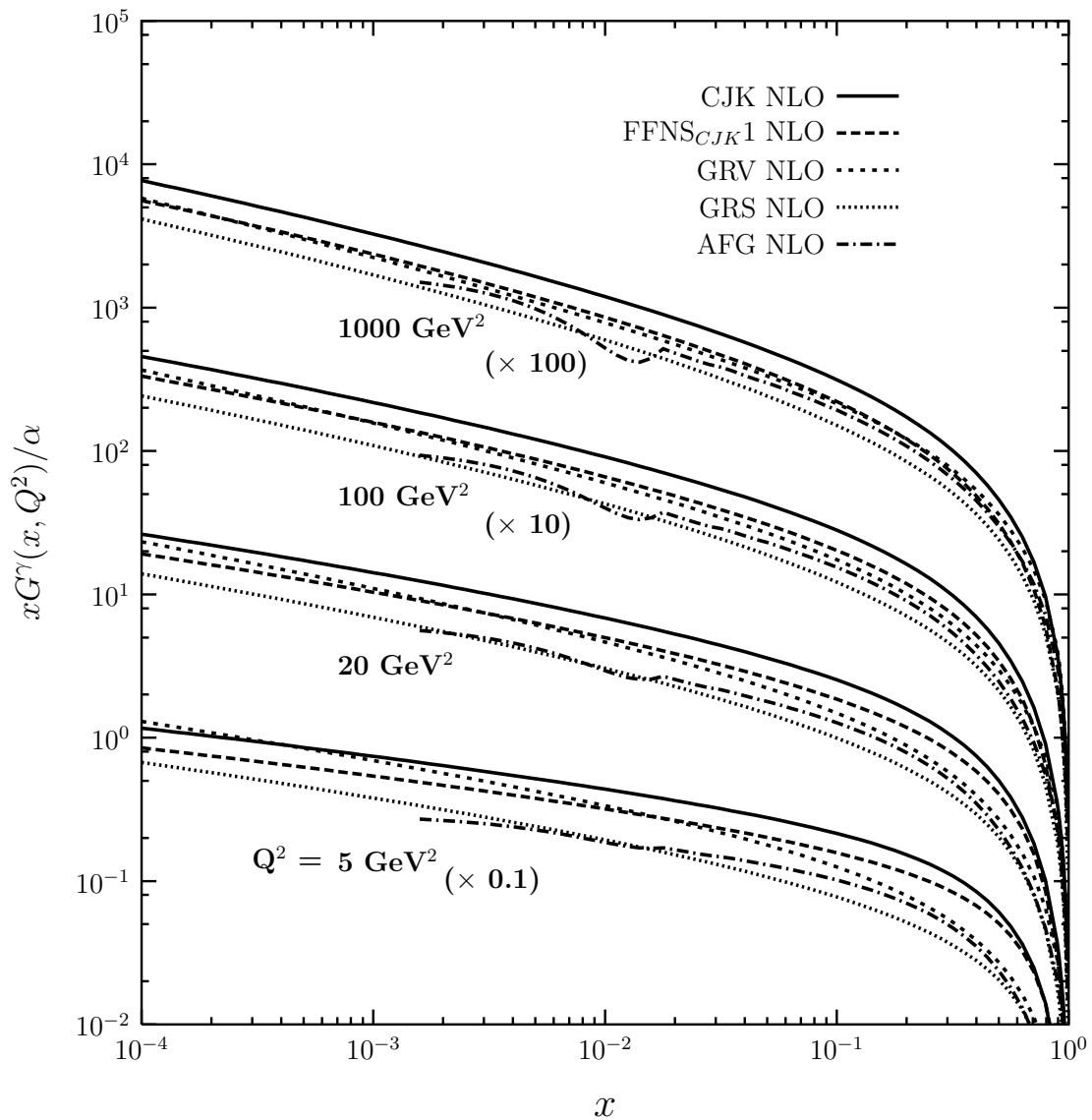
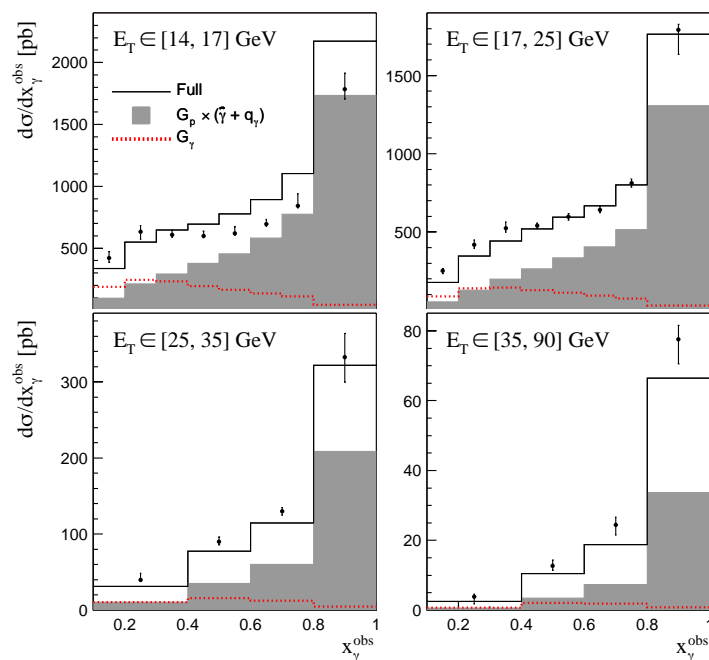


Figure 9.20: Comparison of the gluon density at four values of Q^2 in the CJK model with the GRV and AFG densities. Figure taken from [101].

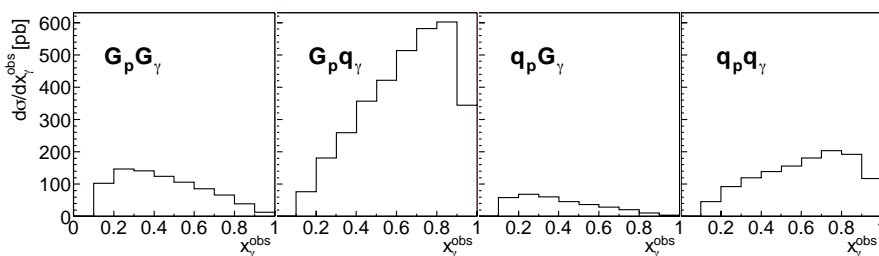
a more rapidly increasing gluon density, with decreasing x (or more precisely, x_γ) than any of the other fits. From figure 9.20 it can be seen that this increased gluon density, relative to AFG and GRV, persists even to high scales. Data on the photon structure function, F_2^γ , essentially determine the quark content of the photon and leaves the gluon poorly constrained. This explains the large differences between the gluon density predicted by CJK and the AFG.

The disagreement between the data and CJK seen in the present analysis (figure 9.1) and that seen in the previous dijet analysis [51] (figure 9.18) could be due to the gluon density in the CJK model. From figure 9.19 it can be seen that the gluon density increases at a greater rate than AFG with decreasing x_γ . This could be used to explain why the disagreement between the data and the CJK prediction in figure 9.1 gets worse as x_γ^{obs} decreases. However, the observation that at high transverse energies CJK describes the data well, coupled with the fact that the difference between the CJK and AFG gluon densities persists even to high scales, implies that the gluon contribution from the photon dies away with increasing scales (transverse energy). Once the gluon contribution has lost its significance at large scales the remaining contribution from the quarks of the photon interacting with the partons from the proton are better described using CJK than AFG. All of this suggests two important issues. Firstly, ZEUS photoproduction data are sensitive to the gluon density in the photon and would provide a way of constraining the gluon in a photon PDF fit. Secondly, a CJK fit incorporating ZEUS photoproduction data would be very interesting as the discrepancy between the data and the CJK prediction at low transverse energies would hopefully be remedied whilst desirably leaving the good agreement between the data and CJK at higher transverse energies untarnished.

At this point it becomes important to discuss the SAL photon parameterisation because this fit includes ZEUS proton structure function (F_2^p) data [102] and dijet photoproduction data from [51] (actually the data shown in figure 9.18) in its fitted data set. The plots in figure 9.21 illustrate the sensitivity of such cross-sections to the gluon density in the photon. It can be seen that the cross-section with respect to x_γ^{obs} does indeed become more sensitive to the gluon density in the photon as x_γ^{obs} decreases. The inclusion of such data in the fitted data set of the SAL fit must therefore constrain the gluon density in the photon. Because the gluon is largely unconstrained in the other photon PDF fits the SAL fit must provide a better model of photon structure in kinematic regions



(a) The dijet cross-sections of figure 9.18 with the contributions (according to the SAL parameterisation) from the gluon from the photon (G_γ) and the gluons from the proton. Figure taken from [96].



(b) Typical contributions (according to the SAL parameterisation) of different parton types, as denoted in the figure, to $d\sigma/dx_\gamma^{obs}$ for $E_T \in (14, 17)$ GeV (the upper left plot from figure 9.18). Figure taken from [96].

Figure 9.21: Two plots which illustrate the sensitivity of dijet photoproduction cross-sections to the gluon density in the photon.

where the gluon contribution to the photon structure is significant. It has been seen that the predictions of AFG04, AFG and GRV are quite similar to SAL which also suggests that the gluon densities used in these parameterisations model the gluon component of the photon more closely than CJK. However, the SAL parameterisation still does not fare as well as the CJK parametrisation at high transverse energies which suggests that in regions where the gluon component of the photon is not so significant CJK provides the better model of photon structure i.e. CJK provides a better model of the quark component of the photon. It is worth reiterating that this discussion has once again illustrated the potential of CJK fits incorporating HERA dijet photoproduction data. Perhaps such a parametrisation is capable of providing a good description of processes involving photon structure at all transverse energies considered in this analysis. Finally, it is worth noting that both the present analysis and the previous dijet analysis [51] were conducted at high transverse energies. By performing high statistics analyses at lower transverse energies it may be possible to obtain data which shows considerable sensitivity to the the gluon content of the photon.

Chapter 10

Results and Discussion - Part II

In the last chapter the cross-sections which have been measured as part of the analysis presented in this thesis were discussed. During the discussion, particular emphasis was placed on the relevance of such measurements in yielding information about the structure of the photon. This chapter will focus attention on proton structure. In particular the results of including the optimised cross-sections in a new QCD fit will be presented.

10.1 Grid Reconstruction of the Optimised Cross-Sections

Before the optimised cross-sections, presented in the previous chapter, can be included in the fitted data set of a QCD fit, a check has to be made that the grid method, used for the fast computation of the cross-section within a QCD fit (see chapter 4), reconstructs the cross-section to a satisfactory level of accuracy. Figure 10.1 shows the ratio of the grid reconstructed optimised cross-sections to the predictions of an independent version of the NLO jet production code of Frixione and Ridolfi [19]. The optimised cross-sections can be reconstructed using the grid reconstruction procedure to an accuracy of $\sim 1-2\%$. The reconstruction is poorer in the first bin due to the very low value of the cross-section in this bin for most of the optimised cross-sections.

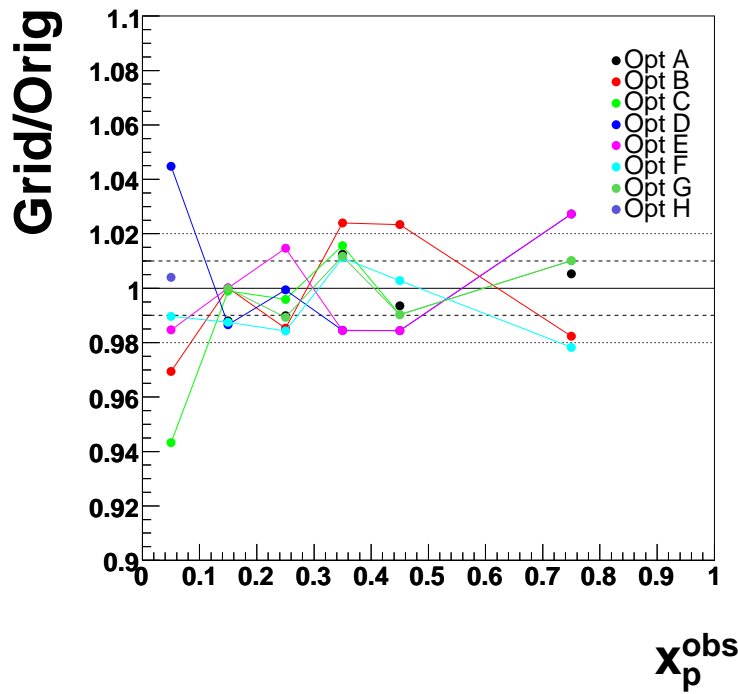


Figure 10.1: The ratio between the grid reconstructed cross-sections and the cross-section predictions of an independent version of the NLO γp jet production code of Frixione and Ridolfi [19]

10.2 QCD Fits Using Optimised Cross-Sections

In this section the effects of including the high and low- x_γ^{obs} optimised cross-sections in the fitted data set¹ of the ZEUS QCD fits, on the extracted gluon PDF, will be discussed. Figure 10.2 shows the fractional uncertainty on the extracted gluon PDF at a range of Q^2 values for a fit which includes both the high and low- x_γ^{obs} cross-sections. Not all the cross-sections can be included in the fit at the same time because optimised cross-section C (OptC) is correlated with optimised cross-section G (OptG) (the latter is the same as the former apart from slightly harder transverse energy cuts). Similarly, optimised cross-section D (OptD) is correlated with optimised cross-section E (OptE). Therefore, only certain combinations of the optimised cross-sections can be included in the fitted data set. However, all combinations have been fitted and the results are very similar so, for clarity, we shall only consider the fits to optimised cross-sections A,B,C,D,F and H in the following discussion. Figure 10.3 shows the fractional uncertainty on the extracted gluon PDF for the case where only the high- x_γ^{obs} cross-sections are included in the fit. Recall from chapter 4 that the motivation

¹The fitted data set of the ZEUS-Jets fit which was discussed in detail in chapter 4

for including only high- x_γ^{obs} dijet cross-sections in the fitted data set is to avoid a significant model uncertainty which arises from the choice of photon PDF.

From figures 10.2 and 10.3 it can be seen that the inclusion of the optimised cross-sections in the fitted data set of the ZEUS QCD fit does not lead to a significant improvement in the precision of the extracted gluon PDF. Although there is little significant improvement in the PDF as a whole, there is at least some improvement at high- x . This is illustrated in figures 10.6 and 10.7 where it can be seen that for the ZEUS-Jets optimised (high- x_γ^{obs}) fit the gluon PDF uncertainties have shrunk by a factor between ~ 0.3 and ~ 0.8 . This effect is masked in figure 10.3 because of the steeply rising shape of the uncertainty band. However, despite this reduction the uncertainty at high- x it still remains large. To quantify the effect of the experimental systematic uncertainties of the optimised cross-section measurements on the precision of the extracted gluon PDF the above fits were carried out with the inclusion of statistical errors only. The results of the statistical error only fit for the case where both the high and low- x_γ^{obs} cross-sections are included in the fitted data set are shown in figure 10.4. The results for the case where just the high- x_γ^{obs} optimised data are used is shown in figure 10.5. For the high- x_γ^{obs} case, comparison of figures 10.3 and 10.5 indicate that there is approximately a factor of two improvement in the reduction of the extracted gluon PDF uncertainty (relative to the ZEUS-Jets fit) when only statistical errors on the cross-section measurements are considered. Comparison of 10.2 and 10.4 for the high and low- x_γ^{obs} case indicate a far larger improvement in the resolved case (by as much as a factor of ten). Systematic errors are therefore partly responsible for washing out the improvement in the precision of the extracted gluon PDF at high- x . However, the improvement in the precision of the extracted gluon PDF for the high- x_γ^{obs} fit, when only statistical errors are included, is nevertheless poor which indicates that this data is not constraining the gluon PDF significantly regardless of the systematic uncertainties on the high- x_γ^{obs} optimised data.

To understand the lack of impact that the optimised cross-sections have on the precision of the extracted gluon PDF, the uncertainties on the theoretical predictions which arise from the uncertainties on the underlying gluon PDF have been compared to the statistical and systematic uncertainties of the measured optimised data. Figures 10.8 and 10.9 show the ZEUS-Type5 (no jets) gluon PDF uncertainties on the low- x_γ^{obs} theoretical predictions compared with the

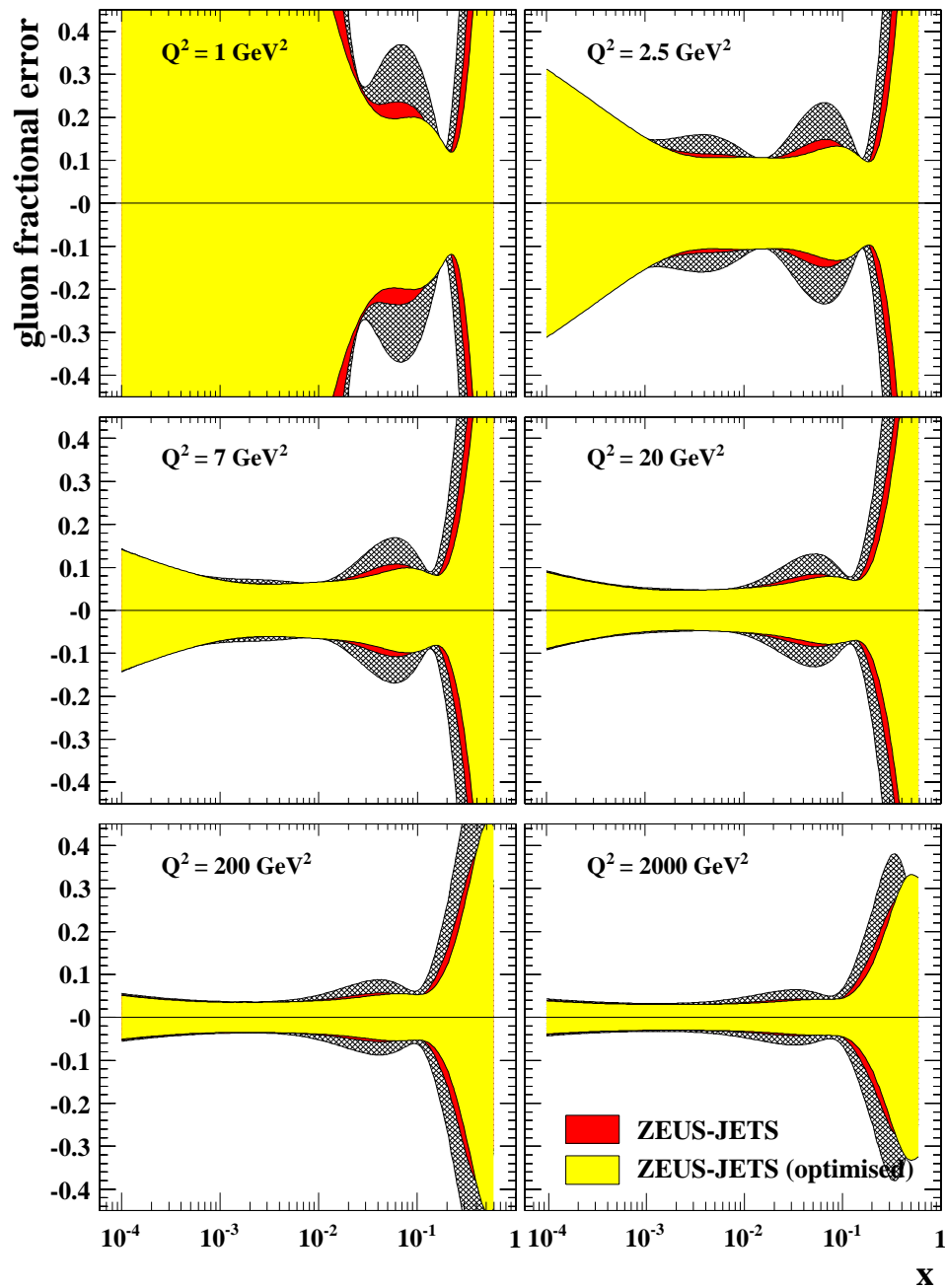


Figure 10.2: The total experimental uncertainty on the gluon PDF for the ZEUS-Jets optimised (low and high- x_{γ}^{obs}) fit (yellow band) compared to the total experimental uncertainties on the gluon PDF for a fit not including the optimised data (ZEUS-Jets fit, red band) and a fit not including any jet data whatsoever (ZEUS-Type5 fit, hatched band). The uncertainties are shown as fractional differences from the central values of the fits, for various values of Q^2 . The total experimental uncertainty includes the statistical, uncorrelated and correlated systematic uncertainties.

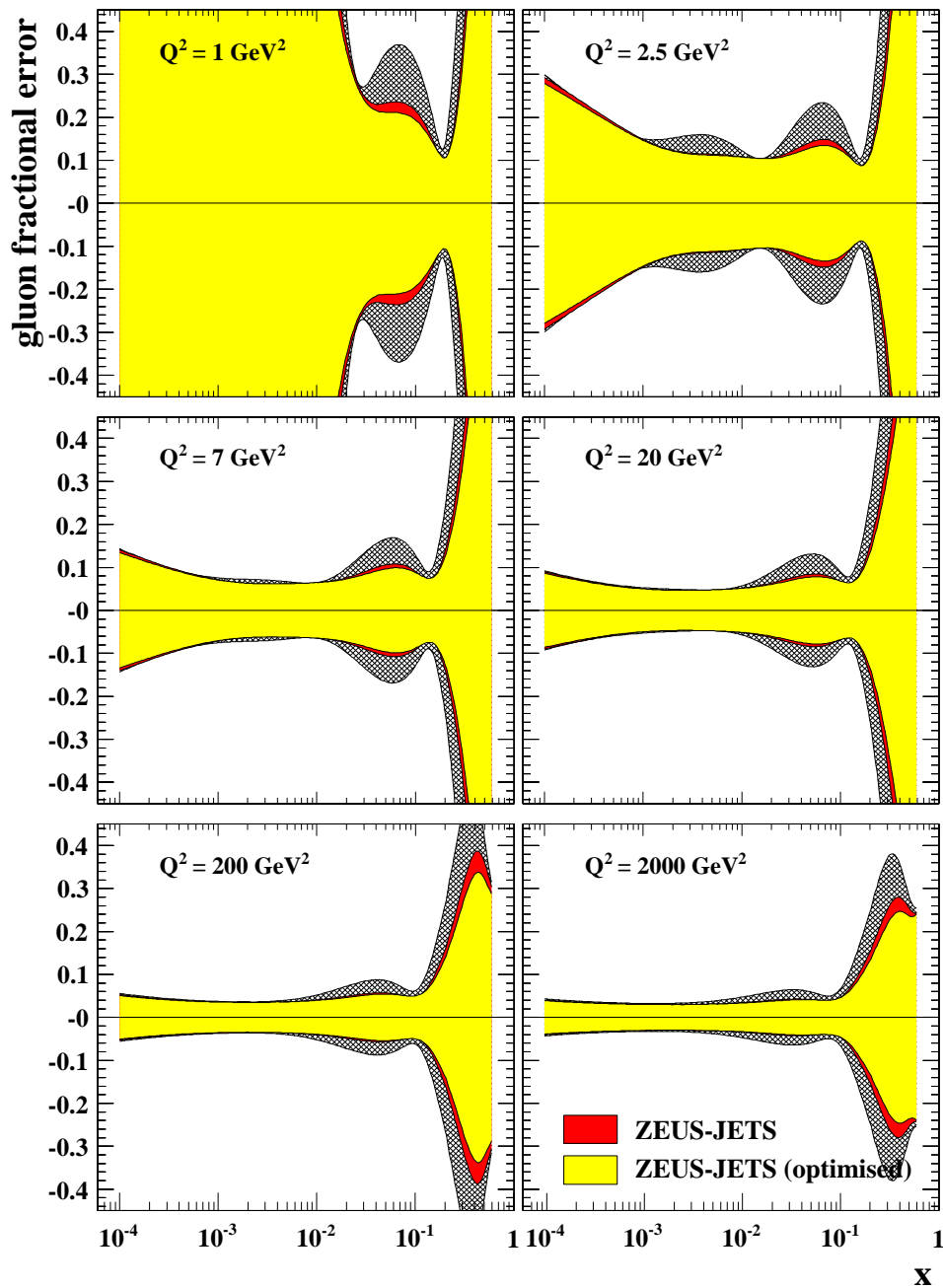


Figure 10.3: The total experimental uncertainty on the gluon PDF for the ZEUS-Jets optimised (high- x_{γ}^{obs}) fit (yellow band) compared to the total experimental uncertainties on the gluon PDF for a fit not including the optimised data (ZEUS-Jets fit, red band) and a fit not including any jet data whatsoever (ZEUS-Type5 fit, hatched band). The uncertainties are shown as fractional differences from the central values of the fits, for various values of Q^2 . The total experimental uncertainty includes the statistical, uncorrelated and correlated systematic uncertainties.

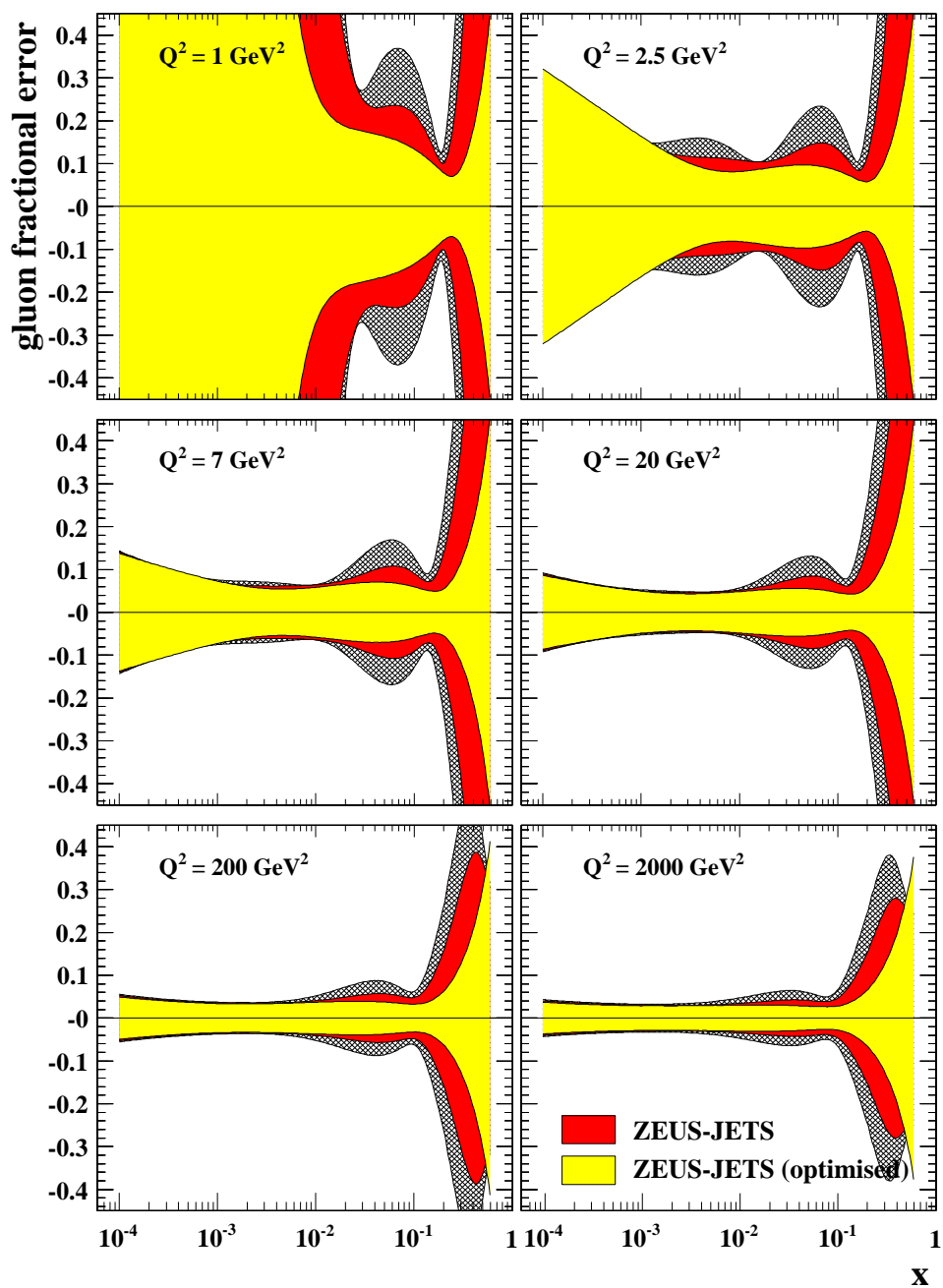


Figure 10.4: The statistical uncertainty on the gluon PDF for the ZEUS-Jets optimised (low and high- x_{γ}^{obs}) fit (yellow band) compared to the statistical uncertainty on the gluon PDF for a fit not including the optimised data (ZEUS-Jets fit, red band) and a fit not including any jet data whatsoever (ZEUS-Type5 fit, hatched band). The uncertainties are shown as fractional differences from the central values of the fits, for various values of Q^2 .

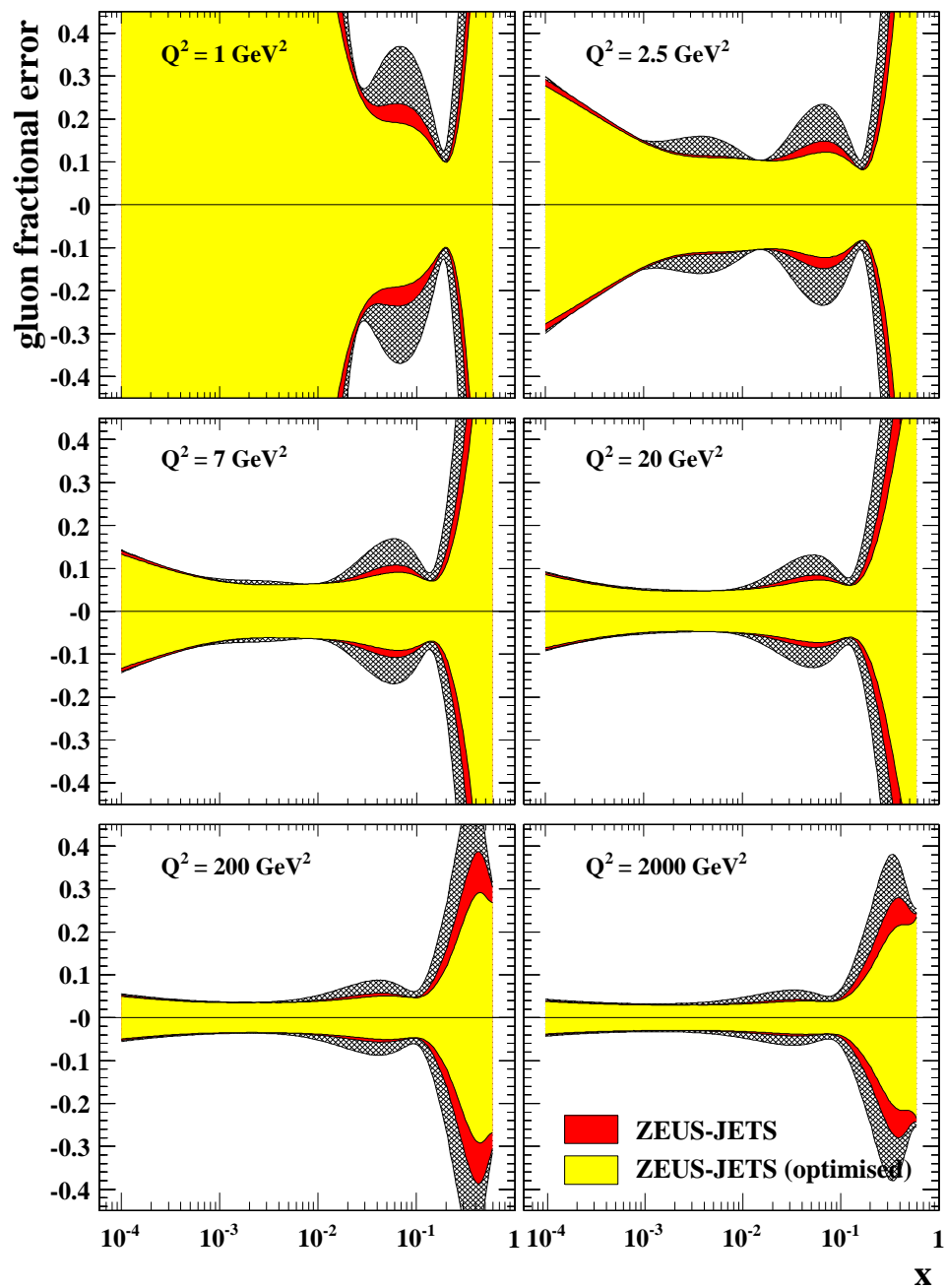


Figure 10.5: The statistical uncertainty on the gluon PDF for the ZEUS-Jets optimised ($high-x_{\gamma}^{obs}$) fit (yellow band) compared to the statistical uncertainty on the gluon PDF for a fit not including the optimised data (ZEUS-Jets fit, red band) and a fit not including any jet data whatsoever (ZEUS-Type5 fit, hatched band). The uncertainties are shown as fractional differences from the central values of the fits, for various values of Q^2 .

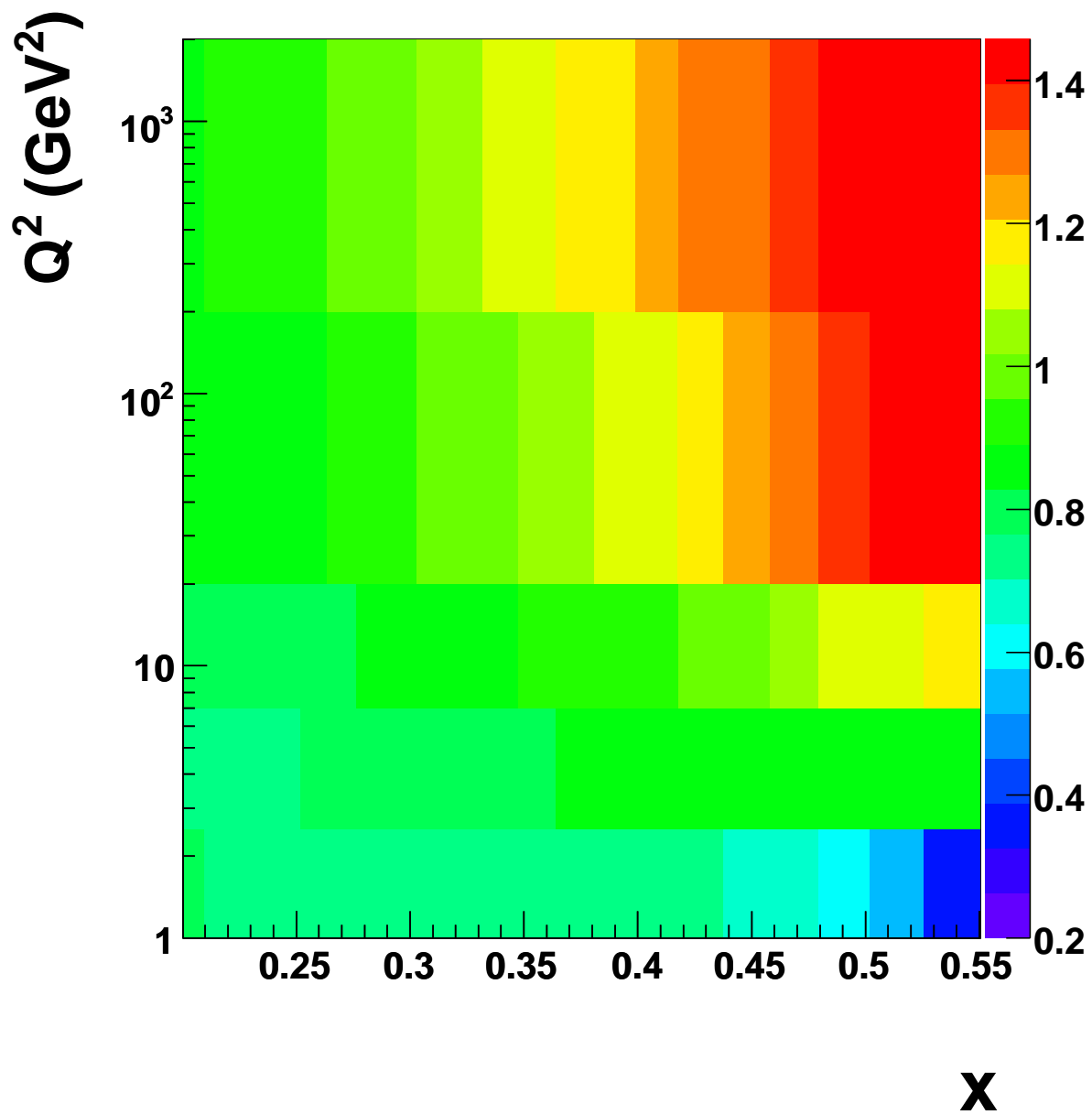


Figure 10.6: Fractional improvement in the gluon PDF at high- x (the ratio of ZEUS-Jets optimised (low and high- x_γ^{obs}) fit) to ZEUS-Jets). This plot corresponds to the information shown in figure 10.2.

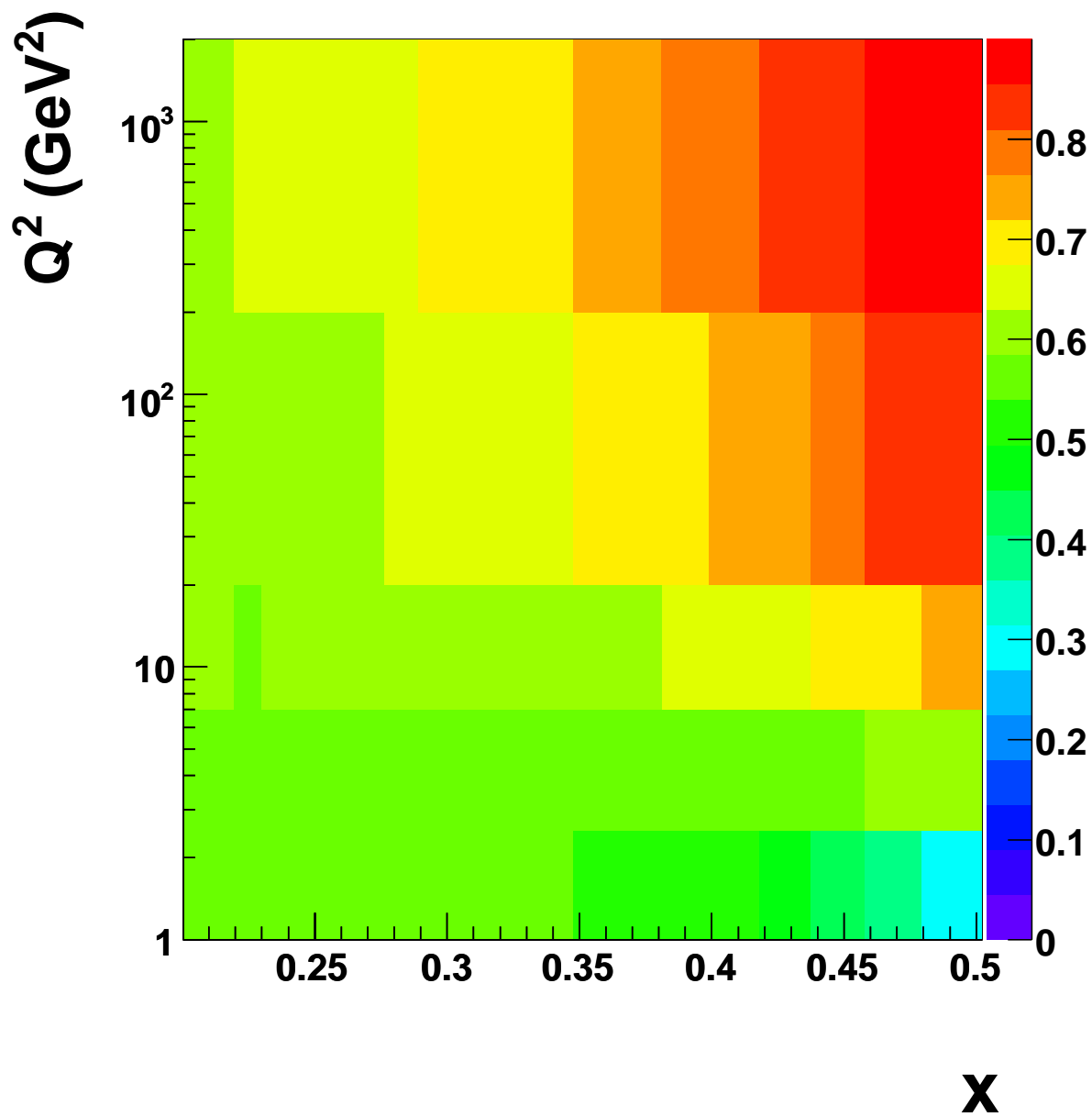


Figure 10.7: Fractional improvement in the gluon PDF at high- x (the ratio of ZEUS-Jets optimised ($high-x_{\gamma}^{obs}$) fit) to ZEUS-Jets). This plot corresponds to the information shown in figure 10.3.

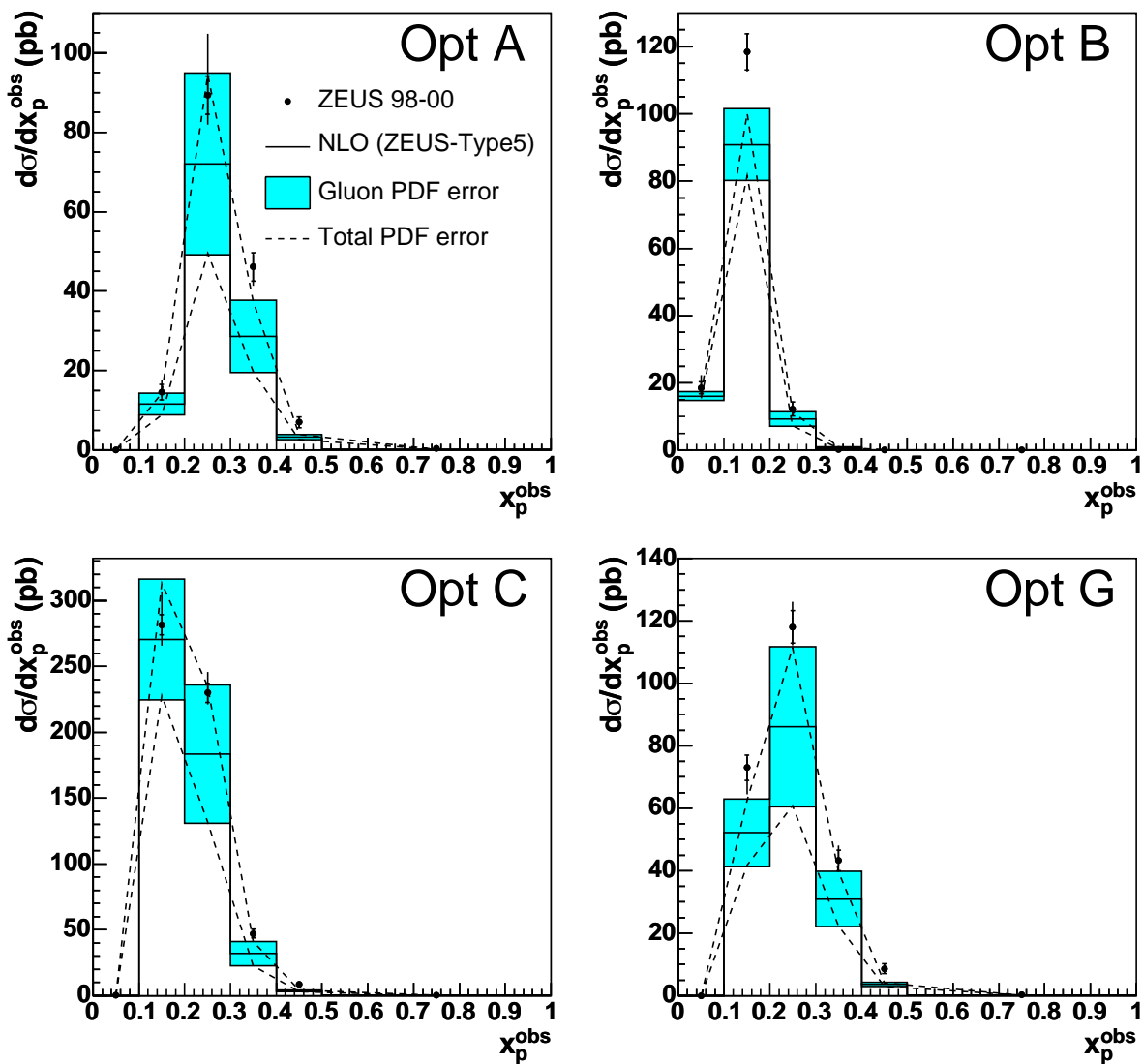


Figure 10.8: Comparison of the uncertainty on the theoretical prediction which arises due to the uncertainties on the underlying gluon PDF from the ZEUS-Type5 fit (no jets) with the statistical (inner bar) and systematic (outer bar) errors of the measured low- x_γ^{obs} optimised data. Statistical and systematic errors are shown separately. The jet energy scale uncertainty, although accounted for in the QCD fits, is not shown here.

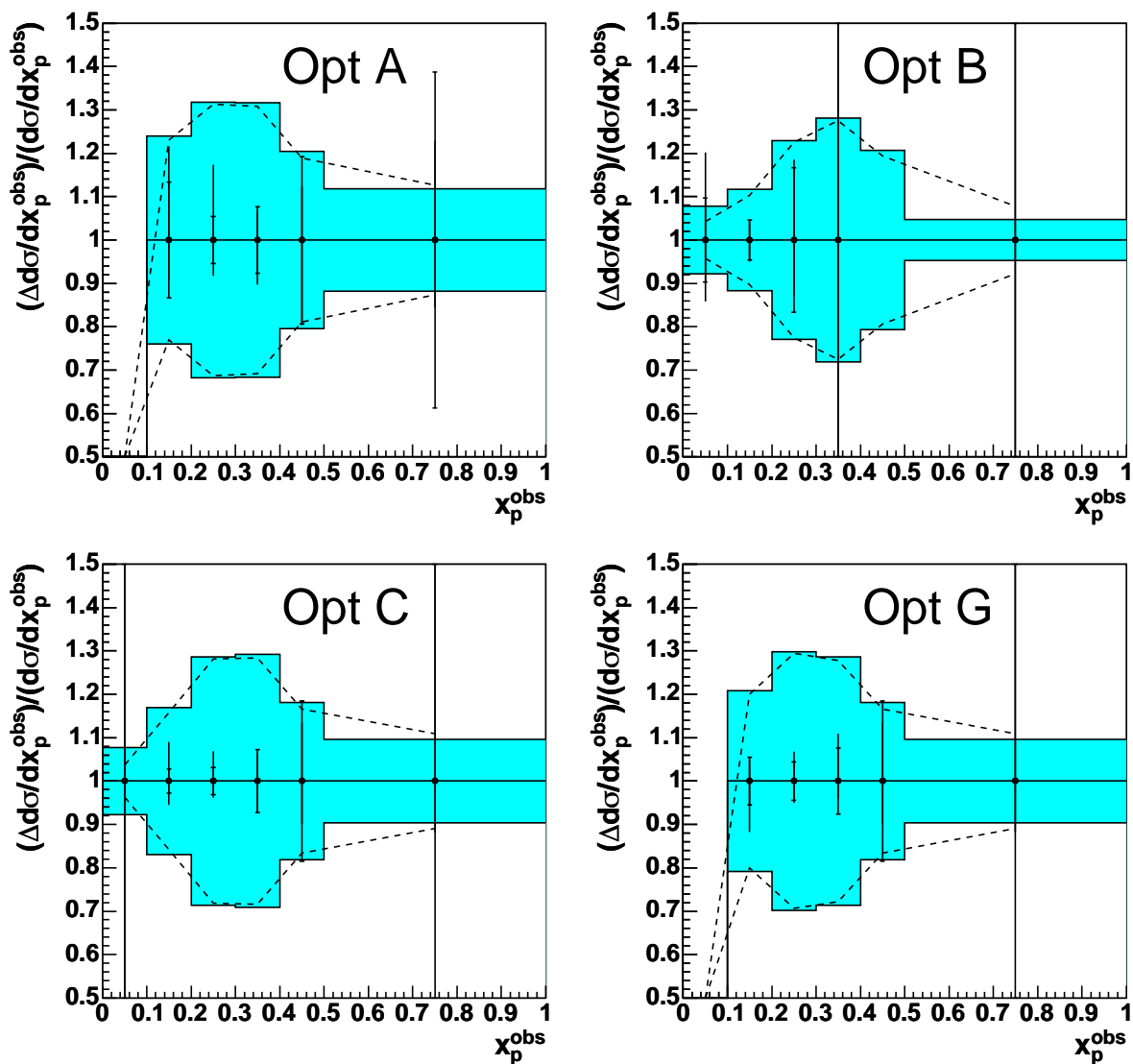


Figure 10.9: Comparison between the gluon PDF uncertainties on the theoretical prediction, expressed as a fraction of the nominal prediction, with the uncertainties on the measured low- x_{γ}^{obs} optimised data, also expressed as a fraction of the nominal theoretical prediction. For the purposes of illustration, the data has been lined up with the theory points in the lower plots to allow a direct comparison of the respective uncertainties. For the accompanying legend, see figure 10.8.

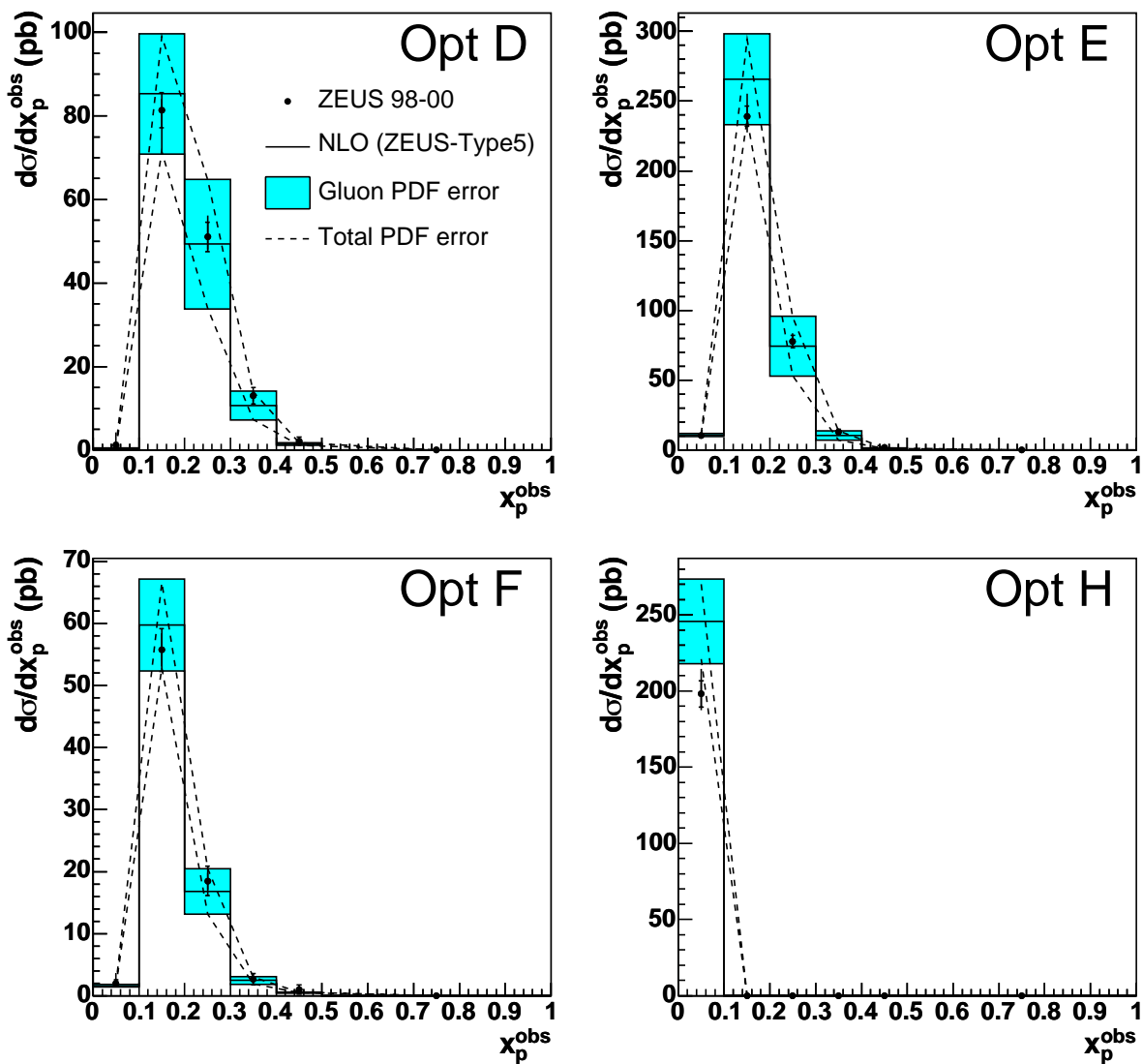


Figure 10.10: Comparison of the uncertainty on the theoretical prediction which arises due to the uncertainties on the underlying gluon PDF from the ZEUS-Type5 fit (no jets) with the statistical (inner bar) and systematic (outer bar) errors of the measured high- x_γ^{obs} optimised data. Statistical and systematic errors are shown separately. The jet energy scale uncertainty, although accounted for in the QCD fits, is not shown here.

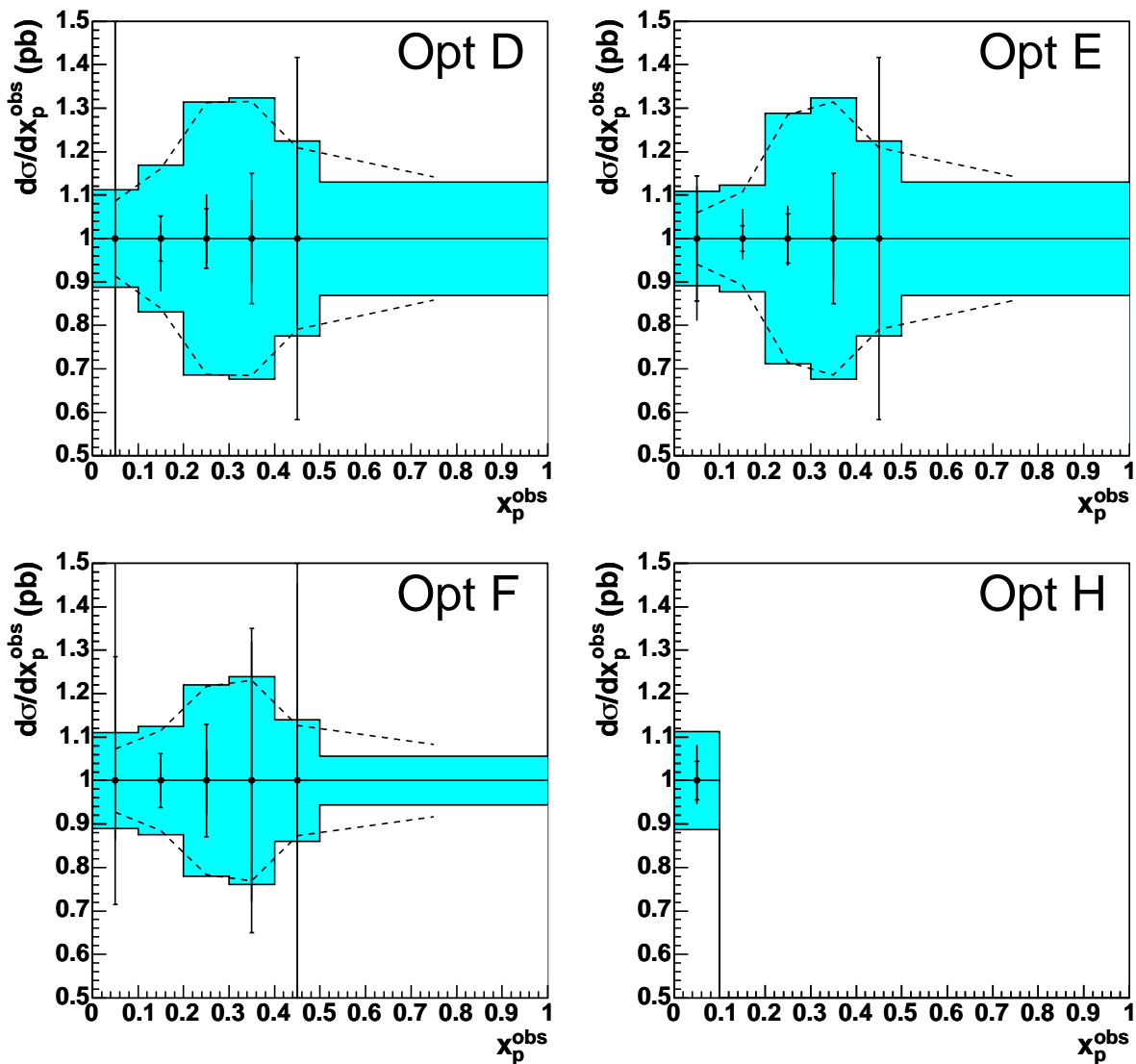


Figure 10.11: Comparison between the gluon PDF uncertainties on the theoretical prediction, expressed as a fraction of the nominal prediction, with the uncertainties on the measured high- x_p^{obs} optimised data, also expressed as a fraction of the nominal theoretical prediction. For the purposes of illustration, the data has been lined up with the theory points in the lower plots to allow a direct comparison of the respective uncertainties. For the accompanying legend, see figure 10.10.

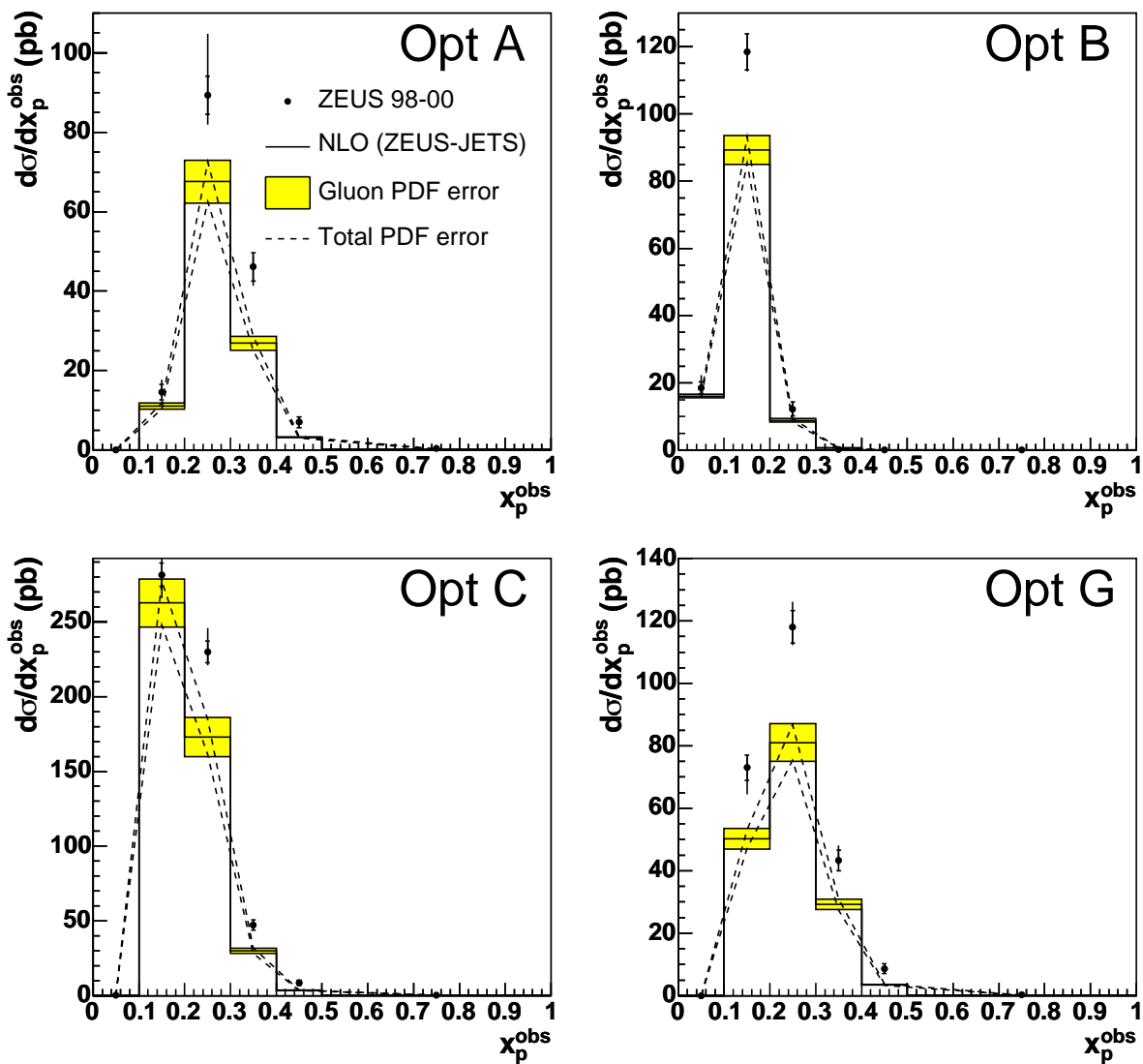


Figure 10.12: Comparison of the uncertainty on the theoretical prediction which arises due to the uncertainties on the underlying gluon PDF from the ZEUS-Jets fit (no jets) with the statistical (inner bar) and systematic (outer bar) errors of the measured low- x_γ^{obs} optimised data. Statistical and systematic errors are shown separately. The jet energy scale uncertainty, although accounted for in the QCD fits, is not shown here.

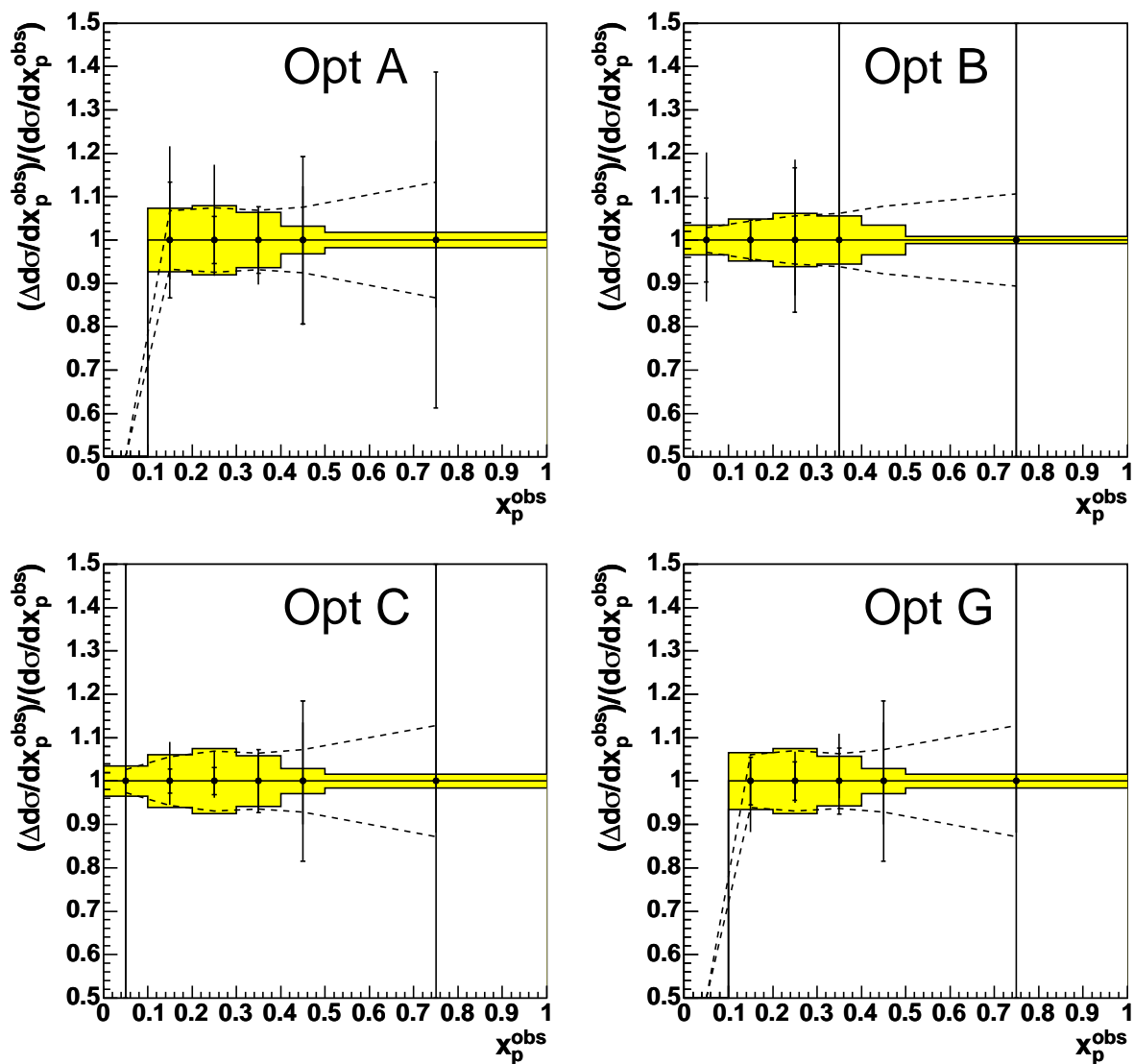


Figure 10.13: Comparison between the gluon PDF uncertainties on the theoretical prediction, expressed as a fraction of the nominal prediction, with the uncertainties on the measured low- x_{γ}^{obs} optimised data, also expressed as a fraction of the nominal theoretical prediction. For the purposes of illustration, the data has been lined up with the theory points in the lower plots to allow a direct comparison of the respective uncertainties. For the accompanying legend, see figure 10.12.

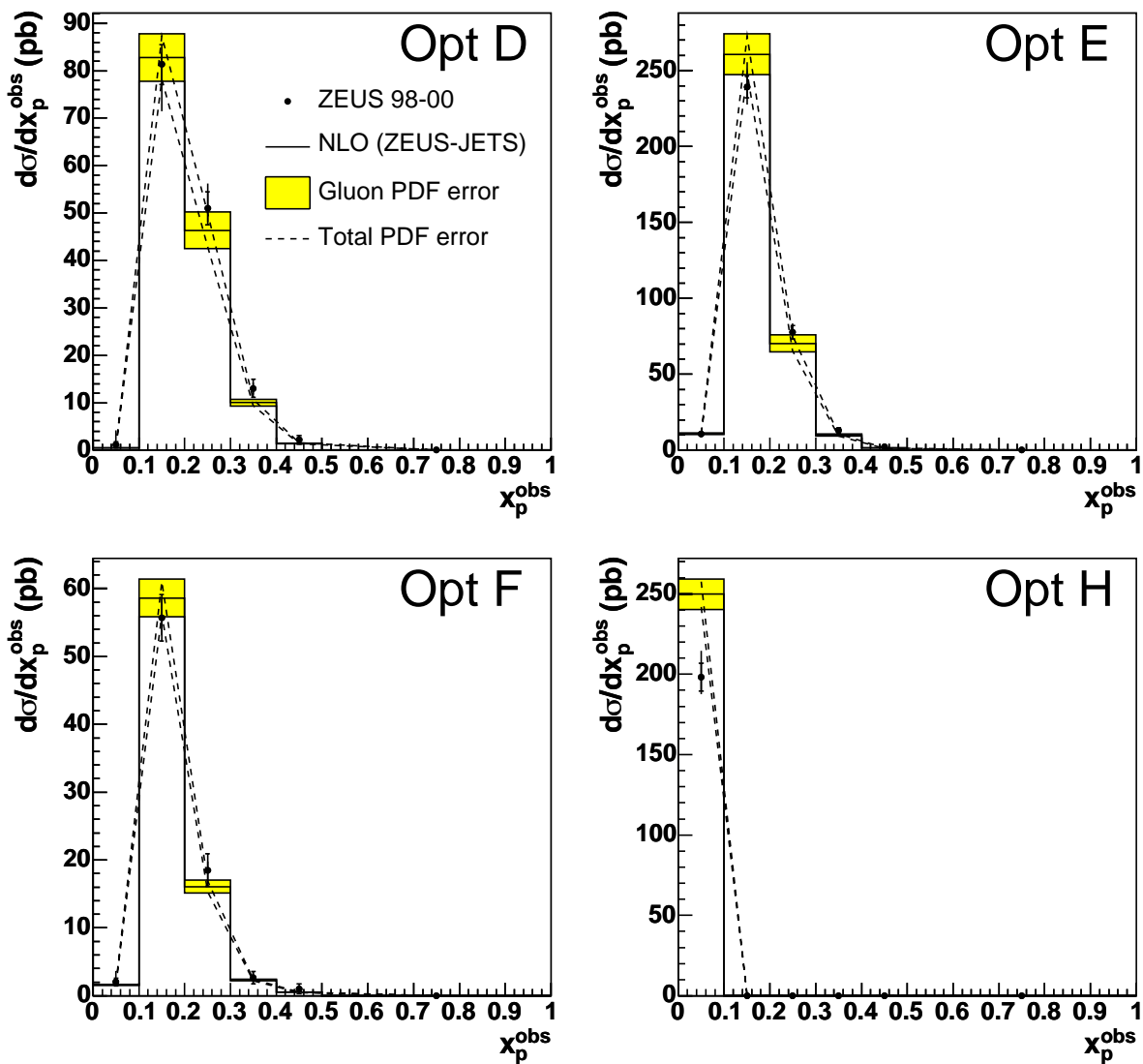


Figure 10.14: Comparison of the uncertainty on the theoretical prediction which arises due to the uncertainties on the underlying gluon PDF from the ZEUS-Jets fit (no jets) with the statistical (inner bar) and systematic (outer bar) errors of the measured high- x_γ^{obs} optimised data. Statistical and systematic errors are shown separately. The jet energy scale uncertainty, although accounted for in the QCD fits, is not shown here.

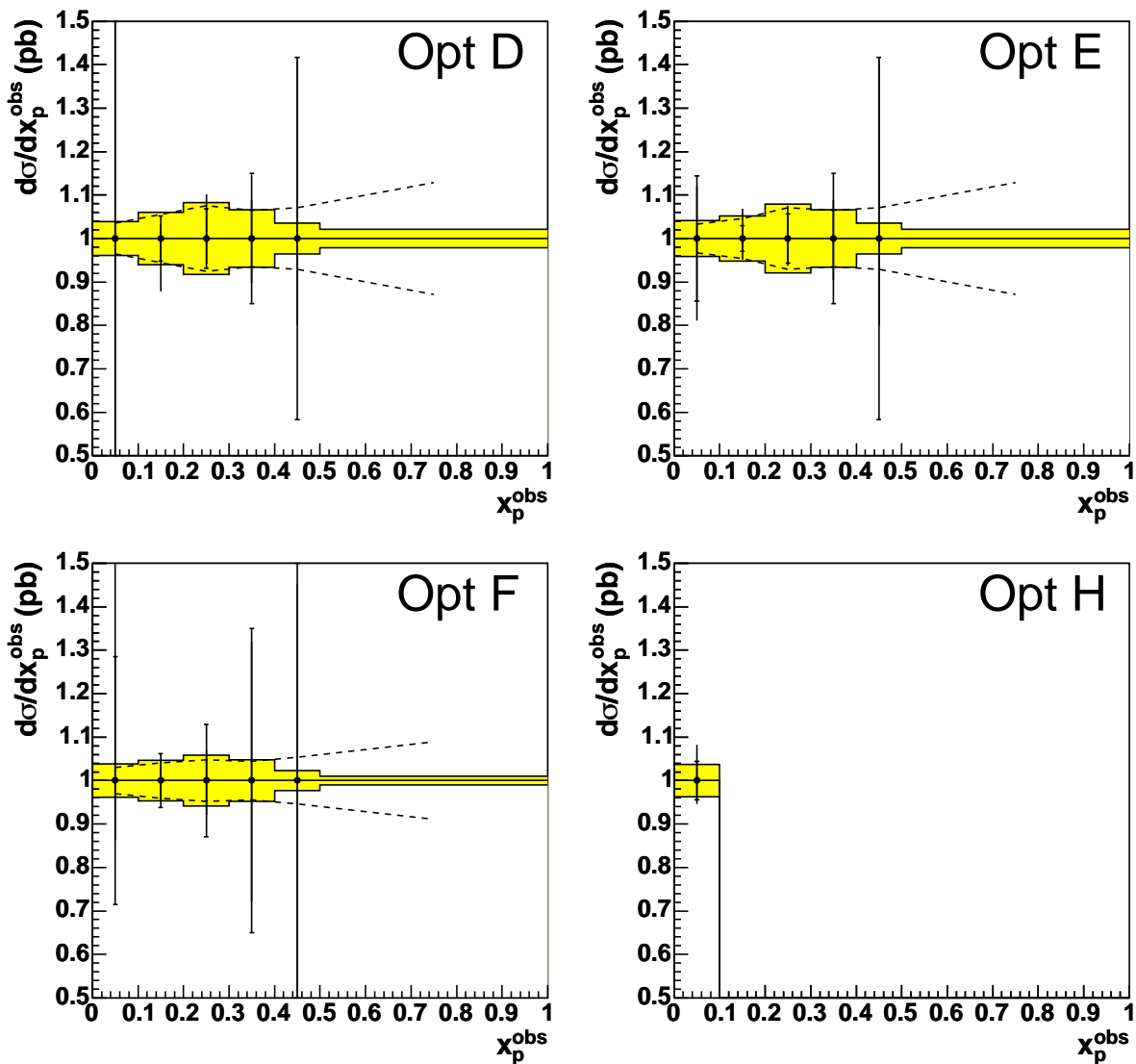


Figure 10.15: Comparison between the gluon PDF uncertainties on the theoretical prediction, expressed as a fraction of the nominal prediction, with the uncertainties on the measured high- x γ optimised data, also expressed as a fraction of the nominal theoretical prediction. For the purposes of illustration, the data has been lined up with the theory points in the lower plots to allow a direct comparison of the respective uncertainties. For the accompanying legend, see figure 10.14.

uncertainties on the corresponding data. Likewise, figures 10.10 and 10.11 show the high- x_γ^{obs} cross-sections. These plots indicate that, with respect to the ZEUS-Type5 fit, the high and low- x_γ^{obs} data have a lot of constraining power over the gluon PDF because the data uncertainties are so much smaller than the gluon PDF uncertainties on the theoretical prediction. Figures 10.12 and 10.13 show the ZEUS-Jets (with jets) gluon PDF uncertainties on the low- x_γ^{obs} theoretical predictions compared with the uncertainties on the corresponding data. Likewise, figures 10.14 and 10.15 show the case for the high- x_γ^{obs} cross-sections. In both the high and low- x_γ^{obs} cases, the size of the gluon PDF uncertainties on the theoretical predictions are much reduced, to the point where, in the vast majority of bins, the data is no longer providing any additional constraint compared with the jet data already included in the fitted data set. This is the principle reason for the lack of impact that the optimised cross-sections have on the precision of the extracted gluon PDF.

10.3 Future Prospects

From the consideration of figures 10.3 and 10.5 it can be said that even with a significant improvement in the systematic uncertainties of the high- x_γ^{obs} optimised measurement only small improvements in the precision of the extracted gluon PDF would be obtained. Larger improvements could be obtained if the systematic uncertainties could be reduced in the low- x_γ^{obs} case but then one has to compete with the large model uncertainty due to the choice of photon PDF and also the theory does not describe the low- x_γ^{obs} cross-sections well. It has already been discussed in the previous chapter that the data might be better described if a new photon PDF fit was performed with the ZEUS γp data that has been published in the past and also that which has been presented in this thesis. If the low- x_γ^{obs} data could be better described using such a method then maybe the complications of including such data in the ZEUS QCD fits could be rectified.

The precision of the extracted gluon PDF, from the ZEUS QCD fits, is dependent on the statistical and systematic errors on the fitted cross-section data. Therefore, by reducing such errors, more precise extractions of the gluon PDF could be made. One way to decrease the statistical errors on the optimised measurements would be to lower the E_T cuts made in the analysis. In chapter 7 the possibility of using cuts for the leading and trailing jets of 15 GeV and 10 GeV respectively

was considered. From figure 7.6 it was concluded that the description of the data was too poor by the MC and therefore the E_T cuts were raised to 20 GeV and 15 GeV in order to improve the comparison. However, with reference to this figure it can be seen that the description at high- x_γ^{obs} is actually very good and there is certainly nothing to stop a high- x_γ^{obs} , low- E_T measurement from going ahead. In actual fact, there are ~ 80000 events at high- x_γ^{obs} in the low- E_T case and approximately ~ 20000 events at high- x_γ^{obs} in the high- E_T case. Therefore, the statistical errors could be brought down by a factor of ~ 2 . Such an approach could also be done in parallel with repeating the previous dijet measurements of [51] (which used the 1996-1997 data set) with the full 1996-2000 data set. This increase in the size of the data set used would lead to a significant reduction in the statistical errors of the previous measurement. Finally, it should be noted that by the end of HERA running (in mid-2007) there will be significantly more dijet photoproduction data available for analysis. Inclusion of such data in the cross-section measurement will also lead to a decrease in the statistical uncertainties of the extracted gluon PDF from the ZEUS QCD fits.

A major issue which was touched upon above in relation to the ZEUS QCD fits and which is of importance to address is that of photon structure. It is clear that ZEUS data provides sensitivity to the photon structure, particularly the gluon component, in kinematic regions that LEP does not. The most obvious next stage is therefore to include ZEUS data in a photon PDF fit. This is not difficult to do (the method presented in chapter 4 is easily extended) and has already been carried out as part of the SAL parameterisation. However, this analysis has illustrated the merits of the CJK parameterisation and concludes that ZEUS data needs to be included in a CJK style fit in order for the data to be described adequately. Another issue which needs to be addressed is that of combined proton-photon QCD fits. That is, fitting the proton and photon PDFs simultaneously in one fit. The problem here is twofold. Firstly, proton and photon evolution routines need to be combined into one single framework. Secondly, the photoproduction cross-sections need to be able to be reconstructed in a fast method that could be used in a QCD fit. The method of grid reconstructed cross-sections, presented in chapter 4, could be extended to the proton-photon case but this would involve grids of the order of N^3 . The storage of such a large number of weights could pose problems and it is uncertain how accurate the resulting reconstructed cross-section predictions would be.

10.4 Summary

During the course of the analysis presented in this thesis two principal issues have been investigated, both of which have revolved around the study of dijet photoproduction. The first issue relates to photon structure. A number of differential cross-sections have been measured and compared to theoretical predictions using a variety of photon parameterisations. The second issue relates to proton structure and involved measuring a set of differential dijet photoproduction cross-sections tailored to better constrain the gluon density in the proton.

It is evident from figure 9.1 that the CJK photon parameterisation has some major shortcomings in relation to the description of the ZEUS data and in its consistency with the predictions of the other photon PDF sets considered here. This observation is also backed up by similar results from a previous analysis [51] (see figure 9.18). However, the shortcomings of the CJK parameterisation from looking at the differential cross-section as a function of x_γ^{obs} are not as drastic as this distribution implies. Previous analyses have reported the observation that ZEUS resolved dijet photoproduction data lie above the theoretical predictions using the AFG and GRV photon parameterisations. The analysis presented in this thesis represents the first time that theoretical predictions using the CJK photon parameterisation have been compared to a comprehensive range of dijet photoproduction differential cross-sections. It can be seen from figure 9.5 and particularly figure 9.6 that the predictions using the CJK parameterisation provide a better description of the resolved cross-sections than the GRV, AFG or SAL parameterisations at relatively high transverse energies. However, the prediction using CJK lies significantly above the data at low transverse energies, an observation also supported by the previous analysis (figure 9.18).

A possible explanation for this is that the CJK densities (especially the gluon density) are not constrained well at lower transverse energies by the LEP data used in the fit. At higher transverse energies, the densities are better constrained by such data and the description of the ZEUS data is better. This lack of constraint is particularly well highlighted by the differential cross-section as a function of x_γ^{obs} where the prediction blows up at low- x_γ^{obs} which is indicative that one of the densities (most probably the gluon density) is poorly constrained in this region. It is therefore very interesting to consider the prospect of a new CJK fit

which includes the ZEUS data presented in this thesis (as well as previous ZEUS dijet data) in the fitted data set. The possibility could then arise of achieving an improved description of resolved data across the full range of transverse energies studied in dijet photoproduction with the ZEUS detector. A final point worthy of mention is that the SAL parameterisation is the only photon parameterisation available which includes ZEUS data in its fitted data set. However, it appears to fair little better than the predictions using GRV and AFG. A similar effect could be observed if the ZEUS data was included in a CJK fit or perhaps the mechanics and theory behind the CJK fit are simply superior to the other fits. This thesis has opened the path up to some exciting future work in relation to photon structure.

The second major line of work pursued during the course of this thesis has been in relation to proton structure. After including existing ZEUS dijet photoproduction into the ZEUS fit (a task which the author was personally responsible for) the precision of the extracted gluon density was noticeably improved (see figure 4.6). In an effort to improve this enhancement a study was conducted to determine differential cross-sections that had the potential to optimise this improvement. These optimised cross-sections were subsequently measured (figures 9.10 and 9.12) and included in a new ZEUS fit to determine the parton densities of the proton. Including the optimised cross-sections in the ZEUS fit did improve the precision of the extracted gluon PDF at high- x (see figures 10.3 and 10.7) however this improvement was not significant and the uncertainty of the extracted gluon PDF, despite being reduced, remains large. A reason why the improvement was not as large as expected was because the optimised cross-section data provide only slightly more constraint in the fit than the dijet data already included in the fitted data set. After inclusion of the dijet data in the fitted data set the size of the gluon PDF uncertainties on the predictions for the optimised cross-sections are comparable to the size of the uncertainties on the measured cross-section which indicates that the optimised data are not capable of providing significantly more constraint on the gluon density.

Appendix A

Running Couplings and the Renormalisation Scale

The running of a coupling constant α with some external energy scale μ^2 is given by the renormalisation group equation,

$$\frac{d\alpha}{d\log\mu^2} = \beta(\alpha), \quad (\text{A.1})$$

where $\alpha \equiv \alpha(\mu^2)$. The renormalised coupling then depends on the scale μ_0 at which the theory is chosen to be renormalised which is an arbitrary parameter that is not defined in QCD. However, it is necessary to make a choice of scale in order to calculate finite values for physical quantities in quantum field theory. Integration of equation A.1 leads to

$$\int_{\mu_0^2}^{\mu^2} d\log\mu^2 = \int_{\alpha(\mu_0^2)}^{\alpha(\mu^2)} \frac{d\alpha}{\beta(\alpha)}, \quad (\text{A.2})$$

$$\log\mu^2 - \log\mu_0^2 = F(\alpha(\mu^2)) - F(\alpha(\mu_0^2)), \quad (\text{A.3})$$

$$\alpha(\mu^2) = F^{-1} \left(F(\alpha(\mu_0^2)) + \log\frac{\mu^2}{\mu_0^2} \right) \text{ and} \quad (\text{A.4})$$

By introducing the dimensionless constant Λ_{QCD} given by

$$\log\Lambda_{QCD}^2 \equiv \log\mu_0^2 - F(\alpha(\mu_0^2)), \quad (\text{A.5})$$

any dependence on the renormalisation scale μ_0 can be removed. Equation A.4 becomes

$$\alpha(\mu^2) = F^{-1} \left(\log \frac{\mu^2}{\Lambda_{QCD}^2} \right), \quad (\text{A.6})$$

where Λ_{QCD} must be evaluated experimentally. The scale μ^2 is often taken to be the four-momentum transfer Q^2 in deep inelastic scattering or the sum of the outgoing parton transverse momenta in the case of photoproduction.

Appendix B

Error Analysis

In section 3.7 the purity, p , efficiency, ϵ , and correction factor, h^{-1} , were defined in terms of the number of events generated in a bin, t , the number of events measured in a bin, m , and the number of events both generated and measured in a bin, u . These quantities are not statistically independent and in order to calculate the errors on these quantities, correctly taking into account the correlations, they must be expressed in terms of some other, statistically independent, quantities. If a is the number of events generated and measured in the same bin, b is the number of events generated in the bin but not detected in it, and c is the number of events not generated in the bin but detected in it; then we must have

$$t = a + b, m = a + c \text{ and } u = a.$$

This then gives:

$$p = \frac{a}{a + c},$$

$$\epsilon = \frac{a}{a + b} \text{ and}$$

$$h^{-1} = \frac{a + b}{a + c}.$$

B.1 Purity

The error on the purity is then given by

$$\begin{aligned}
 \delta p^2 &= \left(\frac{\delta p}{\delta a}\right)^2 V_a + \left(\frac{\delta p}{\delta c}\right)^2 V_c \\
 &= \left[\frac{1}{a+c} - \frac{a}{(a+c)^2}\right]^2 V_a + \left[\frac{a}{(a+c)^2}\right]^2 V_c \\
 &= \frac{c^2 V_a^2 + a^2 V_c}{(a+c)^4},
 \end{aligned}$$

where V_a is the variance of the mean of a etc. This can be rewritten in terms of the original variables as follows:

$$\delta p = \sqrt{\frac{m^2 V_u + u^2 V_m - 2mu V_u}{m^4}}. \quad (\text{B.1})$$

B.2 Efficiency

The error on the efficiency can be derived using a similar method and is stated below:

$$\delta \epsilon = \sqrt{\frac{t^2 V_u + u^2 V_t - 2tu V_u}{t^4}}. \quad (\text{B.2})$$

B.3 Correction Factor

The error on the correction factor is derived below:

$$\begin{aligned}
 \delta C^2 &= \left(\frac{\delta p}{\delta a}\right)^2 V_a + \left(\frac{\delta p}{\delta b}\right)^2 V_b + \left(\frac{\delta p}{\delta c}\right)^2 V_c \\
 &= \left[\frac{1}{a+c} - \frac{a+b}{(a+c)^2}\right]^2 V_a + \left[\frac{1}{a+c}\right]^2 V_b + \left[\frac{a+b}{(a+c)^2}\right]^2 V_c \\
 &= \frac{(c-b)^2 V_a + (a+c)^2 V_b + (a+b)^2 V_c}{(a+c)^4},
 \end{aligned}$$

which, in terms of the original variables, is

$$\delta C = \sqrt{\frac{m^2 V_t + t^2 V_m - 2mtV_u}{m^4}}. \quad (\text{B.3})$$

For unweighted events (which are Poisson distributed) the variance is simply equal to the relevant bin content:

$$V_t = t, V_m = m \text{ and } V_u = u.$$

The expression for the correction factor error reduces to

$$\delta C = \sqrt{\frac{t}{m^3} [t + m - 2u]}. \quad (\text{B.4})$$

Appendix C

CTEQ and MRST Gluon PDF Errors

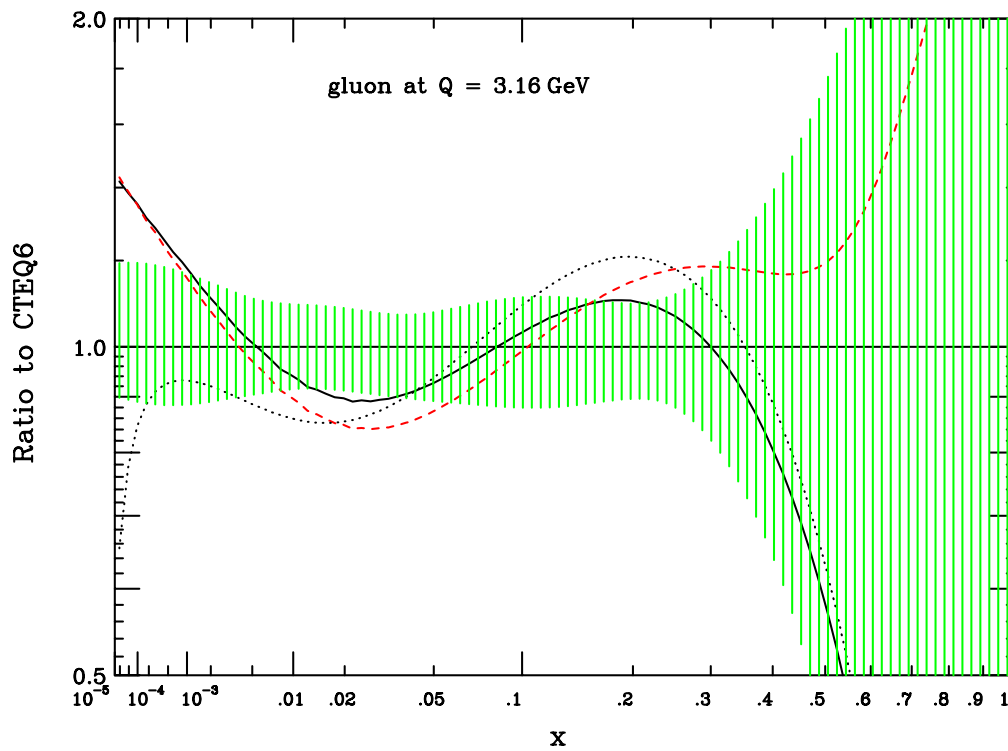


Figure C.1: Uncertainty band for the gluon distribution function at $Q^2 = 10 \text{ GeV}^2$ from the CTEQ6M1 fit. The curves correspond to CTEQ5M1 (solid), CTEQ5HJ (dashed), and MRST2001 (dotted). Figure taken from [62]

Uncertainty of gluon from Hessian method

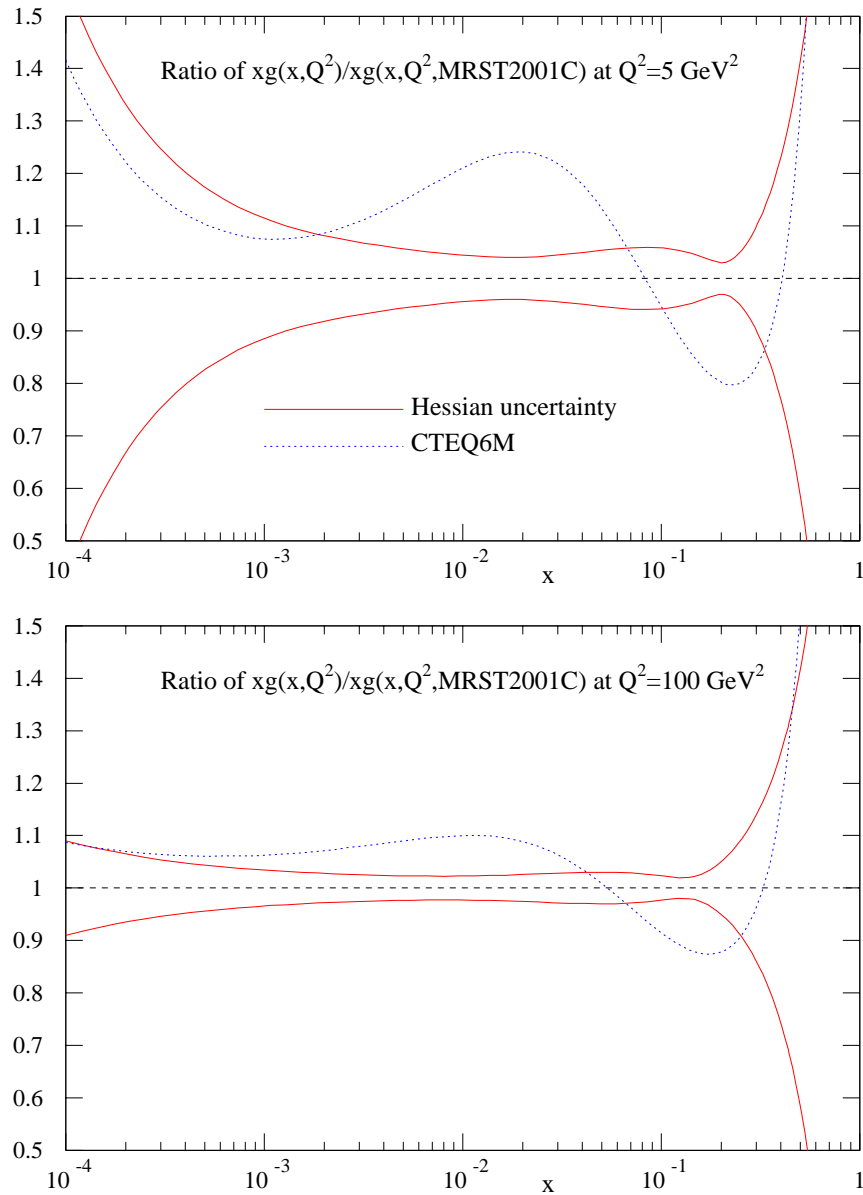


Figure C.2: The uncertainty on the extracted gluon PDF from the MRST2001 fit. The uncertainty on $g(x, Q^2)$ at $Q^2 = 5 \text{ GeV}^2$ and 100 GeV^2 is shown. Also shown is the CTEQ6M distribution. The uncertainties are shown relative to the MRST2001 central values for $g(x, Q^2)$. Figure taken from [65].

Appendix D

Calculation of the PDF Uncertainties

D.1 Total PDF Uncertainties

The calculation of the total PDF uncertainty on a particular cross-section is compounded by the fact that the uncertainties on the underlying PDFs are correlated. The proton PDFs are parameterised in the ZEUS-Type5 fit by 12 parameters. The results of the fit are the determination of the 12 central values for these parameters along with a 12x12 covariance matrix containing all the information about the variances and correlations of the fitted parameters. This matrix is non-diagonal due to the correlations which exist between the parameters. However, a general covariance matrix is a real symmetric matrix and, thus, by the spectral decomposition theorem can always be diagonalised. The 12 eigenvectors corresponding to the diagonalised matrix represent linear combinations of the original 12 parameters. Each eigenvector represents a set of proton PDFs (called the *i*'th eigenvector PDFs). The diagonal elements of the diagonalised matrix represent the variance on each eigenvector. The crucial point to note is that the uncertainties on each eigenvector PDF set are uncorrelated with those of the remaining 11 eigenvector PDF sets. There are, in total, 24 PDF sets to consider with each one corresponding to the up or down values of one of the 12 eigenvector sets. Let σ_i^{up} denote the cross-section prediction, calculated with the up values of the *i*'th eigenvector PDF set and σ_i^{dn} denote the cross-section calculated with the down values. The total PDF uncertainty on the cross-section is then given by

$$\frac{10}{2} \sqrt{\sum_i (\sigma_i^{up} - \sigma_i^{dn})^2} . \quad (\text{D.1})$$

The factor of $\frac{1}{2}$ is just to symmetrise the uncertainty and the factor of 10 is a compensatory factor which arises from the eigenvector procedure.

D.2 Gluon PDF Uncertainties

To calculate the gluon PDF uncertainties the valence and sea PDFs are held at their central values and each cross-section is calculated twice. Once with the gluon PDF at its up values (central gluon PDF plus its error) and once with the gluon PDF at its down values (central gluon PDF minus its error).

Appendix E

Jet Energy Scale Study

This appendix details the jet energy scale study that was performed in support of the analysis presented in this thesis. Jet energy scale corrections are derived using the method outlined in [83–85], using (γp) ZEUS data and (γp) PYTHIA MC. These corrections are then applied to an independent NC DIS sample, of data and MC, to check their validity and derive the jet energy scale uncertainty. The study therefore consists of two principal parts: the derivation of the jet energy scale corrections using a γp sample and the check using an independent NC DIS sample.

E.1 γp Sample Definition

This section describes the cuts used to define the data and MC γp samples from which the jet energy scale corrections are calculated.

E.1.1 Trigger and Cleaning Cuts

- DST65 (HPP02), FLT 40 or FLT 41 or FLT 42 or FLT 43
- $-40 < z_{vtx} < 40$ cms
- $n_{trks}^{pri}/n_{trks} > 0.1$
- $\frac{P_T}{\sqrt{E_T}} < 1.5\sqrt{GeV}$
- Event accepted as γp if no e^\pm is found.
- Misidentified electron if e^\pm is found with $E > 5$ GeV and $y < 0.7$.
- $0.15 < y_{JB} < 0.70$ (y_{JB} is uncorrected).

E.1.2 Jet Cuts

- At least two jets found satisfying

$$E_T^{Cal} > 10 \text{ GeV}$$

$$-1 < \eta < 3$$

E.2 Correction Procedure

The following correction procedure was taken from the method outlined in [83–85]. In the central region, $|\eta^{jet}| < 1$, the multiplicity distribution and the p_T spectrum of charged particles associated with calorimeter jets was compared for data and MC samples using the reconstructed track information. The particle tracks were required to be in the range $|\eta^{track}| < 1.5$ and $p_T^{track} > 300 \text{ MeV}$, where η^{track} is the track pseudorapidity and p_T^{track} is the transverse momentum of the track with respect to the beam axis. Tracks were then associated with a calorimeter jet when the extrapolated track trajectory reached the calorimeter within a cone of unit radius in the η - ϕ plane concentric with the calorimeter jet axis. For the central η^{jet} region, the momenta of the tracks in the calorimeter jet were used to determine the total transverse energy carried by the charged particles, $E_{T,tracks}^{jet}$. Then, the ratio $r_{tracks} = E_{T,tracks}^{jet}/E_{T,Cal}^{jet}$ was calculated and the distributions of this ratio for data was compared to MC. The mean values of the distribution in r_{tracks} was determined as a function of η^{jet} for data ($\langle r_{tracks} \rangle_{data}$) and MC events ($\langle r_{tracks} \rangle_{MC}$). The transverse energy of the calorimeter jets in the data were then modified as a function of η^{jet} to correct for any differences in the comparison.

In the forward region, $1 < \eta^{jet} < 3$, the energy scale of the jets was studied using the transverse energy imbalance in dijet events with one jet in the central region and the other in the forward region. The distributions of the ratio $r_{dijet} = E_{T,Cal}^{jet}(forward)/E_{T,Cal}^{jet}(central)$ were compared for data ($\langle r_{dijets} \rangle_{data}$) and MC events ($\langle r_{dijets} \rangle_{MC}$). The transverse energies of the forward calorimeter jets in the data were then modified as a function of η^{jet} to correct for these differences.

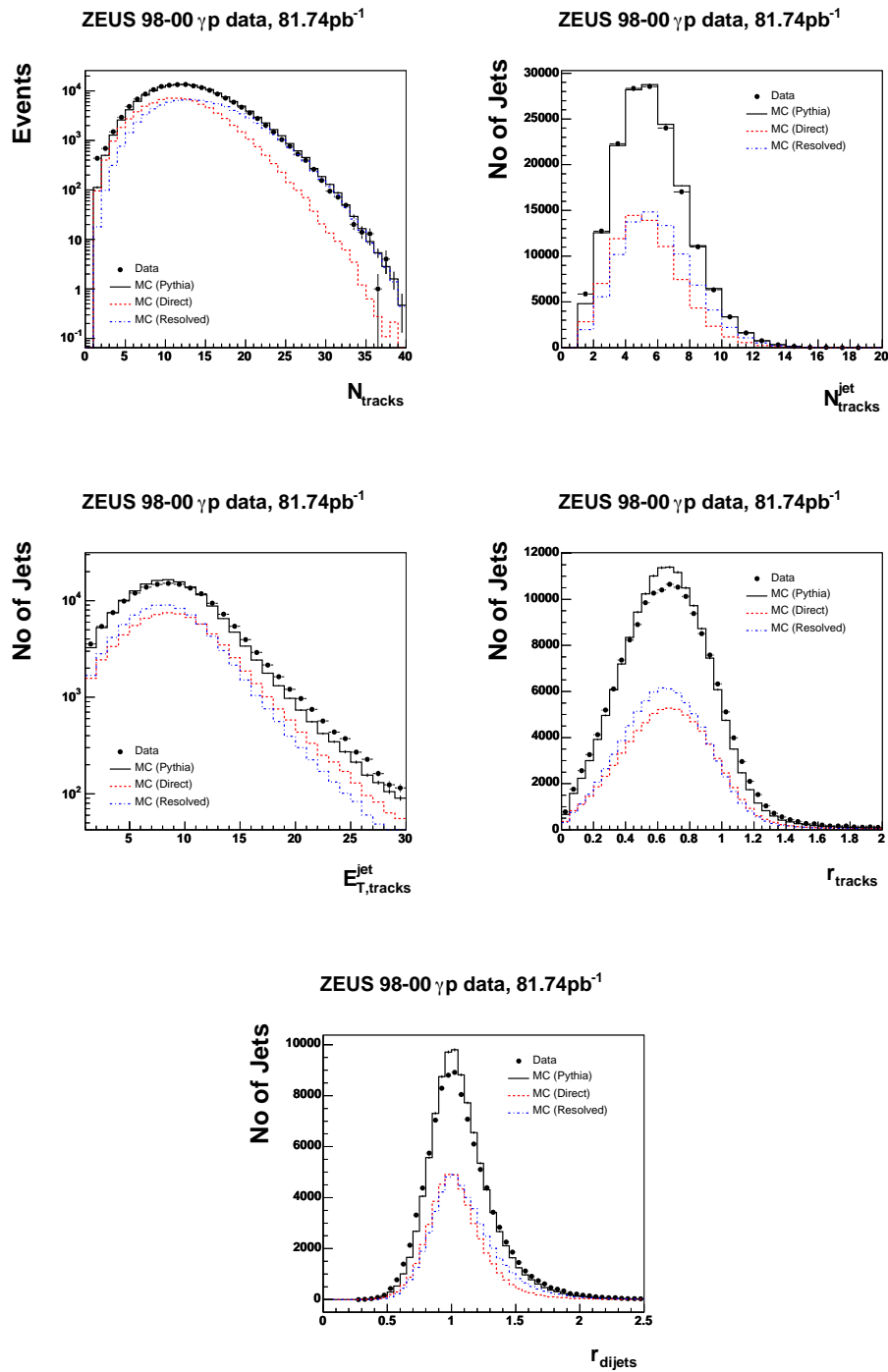


Figure E.1: Comparison between MC and data for the quantities N_{tracks} (number of tracks in the event passing the initial track cuts), $N_{\text{tracks}}^{\text{jet}}$ (number of tracks associated with a particular calorimeter jet), $E_{T,\text{tracks}}^{\text{jet}}$ (the sum of the transverse energies of tracks associated to a particular calorimeter jet), r_{tracks} (see text for explanation) and r_{dijets} (see text for explanation).

E.3 Results of the Correction Procedure

Some control plots for the various quantities considered during the course of deriving the energy scale correction factors are shown in figure E.1. Figure E.2 shows the comparison between data and MC for the distribution of $\langle r_{tracks} \rangle$ and $\langle r_{dijets} \rangle$ as a function of η^{jet} . The ratio of $\langle r_{tracks} \rangle$ and $\langle r_{dijets} \rangle$ in the data to that in the MC, as a function of η^{jet} , is shown in figure E.3, from which differences between the data and MC of within 1% are observed. The jets in the data are then modified by the correction factors shown in table E.1 (which are simply the values of the various points shown in figure E.3). Figure E.4 shows the ratio of $\langle r_{tracks} \rangle$ and $\langle r_{dijets} \rangle$ in the data to that in the MC, as a function of η^{jet} , after the application of the jet energy scale corrections to the calorimeter level jets in the data.

η range	Correction factor
$-1 < \eta^{jet} < -0.75$	1.00775
$-0.75 < \eta^{jet} < -0.50$	1.00778
$-0.50 < \eta^{jet} < -0.25$	1.00688
$-0.25 < \eta^{jet} < 0.00$	1.01058
$0.00 < \eta^{jet} < 0.25$	1.00849
$0.25 < \eta^{jet} < 0.50$	1.00873
$0.50 < \eta^{jet} < 0.75$	1.00785
$0.75 < \eta^{jet} < 1.00$	1.01649
$1.00 < \eta^{jet} < 1.25$	1.00588
$1.25 < \eta^{jet} < 1.50$	1.01244
$1.50 < \eta^{jet} < 1.75$	1.00188
$1.75 < \eta^{jet} < 2.00$	0.992406
$2.00 < \eta^{jet} < 2.25$	0.989043
$2.25 < \eta^{jet} < 2.50$	0.98445
$2.50 < \eta^{jet} < 2.75$	0.998236
$2.75 < \eta^{jet} < 3.00$	0.99677

Table E.1: Jet energy scale correction factors. The corrected jet energy is given by multiplying the uncorrected jet energy by the appropriate factor from the table. The factors shown are valid for the correction of data calorimeter jets only.

E.4 DIS Check

The jet energy scale corrections evaluated in the previous section have to be applied to an independent set of data and MC using an independent method of

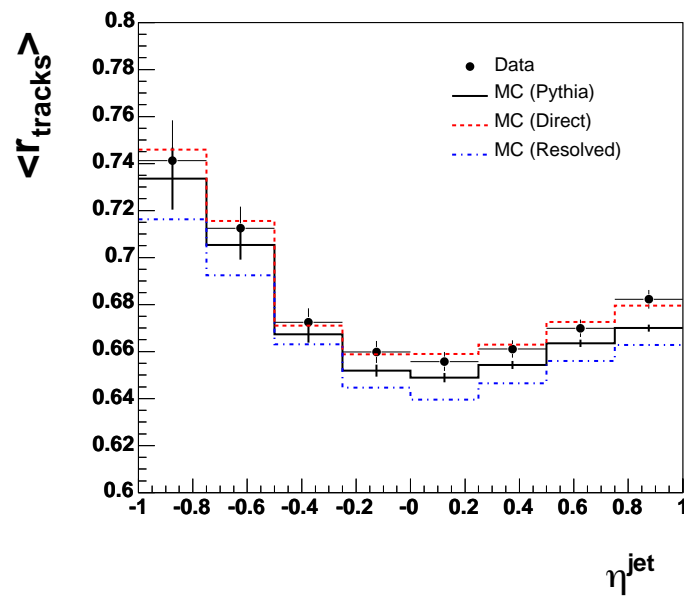
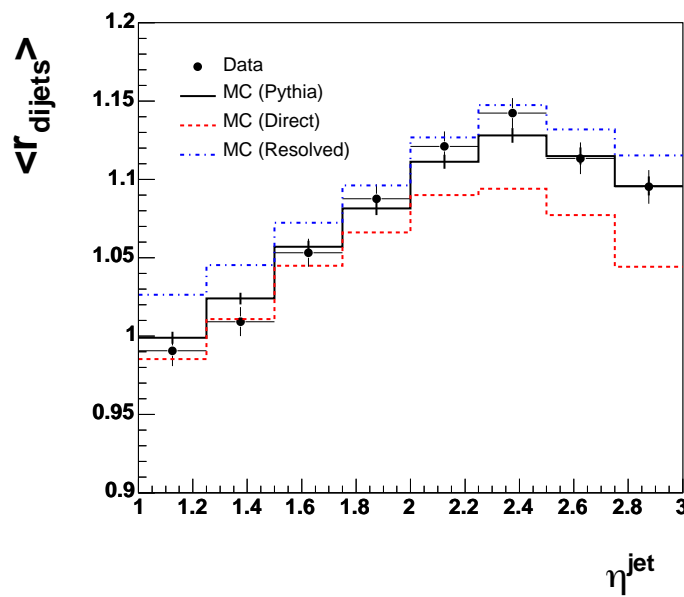
ZEUS 98-00 γp data, 81.74pb^{-1} ZEUS 98-00 γp data, 81.74pb^{-1} 

Figure E.2: Comparison between data and MC for the distribution of $\langle r_{\text{tracks}} \rangle$ and $\langle r_{\text{dijets}} \rangle$ as a function of η^{jet}

ZEUS 98-00 γp data, 81.74pb^{-1}

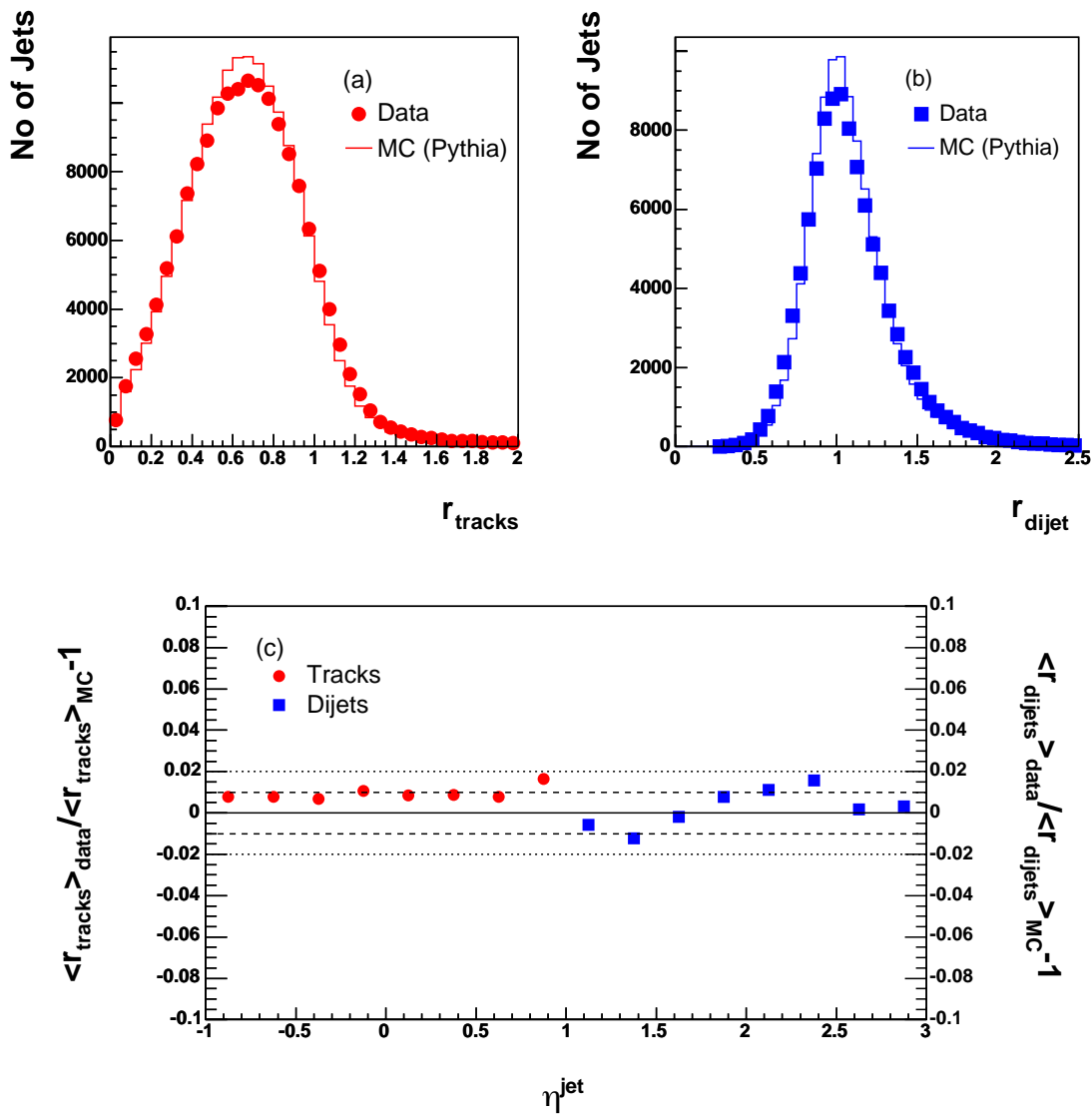


Figure E.3: (a) r_{tracks} control plot (b) r_{dijets} control plot (c) $(\langle r_{tracks} \rangle_{data} / \langle r_{tracks} \rangle_{MC}) - 1$ and $(\langle r_{dijets} \rangle_{data} / \langle r_{dijets} \rangle_{MC}) - 1$ as a function of η^{jet} .

ZEUS 98-00 γp data, 81.74pb^{-1}

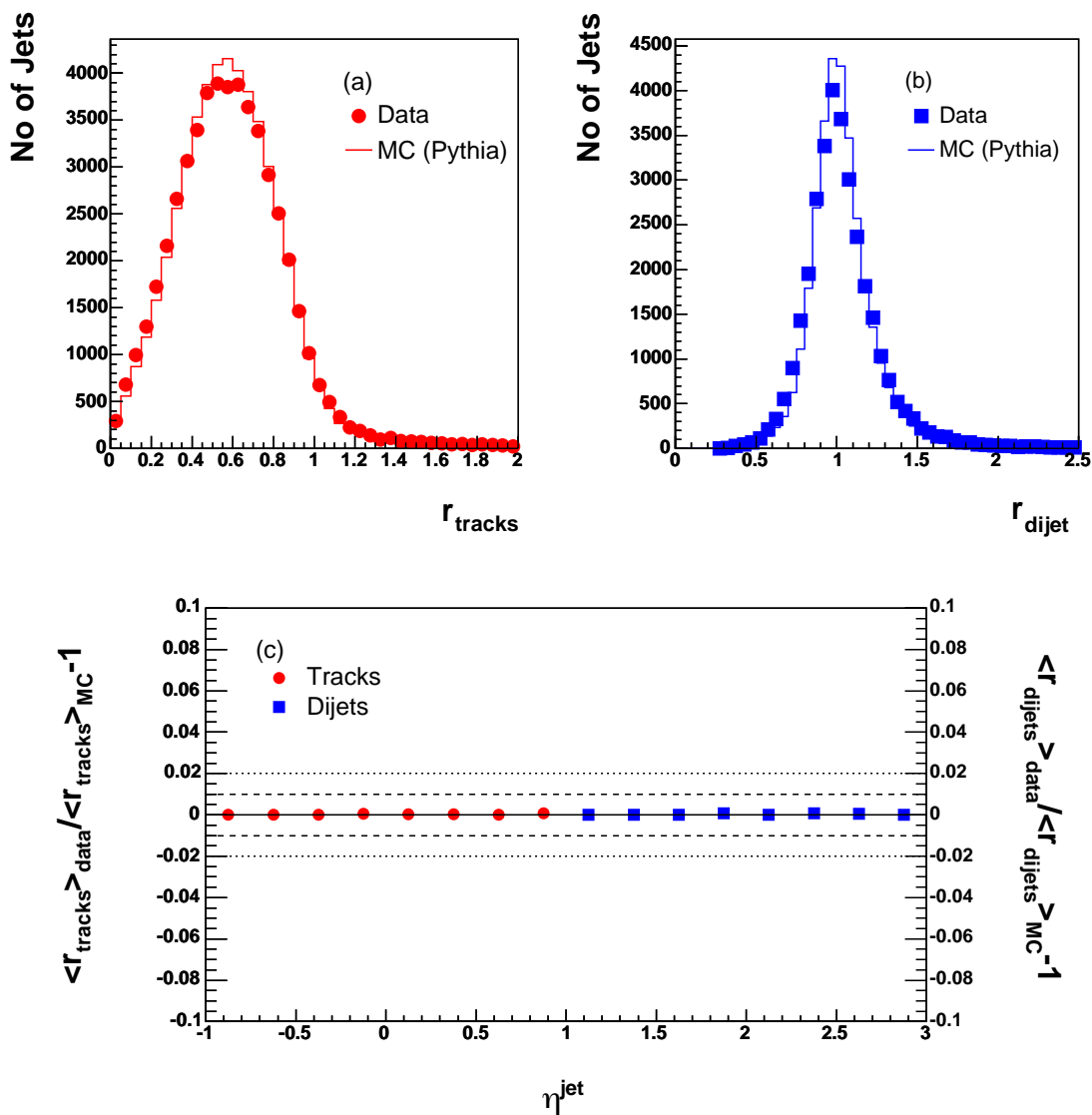


Figure E.4: (a) r_{tracks} control plot (post correction) (b) r_{dijets} control plot (post correction) (c) $(\langle r_{tracks} \rangle_{data} / \langle r_{tracks} \rangle_{MC}) - 1$ and $(\langle r_{dijets} \rangle_{data} / \langle r_{dijets} \rangle_{MC}) - 1$ as a function of η^{jet} (post correction)

assessing the jet energy scale differences in order to check their validity. A high- Q^2 sample of NC DIS data and MC¹ is used in the check which compares the transverse energy of the scattered electron with that of the jet, in well-defined single jet NC DIS events. In such events, it is expected that the transverse energies of the scattered electron and the jet should balance. This fact can be used to investigate the differences in the energy scale between the data and MC. By applying the jet energy corrections derived in the last section to the DIS data jets one can check whether or not the correction method improves the differences between the energy scales of the data and MC in the DIS sample.

E.5 DIS Sample Definition

This section describes the cuts used to define the data and MC DIS samples which were used to check the jet energy scale (the following selection is taken from [86]).

E.5.1 Trigger and Cleaning Cuts

- DST65 (HPP02), FLT 40 or FLT 41 or FLT 42 or FLT 43
- Event preliminarily accepted as NC DIS if an electron is found (highest probability candidate satisfying $P_{Si} > 0.9$)
- $E'_e > 10$ GeV ($E'_e \equiv$ uncorrected CAL energy)
- $E_{notelec}^{cone} \leq 5$ GeV
- If the electron is within the CTD acceptance i.e. $23^\circ < \theta \leq 156^\circ$ then the existence of a matching track is required. The distance of closest approach (DCA) between the calorimeter cluster and the endpoint of the extrapolated CTD track is required to be less than 10 cms.
- If the electron is within the CTD acceptance i.e. $23^\circ < \theta \leq 156^\circ$ then we require $P_e^{trk} > 5$ GeV.
- For electrons scattered outside the forward acceptance of the CTD ($\theta \leq 23^\circ$) we require $P_{T,e} > 30$ GeV.

¹A sample of 109.05 pb⁻¹ ARIADNE (Djangoh) NC e^+p DIS MC was used.

- Super-crack cuts. Events are rejected if the scattered electron cluster is reconstructed in the edges of the BCAL. Events are rejected if $-104 < z \leq -98.5$ cms or $164 < z \leq 174$ cms.
- $-50 < z_{vtx} \leq 50$ cms
- $38 < \delta_{tot} \leq 65$ GeV
- $y_e \leq 0.95$
- $\frac{P_T}{\sqrt{E_T}} \leq 4.0\sqrt{GeV}$
- $y_{JB}(1 - x_{DA})^2 > 0.004$
- $Q_{DA}^2 > 200$ GeV²
- $|\phi_{jet,1} - \phi_e| - \pi \leq 0.2rad$
- $0.9 < E_{T,1}/P_{T,had}(cells) \leq 1.1$

E.5.2 Jet Cuts

- At least one jet found satisfying

$$E_T^{Cal} > 10 \text{ GeV}$$

$$-1 < \eta \leq 3$$

If there is more than one jet satisfying the above criteria then a further restriction is imposed:

$$E_{T,i}^{Cal} \leq 0.25E_{T,1}^{Cal} \text{ for } i \geq 2.$$

E.6 Discussion

For events which pass the selection criteria outlined in the previous section the quantity $E_T^{jet}/P_{T,DA}$ (where $P_{T,DA}$ is the transverse energy of the scattered electron, reconstructed using the double-angle method [81]) is plotted as a function of various DIS electron and jet variables². These distributions are shown for data and MC, along with the corresponding ratios, in figures E.6 and E.7.

²For details about the reconstruction of these variables the reader is referred to [81], [86] or [87].

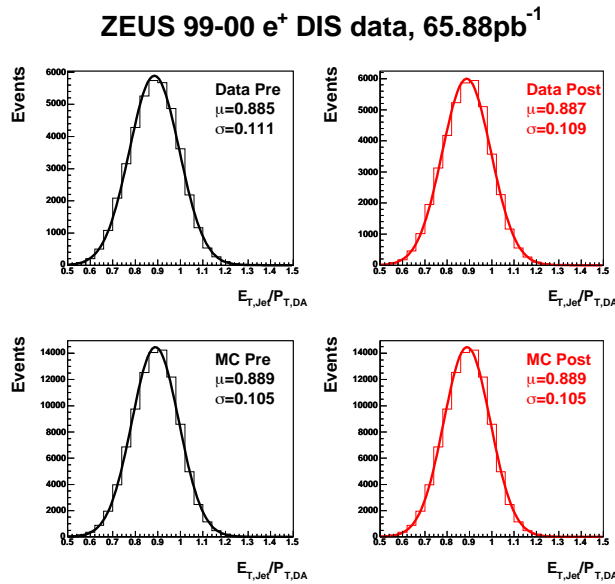


Figure E.5: The distribution of $E_T^{jet}/P_{T,DA}$ in data and MC, before (left plots) and after (right plots) correction using the correction method of section E.2

Without the application of any jet energy scale corrections it can be seen that the difference in the energy scale between data and MC is of the order of $\pm 1\%$ with respect to all the electron and jet variables (within statistical errors). It can also be seen that the application of the jet energy scale corrections evaluated in section E.2 does not improve the energy scale significantly. This indicates that there is actually little need to make an additional correction beyond the calorimeter cell corrections of section 6.2. Indeed, this additional correction method, which resulted in the quotation of a jet energy scale uncertainty of $\pm 1\%$ by the authors of [83, 84] was performed using outdated cell corrections, different to the up-to-date ones used in the present analysis. In effect, two completely independent methods (one which uses jet track information and the balancing of dijets and one which uses calorimeter cell corrections) have produced the same result for the jet energy scale uncertainty. This gives us some confidence that the jet energy scale uncertainty (within statistical errors) really is of the order of $\pm 1\%$. Therefore, no additional jet energy scale correction is used in the present analysis. As an additional point, from figure E.7 it can be seen that there are no problems with quoting an uncertainty of $\pm 1\%$ for jets which lie in the forward region of the detector, $2.5 < \eta^{jet} < 3.0$. Therefore, a jet energy scale uncertainty of $\pm 1\%$ is quoted for jets which lie in the region $-1 < \eta < 3$.

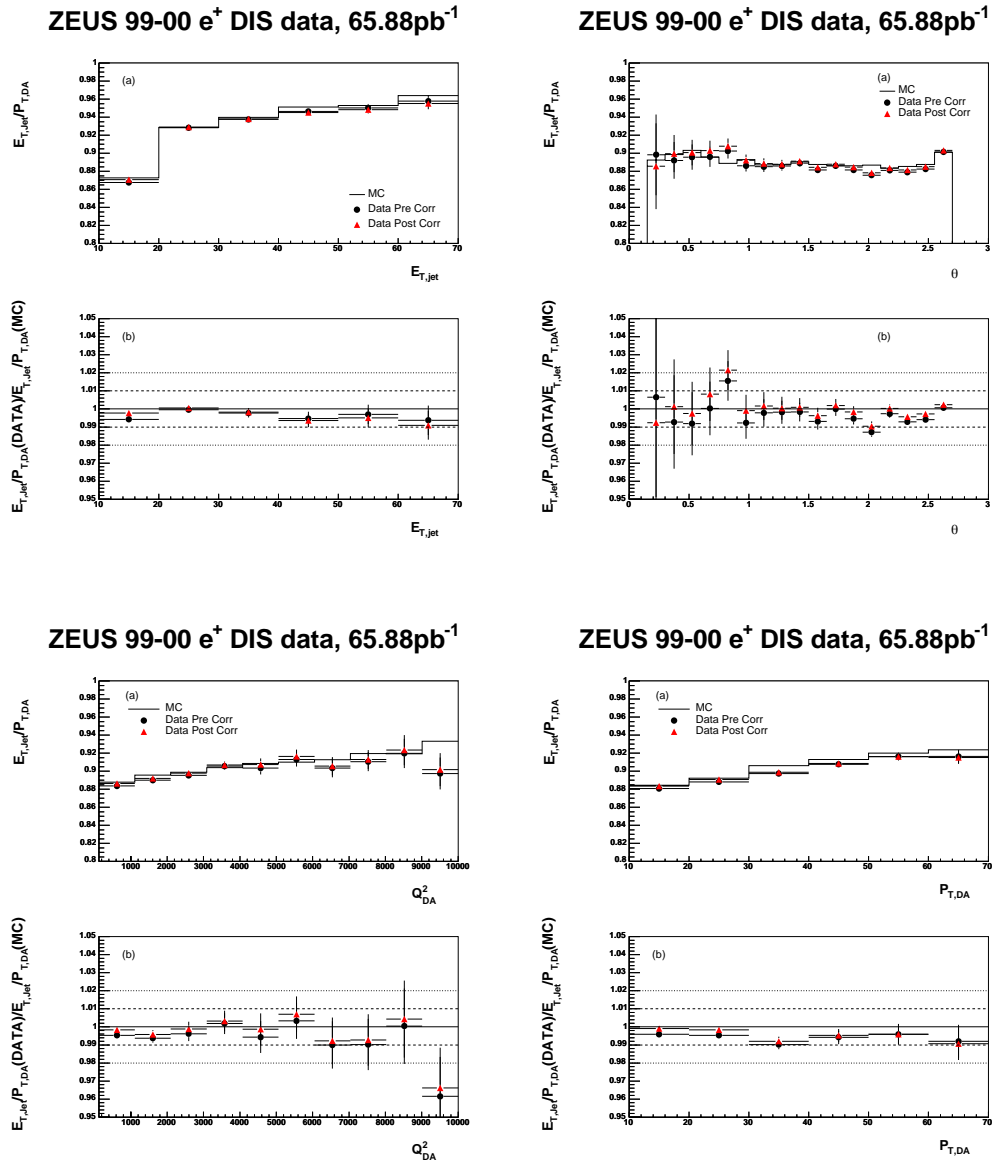


Figure E.6: The distribution of $E_T^{jet}/P_{T,DA}$ in data and MC, before (black) and after (red) correction using the method of section E.2, as a function of various electron and jet variables. The upper plots show the data and MC comparisons while the lower plots show their ratio.

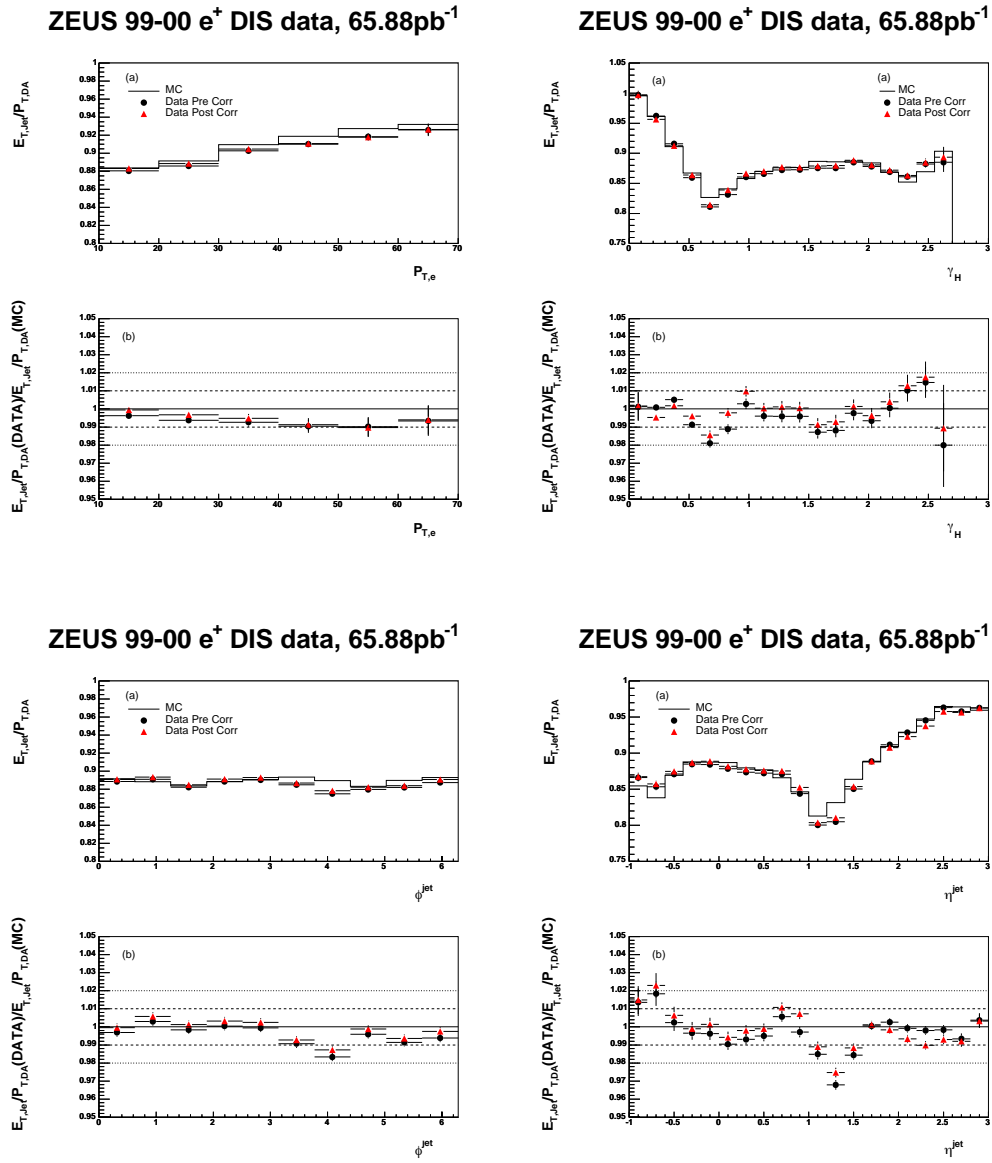


Figure E.7: The distribution of $E_T^{jet}/P_{T,DA}$ in data and MC, before (black) and after (red) correction using the method of section E.2, as a function of various electron and jet variables. The upper plots show the data and MC comparisons while the lower plots show their ratio.

Appendix F

Efficiencies and Purities

This appendix shows the efficiencies and purities for all of the cross-sections measured as part of the analysis presented in this thesis. For more details the reader is referred to chapters 3 and 8.

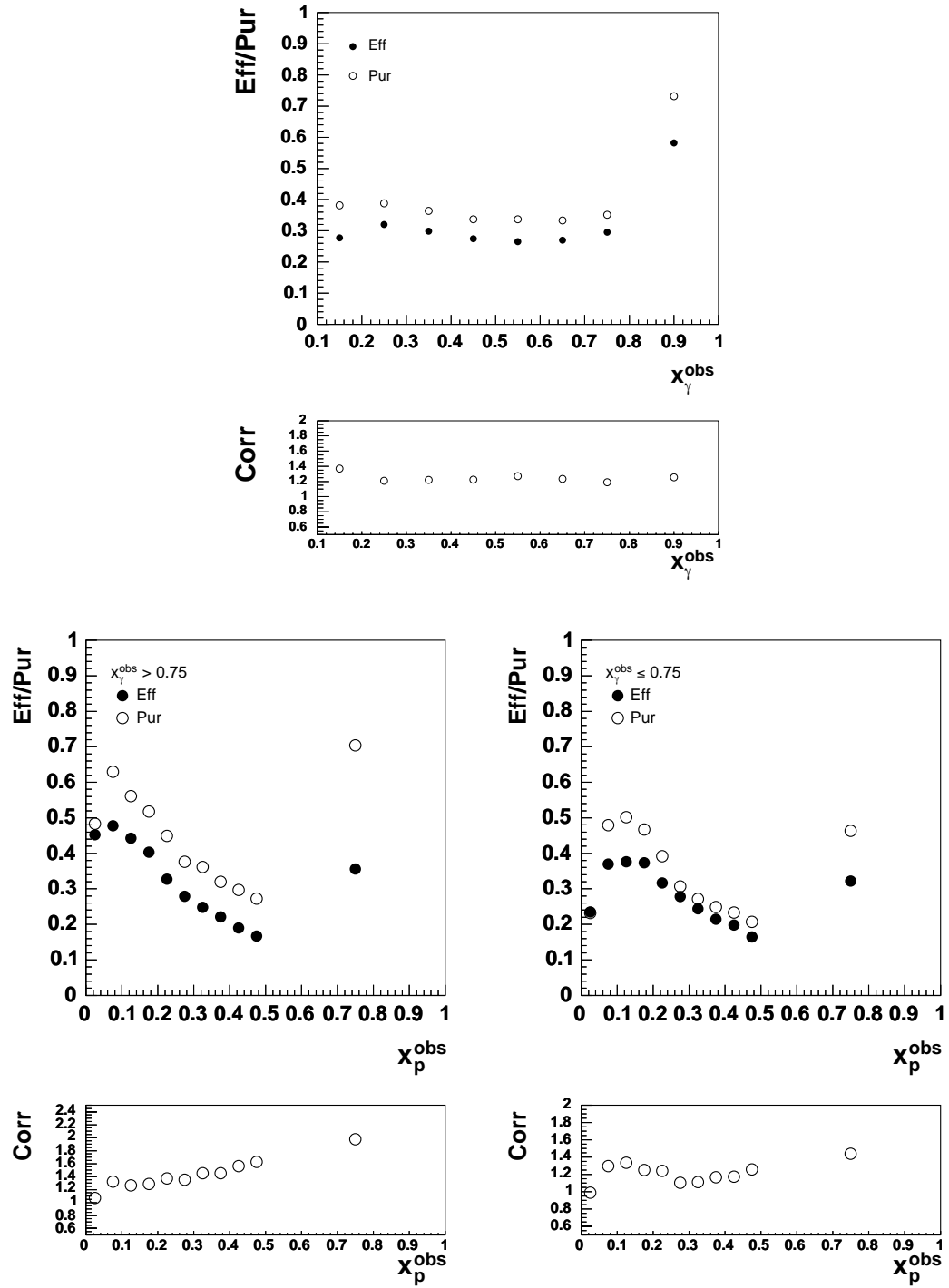


Figure F.1: x_γ^{obs} and x_p^{obs} efficiencies and purities.

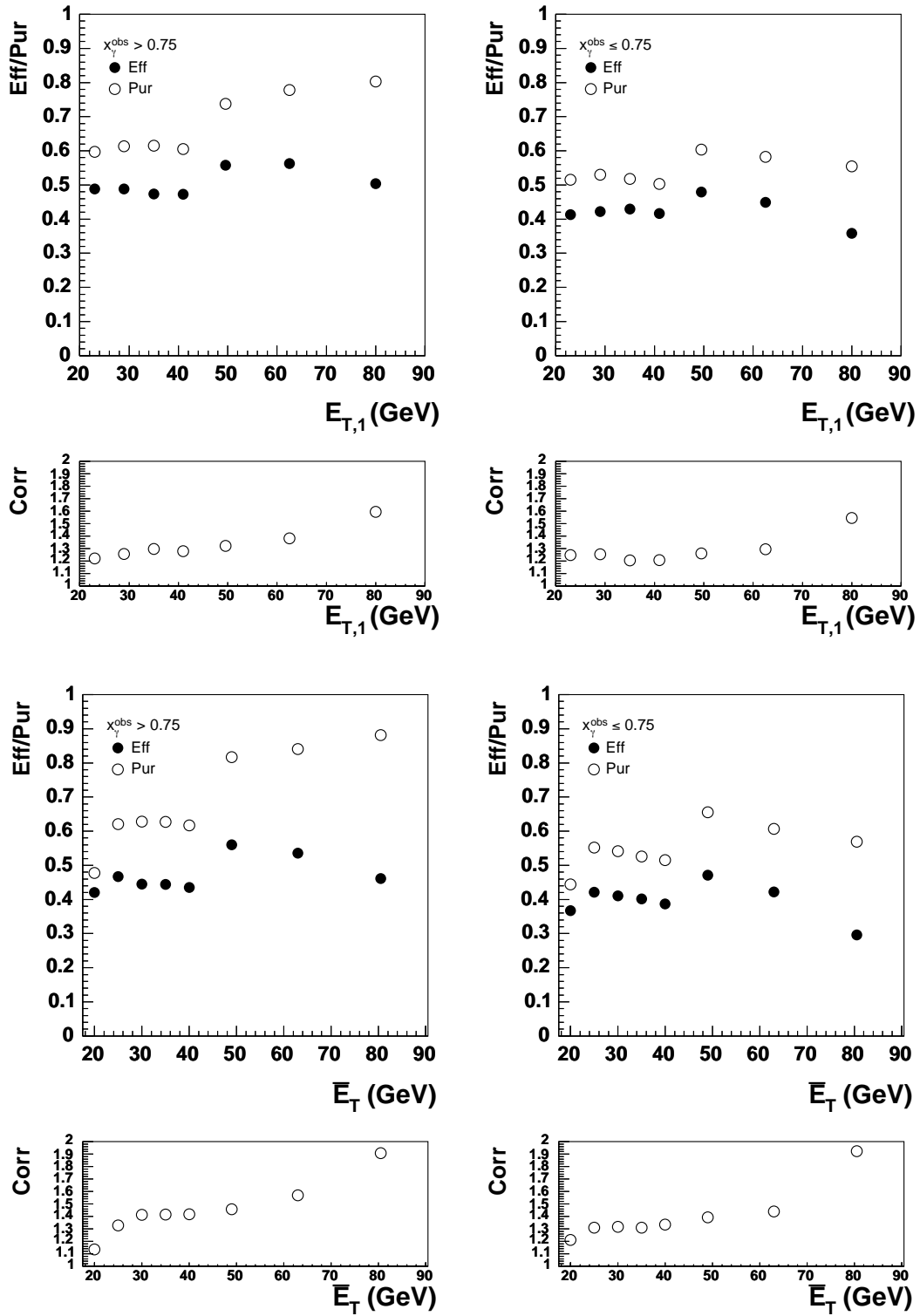


Figure F.2: E_T and \bar{E}_T efficiencies and purities.

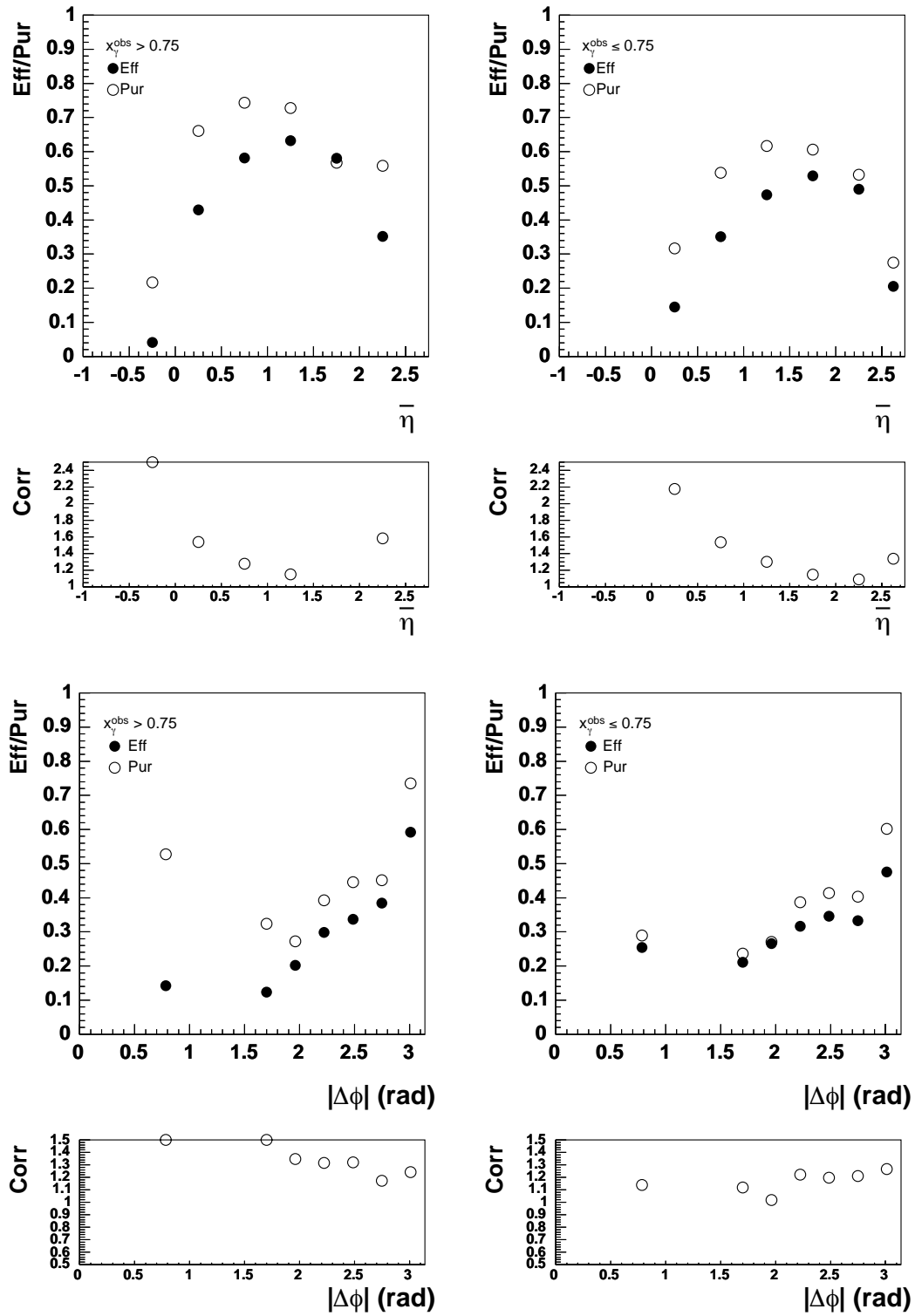


Figure F.3: $\bar{\eta}$ and $|\Delta\phi|$ efficiencies and purities.

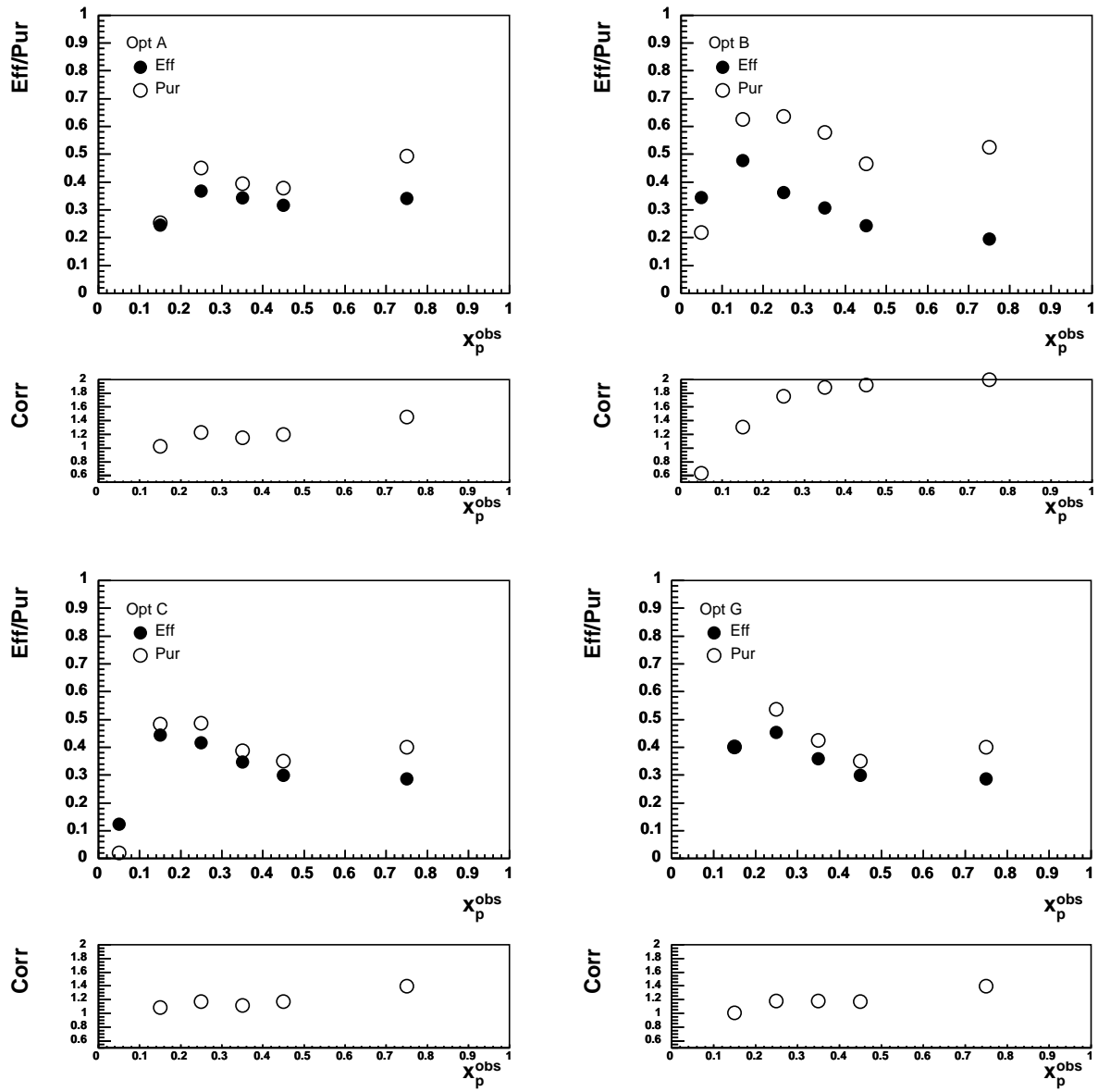


Figure F.4: Low- x_γ^{obs} optimised efficiencies and purities.

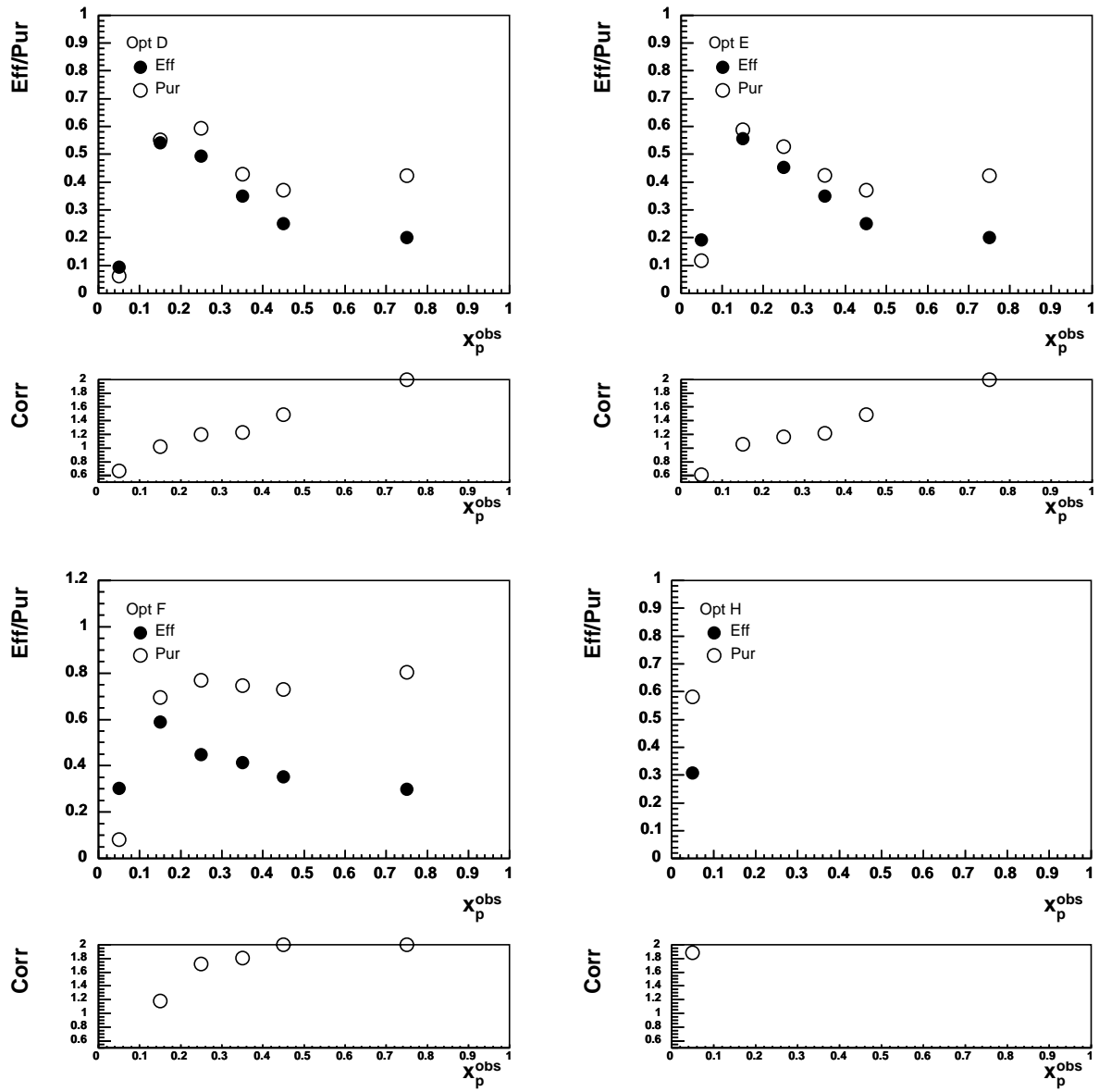


Figure F.5: High- x_γ^{obs} optimised efficiencies and purities.

Appendix G

Hadronisation Corrections

This appendix shows the hadronisation corrections for all of the cross-sections measured as part of the analysis presented in this thesis. For more details the reader is referred to chapters 3 and 8.

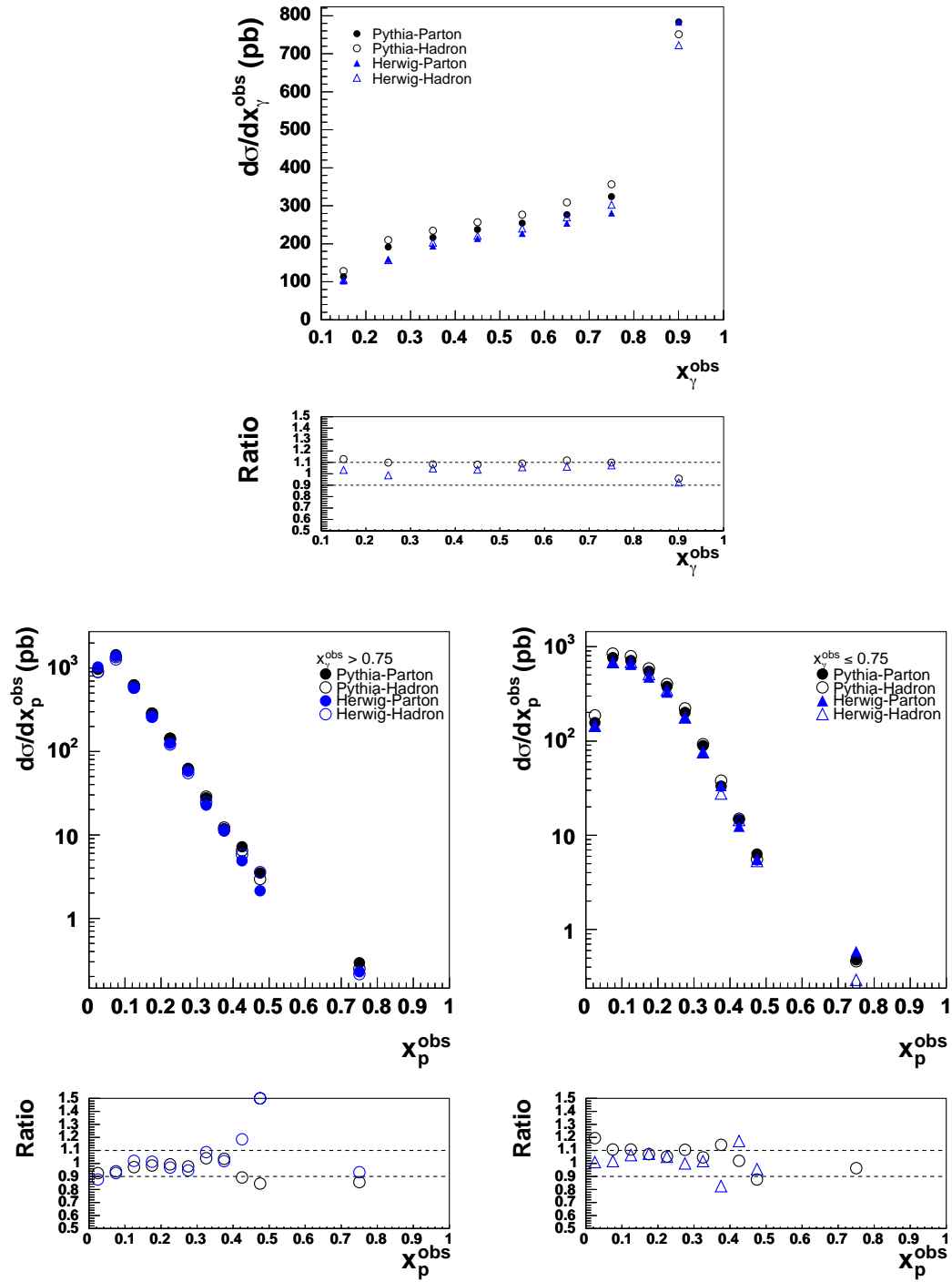


Figure G.1: x_γ^{obs} and x_p^{obs} hadronisation corrections.

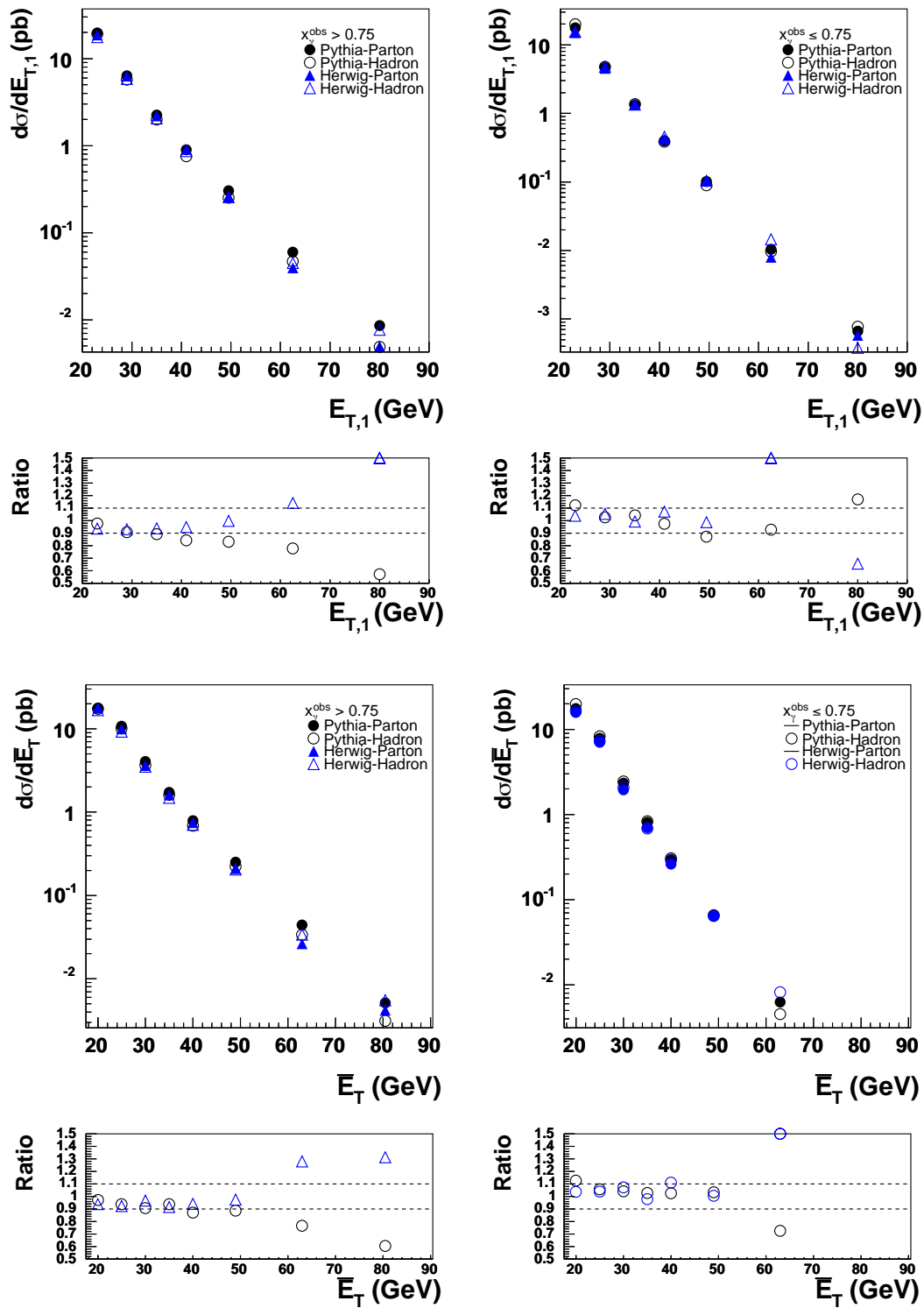


Figure G.2: E_T and \bar{E}_T hadronisation corrections.

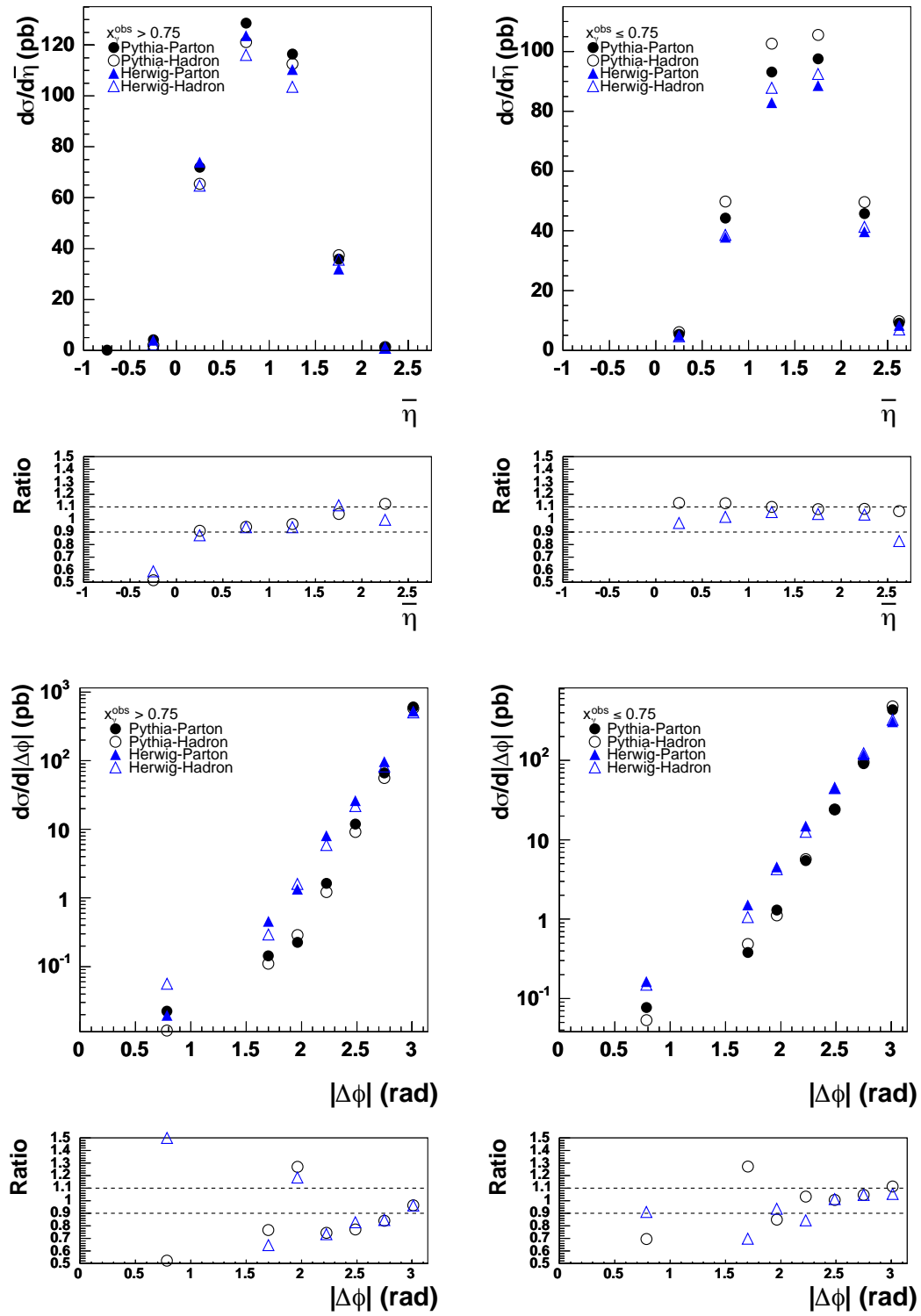


Figure G.3: $\bar{\eta}$ and $|\Delta\phi|$ hadronisation corrections.

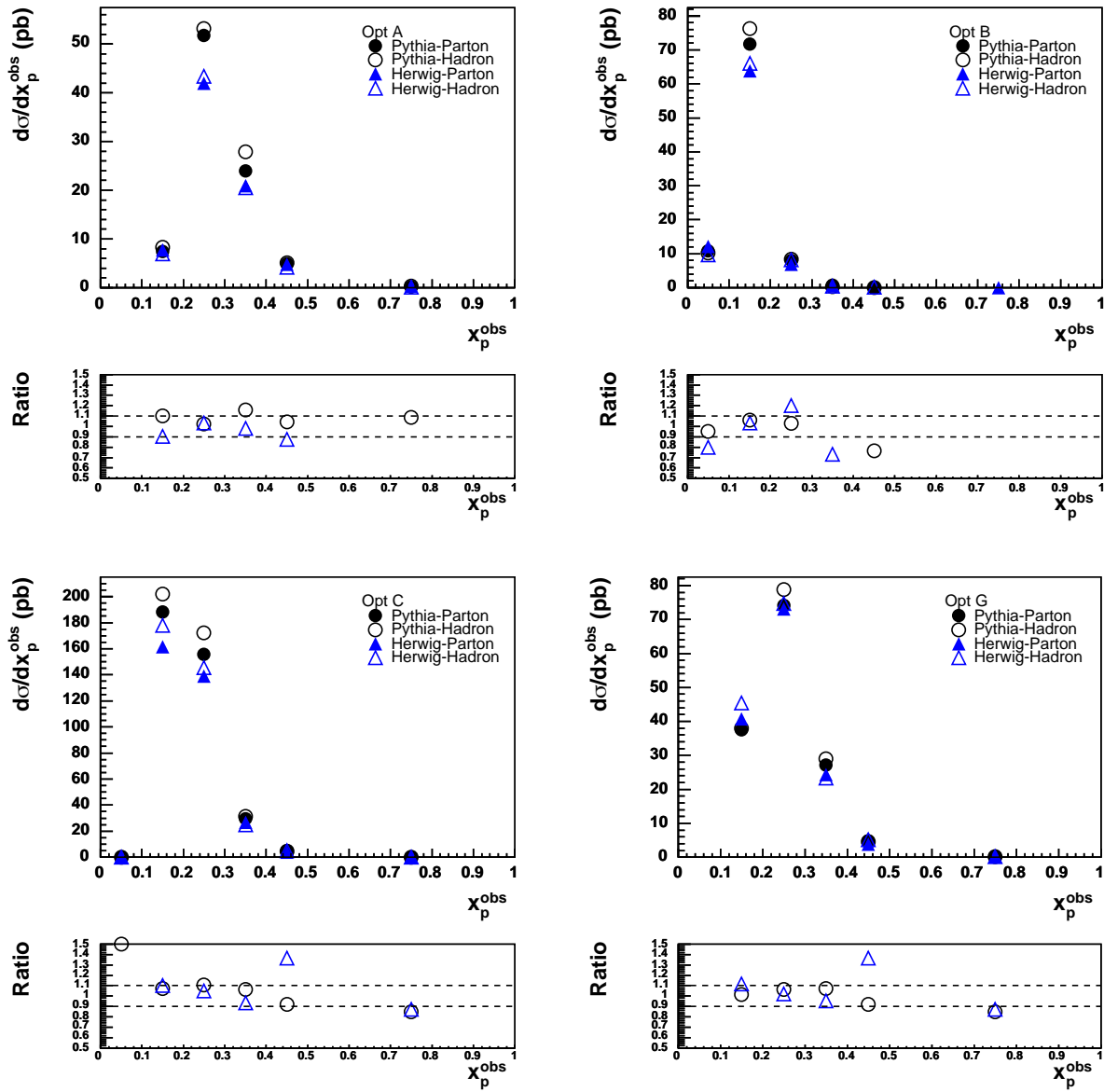


Figure G.4: Low- x_γ^{obs} optimised hadronisation corrections.

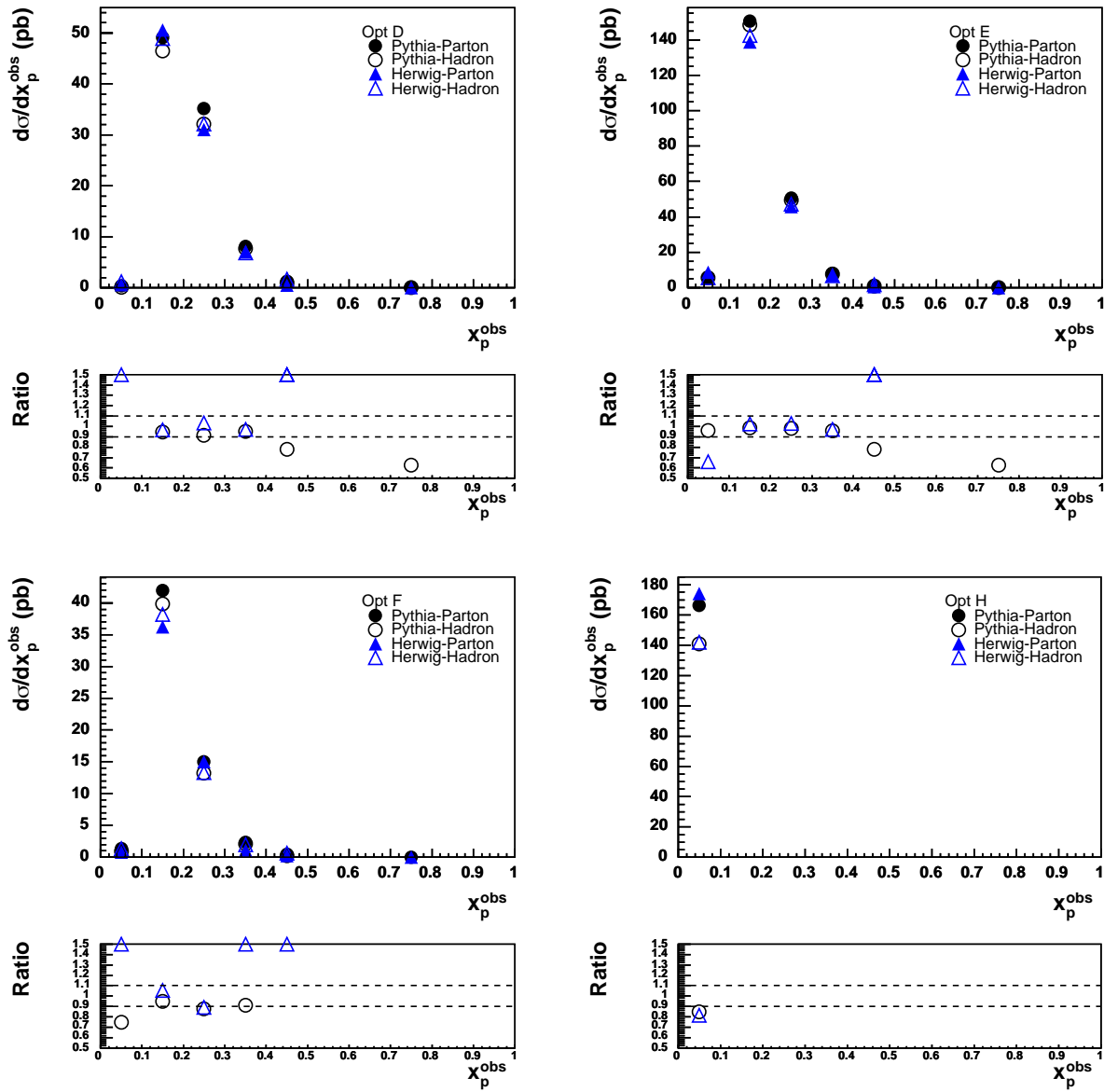


Figure G.5: High- x_γ^{obs} optimised hadronisation corrections.

Appendix H

Theoretical Uncertainties I

This appendix illustrates some of the theoretical uncertainties for the cross-section predictions presented in this thesis. In particular the theoretical uncertainties on the cross-section due to the choice of $\alpha_s(M_Z)$ are considered. Cross-section predictions are made using CTEQ4M ($\alpha_s(M_Z = 0.116)$), CTEQ4A2 ($\alpha_s(M_Z = 0.113)$) and CTEQ4A4 ($\alpha_s(M_Z = 0.119)$). For more details the reader is referred to chapter 8.

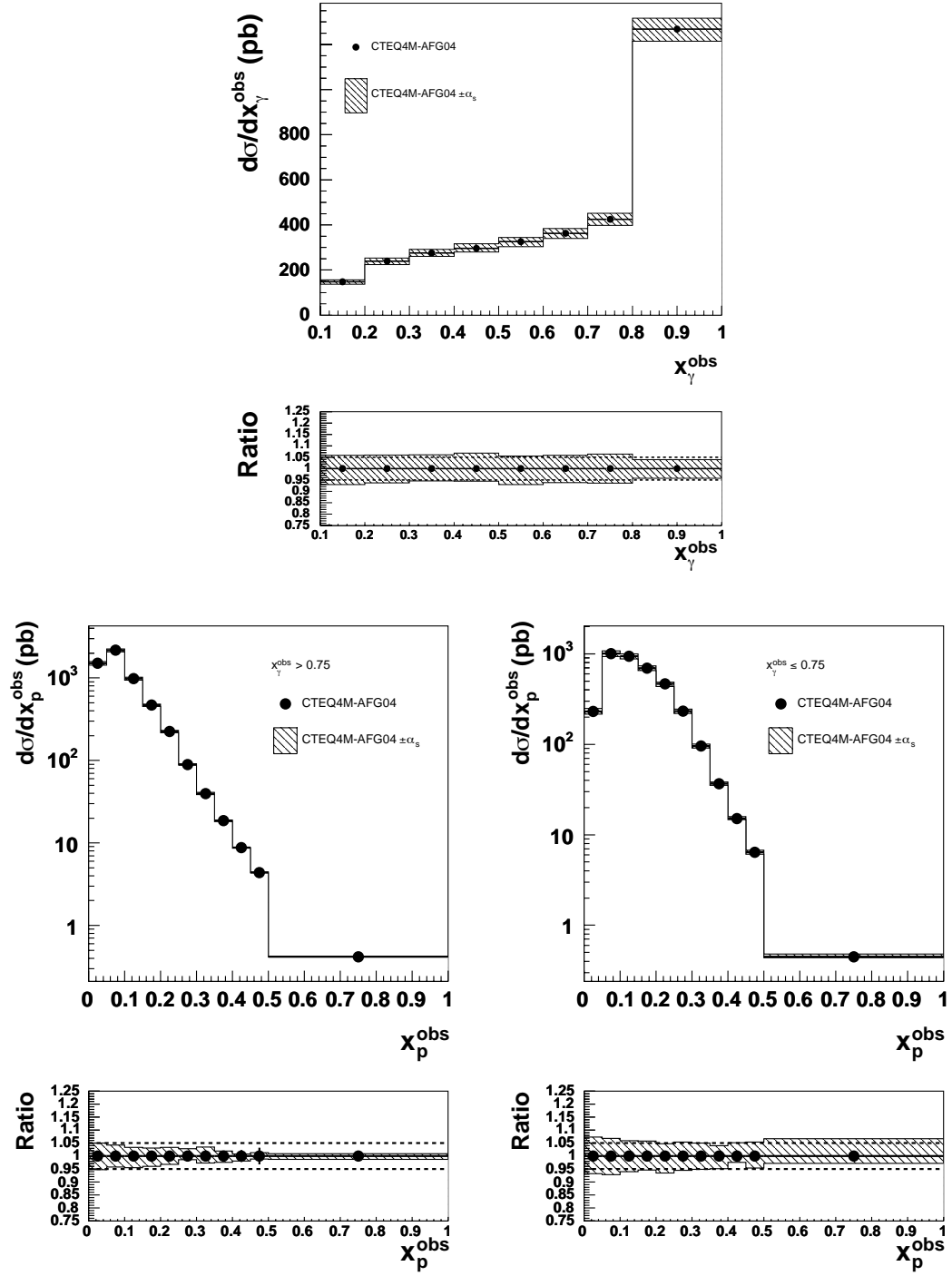


Figure H.1: x_γ^{obs} and x_p^{obs} $\alpha_s(M_Z)$ theoretical uncertainties.

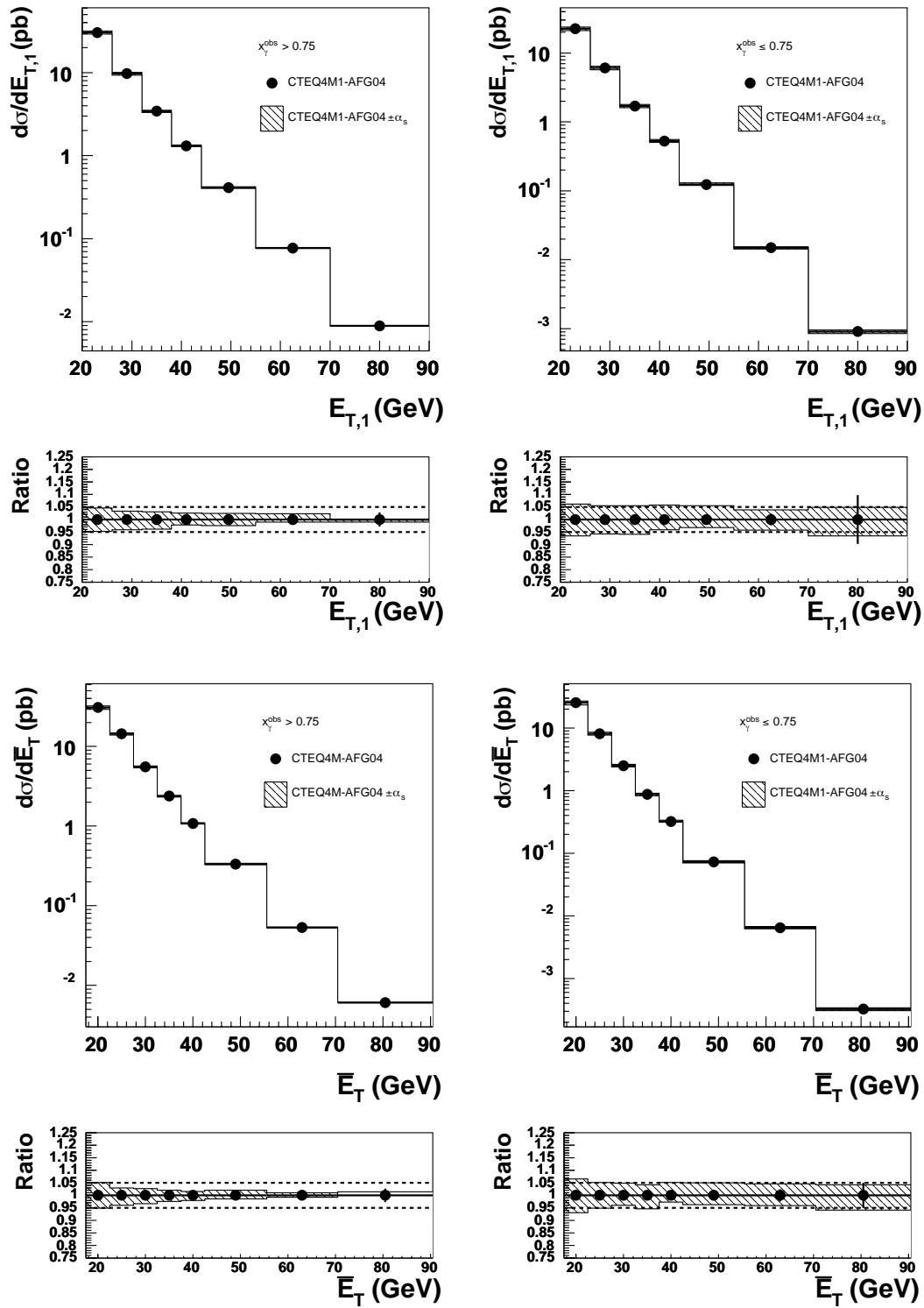


Figure H.2: E_T and \bar{E}_T $\alpha_s(M_Z)$ theoretical uncertainties.

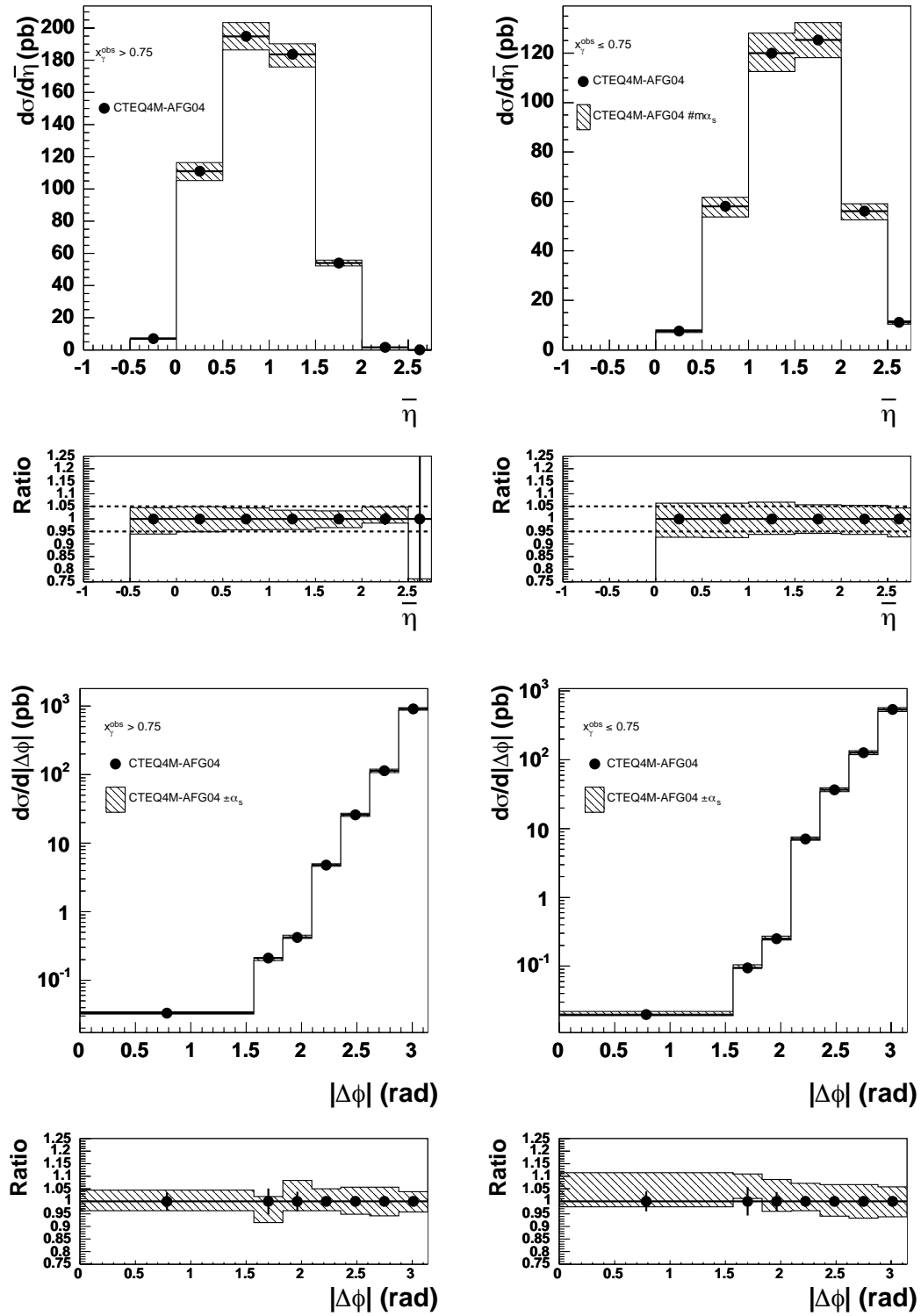


Figure H.3: $\bar{\eta}$ and $|\Delta\phi|$ $\alpha_s(M_Z)$ theoretical uncertainties.

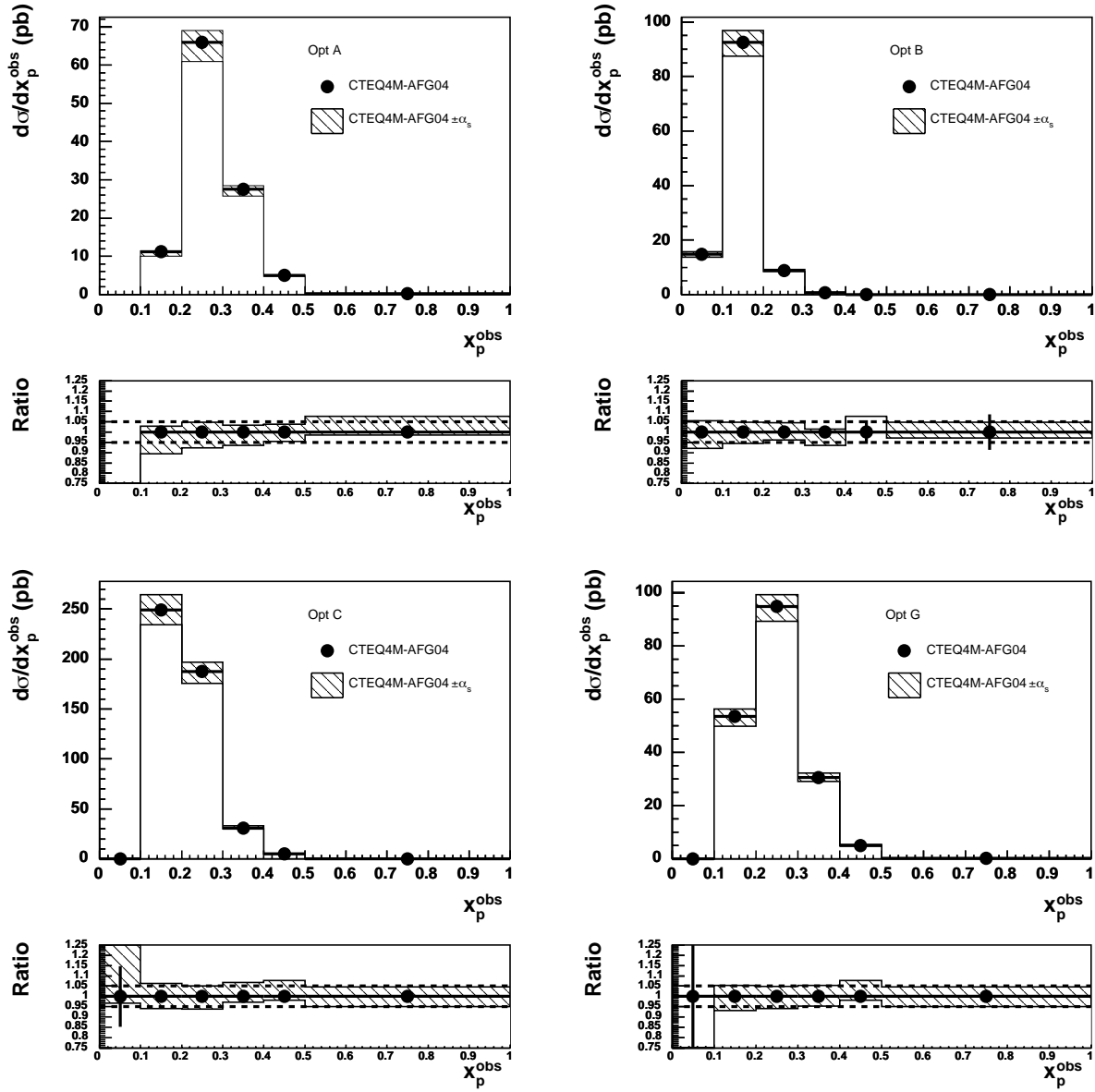


Figure H.4: Low- x_γ^{obs} optimised $\alpha_s(M_Z)$ theoretical uncertainties.

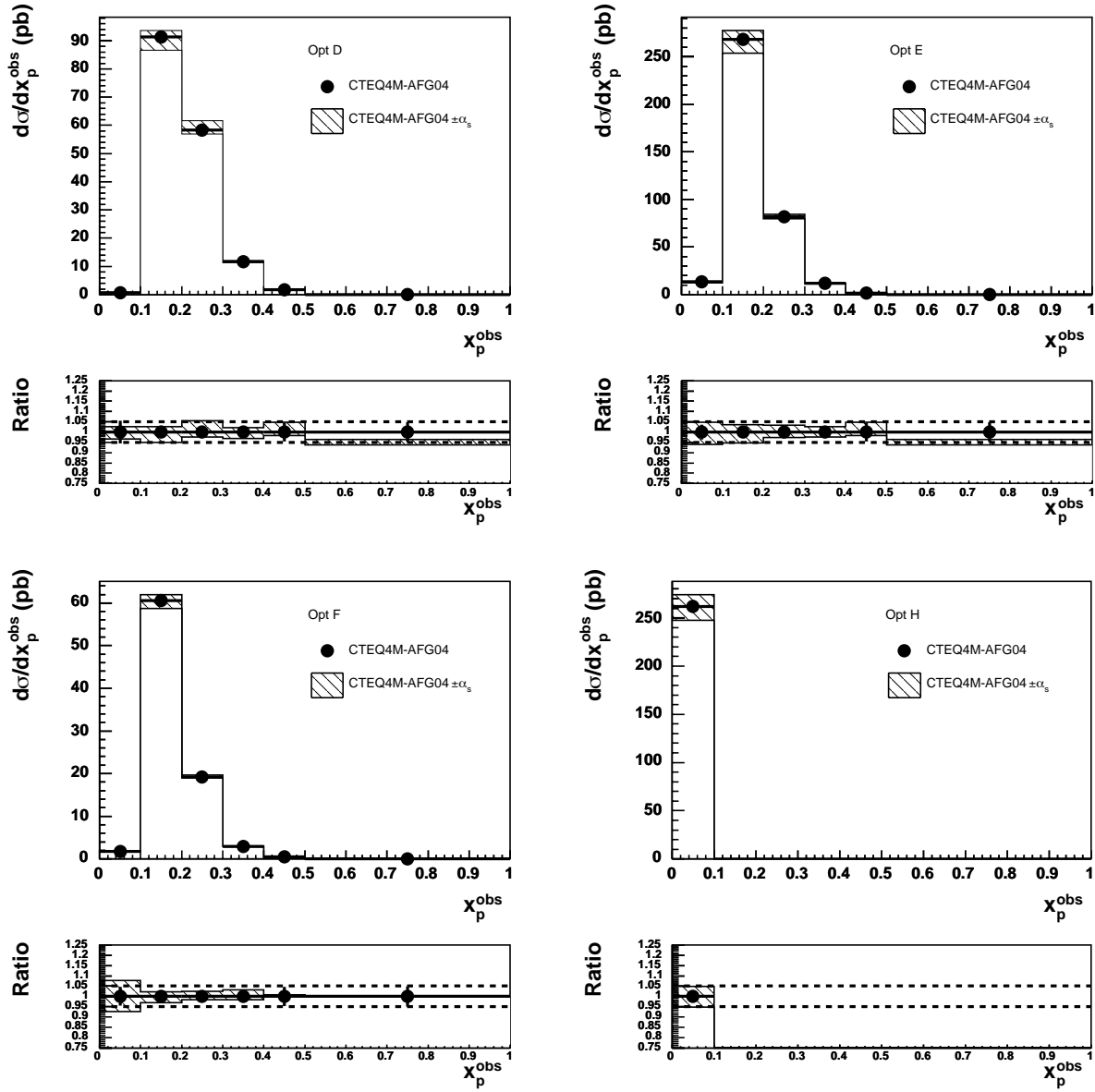


Figure H.5: High- x_γ^{obs} optimised $\alpha_s(M_Z)$ theoretical uncertainties.

Appendix I

Theoretical Uncertainties II

This appendix illustrates some of the theoretical uncertainties for the cross-section predictions presented in this thesis. In particular the theoretical uncertainties on the cross-section due to the choice of renormalisation and factorisation scales are considered. For more details the reader is referred to chapter 8.

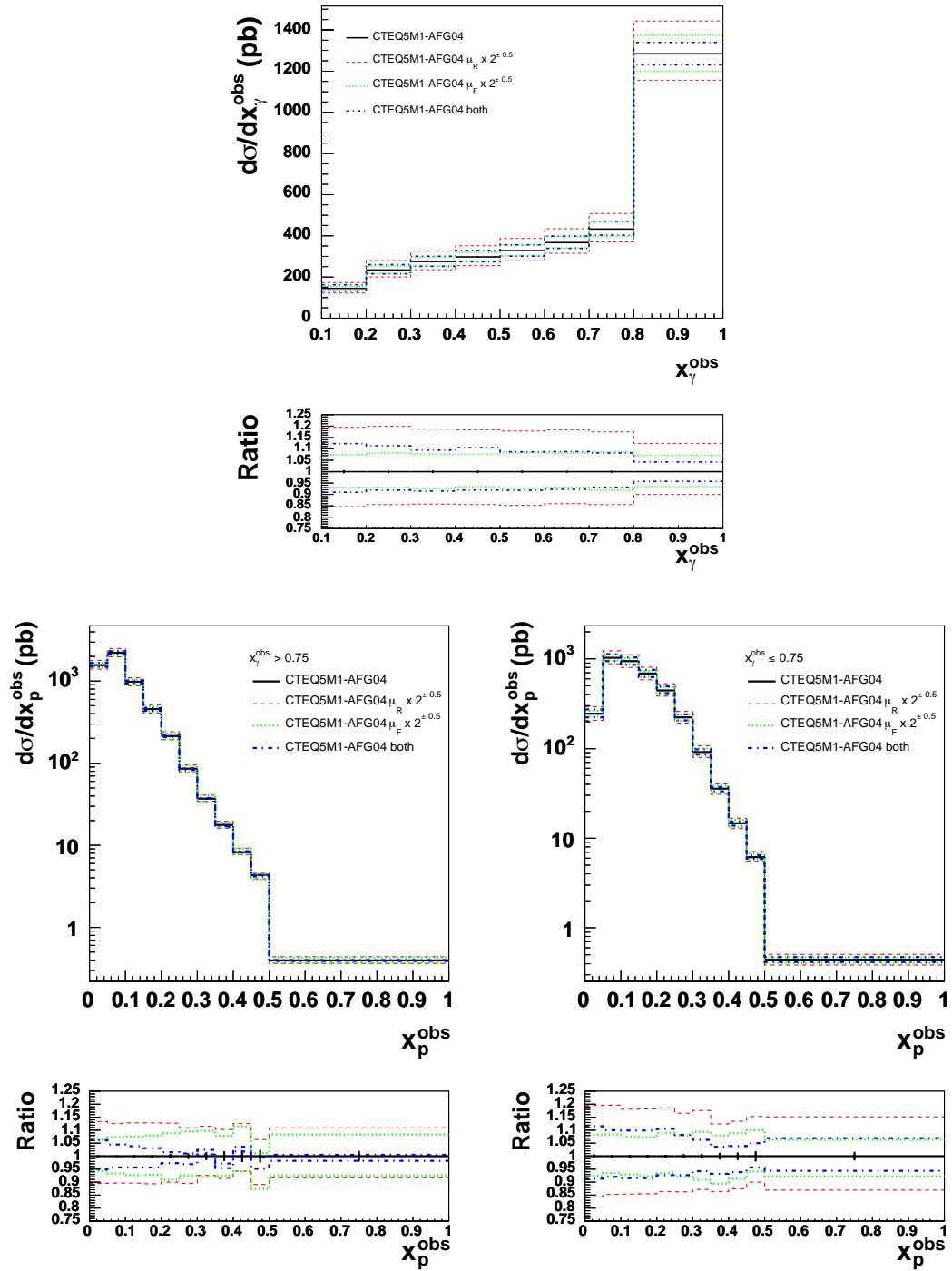


Figure I.1: x_γ^{obs} and x_p^{obs} scale theoretical uncertainties.

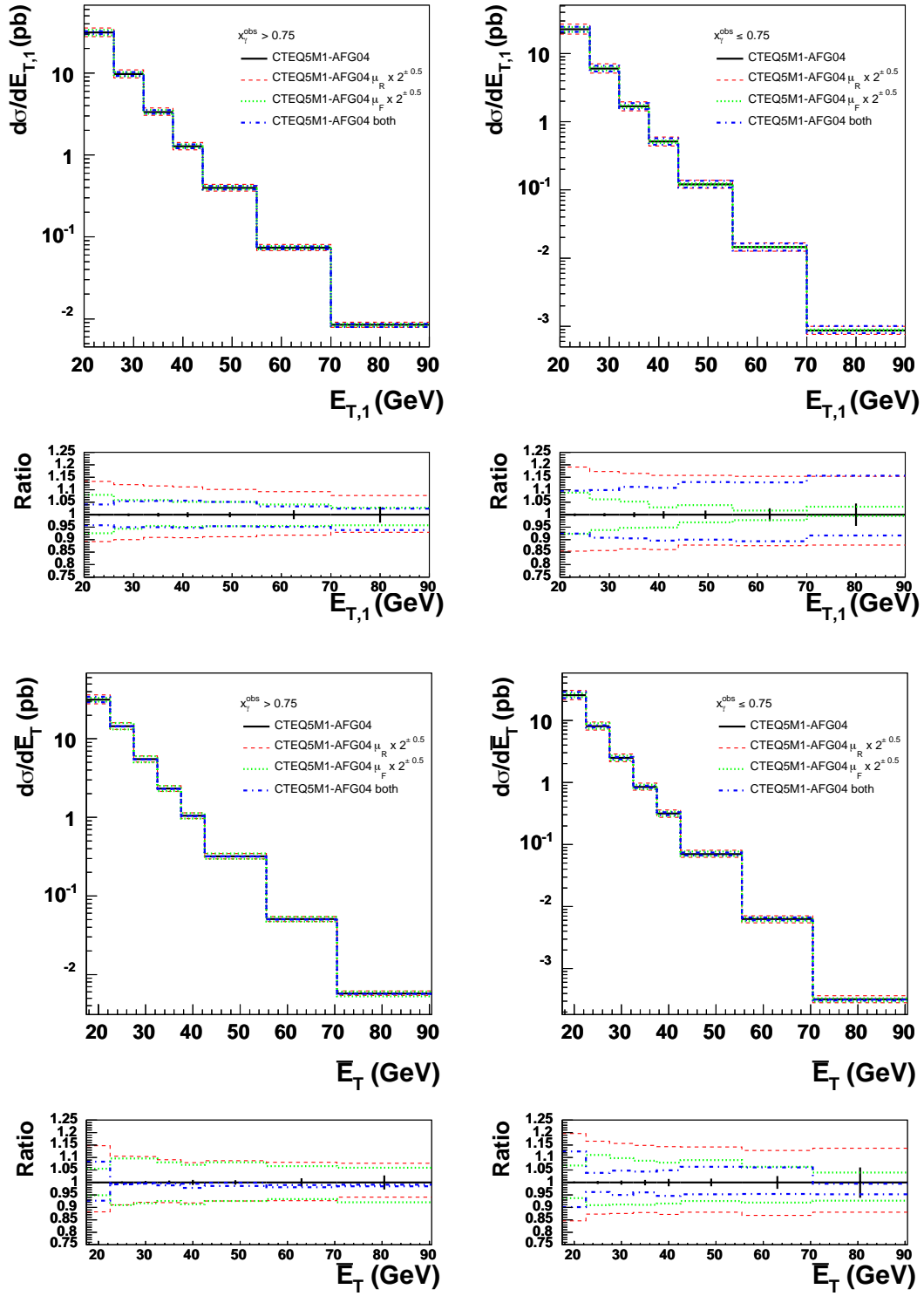


Figure I.2: E_T and \bar{E}_T scale theoretical uncertainties.

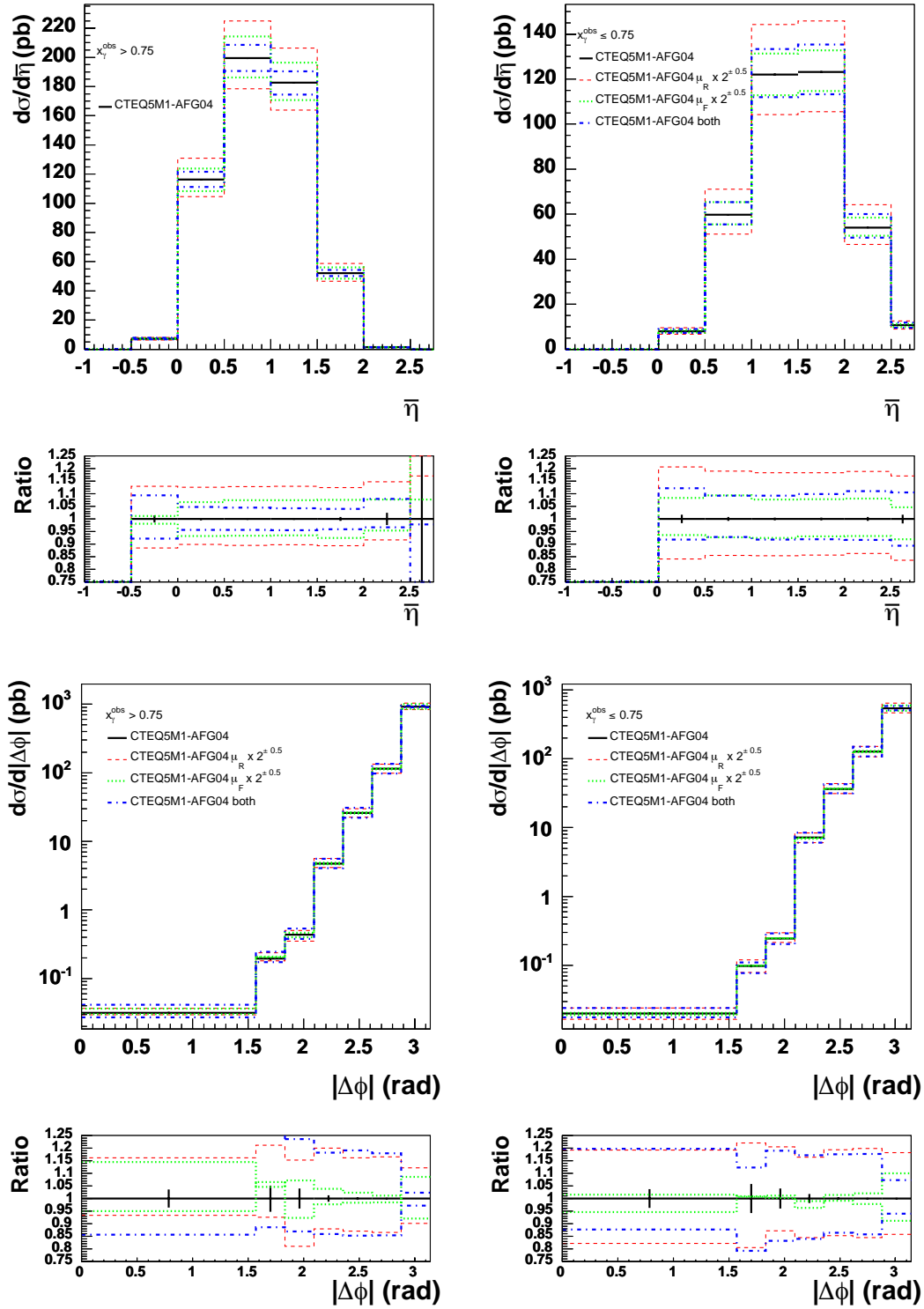


Figure I.3: $\bar{\eta}$ and $|\Delta\phi|$ scale theoretical uncertainties.

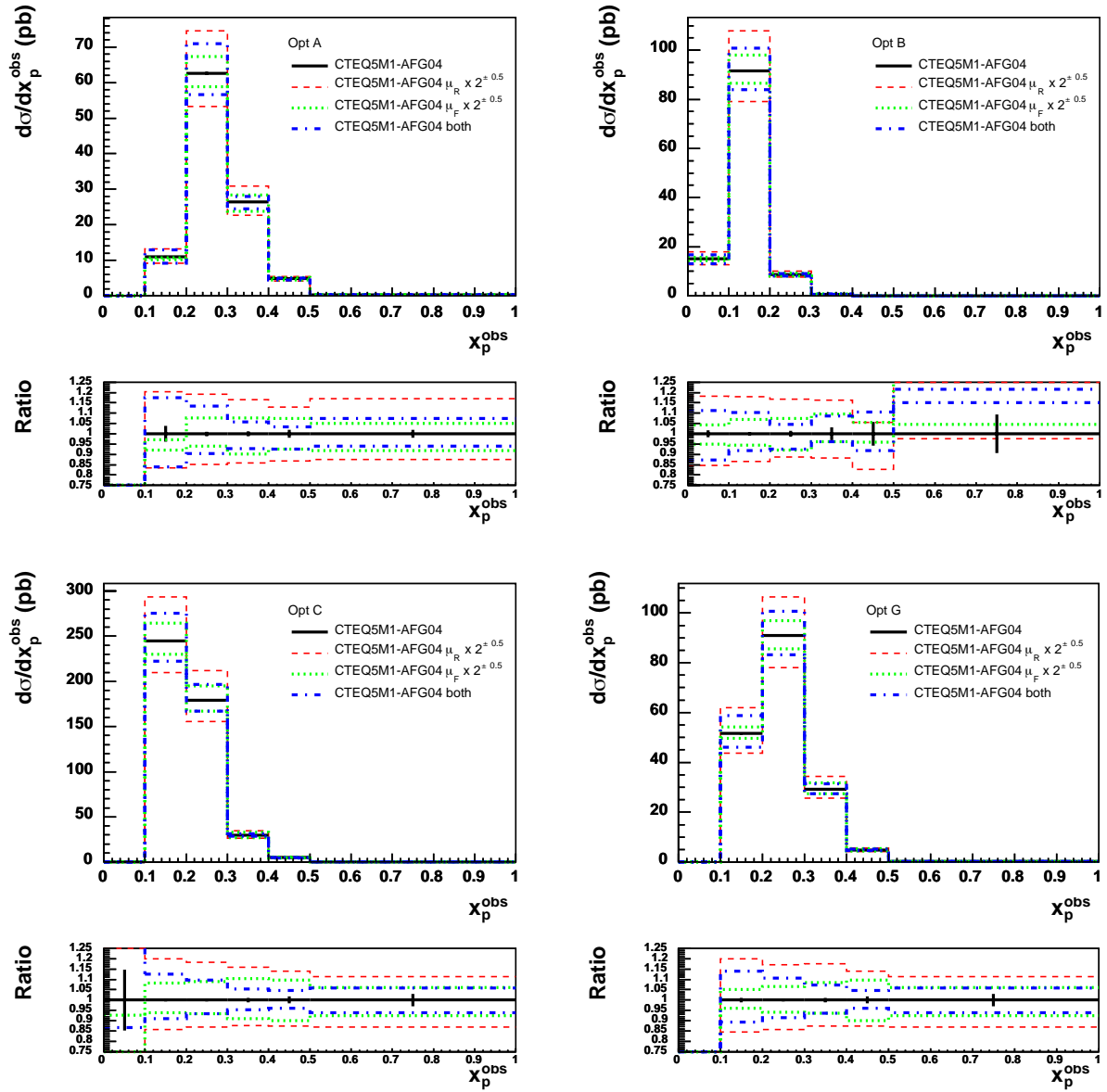


Figure I.4: Low- x_γ^{obs} optimised scale theoretical uncertainties.

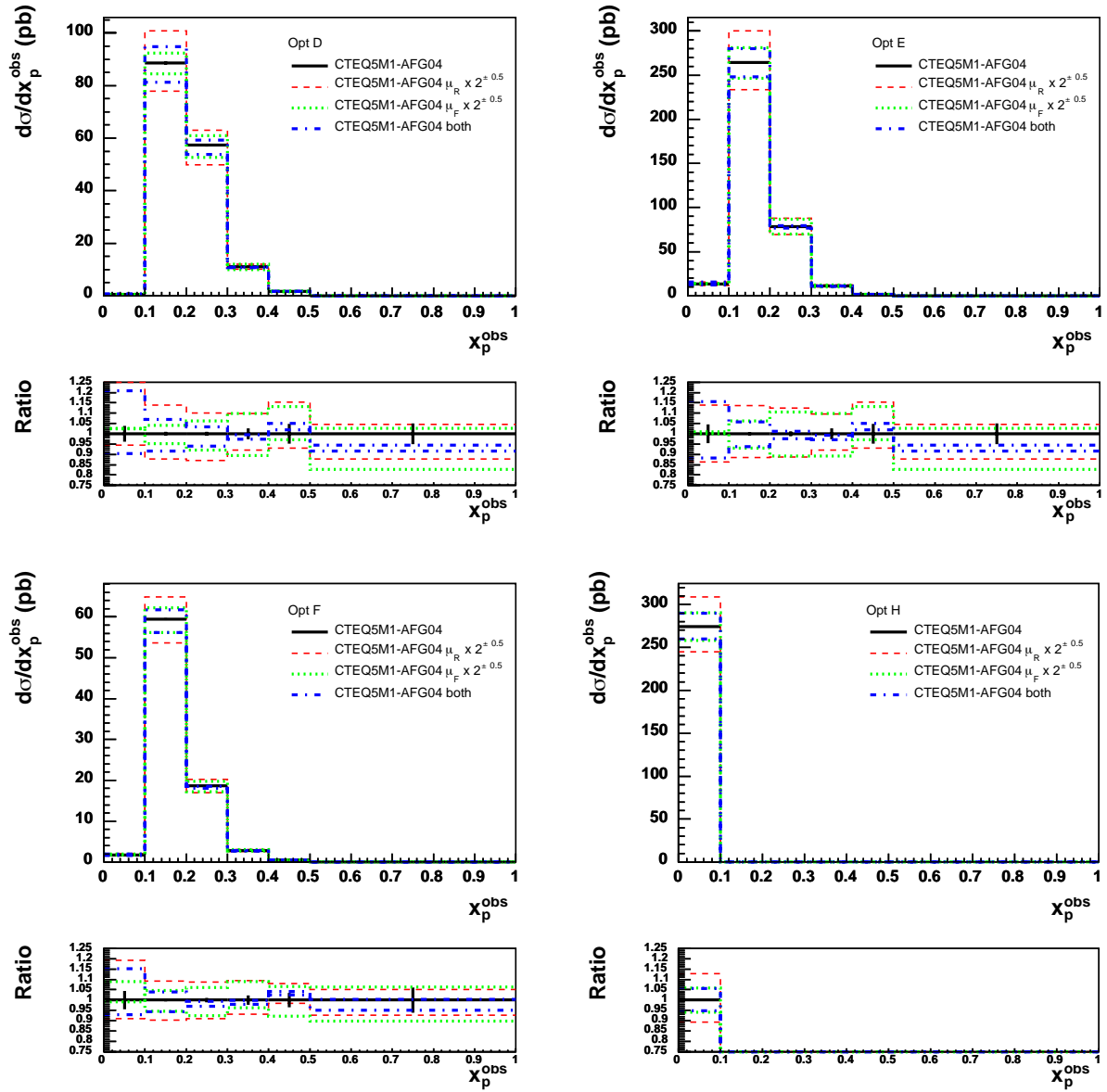


Figure I.5: High- x_γ^{obs} optimised scale theoretical uncertainties.

Appendix J

Cross-Section Tables

Bin	$\frac{d\sigma}{dx_\gamma^{obs}} (pb)$	δ_{stat}	δ_{syst}	δ_{ES}	C_{had}
0.10,0.20	169.26949	± 6.85058	23.26697 11.82230	12.76239 12.93031	1.08052 ± 0.04605
0.20,0.30	271.16199	± 8.11681	16.24563 12.16711	16.12473 16.42062	1.04237 ± 0.05564
0.30,0.40	324.72559	± 9.01453	11.84822 15.80618	16.71381 18.80301	1.06490 ± 0.01737
0.40,0.50	345.30563	± 9.38673	19.46999 13.99836	16.19321 16.04327	1.05813 ± 0.02264
0.50,0.60	383.60468	± 10.09959	20.56751 17.48383	19.87906 18.48135	1.07238 ± 0.01610
0.60,0.70	455.33463	± 11.10044	34.06429 16.08694	18.57584 19.33096	1.08865 ± 0.02795
0.70,0.80	552.40930	± 12.07992	24.06221 34.82713	28.20190 22.09637	1.08661 ± 0.01147
0.80,1.00	1120.63220	± 11.27825	25.31853 15.57937	45.39148 45.31458	0.94046 ± 0.01787

Table J.1: Results of the measurement for the differential cross-section with respect to x_γ^{obs}

Bin	$\frac{d\sigma}{dx_p^{obs}} (pb)$	δ_{stat}	δ_{syst}	δ_{ES}	C_{had}
0.00,0.05	1264.78333	± 24.04571	56.56883 62.59602	84.92859 79.44092	0.90150 ± 0.02470
0.05,0.10	1964.13367	± 31.67994	46.70108 66.71955	71.65759 75.85413	0.93237 ± 0.00725
0.10,0.15	927.78864	± 21.95629	63.88697 19.25457	27.89880 26.65875	0.99613 ± 0.02420
0.15,0.20	480.63983	± 16.50419	16.40181 28.84536	12.25159 13.82233	0.99874 ± 0.01507
0.20,0.25	222.24133	± 11.69718	11.38784 16.29433	2.68164 3.35207	0.98159 ± 0.01212
0.25,0.30	97.21296	± 7.84765	5.71026 2.91674	0.00000 0.00000	0.96298 ± 0.01539
0.30,0.35	49.10360	± 5.96902	2.91181 4.58425	0.00000 0.00000	1.06346 ± 0.02313
0.35,0.40	23.79963	± 4.24994	1.76397 2.74654	0.00000 0.00000	1.02724 ± 0.00818
0.40,0.45	9.94777	± 2.72973	2.40030 0.88635	0.00000 0.00000	1.03896 ± 0.14718
0.45,0.50	3.19058	± 1.43958	2.70268 1.22661	0.00000 0.00000	1.26268 ± 0.41571
0.50,1.00	0.33876	± 0.15421	0.16854 0.18373	0.00000 0.00000	0.89421 ± 0.03883

Table J.2: Results of the measurement for the differential cross-section with respect to x_p^{obs} ($x_\gamma^{obs} > 0.75$).

Bin	$\frac{d\sigma}{dx_p^{obs}} (pb)$	δ_{stat}	δ_{syst}	δ_{ES}	C_{had}
0.00,0.05	236.44737	± 10.25751	35.98560 22.70582	23.93489 18.13246	1.10271 ± 0.09179
0.05,0.10	1128.06494	± 23.73773	74.10019 82.31637	67.55078 67.86768	1.06338 ± 0.04564
0.10,0.15	1125.90247	± 24.10548	64.76612 82.22835	60.75366 62.71338	1.08606 ± 0.02204
0.15,0.20	829.33923	± 20.10274	52.01127 53.10240	42.81250 40.06024	1.07356 ± 0.00110
0.20,0.25	559.27734	± 16.81916	36.85657 28.29419	29.46765 23.08801	1.05312 ± 0.00066
0.25,0.30	303.58258	± 12.23723	42.15493 18.60362	5.14090 8.92886	1.05226 ± 0.05218
0.30,0.35	143.35396	± 8.74491	12.57402 11.48558	0.54404 3.26424	1.03203 ± 0.01438
0.35,0.40	64.46768	± 6.22424	5.09612 14.25296	0.28525 0.00000	0.98504 ± 0.16012
0.40,0.45	26.71716	± 4.11555	3.56063 4.41988	0.00000 0.00000	1.09671 ± 0.07628
0.45,0.50	7.68395	± 2.10004	0.71475 1.41281	0.00000 0.00000	0.91680 ± 0.04028
0.50,1.00	0.84465	± 0.24498	0.36428 0.06920	0.00000 0.00000	0.73277 ± 0.23279

Table J.3: Results of the measurement for the differential cross-section with respect to x_p^{obs} ($x_\gamma^{obs} \leq 0.75$).

Bin	$\frac{d\sigma}{dE_{T,1}}(pb/GeV)$	δ_{stat}	δ_{syst}	δ_{ES}	C_{had}
20.00,26.00	27.34885	± 0.33104	0.99764 0.81094	1.02067 1.10282	0.95696 ± 0.02141
26.00,32.00	9.23385	± 0.19665	0.24211 0.17813	0.47616 0.36864	0.91976 ± 0.01090
32.00,38.00	3.34997	± 0.12131	0.13729 0.16814	0.09004 0.09798	0.91598 ± 0.02394
38.00,44.00	1.25219	± 0.07338	0.14500 0.03293	0.07044 0.09131	0.89602 ± 0.05229
44.00,55.00	0.37188	± 0.02839	0.01091 0.03303	0.02940 0.02499	0.91462 ± 0.08299
55.00,70.00	0.05640	± 0.00937	0.00995 0.00722	0.00677 0.00226	0.95965 ± 0.18187
70.00,90.00	0.00975	± 0.00387	0.00574 0.00115	0.00098 0.00098	1.05382 ± 0.48198

Table J.4: Results of the measurement for the differential cross-section with respect to $E_{T,1}$ ($x_\gamma^{obs} > 0.75$).

Bin	$\frac{d\sigma}{dE_{T,1}}(pb/GeV)$	δ_{stat}	δ_{syst}	δ_{ES}	C_{had}
20.00,26.00	25.41052	± 0.31441	1.35452 1.05857	1.32789 1.21087	1.08121 ± 0.04322
26.00,32.00	8.07963	± 0.18242	0.34564 0.47101	0.41395 0.47016	1.04055 ± 0.01463
32.00,38.00	2.37390	± 0.09895	0.15365 0.13709	0.08856 0.09594	1.01659 ± 0.02517
38.00,44.00	0.71183	± 0.05468	0.03330 0.04164	0.05665 0.05172	1.02334 ± 0.04835
44.00,55.00	0.17949	± 0.02052	0.02885 0.01224	0.01683 0.01402	0.92882 ± 0.05736
55.00,70.00	0.01796	± 0.00581	0.00507 0.00417	0.00211 0.00211	1.38297 ± 0.45333
70.00,90.00	0.00189	± 0.00220	0.00237 0.00195	0.00000 0.00095	0.91294 ± 0.25624

Table J.5: Results of the measurement for the differential cross-section with respect to $E_{T,1}$ ($x_\gamma^{obs} \leq 0.75$).

Bin	$\frac{d\sigma}{dE_T}(pb/GeV)$	δ_{stat}	δ_{syst}	δ_{ES}	C_{had}
17.50,22.50	25.80509	± 0.35646	1.18721 1.07558	1.04187 1.03354	0.95524 ± 0.01741
22.50,27.50	14.69710	± 0.27740	0.32121 0.44645	0.50063 0.63392	0.93146 ± 0.00765
27.50,32.50	5.58339	± 0.17652	0.14256 0.26030	0.33881 0.21089	0.93697 ± 0.02904
32.50,37.50	2.37406	± 0.11522	0.13228 0.10858	0.07614 0.06921	0.92652 ± 0.01152
37.50,42.50	0.96450	± 0.07225	0.07102 0.02748	0.07286 0.04510	0.90698 ± 0.03448
42.50,55.50	0.30040	± 0.02393	0.00936 0.02744	0.01646 0.02058	0.93153 ± 0.04368
55.50,70.50	0.04608	± 0.00907	0.00688 0.00736	0.00128 0.00128	1.02323 ± 0.25549
70.50,90.50	0.00934	± 0.00433	0.00211 0.00234	0.00117 0.00234	0.96012 ± 0.35406

Table J.6: Results of the measurement for the differential cross-section with respect to \bar{E}_T ($x_\gamma^{obs} > 0.75$).

Bin	$\frac{d\sigma}{E_T}(pb/GeV)$	δ_{stat}	δ_{syst}	δ_{ES}	C_{had}
17.50,22.50	26.91343	± 0.35744	1.56714 1.32170	1.41790 1.39422	1.08183 ± 0.04494
22.50,27.50	11.91610	± 0.24388	0.42995 0.63321	0.44894 0.55476	1.04727 ± 0.00884
27.50,32.50	3.67852	± 0.13787	0.21292 0.16804	0.31567 0.17394	1.05699 ± 0.01573
32.50,37.50	1.23049	± 0.08030	0.11962 0.06357	0.05768 0.05447	1.00389 ± 0.02396
37.50,42.50	0.45687	± 0.04987	0.03423 0.04236	0.05548 0.03590	1.06874 ± 0.04308
42.50,55.50	0.08909	± 0.01322	0.01554 0.00401	0.00655 0.00786	1.01916 ± 0.01484
55.50,70.50	0.01055	± 0.00505	0.00710 0.00361	0.00000 0.00117	1.69076 ± 0.96592
70.50,90.50	0.00118	± 0.00226	0.00153 0.00180	0.00000 0.00000	1.00000 ± 0.00000

Table J.7: Results of the measurement for the differential cross-section with respect to \bar{E}_T ($x_\gamma^{obs} \leq 0.75$).

Bin	$\frac{d\sigma}{d\bar{\eta}}(pb)$	δ_{stat}	δ_{syst}	δ_{ES}	C_{had}
-1.00,-0.50	0.00000	± 0.00000	0.00000 0.00000	0.00000 0.00000	0.50000 ± 0.50000
-0.50,0.00	4.80881	± 1.17764	0.78008 7.23841	0.90977 1.16971	0.55135 ± 0.03663
0.00,0.50	90.22646	± 2.29761	6.99920 2.89485	6.66253 5.26980	0.89242 ± 0.01810
0.50,1.00	178.13539	± 2.84429	4.61887 9.08192	6.68790 7.34418	0.94049 ± 0.00127
1.00,1.50	168.38661	± 2.62420	5.83420 5.18042	6.50456 6.67352	0.95185 ± 0.01355
1.50,2.00	58.98626	± 1.54024	1.39881 1.33960	1.31559 1.38735	1.07857 ± 0.03482
2.00,2.50	2.75378	± 0.45539	1.02490 0.85876	0.00000 0.00000	1.06192 ± 0.06439
2.50,2.75	0.00000	± 0.00000	0.00000 0.00000	0.00000 0.00000	1.00000 ± 0.00000

Table J.8: Results of the measurement for the differential cross-section with respect to $\bar{\eta}$ ($x_{\gamma}^{obs} > 0.75$).

Bin	$\frac{d\sigma}{d\bar{\eta}}(pb)$	δ_{stat}	δ_{syst}	δ_{ES}	C_{had}
-1.00,-0.50	0.00000	± 0.00000	0.00000 0.00000	0.00000 0.00000	1.00000 ± 0.00000
-0.50,0.00	0.00000	± 0.00000	0.00000 0.00000	0.00000 0.00000	1.00000 ± 0.00000
0.00,0.50	7.08929	± 0.77009	1.88765 0.75345	0.74624 0.42642	1.05173 ± 0.07976
0.50,1.00	65.39553	± 1.93489	5.96122 5.28514	4.24451 3.79377	1.07416 ± 0.05365
1.00,1.50	143.38754	± 2.58815	9.09018 11.60877	7.48305 7.83328	1.08001 ± 0.02131
1.50,2.00	146.36679	± 2.44916	7.55472 8.66808	6.89511 6.39058	1.06273 ± 0.01933
2.00,2.50	71.14087	± 1.72942	6.20292 3.22633	3.78069 3.46120	1.06220 ± 0.02237
2.50,2.75	18.38927	± 1.57059	0.81700 3.15419	0.45810 1.30885	0.94801 ± 0.11853

Table J.9: Results of the measurement for the differential cross-section with respect to $\bar{\eta}$ ($x_{\gamma}^{obs} \leq 0.75$).

Bin	$\frac{d\sigma}{d \Delta\phi } (pb/rad)$	δ_{stat}	δ_{syst}	δ_{ES}	C_{had}
0.00,1.57	0.08684	± 0.09214	0.23162 0.12170	0.05789 0.00000	1.70216 ± 1.17938
1.57,1.83	0.00000	± 0.00000	0.53874 0.00000	0.00000 0.00000	0.70741 ± 0.06023
1.83,2.09	1.69869	± 0.50761	0.22701 0.81452	0.18874 0.12583	1.22735 ± 0.04195
2.09,2.36	7.81585	± 0.98885	2.11574 0.71676	0.36925 0.43079	0.73864 ± 0.00600
2.36,2.62	36.20153	± 2.18568	2.26995 4.91949	1.97688 2.34754	0.79979 ± 0.02755
2.62,2.88	133.68221	± 3.93805	8.35105 8.29246	6.46759 6.85129	0.84409 ± 0.00224
2.88,3.14	781.47485	± 8.06019	24.89633 30.92350	30.34454 29.41632	0.96323 ± 0.00141

Table J.10: Results of the measurement for the differential cross-section with respect to $|\Delta\phi|$ ($x_\gamma^{obs} > 0.75$).

Bin	$\frac{d\sigma}{d \Delta\phi } (pb/rad)$	δ_{stat}	δ_{syst}	δ_{ES}	C_{had}
0.00,1.57	0.25736	± 0.07115	0.12137 0.01368	0.05325 0.00887	0.80334 ± 0.10816
1.57,1.83	2.87642	± 0.59629	0.71587 0.50954	0.15690 0.15690	0.98444 ± 0.28677
1.83,2.09	6.61882	± 0.76376	0.57994 0.24835	0.47617 0.66664	0.89206 ± 0.04363
2.09,2.36	28.13800	± 1.70044	1.77854 3.55387	1.88348 1.99763	0.93927 ± 0.09454
2.36,2.62	78.39278	± 2.80102	6.27786 4.34798	4.02588 4.36137	1.01019 ± 0.00414
2.62,2.88	203.08003	± 4.57502	13.64571 19.47365	12.04903 11.31364	1.04605 ± 0.00081
2.88,3.14	523.82666	± 6.66417	40.10539 35.94790	24.87646 23.81027	1.08367 ± 0.03014

Table J.11: Results of the measurement for the differential cross-section with respect to $|\Delta\phi|$ ($x_\gamma^{obs} \leq 0.75$).

Bin	$\frac{d\sigma}{dx_p^{obs}}(pb)$	δ_{stat}	δ_{syst}	δ_{ES}	C_{had}
0.00,0.10	0.00000	± 0.00000	0.00000 0.00000	0.00000 0.00000	1.00000 ± 0.00000
0.10,0.20	14.61543	± 1.94451	3.16304 1.32325	1.88993 1.76393	1.00372 ± 0.09890
0.20,0.30	89.28519	± 4.83092	15.45490 7.40956	4.50178 6.45255	1.02977 ± 0.00347
0.30,0.40	46.12372	± 3.53386	3.04252 4.75701	0.28124 1.40621	1.07004 ± 0.09028
0.40,0.50	7.02864	± 1.35700	0.87342 1.37589	0.00000 0.00000	0.96041 ± 0.08309
0.50,1.00	0.46096	± 0.17866	0.10559 0.07208	0.00000 0.00000	0.71293 ± 0.37180

Table J.12: Results of the measurement for the differential cross-section with respect to x_p^{obs} ($x_\gamma^{obs} \leq 0.75$, OptA).

Bin	$\frac{d\sigma}{dx_p^{obs}}(pb)$	δ_{stat}	δ_{syst}	δ_{ES}	C_{had}
0.00,0.10	18.55461	± 1.79272	3.75507 2.61813	1.39742 2.09613	0.87591 ± 0.07692
0.10,0.20	118.42126	± 5.40168	5.05962 5.90050	4.96089 4.64082	1.04837 ± 0.01373
0.20,0.30	12.24064	± 2.03849	2.27447 1.56682	0.00000 0.00000	1.11610 ± 0.08518
0.30,0.40	0.23014	± 0.25128	0.56873 0.23235	0.00000 0.00000	0.60424 ± 0.12709
0.40,0.50	0.00000	± 0.00000	0.00000 0.00000	0.00000 0.00000	0.88373 ± 0.11627
0.50,1.00	0.06583	± 0.34672	0.12127 0.13801	0.00000 0.00000	0.50000 ± 0.50000

Table J.13: Results of the measurement for the differential cross-section with respect to x_p^{obs} ($x_\gamma^{obs} \leq 0.75$, OptB).

Bin	$\frac{d\sigma}{dx_p^{obs}}(pb)$	δ_{stat}	δ_{syst}	δ_{ES}	C_{had}
0.00,0.10	0.19907	± 0.12024	0.18040 0.23192	0.03981 0.03981	1.11340 ± 0.61340
0.10,0.20	281.51123	± 7.67758	25.53798 15.56522	19.43292 17.43640	1.08696 ± 0.01459
0.20,0.30	229.99171	± 7.24623	15.98416 8.88638	8.02464 6.59167	1.07799 ± 0.02968
0.30,0.40	47.14978	± 3.41260	3.04704 3.46492	0.13667 0.13667	0.99931 ± 0.06432
0.40,0.50	8.63306	± 1.59903	1.17122 0.86181	0.00000 0.00000	1.14338 ± 0.22313
0.50,1.00	0.23946	± 0.12068	0.25773 0.02843	0.00000 0.00000	0.85904 ± 0.01030

Table J.14: Results of the measurement for the differential cross-section with respect to x_p^{obs} ($x_\gamma^{obs} \leq 0.75$, OptC).

Bin	$\frac{d\sigma}{dx_p^{obs}}(pb)$	δ_{stat}	δ_{syst}	δ_{ES}	C_{had}
0.00,0.10	0.00000	± 0.00000	0.00000 0.00000	0.00000 0.00000	1.00000 ± 0.00000
0.10,0.20	72.99507	± 4.02105	3.53477 8.54449	5.90855 5.41616	1.06605 ± 0.05207
0.20,0.30	118.07422	± 5.19526	8.05612 5.89210	5.93265 5.35386	1.04188 ± 0.02066
0.30,0.40	43.28103	± 3.31722	4.72922 1.71841	0.86852 0.28951	1.01307 ± 0.05886
0.40,0.50	8.63306	± 1.59903	1.17125 0.86181	0.00000 0.00000	1.14338 ± 0.22313
0.50,1.00	0.23946	± 0.12068	0.25773 0.02843	0.00000 0.00000	0.85904 ± 0.01030

Table J.15: Results of the measurement for the differential cross-section with respect to x_p^{obs} ($x_\gamma^{obs} \leq 0.75$, OptG).

Bin	$\frac{d\sigma}{dx_p^{obs}}(pb)$	δ_{stat}	δ_{syst}	δ_{ES}	C_{had}
0.00,0.10	1.14002	± 0.65165	3.07069 0.77760	0.08143 0.08143	1.13567 ± 0.75514
0.10,0.20	81.32364	± 4.21102	2.70552 9.84977	4.12238 4.37225	0.95709 ± 0.01013
0.20,0.30	51.03179	± 3.49660	5.17358 2.97727	2.05892 0.73532	0.97351 ± 0.05924
0.30,0.40	13.05089	± 1.95227	1.15774 1.34061	0.00000 0.00000	0.96233 ± 0.00992
0.40,0.50	2.18734	± 0.91186	0.89905 0.43436	0.00000 0.00000	1.95955 ± 1.18119
0.50,1.00	0.00000	± 0.00000	0.06358 0.00000	0.00000 0.00000	0.31357 ± 0.31357

Table J.16: Results of the measurement for the differential cross-section with respect to x_p^{obs} ($x_\gamma^{obs} > 0.75$, OptD).

Bin	$\frac{d\sigma}{dx_p^{obs}}(pb)$	δ_{stat}	δ_{syst}	δ_{ES}	C_{had}
0.00,0.10	10.58729	± 1.52755	1.27934 1.99958	1.57683 1.42666	0.81046 ± 0.15027
0.10,0.20	239.10599	± 7.19095	16.38229 11.45011	11.63219 10.85670	1.00562 ± 0.02067
0.20,0.30	77.76797	± 4.37432	5.83722 4.89627	0.56973 1.28189	1.00489 ± 0.02568
0.30,0.40	12.94171	± 1.93481	1.15325 1.23962	0.00000 0.00000	0.96361 ± 0.00864
0.40,0.50	2.18734	± 0.91186	0.89905 0.43436	0.00000 0.00000	1.95955 ± 1.18119
0.50,1.00	0.00000	± 0.00000	0.06358 0.00000	0.00000 0.00000	0.31357 ± 0.31357

Table J.17: Results of the measurement for the differential cross-section with respect to x_p^{obs} ($x_\gamma^{obs} > 0.75$, OptE).

Bin	$\frac{d\sigma}{dx_p^{obs}}(pb)$	δ_{stat}	δ_{syst}	δ_{ES}	C_{had}
0.00,0.10	2.02447	± 0.57716	1.62784 0.27932	0.13275 0.26550	1.20676 ± 0.45752
0.10,0.20	55.70115	± 3.44653	2.73599 2.61313	2.88607 1.73164	1.00145 ± 0.05252
0.20,0.30	18.50376	± 2.38611	1.29086 1.44330	0.00000 0.00000	0.88422 ± 0.00536
0.30,0.40	2.64548	± 0.92723	0.84926 0.73881	0.00000 0.00000	1.35345 ± 0.44204
0.40,0.50	1.01287	± 0.74310	0.45921 0.74062	0.00000 0.00000	1.64693 ± 1.19210
0.50,1.00	0.00000	± 0.00000	0.06343 0.00000	0.00000 0.00000	0.00000 ± 0.00000

Table J.18: Results of the measurement for the differential cross-section with respect to x_p^{obs} ($x_\gamma^{obs} > 0.75$, OptF).

Bin	$\frac{d\sigma}{dx_p^{obs}}(pb)$	δ_{stat}	δ_{syst}	δ_{ES}	C_{had}
0.00,0.10	198.16376	± 8.71663	16.28093 10.66933	20.99289 16.14839	0.83234 ± 0.01707
0.10,0.20	0.00000	± 0.00000	0.00000 0.00000	0.00000 0.00000	1.00000 ± 0.00000
0.20,0.30	0.00000	± 0.00000	0.00000 0.00000	0.00000 0.00000	1.00000 ± 0.00000
0.30,0.40	0.00000	± 0.00000	0.00000 0.00000	0.00000 0.00000	1.00000 ± 0.00000
0.40,0.50	0.00000	± 0.00000	0.00000 0.00000	0.00000 0.00000	1.00000 ± 0.00000
0.50,1.00	0.00000	± 0.00000	0.00000 0.00000	0.00000 0.00000	1.00000 ± 0.00000

Table J.19: Results of the measurement for the differential cross-section with respect to x_p^{obs} ($x_\gamma^{obs} > 0.75$, OptH).

Appendix K

Systematic Uncertainty Tables

For more details the reader is referred to chapter 8.

Systematic	1	2	3	4	5	6	7	8
Nominal	0.0	0.0	0.0	0.0	0.0	0.0	0.0	0.0
ES up	7.5	5.9	5.1	4.7	5.2	4.1	5.1	4.1
ES dn	-7.6	-6.1	-5.8	-4.6	-4.8	-4.2	-4.0	-4.0
Hrw E_T corrs	0.3	0.1	-0.1	-0.5	-0.0	-0.5	-0.3	-0.0
$\eta + \sigma$	-0.5	-0.7	-0.5	-0.3	-0.0	-0.1	0.0	0.1
$\eta - \sigma$	-0.8	0.3	0.6	-0.3	0.7	0.4	-0.1	-0.1
$E_T + \sigma$	0.5	0.0	2.1	3.3	4.8	5.6	2.9	0.6
$E_T - \sigma$	1.3	2.5	1.2	-0.2	1.1	0.9	1.5	1.8
$y_{jb} + \sigma$	-5.6	-3.8	-3.8	-3.7	-3.6	-2.7	-2.8	0.7
$y_{jb} - \sigma$	6.9	2.9	2.6	3.0	1.7	2.3	1.2	-0.1
$x_\gamma^{obs} + \sigma$	0.0	0.0	0.0	0.0	0.0	0.0	0.0	0.0
$x_\gamma^{obs} - \sigma$	0.0	0.0	0.0	0.0	0.0	0.0	0.0	0.0
MC weights	-0.4	-0.6	-1.0	-1.4	-1.4	-2.1	-2.8	0.8
Herwig	11.7	4.6	0.3	2.4	1.1	1.1	1.0	0.2
Vtx up	0.7	-0.2	0.0	-0.1	-0.2	0.1	0.0	-0.1
Vtx dn	0.6	0.0	-0.4	0.3	-0.1	0.0	0.3	0.0
Trks up	-0.1	-0.3	-0.2	-0.2	-0.4	-0.3	-0.3	-0.2
Trks dn	-0.0	-0.0	0.0	0.1	0.0	0.0	0.0	0.0
Miss E_T up	-0.1	0.0	-0.0	0.2	0.1	0.1	-0.1	0.2
Miss E_T dn	-0.4	0.2	-0.2	0.0	-0.3	-0.4	-0.3	-0.5
E_e up	0.0	0.0	-0.0	-0.0	-0.0	-0.0	0.0	0.0
E_e dn	0.0	0.0	0.0	0.0	0.0	0.0	0.0	0.0
y_{el} up	-0.5	0.3	-0.1	-0.2	-0.5	-0.2	-0.2	-0.6
y_{el} dn	0.2	0.3	0.3	0.4	0.4	0.1	0.3	0.6
CTEQ4L	1.0	-0.5	-2.8	0.9	-1.7	2.7	2.5	-0.4
WHIT2	-4.0	-2.2	-0.5	2.2	-1.5	3.1	-4.9	-1.0

Table K.1: Systematic uncertainties for the measurement of the differential cross-section with respect to x_γ^{obs}

Systematic	1	2	3	4	5	6	7	8	9	10	11
Nominal	0.0	0.0	0.0	0.0	0.0	0.0	0.0	0.0	0.0	0.0	0.0
ES up	6.7	3.6	3.0	2.5	1.2	0.0	0.0	0.0	0.0	0.0	0.0
ES dn	-6.3	-3.9	-2.9	-2.9	-1.5	0.0	0.0	0.0	0.0	0.0	0.0
Hrw E_T corrs	-0.2	-0.2	-0.3	0.7	0.1	-0.3	-0.0	0.0	0.0	0.0	0.0
$\eta + \sigma$	0.0	0.0	-0.0	-0.1	0.1	1.1	0.3	1.1	0.7	-7.3	-5.7
$\eta - \sigma$	0.0	-0.0	0.0	-0.5	1.1	-0.3	-4.4	-4.9	4.9	8.6	6.8
$E_T + \sigma$	1.8	0.6	-0.5	-2.0	-1.7	0.6	-1.4	0.0	0.0	0.0	0.0
$E_T - \sigma$	-4.1	-0.8	1.9	-1.1	2.4	0.8	-0.1	0.0	0.0	0.0	0.0
$y_{jb} + \sigma$	1.2	0.8	0.9	-1.4	-5.0	-1.7	-2.6	-7.3	1.0	-14.4	-2.8
$y_{jb} - \sigma$	-0.7	-0.7	-0.5	0.8	2.4	2.7	1.6	-1.5	-7.6	4.4	4.0
$x_\gamma^{obs} + \sigma$	0.8	2.0	2.3	2.9	1.9	0.3	5.0	6.8	5.7	4.3	-31.4
$x_\gamma^{obs} - \sigma$	-1.8	-2.0	-1.8	-1.8	-3.4	0.3	-4.9	-5.5	1.3	31.5	26.3
MC weights	0.8	0.6	1.0	1.4	2.4	2.7	2.5	1.4	1.9	1.3	1.5
Herwig	3.6	-0.1	0.8	-3.4	-3.5	0.7	-0.4	1.1	1.6	-12.4	1.9
Vtx up	-0.1	-0.0	-0.0	-0.1	-0.1	0.5	-0.9	-1.1	2.7	-1.4	-1.3
Vtx dn	0.1	-0.1	0.3	0.2	-0.6	-1.0	-0.6	1.8	1.8	-10.8	2.1
Trks up	-0.1	-0.1	-0.4	-0.4	-0.6	-0.3	-1.0	0.7	-3.0	1.1	1.3
Trks dn	0.0	-0.0	0.0	0.1	0.1	-0.1	-0.1	-0.2	-0.2	-0.3	-0.3
Miss E_T up	0.3	0.3	-0.0	-0.1	-0.1	-0.0	0.4	0.8	-0.7	-0.9	-0.7
Miss E_T dn	-0.5	-0.5	-0.2	-0.6	-0.8	-0.2	-1.2	0.1	-0.5	2.7	2.0
E_e up	0.0	0.0	0.0	0.0	0.0	0.0	0.0	0.0	0.0	0.0	0.0
E_e dn	0.0	0.0	0.0	0.0	0.0	0.0	0.0	0.0	0.0	0.0	0.0
y_{el} up	-0.8	-0.5	-0.5	-0.7	-0.4	-0.2	-0.9	-2.5	-3.4	0.4	0.5
y_{el} dn	0.8	0.5	0.3	0.3	0.7	0.3	1.2	-0.2	3.6	-0.2	-0.3
CTEQ4L	0.4	-1.3	6.0	-2.4	-0.4	4.1	-4.3	-3.9	11.7	-30.7	41.3
WHIT2	-1.6	-2.1	0.2	-2.6	2.0	-2.2	-3.5	-1.0	18.9	77.9	-43.7

Table K.2: Systematic uncertainties for the measurement of the differential cross-section with respect to x_p^{obs} ($x_\gamma^{obs} > 0.75$).

Systematic	1	2	3	4	5	6	7	8	9	10	11
Nominal	0.0	0.0	0.0	0.0	0.0	0.0	0.0	0.0	0.0	0.0	0.0
ES up	10.1	6.0	5.4	5.2	5.3	1.7	0.4	0.4	0.0	0.0	0.0
ES dn	-7.7	-6.0	-5.6	-4.8	-4.1	-2.9	-2.3	0.0	0.0	0.0	0.0
Hrw E_T corrs	-1.0	-0.4	-0.3	0.1	0.5	0.2	-0.9	-0.1	-0.1	-0.0	0.0
$\eta + \sigma$	0.1	0.1	0.0	-0.0	-0.5	-2.5	-4.7	-4.8	-6.9	-2.3	1.6
$\eta - \sigma$	0.2	0.0	-0.0	-0.1	1.5	2.8	4.4	7.1	-13.2	1.3	10.8
$E_T + \sigma$	11.3	5.3	4.1	4.3	0.5	-4.0	-5.4	-0.0	0.1	0.3	0.0
$E_T - \sigma$	-4.8	-6.5	-6.0	-2.8	3.9	4.0	0.8	0.6	-0.0	-0.0	0.0
$y_{jb} + \sigma$	-5.4	-2.1	-3.4	-4.4	-4.2	-3.4	-3.3	-6.2	-6.7	-8.7	-3.9
$y_{jb} - \sigma$	4.1	2.9	2.0	3.6	2.6	1.7	2.4	3.2	2.5	-2.3	7.6
$x_\gamma^{obs} + \sigma$	6.4	2.4	1.7	2.2	1.6	1.1	0.1	-0.7	-1.7	-2.1	3.9
$x_\gamma^{obs} - \sigma$	0.7	-1.5	-1.6	-2.6	-0.7	-1.3	0.5	1.2	0.0	-11.2	-6.4
MC weights	-2.5	-1.9	-1.5	-1.1	-1.0	-0.9	-1.2	-1.2	-1.5	-1.9	-2.4
Herwig	1.3	0.8	2.1	1.7	4.0	10.5	4.4	0.8	10.4	-10.2	7.3
Vtx up	-0.2	0.3	-0.3	-0.2	0.1	0.2	0.6	-0.4	-0.7	-0.9	-0.7
Vtx dn	0.2	-0.1	0.4	-0.1	0.2	0.0	-0.3	-0.3	-0.3	-2.5	1.6
Trks up	0.0	-0.1	-0.3	-0.4	-0.2	-0.4	-0.0	-1.5	0.3	0.4	0.5
Trks dn	-0.0	-0.0	-0.0	0.1	0.1	0.1	-0.0	-0.1	-0.0	-0.1	-0.3
Miss E_T up	-0.0	0.1	0.1	0.1	0.0	-0.1	0.1	-0.4	-0.8	-0.5	-0.7
Miss E_T dn	-0.4	-0.3	-0.0	0.0	-0.2	-0.1	-0.3	-1.4	-0.7	-2.9	-2.1
E_e up	0.0	-0.0	-0.0	-0.0	-0.0	-0.0	0.0	0.0	0.0	0.0	0.0
E_e dn	0.0	0.0	0.0	0.0	0.0	0.0	0.0	0.0	0.0	0.0	0.0
y_{el} up	-0.8	-0.2	0.1	-0.1	-0.3	-0.4	0.4	0.2	0.7	0.5	0.8
y_{el} dn	0.6	0.5	0.1	0.1	0.2	0.2	0.5	-0.1	-0.5	-0.4	3.8
CTEQ4L	6.7	-0.7	1.1	-2.1	-1.9	6.2	5.2	-16.8	1.0	9.1	31.8
WHIT2	-5.6	0.1	2.0	-1.0	-1.5	3.9	2.0	-11.7	7.8	1.4	24.2

Table K.3: Systematic uncertainties for the measurement of the differential cross-section with respect to x_p^{obs} ($x_\gamma^{obs} \leq 0.75$).

Systematic	1	2	3	4	5	6	7
Nominal	0.0	0.0	0.0	0.0	0.0	0.0	0.0
ES up	3.7	5.2	2.7	5.6	7.9	12.0	10.0
ES dn	-4.0	-4.0	-2.9	-7.3	-6.7	-4.0	-10.0
Hrw E_T corrs	-0.3	0.6	-0.6	0.1	-1.5	4.5	5.5
$\eta + \sigma$	0.1	0.1	0.0	0.1	-0.0	-0.0	0.0
$\eta - \sigma$	-0.1	-0.1	-0.2	0.4	0.1	-0.0	0.0
$E_T + \sigma$	-0.2	-0.7	-0.4	-0.0	0.0	0.0	0.0
$E_T - \sigma$	2.5	1.2	0.2	-0.1	-0.0	-0.0	0.0
$y_{jb} + \sigma$	0.1	0.2	-0.7	1.2	1.9	6.7	-1.1
$y_{jb} - \sigma$	0.4	-0.4	-2.3	-0.5	-4.8	-11.7	2.7
$x_\gamma^{obs} + \sigma$	2.3	1.2	-0.7	-1.6	-2.0	4.7	5.8
$x_\gamma^{obs} - \sigma$	-2.1	-1.1	-1.9	1.2	0.0	-0.4	6.2
MC weights	0.9	0.7	0.8	0.6	0.4	0.4	0.2
Herwig	0.4	1.7	-1.5	2.5	1.2	13.8	40.1
Vtx up	0.0	-0.2	-0.1	0.1	-0.9	0.9	-1.0
Vtx dn	0.1	0.0	-0.0	-0.7	-1.6	-2.3	2.1
Trks up	-0.2	-0.1	-0.4	-1.2	-0.8	0.6	0.9
Trks dn	0.0	-0.0	0.1	0.1	-0.1	-0.2	-0.4
Miss E_T up	0.1	0.2	0.7	0.5	0.4	-0.8	-1.0
Miss E_T dn	-0.3	-0.5	-0.5	-1.3	-2.2	-2.5	-8.0
E_e up	0.0	0.0	0.0	0.0	0.0	0.0	0.0
E_e dn	0.0	0.0	0.0	0.0	0.0	0.0	0.0
y_{el} up	-0.5	-0.7	-0.5	-0.7	-2.4	-2.9	-8.4
y_{el} dn	0.5	0.6	0.2	0.6	1.8	-0.7	-1.2
CTEQ4L	0.5	-0.9	3.9	4.9	-0.6	-2.6	20.8
WHIT2	-1.9	-0.4	-3.4	10.0	-5.9	5.8	36.1

Table K.4: Systematic uncertainties for the measurement of the differential cross-section with respect to $E_{T,1}$ ($x_\gamma^{obs} > 0.75$).

Systematic	1	2	3	4	5	6	7
Nominal	0.0	0.0	0.0	0.0	0.0	0.0	0.0
ES up	5.2	5.1	3.7	8.0	9.4	11.8	0.0
ES dn	-4.8	-5.8	-4.0	-7.3	-7.8	-11.8	-50.0
Hrw E_T corrs	-0.1	-0.2	-0.6	-1.2	3.6	-3.8	-46.8
$\eta + \sigma$	-0.4	-0.3	0.2	-0.1	-0.4	-0.1	0.0
$\eta - \sigma$	0.2	0.5	0.3	-0.7	0.7	0.2	0.0
$E_T + \sigma$	1.7	-1.6	-1.5	0.3	0.1	0.0	0.0
$E_T - \sigma$	1.9	0.8	0.3	-0.5	-0.2	-0.0	0.0
$y_{jb} + \sigma$	-3.8	-5.0	-4.0	-0.0	-3.3	-3.5	-36.6
$y_{jb} - \sigma$	3.4	2.2	1.8	1.6	10.3	1.6	88.6
$x_\gamma^{obs} + \sigma$	1.9	1.5	2.8	3.6	1.3	-16.7	-35.0
$x_\gamma^{obs} - \sigma$	-1.1	-1.3	0.8	-4.6	1.9	11.8	-22.9
MC weights	-1.2	-1.3	-1.8	-2.3	-2.7	-3.4	-3.5
Herwig	2.4	3.0	3.0	-1.2	9.1	7.2	-27.3
Vtx up	0.0	-0.1	0.2	-0.5	-0.8	-1.2	-0.8
Vtx dn	0.0	0.1	0.3	-0.8	0.1	1.8	2.0
Trks up	-0.2	-0.2	-0.5	-0.1	-1.3	0.4	0.7
Trks dn	-0.0	0.1	0.1	0.3	-0.0	-0.1	-0.2
Miss E_T up	0.1	-0.2	-0.2	0.7	0.0	-1.2	-2.1
Miss E_T dn	-0.1	-0.1	-0.0	-1.6	-3.3	1.6	2.5
E_e up	-0.0	-0.0	0.0	-0.0	-0.0	0.0	0.0
E_e dn	0.0	0.0	0.0	0.0	0.0	0.0	0.0
y_{el} up	-0.1	-0.0	-0.7	-0.3	0.0	1.0	1.0
y_{el} dn	0.3	0.2	0.1	-0.1	1.1	-0.6	-0.5
CTEQ4L	1.0	-1.8	-3.3	2.4	-3.9	24.4	-67.7
WHIT2	-0.6	1.1	4.6	0.0	6.9	-14.7	88.2

Table K.5: Systematic uncertainties for the measurement of the differential cross-section with respect to $E_{T,1}$ ($x_\gamma^{obs} \leq 0.75$).

Systematic	1	2	3	4	5	6	7	8
Nominal	0.0	0.0	0.0	0.0	0.0	0.0	0.0	0.0
ES up	4.0	3.4	6.1	3.2	7.6	5.5	2.8	12.5
ES dn	-4.0	-4.3	-3.8	-2.9	-4.7	-6.8	-2.8	-25.0
Hrw E_T corrs	-0.2	-0.4	0.9	-0.2	2.0	-0.9	-0.4	-7.8
$\eta + \sigma$	0.1	0.1	0.1	0.1	-0.1	-0.1	-0.0	0.0
$\eta - \sigma$	-0.1	-0.1	-0.2	0.1	0.3	0.1	0.0	0.0
$E_T + \sigma$	3.1	-0.2	-0.0	0.0	0.0	0.0	0.0	0.0
$E_T - \sigma$	-3.0	0.2	-0.0	-0.0	0.0	0.0	0.0	0.0
$y_{jb} + \sigma$	0.1	0.3	0.1	-0.3	2.9	2.8	5.1	-16.5
$y_{jb} - \sigma$	0.6	-1.1	-0.2	-2.9	1.6	-6.6	-14.1	-5.2
$x_\gamma^{obs} + \sigma$	2.1	1.6	1.2	-2.7	0.0	0.2	3.8	3.4
$x_\gamma^{obs} - \sigma$	-2.3	-1.4	-1.1	-1.2	2.4	-1.4	3.9	9.9
MC weights	0.5	1.0	0.8	1.0	0.5	0.2	0.4	0.1
Herwig	2.4	-2.0	1.5	-1.4	2.4	-1.3	12.6	15.4
Vtx up	-0.0	-0.0	-0.4	0.6	-0.6	-0.9	1.6	-1.0
Vtx dn	0.2	-0.1	-0.2	-0.2	-0.7	-1.6	-1.0	2.3
Trks up	-0.2	-0.3	-0.3	-0.5	-0.8	-0.9	0.8	1.1
Trks dn	0.0	-0.0	0.0	0.2	-0.1	-0.1	-0.2	-0.4
Miss E_T up	0.1	0.2	0.5	0.1	0.4	-0.4	-0.4	-0.6
Miss E_T dn	-0.4	-0.6	-0.4	-0.9	-1.4	-0.1	-4.6	-11.6
E_e up	0.0	0.0	0.0	0.0	0.0	0.0	0.0	0.0
E_e dn	0.0	0.0	0.0	0.0	0.0	0.0	0.0	0.0
y_{el} up	-0.6	-0.6	-0.3	-0.8	-1.0	-2.0	-4.2	-11.0
y_{el} dn	0.6	0.4	0.9	0.1	1.0	1.3	-0.8	-1.3
CTEQ4L	0.3	0.8	0.7	3.7	-1.9	-1.1	-4.1	-2.3
WHIT2	-1.6	-1.0	-4.5	4.0	5.1	-5.1	2.4	12.5

Table K.6: Systematic uncertainties for the measurement of the differential cross-section with respect to \bar{E}_T ($x_\gamma^{obs} > 0.75$).

Systematic	1	2	3	4	5	6	7	8
Nominal	0.0	0.0	0.0	0.0	0.0	0.0	0.0	0.0
ES up	5.3	3.8	8.6	4.7	12.1	7.4	0.0	0.0
ES dn	-5.2	-4.7	-4.7	-4.4	-7.9	-8.8	-11.1	0.0
Hrw E_T corrs	-0.1	-0.9	1.4	-0.8	1.0	-0.3	2.1	6.3
$\eta + \sigma$	-0.3	-0.4	-0.0	-0.2	0.1	-0.3	-0.0	0.0
$\eta - \sigma$	0.1	0.6	0.3	-0.2	0.3	0.5	0.1	0.0
$E_T + \sigma$	3.6	-0.9	-0.0	0.0	0.0	0.0	0.0	0.0
$E_T - \sigma$	-2.5	0.1	-0.0	-0.0	0.0	0.0	0.0	0.0
$y_{jb} + \sigma$	-3.8	-4.8	-3.9	-0.6	-0.7	4.8	-19.8	-43.4
$y_{jb} - \sigma$	3.2	2.7	1.0	5.5	-1.4	10.4	17.7	117.6
$x_\gamma^{obs} + \sigma$	2.1	1.3	1.0	5.7	-0.4	1.1	-23.7	-38.8
$x_\gamma^{obs} - \sigma$	-1.1	-1.0	-0.7	0.3	-5.9	3.8	-3.5	-100.0
MC weights	-1.3	-1.6	-2.2	-2.7	-3.0	-3.7	-5.2	-7.2
Herwig	2.4	1.0	5.0	3.1	7.4	6.6	36.0	56.1
Vtx up	0.1	-0.2	0.1	-0.0	-0.2	-0.9	-1.0	-0.5
Vtx dn	0.0	0.1	0.7	-1.4	-2.1	1.7	1.6	2.7
Trks up	-0.2	-0.3	-0.2	-0.3	-0.4	-1.2	0.6	0.5
Trks dn	-0.0	0.0	0.2	-0.0	-0.0	-0.1	-0.2	0.0
Miss E_T up	0.1	-0.1	0.0	0.9	-0.3	-0.4	-0.4	-0.5
Miss E_T dn	-0.1	-0.4	0.1	-1.1	-1.3	0.7	1.3	0.5
E_e up	-0.0	-0.0	-0.0	0.0	-0.0	-0.0	0.0	0.0
E_e dn	0.0	0.0	0.0	0.0	0.0	0.0	0.0	0.0
y_{el} up	-0.2	0.1	-0.5	-0.3	-0.7	-0.5	1.5	0.5
y_{el} dn	0.2	0.3	0.2	0.5	-0.4	2.3	-0.7	-1.0
CTEQ4L	0.2	0.2	2.0	-3.9	-5.1	-1.9	53.9	-100.0
WHIT2	-0.9	1.6	0.5	4.7	-2.4	10.3	-13.3	4.0

Table K.7: Systematic uncertainties for the measurement of the differential cross-section with respect to \bar{E}_T ($x_\gamma^{obs} \leq 0.75$).

Systematic	1	2	3	4	5	6	7	8
Nominal	0.0	0.0	0.0	0.0	0.0	0.0	0.0	0.0
ES up	0.0	18.9	7.4	3.8	3.9	2.2	0.0	0.0
ES dn	0.0	-24.3	-5.8	-4.1	-4.0	-2.4	0.0	0.0
Hrw E_T corrs	0.0	-11.8	0.5	-0.5	0.1	-0.1	0.0	0.0
$\eta + \sigma$	0.0	0.0	-0.0	0.0	0.1	-0.0	1.4	0.0
$\eta - \sigma$	0.0	0.0	0.1	0.0	-0.1	-0.1	-1.8	0.0
$E_T + \sigma$	0.0	-100.0	2.5	1.2	0.1	-1.6	-4.0	0.0
$E_T - \sigma$	0.0	-40.4	-1.1	-3.8	0.6	-0.4	-0.2	0.0
$y_{jb} + \sigma$	0.0	-16.4	2.2	0.5	0.5	0.1	-27.0	0.0
$y_{jb} - \sigma$	0.0	-100.0	-2.3	-1.7	-0.4	1.1	37.1	0.0
$x_\gamma^{obs} + \sigma$	0.0	0.0	0.2	1.6	3.0	1.4	-10.6	0.0
$x_\gamma^{obs} - \sigma$	0.0	0.0	-1.4	-2.1	-2.3	-1.1	-0.9	0.0
MC weights	0.0	-0.9	0.3	0.2	1.0	0.1	-1.5	0.0
Herwig	0.0	3.8	5.6	1.4	-1.0	1.1	-5.4	0.0
Vtx up	0.0	-1.4	-0.0	-0.1	-0.1	0.1	-2.1	0.0
Vtx dn	0.0	3.1	0.3	-0.1	0.0	-0.0	3.1	0.0
Trks up	0.0	0.0	-0.1	-0.2	-0.2	-0.5	-1.8	0.0
Trks dn	0.0	0.0	0.0	-0.0	0.0	-0.0	-0.3	0.0
Miss E_T up	0.0	0.0	0.3	0.3	0.1	0.0	-0.2	0.0
Miss E_T dn	0.0	-2.4	-0.4	-0.8	-0.3	-0.4	0.7	0.0
E_e up	0.0	0.0	0.0	0.0	0.0	0.0	0.0	0.0
E_e dn	0.0	0.0	0.0	0.0	0.0	0.0	0.0	0.0
y_{el} up	0.0	-2.3	-1.2	-0.6	-0.5	-0.3	0.0	0.0
y_{el} dn	0.0	2.6	1.0	0.7	0.4	0.3	-0.0	0.0
CTEQ4L	0.0	-24.6	4.1	-0.5	1.1	1.0	0.6	0.0
WHIT2	0.0	15.3	0.2	-1.7	-1.5	-0.7	-8.5	0.0

Table K.8: Systematic uncertainties for the measurement of the differential cross-section with respect to $\bar{\eta}$ ($x_\gamma^{obs} > 0.75$).

Systematic	1	2	3	4	5	6	7	8
Nominal	0.0	0.0	0.0	0.0	0.0	0.0	0.0	0.0
ES up	0.0	0.0	10.5	6.5	5.2	4.7	5.3	2.5
ES dn	0.0	0.0	-6.0	-5.8	-5.5	-4.4	-4.9	-7.1
Hrw E_T corrs	0.0	0.0	-1.1	-0.7	-0.1	-0.4	0.6	-4.3
$\eta + \sigma$	0.0	0.0	0.2	0.1	0.0	-0.5	-1.2	-5.4
$\eta - \sigma$	0.0	0.0	0.7	0.1	-0.0	0.5	1.6	0.8
$E_T + \sigma$	0.0	0.0	7.3	6.6	4.7	3.8	0.5	-0.4
$E_T - \sigma$	0.0	0.0	4.4	-6.6	-7.2	-3.8	0.2	-6.1
$y_{jb} + \sigma$	0.0	0.0	-5.7	-3.5	-2.9	-3.4	-4.1	-6.1
$y_{jb} - \sigma$	0.0	0.0	11.0	4.0	2.8	2.0	2.8	1.0
$x_\gamma^{obs} + \sigma$	0.0	0.0	19.1	4.3	1.8	2.2	0.5	-0.0
$x_\gamma^{obs} - \sigma$	0.0	0.0	5.7	-1.3	-1.5	-2.4	-0.4	0.0
MC weights	0.0	0.0	-3.2	-2.5	-1.7	-1.6	-1.0	-0.5
Herwig	0.0	0.0	-0.9	0.7	2.5	1.3	7.4	4.0
Vtx up	0.0	0.0	0.9	0.0	-0.0	-0.0	-0.1	0.8
Vtx dn	0.0	0.0	1.1	0.2	0.1	-0.0	0.1	0.8
Trks up	0.0	0.0	0.0	0.0	-0.2	-0.3	-0.5	0.1
Trks dn	0.0	0.0	0.0	-0.0	0.0	0.0	0.1	-0.0
Miss E_T up	0.0	0.0	-0.2	0.1	0.1	0.1	-0.0	0.3
Miss E_T dn	0.0	0.0	-1.2	-0.3	-0.2	-0.1	-0.2	-0.6
E_e up	0.0	0.0	0.0	0.0	-0.0	-0.0	0.0	0.0
E_e dn	0.0	0.0	0.0	0.0	0.0	0.0	0.0	0.0
y_{el} up	0.0	0.0	-0.7	-0.4	-0.4	0.1	-0.2	0.8
y_{el} dn	0.0	0.0	-0.1	0.8	0.4	-0.0	0.3	0.3
CTEQ4L	0.0	0.0	10.7	1.8	0.4	-0.8	3.2	-12.5
WHIT2	0.0	0.0	-8.1	0.2	-0.4	1.2	-0.7	-3.9

Table K.9: Systematic uncertainties for the measurement of the differential cross-section with respect to $\bar{\eta}$ ($x_\gamma^{obs} \leq 0.75$).

Systematic	1	2	3	4	5	6	7
Nominal	0.0	0.0	0.0	0.0	0.0	0.0	0.0
ES up	66.7	0.0	11.1	4.7	5.5	4.8	3.9
ES dn	0.0	0.0	-7.4	-5.5	-6.5	-5.1	-3.8
Hrw E_T corrs	44.5	0.0	2.5	-0.4	1.1	-0.5	-0.2
$\eta + \sigma$	6.4	0.0	4.5	2.3	0.5	-0.1	0.0
$\eta - \sigma$	0.4	0.0	3.9	-0.7	-0.3	0.0	-0.1
$E_T + \sigma$	258.4	0.0	-0.2	20.2	-7.4	3.4	1.3
$E_T - \sigma$	-47.5	0.0	-23.8	-2.9	-7.8	-3.7	-3.0
$y_{jb} + \sigma$	-15.1	0.0	-6.3	0.3	-2.1	-1.0	0.2
$y_{jb} - \sigma$	-60.1	0.0	-23.1	-3.6	1.2	0.4	0.1
$x_\gamma^{obs} + \sigma$	3.8	0.0	4.1	8.8	5.2	2.8	2.5
$x_\gamma^{obs} - \sigma$	-49.4	0.0	-17.2	2.3	-6.5	-4.9	-1.9
MC weights	-0.4	0.0	-3.7	0.8	1.1	1.7	1.2
Herwig	48.1	0.0	6.4	0.1	0.4	3.9	0.3
Vtx up	0.0	0.0	-0.4	1.6	-0.4	-0.1	-0.0
Vtx dn	3.8	0.0	-2.8	0.1	-0.0	0.5	-0.0
Trks up	0.0	0.0	0.2	-0.8	-0.6	0.0	-0.3
Trks dn	0.0	0.0	0.0	-0.0	-0.0	-0.0	0.0
Miss E_T up	-11.1	0.0	-0.9	-0.8	0.9	0.2	0.2
Miss E_T dn	2.3	0.0	-2.4	1.6	0.1	-0.4	-0.5
E_e up	0.0	0.0	0.0	0.0	0.0	0.0	0.0
E_e dn	0.0	0.0	0.0	0.0	0.0	0.0	0.0
y_{el} up	0.8	0.0	-2.9	-0.4	-1.0	-0.2	-0.7
y_{el} dn	0.0	0.0	-0.2	0.5	0.2	0.5	0.6
CTEQ4L	-31.4	0.0	8.9	-7.8	2.7	1.1	0.5
WHIT2	-100.0	0.0	-28.8	15.1	-4.6	-0.2	-1.5

Table K.10: Systematic uncertainties for the measurement of the differential cross-section with respect to $|\Delta\phi|$ ($x_\gamma^{obs} > 0.75$).

Systematic	1	2	3	4	5	6	7
Nominal	0.0	0.0	0.0	0.0	0.0	0.0	0.0
ES up	20.7	5.5	7.2	6.7	5.1	5.9	4.7
ES dn	-3.4	-5.5	-10.1	-7.1	-5.6	-5.6	-4.5
Hrw E_T corrs	0.3	-1.9	-2.0	2.2	-1.2	-0.6	-0.1
$\eta + \sigma$	2.0	-0.9	-0.5	-0.2	-0.0	-0.2	-0.5
$\eta - \sigma$	4.8	-0.6	-1.8	-1.6	-0.4	0.5	0.4
$E_T + \sigma$	40.6	6.6	1.6	-1.1	4.2	4.8	5.4
$E_T - \sigma$	-0.7	-14.1	4.1	-6.4	-2.1	-7.2	-5.3
$y_{jb} + \sigma$	-2.3	-7.4	-1.0	-6.1	-4.7	-4.8	-3.4
$y_{jb} - \sigma$	7.5	3.9	3.8	5.8	3.8	2.8	3.1
$x_\gamma^{obs} + \sigma$	2.1	-3.9	2.8	1.0	3.1	3.7	1.5
$x_\gamma^{obs} - \sigma$	3.0	-5.9	-0.1	-3.6	-1.6	-1.0	-1.0
MC weights	-2.3	-0.9	-0.3	-0.5	0.1	-0.2	-2.4
Herwig	19.6	9.5	2.4	-1.8	1.5	-0.5	4.0
Vtx up	-0.8	-0.5	-0.2	0.1	-0.1	-0.1	0.0
Vtx dn	-2.0	2.3	-0.7	0.3	0.2	-0.0	0.1
Trks up	-3.4	-1.8	0.0	-0.5	-0.4	-0.1	-0.3
Trks dn	0.0	0.0	0.7	-0.1	0.1	-0.0	0.0
Miss E_T up	5.0	0.8	-0.7	-0.3	0.2	0.0	0.0
Miss E_T dn	-0.8	2.0	-2.2	-0.0	-0.0	-0.2	-0.2
E_e up	0.0	0.0	0.0	0.0	-0.0	-0.0	-0.0
E_e dn	0.0	0.0	0.0	0.0	0.0	0.0	0.0
y_{el} up	1.8	1.5	-0.1	-0.1	0.0	0.2	-0.3
y_{el} dn	-0.2	-0.1	0.3	-0.2	0.2	0.1	0.3
CTEQ4L	7.0	21.4	5.1	-1.9	1.1	-2.8	1.1
WHIT2	3.7	-0.4	1.7	-7.5	4.3	-2.8	0.6

Table K.11: Systematic uncertainties for the measurement of the differential cross-section with respect to $|\Delta\phi|$ ($x_\gamma^{obs} \leq 0.75$).

Systematic	1	2	3	4	5	6
Nominal	0.0	0.0	0.0	0.0	0.0	0.0
ES up	0.0	12.9	5.0	0.6	0.0	0.0
ES dn	0.0	-12.1	-7.2	-3.0	0.0	0.0
Hrw E_T corrs	0.0	1.7	-0.6	-1.3	-0.1	0.0
$\eta + \sigma$	0.0	8.3	0.9	-0.7	-4.5	-0.6
$\eta - \sigma$	0.0	-9.0	-1.8	3.2	-17.3	14.1
$E_T + \sigma$	0.0	4.2	-3.2	-5.2	0.2	0.1
$E_T - \sigma$	0.0	4.0	4.8	-0.9	0.0	0.0
$y_{jb} + \sigma$	0.0	-0.7	-6.3	-5.4	-7.1	-5.6
$y_{jb} - \sigma$	0.0	5.6	3.3	0.6	-1.3	10.7
$x_\gamma^{obs} + \sigma$	0.0	0.0	-0.0	-0.2	-1.2	11.1
$x_\gamma^{obs} - \sigma$	0.0	0.0	0.1	-0.0	-1.0	-4.8
MC weights	0.0	-0.9	-0.7	-0.8	-1.2	-2.4
Herwig	0.0	4.7	16.2	5.7	12.1	-6.7
Vtx up	0.0	-0.3	0.3	0.2	-0.8	-0.9
Vtx dn	0.0	2.1	0.5	0.6	-2.0	1.7
Trks up	0.0	0.1	-0.2	-0.4	0.3	0.5
Trks dn	0.0	0.0	0.2	-0.0	-0.0	-0.4
Miss E_T up	0.0	0.0	-0.0	0.2	-0.2	-0.2
Miss E_T dn	0.0	0.1	-0.1	-0.1	-1.7	0.6
E_e up	0.0	0.0	0.0	0.0	0.0	0.0
E_e dn	0.0	0.0	0.0	0.0	0.0	0.0
y_{el} up	0.0	-0.2	0.3	0.6	0.6	0.6
y_{el} dn	0.0	1.6	0.7	0.1	-0.4	7.2
CTEQ4L	0.0	0.8	1.3	-5.7	1.8	5.7
WHIT2	0.0	17.4	-3.9	-3.6	1.8	-11.7

Table K.12: Systematic uncertainties for the measurement of the differential cross-section with respect to x_p^{obs} ($x_\gamma^{obs} \leq 0.75$, OptA).

Systematic	1	2	3	4	5	6
Nominal	0.0	0.0	0.0	0.0	0.0	0.0
ES up	7.5	4.2	0.0	0.0	0.0	0.0
ES dn	-11.3	-3.9	0.0	0.0	0.0	0.0
Hrw E_T corrs	-1.3	-0.4	-0.1	0.0	0.0	0.0
$\eta + \sigma$	1.0	-1.0	14.7	219.8	0.0	-41.9
$\eta - \sigma$	-0.3	1.5	-5.8	63.8	0.0	76.5
$E_T + \sigma$	6.3	-1.5	0.0	0.0	0.0	0.0
$E_T - \sigma$	-11.1	-0.6	-0.0	0.0	0.0	0.0
$y_{jb} + \sigma$	-2.0	-3.6	-7.8	69.4	0.0	-35.9
$y_{jb} - \sigma$	5.4	2.0	1.0	-100.0	0.0	167.6
$x_\gamma^{obs} + \sigma$	0.3	0.1	6.8	53.3	0.0	-29.0
$x_\gamma^{obs} - \sigma$	-1.0	-0.1	-1.0	29.1	0.0	-100.0
MC weights	-2.5	-2.8	-4.0	-5.3	0.0	-7.9
Herwig	16.2	2.1	5.2	13.6	0.0	-100.0
Vtx up	-0.0	-0.4	0.6	-0.9	0.0	0.0
Vtx dn	-0.4	0.6	-2.1	2.2	0.0	0.0
Trks up	-0.4	-0.2	0.3	0.5	0.0	0.0
Trks dn	0.0	0.1	1.7	-0.1	0.0	0.0
Miss E_T up	0.1	0.3	-0.2	-0.2	0.0	0.0
Miss E_T dn	-1.0	-0.2	0.5	0.5	0.0	0.0
E_e up	-0.0	-0.0	-0.0	0.0	0.0	0.0
E_e dn	0.0	0.0	0.0	0.0	0.0	0.0
y_{el} up	0.0	-0.5	-1.1	0.8	0.0	0.0
y_{el} dn	-0.4	0.3	-0.4	-0.3	0.0	0.0
CTEQ4L	8.8	2.6	7.2	-11.7	0.0	-100.0
WHIT2	-7.8	0.3	-6.8	-5.3	0.0	-100.0

Table K.13: Systematic uncertainties for the measurement of the differential cross-section with respect to x_p^{obs} ($x_\gamma^{obs} \leq 0.75$, OptB).

Systematic	1	2	3	4	5	6
Nominal	0.0	0.0	0.0	0.0	0.0	0.0
ES up	20.0	6.9	3.5	0.3	0.0	0.0
ES dn	-20.0	-6.2	-2.9	-0.3	0.0	0.0
Hrw E_T corrs	-6.2	0.0	0.6	-0.3	-0.0	0.0
$\eta + \sigma$	28.7	-0.2	-1.1	-4.9	-7.2	20.8
$\eta - \sigma$	27.9	2.0	1.4	4.0	0.8	3.3
$E_T + \sigma$	-100.0	7.9	-0.8	-0.1	0.0	0.0
$E_T - \sigma$	19.8	-2.0	2.3	0.8	-0.1	0.0
$y_{jb} + \sigma$	-7.3	-4.5	-3.2	-3.7	-4.7	4.5
$y_{jb} - \sigma$	-0.8	3.1	2.0	4.2	-0.2	-3.7
$x_\gamma^{obs} + \sigma$	-8.3	1.3	1.1	0.2	-4.1	2.1
$x_\gamma^{obs} - \sigma$	7.3	-1.7	-1.0	0.6	-1.0	10.7
MC weights	-3.5	-1.5	-1.1	-1.5	-2.1	-2.7
Herwig	-54.9	1.9	5.5	0.0	-1.2	26.7
Vtx up	0.0	-0.2	-0.1	0.2	-0.8	-0.4
Vtx dn	-19.7	-0.0	0.2	-1.2	-0.3	1.5
Trks up	0.0	-0.4	-0.5	-0.7	0.4	0.5
Trks dn	0.0	0.0	0.0	-0.0	-0.0	-0.1
Miss E_T up	0.0	0.2	0.1	-0.1	-0.9	-1.0
Miss E_T dn	0.2	0.0	-0.3	-0.6	1.8	-10.9
E_e up	0.0	-0.0	-0.0	0.0	0.0	0.0
E_e dn	0.0	0.0	0.0	0.0	0.0	0.0
y_{el} up	0.2	0.4	-0.5	0.1	0.6	0.8
y_{el} dn	-0.2	-0.1	0.2	0.1	-0.5	-0.3
CTEQ4L	47.6	0.2	1.1	2.7	9.2	83.9
WHIT2	62.5	-0.8	2.2	-3.4	9.7	56.9

Table K.14: Systematic uncertainties for the measurement of the differential cross-section with respect to x_p^{obs} ($x_\gamma^{obs} \leq 0.75$, OptC).

Systematic	1	2	3	4	5	6
Nominal	0.0	0.0	0.0	0.0	0.0	0.0
ES up	0.0	8.1	5.0	2.0	0.0	0.0
ES dn	0.0	-7.4	-4.5	-0.7	0.0	0.0
Hrw E_T corrs	0.0	0.5	0.4	-0.3	-0.0	0.0
$\eta + \sigma$	0.0	1.3	-0.7	-1.1	-7.2	20.8
$\eta - \sigma$	0.0	-0.4	1.5	3.5	0.8	3.3
$E_T + \sigma$	0.0	2.2	-1.4	4.8	0.1	0.0
$E_T - \sigma$	0.0	-7.6	-2.0	1.0	-0.1	0.0
$y_{jb} + \sigma$	0.0	-4.3	-3.6	-3.2	-4.7	4.5
$y_{jb} - \sigma$	0.0	2.5	1.2	2.9	-0.2	-3.7
$x_\gamma^{obs} + \sigma$	0.0	0.9	1.1	0.3	-4.1	2.1
$x_\gamma^{obs} - \sigma$	0.0	-2.6	-1.5	0.7	-1.0	10.7
MC weights	0.0	-1.3	-1.5	-1.6	-2.1	-2.7
Herwig	0.0	2.9	5.2	2.0	-1.2	26.7
Vtx up	0.0	-0.3	-0.4	0.4	-0.8	-0.4
Vtx dn	0.0	0.3	0.3	-0.2	-0.3	1.5
Trks up	0.0	-0.6	-0.5	-0.8	0.4	0.5
Trks dn	0.0	0.2	0.1	-0.1	-0.0	-0.1
Miss E_T up	0.0	0.1	0.1	-0.1	-0.9	-1.0
Miss E_T dn	0.0	0.3	-0.4	-0.2	1.8	-10.9
E_e up	0.0	-0.0	-0.0	0.0	0.0	0.0
E_e dn	0.0	0.0	0.0	0.0	0.0	0.0
y_{el} up	0.0	0.5	-0.5	-0.1	0.6	0.8
y_{el} dn	0.0	-0.0	0.2	0.2	-0.5	-0.3
CTEQ4L	0.0	-7.2	-0.3	8.3	9.2	83.9
WHIT2	0.0	0.9	3.7	-0.9	9.7	56.9

Table K.15: Systematic uncertainties for the measurement of the differential cross-section with respect to x_p^{obs} ($x_\gamma^{obs} \leq 0.75$, OptG).

Systematic	1	2	3	4	5	6
Nominal	0.0	0.0	0.0	0.0	0.0	0.0
ES up	7.1	5.1	4.0	0.0	0.0	0.0
ES dn	-7.1	-5.4	-1.4	0.0	0.0	0.0
Hrw E_T corrs	-5.4	0.2	0.4	-0.4	0.0	0.0
$\eta + \sigma$	78.1	1.1	4.3	3.1	-9.7	0.0
$\eta - \sigma$	-18.5	-1.9	2.0	2.7	11.1	0.0
$E_T + \sigma$	257.5	-8.0	8.1	1.9	0.1	0.0
$E_T - \sigma$	-33.0	1.8	1.7	-0.9	0.0	0.0
$y_{jb} + \sigma$	-1.1	0.8	-0.6	-1.9	-8.6	0.0
$y_{jb} - \sigma$	6.4	-1.2	-1.2	-1.3	-5.1	0.0
$x_\gamma^{obs} + \sigma$	2.4	1.7	0.1	5.9	-8.0	0.0
$x_\gamma^{obs} - \sigma$	-16.2	-2.5	-3.9	-3.2	7.3	0.0
MC weights	4.4	1.7	2.2	3.3	3.4	0.0
Herwig	-15.9	-3.6	-3.4	2.3	13.3	0.0
Vtx up	7.1	-0.4	-0.3	-0.8	-0.8	0.0
Vtx dn	1.6	-0.6	-0.2	0.3	-7.1	0.0
Trks up	0.6	-0.3	-0.9	0.3	0.6	0.0
Trks dn	0.0	0.1	0.2	-0.0	-0.1	0.0
Miss E_T up	-1.7	-0.2	-0.1	1.7	-1.6	0.0
Miss E_T dn	1.8	-0.5	-0.5	0.3	-5.0	0.0
E_e up	0.0	0.0	0.0	0.0	0.0	0.0
E_e dn	0.0	0.0	0.0	0.0	0.0	0.0
y_{el} up	1.0	-0.4	-1.0	-1.4	-7.6	0.0
y_{el} dn	0.0	0.3	1.4	1.8	7.6	0.0
CTEQ4L	-51.7	0.3	-1.8	0.2	3.9	0.0
WHIT2	0.3	-7.6	2.0	-9.3	35.4	0.0

Table K.16: Systematic uncertainties for the measurement of the differential cross-section with respect to x_p^{obs} ($x_\gamma^{obs} > 0.75$, OptD).

Systematic	1	2	3	4	5	6
Nominal	0.0	0.0	0.0	0.0	0.0	0.0
ES up	14.9	4.9	0.7	0.0	0.0	0.0
ES dn	-13.5	-4.5	-1.6	0.0	0.0	0.0
Hrw E_T corrs	0.5	0.1	-0.1	0.0	0.0	0.0
$\eta + \sigma$	1.3	1.3	2.3	2.5	-9.7	0.0
$\eta - \sigma$	-10.5	-1.2	0.2	3.6	11.1	0.0
$E_T + \sigma$	8.9	-0.7	-1.4	-0.5	0.1	0.0
$E_T - \sigma$	-10.6	-0.3	3.4	0.0	0.0	0.0
$y_{jb} + \sigma$	-1.0	-1.1	-1.8	-1.9	-8.6	0.0
$y_{jb} - \sigma$	-0.0	-0.5	-0.6	-1.4	-5.1	0.0
$x_\gamma^{obs} + \sigma$	6.0	4.6	2.9	6.0	-8.0	0.0
$x_\gamma^{obs} - \sigma$	-7.0	-3.3	-3.2	-3.3	7.3	0.0
MC weights	0.6	1.5	2.6	3.4	3.4	0.0
Herwig	4.9	-1.9	-4.7	2.5	13.3	0.0
Vtx up	0.1	0.3	0.4	-0.8	-0.8	0.0
Vtx dn	0.2	0.2	-0.5	0.3	-7.1	0.0
Trks up	-0.6	-0.3	-0.7	0.3	0.6	0.0
Trks dn	-0.0	0.1	0.1	-0.0	-0.1	0.0
Miss E_T up	-0.1	-0.1	-0.0	1.7	-1.6	0.0
Miss E_T dn	-0.3	-0.2	-0.6	0.3	-5.0	0.0
E_e up	0.0	0.0	0.0	0.0	0.0	0.0
E_e dn	0.0	0.0	0.0	0.0	0.0	0.0
y_{el} up	-2.6	-0.9	-0.4	-1.4	-7.6	0.0
y_{el} dn	2.0	0.5	1.0	1.8	7.6	0.0
CTEQ4L	-6.8	4.6	-0.9	0.0	3.9	0.0
WHIT2	-5.6	-2.1	4.9	-8.5	35.4	0.0

Table K.17: Systematic uncertainties for the measurement of the differential cross-section with respect to x_p^{obs} ($x_\gamma^{obs} > 0.75$, OptE).

Systematic	1	2	3	4	5	6
Nominal	0.0	0.0	0.0	0.0	0.0	0.0
ES up	6.6	5.2	0.0	0.0	0.0	0.0
ES dn	-13.1	-3.1	0.0	0.0	0.0	0.0
Hrw E_T corrs	-0.5	0.7	-0.0	0.0	0.0	0.0
$\eta + \sigma$	2.9	1.0	-1.3	32.1	-25.8	0.0
$\eta - \sigma$	-7.1	1.6	1.7	-2.6	-66.3	0.0
$E_T + \sigma$	12.0	2.2	1.5	0.0	0.0	0.0
$E_T - \sigma$	-11.1	3.2	-0.0	0.0	0.0	0.0
$y_{jb} + \sigma$	0.0	0.1	-0.7	-4.0	-8.5	0.0
$y_{jb} - \sigma$	0.0	-1.0	-1.4	-10.6	-12.4	0.0
$x_\gamma^{obs} + \sigma$	-4.0	0.8	-6.1	-0.5	5.0	0.0
$x_\gamma^{obs} - \sigma$	-1.3	-1.3	0.7	-5.5	-4.2	0.0
MC weights	0.4	0.5	0.3	0.3	-0.4	0.0
Herwig	23.0	1.6	5.7	1.6	-5.3	0.0
Vtx up	0.5	-0.3	-0.8	-1.0	-1.5	0.0
Vtx dn	2.2	-0.8	-0.7	-6.7	2.8	0.0
Trks up	0.1	-0.5	-2.9	-7.6	1.1	0.0
Trks dn	-0.0	0.5	-0.1	-0.2	-0.3	0.0
Miss E_T up	0.7	1.1	0.9	-0.4	-0.3	0.0
Miss E_T dn	2.0	0.3	-1.5	-16.0	0.5	0.0
E_e up	0.0	0.0	0.0	0.0	0.0	0.0
E_e dn	0.0	0.0	0.0	0.0	0.0	0.0
y_{el} up	0.0	-0.2	-0.8	-7.4	1.0	0.0
y_{el} dn	0.0	0.2	-0.2	-0.4	-0.6	0.0
CTEQ4L	54.7	-4.3	-2.5	-13.0	44.9	0.0
WHIT2	52.7	0.1	3.2	-5.5	-3.4	0.0

Table K.18: Systematic uncertainties for the measurement of the differential cross-section with respect to x_p^{obs} ($x_\gamma^{obs} > 0.75$, OptF).

Systematic	1	2	3	4	5	6
Nominal	0.0	0.0	0.0	0.0	0.0	0.0
ES up	10.6	0.0	0.0	0.0	0.0	0.0
ES dn	-8.1	0.0	0.0	0.0	0.0	0.0
Hrw E_T corrs	0.5	0.0	0.0	0.0	0.0	0.0
$\eta + \sigma$	-0.9	0.0	0.0	0.0	0.0	0.0
$\eta - \sigma$	-1.6	0.0	0.0	0.0	0.0	0.0
$E_T + \sigma$	4.9	0.0	0.0	0.0	0.0	0.0
$E_T - \sigma$	-4.9	0.0	0.0	0.0	0.0	0.0
$y_{jb} + \sigma$	3.4	0.0	0.0	0.0	0.0	0.0
$y_{jb} - \sigma$	-0.0	0.0	0.0	0.0	0.0	0.0
$x_\gamma^{obs} + \sigma$	0.3	0.0	0.0	0.0	0.0	0.0
$x_\gamma^{obs} - \sigma$	-0.3	0.0	0.0	0.0	0.0	0.0
MC weights	0.4	0.0	0.0	0.0	0.0	0.0
Herwig	5.5	0.0	0.0	0.0	0.0	0.0
Vtx up	-0.3	0.0	0.0	0.0	0.0	0.0
Vtx dn	0.1	0.0	0.0	0.0	0.0	0.0
Trks up	-0.2	0.0	0.0	0.0	0.0	0.0
Trks dn	0.1	0.0	0.0	0.0	0.0	0.0
Miss E_T up	0.3	0.0	0.0	0.0	0.0	0.0
Miss E_T dn	-0.8	0.0	0.0	0.0	0.0	0.0
E_e up	0.0	0.0	0.0	0.0	0.0	0.0
E_e dn	0.0	0.0	0.0	0.0	0.0	0.0
y_{el} up	-0.6	0.0	0.0	0.0	0.0	0.0
y_{el} dn	0.3	0.0	0.0	0.0	0.0	0.0
CTEQ4L	0.5	0.0	0.0	0.0	0.0	0.0
WHIT2	0.8	0.0	0.0	0.0	0.0	0.0

Table K.19: Systematic uncertainties for the measurement of the differential cross-section with respect to x_p^{obs} ($x_\gamma^{obs} > 0.75$, OptH).

Bibliography

- [1] <http://www-h1.desy.de>
- [2] <http://www-hera-b.desy.de>
- [3] <http://www-hermes.desy.de>
- [4] ZEUS Collaboration, *A detector for HERA*, PRC 87-02
ZEUS Collaboration, *The ZEUS Detector*, DESY Status Report, (1993).
- [5] B.Foster et al., Nucl. Instrum. Methods. **A338** 254 (1994).
- [6] R.Hall-Wilton, N.McCubbin, P.Nylander, M.Sutton, M.Wing, ZEUS-Note 99-024 (1999).
- [7] M.Derrick et al, Nucl. Inst. Meth. **A309** 77 (1991).
A.Andresen et al, Nucl. Inst. Meth. **A309** 101 (1991).
A.Caldwell et al, Nucl. Inst. Meth. **A321** 356 (1992).
A.Bernstein et al, Nucl. Inst. Meth. **A336** 23 (1993).
- [8] H.Bethe and W.Heitler, Proc.Roy.Soc. **A146** 83 (1934).
- [9] O. Kind *et al.*, eConf **C0303241** (2003) MOLT002 [arXiv:hep-ex/0305095].
- [10] Rene Brun and Fons Rademakers, *ROOT - An Object Orientated Data Analysis Framework*, Proceedings AIHENP'96 Workshop, Lausanne, Sep.1996, Nucl.Inst.& Meth. in Phys.Res. **A 389** 81-86 (1997). See also <http://root.cern.ch>.
- [11] See for example: Robin Devenish and Amanda Cooper-Sarkar, *Deep Inelastic Scattering*, Oxford University Press (2004).

-
- [12] B.R.Martin and G.Shaw, *Particle Physics*, Wiley (1992).
- [13] V. N. Gribov and L. N. Lipatov, *Sov. J. Nucl. Phys.* **15** 438 (1972)
Yu. L. Dokshitzer, *Sov. Phys. JETP* **46** 641 (1977)
G. Altarelli and G. Parisi, *Nucl. Phys.* **B126** 298 (1977).
- [14] C. F. von Weizsacker, *Z. Phys.* **88** 612 (1934)
E.J. Williams, *Phys. Rev.* **45** 729 (1934).
- [15] M.H.Seymour, *Jet Phenomenology*, hep-ph/9707349
- [16] S. Catani, Yu. L. Dokshitzer, M. H. Seymour and B. R. Webber, *Longitudinally invariant k_T clustering Algorithms for Hadron-Hadron collisions*, *Nucl. Phys.* **B406** 187 (1993).
- [17] S.D.Ellis and D.E.Soper, *Successive combination jet algorithm for hadron collisions*, *Phys.Rev.* **D48** 3160 (1993).
- [18] R.Donaldson (ed.) and J.N.Marx (ed.), *Physics of the superconducting supercollider*, Proceedings, Snowmass, USA, June 23-July 11, 1986.
- [19] S.Frixione, *A general approach to jet cross-sections in QCD*, *Nucl.Phys.* **B507** 295 (1997).
- [20] G.Corcella, I.G.Knowles, G.Marchesini, S.Moretti, K.Odagiri, P.Richardson, M.H.Seymour and B.R.Webber, HERWIG 6.5, *JHEP* 0101 (2001) 010, hep-ph/0011363, hep-ph/0210213 (For more information see <http://hepwww.rl.ac.uk/theory/seymour/herwig/>)
- [21] B.I.Ermolaev and V.S.Fadin, *JETP Lett.***33**, 269 (1981);
A.H.Mueller, *Phys.Lett.***B104**, 161 (1961).
- [22] J.M.Butterworth, J.R.Forshaw and M.H.Seymour,*Z.Phys.* **C 72** 637 (1996).
- [23] R.Saunders, *A measurement of Dijet Photoproduction at HERA using the ZEUS Detector*, Ph.D Thesis, UCL (1997).
- [24] ZEUS Collab.,J.Breitweg et al.,*Eur. Phys. J.* **C1** 1/2 109 (1998).
- [25] T.Sjöstrand et al., *Computer Phys.Commun.* **135** 238 (2001).
- [26] B.R.Webber,*Nucl.Phys.* **B 238** 192 (1984).

-
- [27] CTEQ Collab., *Global QCD analysis of Parton structure of the Nucleon: CTEQ5 Parton distributions*, hep-ph/9903282
- [28] M.Glück,E.Reya and A.Vogt, *Photonic parton distributions.*, Phys.Rev. **D 46** 1973 (1992)
- [29] G.A.Schuler and T.Sjöstrand, Phys.Lett. **B 300** 169 (1993).
- [30] A.Anderson et al.,*Parton fragmentation and string dynamics*, Phys.Rep. **97** 31 (1983).
- [31] T.Sjöstrand. *The Lund Monte Carlo for jet fragmentation and e^+e^- physics: JETSET version 6.2*, Comp.Phys.Comm. **39** 347 (1986).
- [32] T.Sjöstrand and M.Bengtsson, *The Lund Monte Carlo for jet fragmentation and e^+e^- physics: JETSET version 6.3: and update*, Comp.Phys.Comm. **43** 367 (1987)
- [33] AMADEUS
<http://www-zeus.desy.de>
- [34] MOZART (Monte carlo for Zeus Analysis, Reconstruction and Trigger)
<http://www-zeus.desy.de>
- [35] CZAR (Complete ZGANA Analysis Routines).
<http://www-zeus.desy.de>
- [36] FUNNEL-The ZEUS Monte Carlo Production Facility.
<http://www-zeus.desy.de>
- [37] J.Bromley et al,HZTOOL,Proceedings of the Workshop *Future Physics at HERA*, edited by G.Ingleman,A.De Roeck,R.Klanner, DESY 96-235, Vol.1 p611. For further details see <http://www.cedar.ac.uk>.
- [38] M.S.Lightwood, *Dijet Production and Multiscale QCD at HERA..* Ph.D.Thesis, UCL (2004).
- [39] G.Altarelli and G.Martinelli, Phys. Lett. **B 76** 89 (1978).
- [40] ZEUS Collab.,S.Chekanov et al,*A ZEUS next-to-leading-order QCD analysis of data on deep inelastic scattering*, Phys. Rev.**D67**, 012007 (2003).

-
- [41] A.M.Cooper-Sarkar,C.Gwenlan,C.Collins-Tooth,*NLO QCD fits using ZEUS data alone*, ZEUS technical note, available from http://www-zeus.desy.de/ZEUS_ONLY/zeus_notes/index.php3 (ZN-04-001)
- [42] ZEUS Collab.,S.Chekanov et al.,*An NLO QCD analysis of inclusive cross-section and jet-production data from the ZEUS experiment*, submitted to Eur. Phys. J. C. Available from http://www-zeus.desy.de/zeus_papers/zeus_papers.html (DESY-05-050).
- [43] ZEUS Collab.,S.Chekanov et al.,Eur. Phys. J. C **21** 443 (2001).
- [44] Particle Data Group, D.E.Groom et al.,Eur.Phys.J. C **15** 1 (2000).
- [45] ZEUS Collab.,J.Breitweg et al.,Eur.Phys.J. C **12** 411 (2000).
- [46] ZEUS Collab.,S.Chekanov et al.,Phys.Lett. B **539** 197 (2002).
- [47] ZEUS Collab.,S.Chekanov et al.,Eur.Phys.J. C **28** 175 (2002).
- [48] ZEUS Collab.,S.Chekanov et al.,Eur.Phys.J. C **32** 1 (2003).
- [49] ZEUS Collab.,S.Chekanov et al.,Phys.Rev. D **70** 052001 (2004).
- [50] ZEUS Collab.,S.Chekanov et al., Phys.Lett. B **547** 164 (2002).
- [51] ZEUS Collab.,S.Chekanov et al., Eur.Phys.J. C **23** 615 (2002).
- [52] P.Amaudruz et al., Phys.Lett.B **295**, 159 (1992).
- [53] P.Amaudruz et al., Phys.Rev.Lett.**66**, 2712 (1991).
- [54] R.S.Towell et al., Phys.Rev.D **64**, 052002 (2002).
- [55] CCFR Collab., A.O.Bazarko et al., Z.Phys.C **65**, 189 (1995).
- [56] G.P.Zeller et al., Phys.Rev.Lett.**88**, 091802 (2002).
- [57] F.James, *Minuit v94.1*, CERN Program Library Long Writeup D506 (unpublished), available from <http://wwwinfo.cern.ch/asdoc/minuit/minmain.html>
- [58] C.Pascaud and F.Zomer, Preprint LAL-95-05, LAL (1995).

- [59] J.Botts et al.,Phys.Lett. **B304** 159 (1993).
CTEQ Coll., H.L.Lai et al., Phys.Rev. **D51** 4763 (1995).
CTEQ Coll., H.L.Lai et al., Eur.Phys.J. **C12** 375 (2000)
- [60] A.D.Martin et al.,Eur.Phys.J. **C4** 463 (1998).
A.D.Martin et al.,Eur.Phys.J. **C14** 133 (2000).
A.D.Martin et al.,Eur.Phys.J. **C23** 73 (2002).
- [61] M.Botje, QCDNUM version 16.12 (unpublished).
- [62] H.L.Lai et al.,Preprint hep-ph/0201195 (2002).
- [63] H.L.Lai et al.,Preprint hep-ph/9903282 (1999).
- [64] H.L.Lai et al.,Phys.Rev. **D55** 1280 (1997)
H.L.Lai et al.,Z.Phys.**C74** 463 (1997)
- [65] A.D.Martin et al.,Preprint hep-ph/0110215 (2002).
- [66] <http://www-bdnew.fnal.gov/tevatron/>
- [67] <http://lhc.web.cern.ch/lhc/>
- [68] The LEP Electroweak Working Group and the SLD Heavy Flavour Group,
Note LEPEWWG/2003-01, <http://lepewwg.web.cern.ch/LEPEWWG>
- [69] A.Djouadi and S.Ferrag, Preprint hep-ph/0310209 (2003).
- [70] S.Alekhin, Phys.Rev. **D63** 094022 (2001) and Phys.Rev.**D68** 014002 (2003).
- [71] C.Targett-Adams, private communication, available from <http://www-zeus.desy.de/target/gluon/gluon.html>.
- [72] ZEUS Collab., S.Chekanov et al., Phys.Lett. **B560** 7 (2003)
- [73] J.Breitweg et al., Dijet Cross Sections in Photoproduction at HERA,
Eur.Phys.J. **C1** 109 (1998).
- [74] W.T.Giele, E.E.N.Glover and D.A.Kosower, The two jet differential cross-section at $\mathcal{O}(\alpha_s^3)$ in hadron collisions, Phys.Rev.Lett. **73** 2019 (1994).
- [75] G.F.Hartner et al.,ZEUS-Note 96-013 (1996).

- [76] A.Savin, ZEUS-Note 98-007 (1998).
- [77] G.Briskin and A.Caldwell, ZEUS-Note 95-035 (1995).
- [78] Energy scale study performed by A.Tapper et al. See http://www-zeus.desy.de/tapperad/ZEUS_ONLY/nc/escale_had.php for details.
- [79] A.Tapper, ZEUS Phantom library
- [80] H.Abramowicz, A.Caldwell, R.Sinkus, Nucl.Inst.Meth. **A365** 508-517 (1995).
- [81] S.Bentvelsen, J.Engelen, P.Kooijman, in *Physics at HERA*, Vol.1, edited by W.Buchmüller, G.Engelman (Proceedings of the workshop, Hamburg 1991), p.23.
- [82] F.Jacquet and A.Blondel, Proceedings of “Study of an *ep* facility for Europe”, Hamburg, ed.U.Amaldi, DESY 79-48, 391 (1979).
- [83] C.Glasman and J.Terron, ZEUS-Note 01-051 (2001).
- [84] C.Glasman and J.Terron, ZEUS-Note 02-024 (2002).
- [85] C.Glasman, *Jet Production at HERA with the ZEUS Detector: Resolved and Direct Processes in Photoproduction and the Gluon Content of the Proton and Photon*, Ph.D Thesis, Weizman Institute of Science (1995).
- [86] R.Goncalo, *Measurement of the high- Q^2 neutral current deep inelastic scattering cross sections with the ZEUS detector at HERA*, Ph.D Thesis, Imperial College London (2003).
- [87] D.Chapin, *A measurement of dijet production in neutral current deep inelastic scattering with ZEUS at HERA*, Ph.D Thesis, University of Wisconsin (2001).
- [88] ZEUS Global First Level Trigger
<http://www-zeus.desy.de/components/gflt/>
- [89] ZEUS Global Second Level Trigger
<http://www-zeus.desy.de/components/gslt/>

-
- [90] ZEUS Global First Level Trigger
<http://www-zeus.desy.de/components/tlt/WWW/>
- [91] Matthew Wing, private communication. Available from: http://www-zeus.desy.de/wing/ZEUS/jets/paper_drafts/control1.ps.gz
- [92] M.Glück,E.Reya and A.Vogt, Phys.Rev. **D 45** 3986 (1992)
M.Glück,E.Reya and A.Vogt, Phys.Rev. **D 46** 1973 (1992)
- [93] P.Aurenche, J.Guillet and M.Fontannaz, Z.Phys. **C 64** 621 (1994)
- [94] C.Cornet, P.Jankowski and M.Krawczyk, Phys.Rev. **D 70** 093004 (2004).
- [95] P.Aurenche, J.Guillet and M.Fontannaz, Preprint hep-ph/0503259 (2005).
- [96] W.Slominski, H.Abramowicz and A.Levy, hep-ph/0504003 (2005).
- [97] K.Hagiwara, M.Tanaka and I.Watanabe, Phys.Rev. **D51** 3197 (1995).
- [98] Matthew Wing, private communication.
- [99] ZEUS Collab.,S.Chekanov et al., awaiting publication, available from http://www-zeus.desy.de/zeus_papers/zeus_papers.html (DESY-05-132).
- [100] S.Frixione and B.R.Webber, JHEP **0206** 029 (2002)
S.Frixione, P.Nason and B.R.Webber, JHEP **0308** 007 (2003).
- [101] C.Cornet, P.Jankowski and M.Krawczyk, hep-ph/0404063 (2004).
- [102] ZEUS Collab.,J.Breitweg et al., Eur.Phys.J. **C7** 609 (1999)
ZEUS Collab.,J.Breitweg et al., Eur.Phys.J. **C21** 443 (2001)